

Syracuse University

**SURFACE**

---

Dissertations - ALL

SURFACE

---

December 2017

## **Rectangular Waveguide Filled with Uniaxial Medium and Negative Resistance Enhanced Composite Right/Left-Handed Transmission Line**

Kepei Sun  
*Syracuse University*

Follow this and additional works at: <https://surface.syr.edu/etd>



Part of the [Engineering Commons](#)

---

### **Recommended Citation**

Sun, Kepei, "Rectangular Waveguide Filled with Uniaxial Medium and Negative Resistance Enhanced Composite Right/Left-Handed Transmission Line" (2017). *Dissertations - ALL*. 814.

<https://surface.syr.edu/etd/814>

This Dissertation is brought to you for free and open access by the SURFACE at SURFACE. It has been accepted for inclusion in Dissertations - ALL by an authorized administrator of SURFACE. For more information, please contact [surface@syr.edu](mailto:surface@syr.edu).

## Abstract

Two wave-guiding problems are treated in this work. The first part addresses the problem of a rectangular waveguide filled with a uniaxially anisotropic or uniaxial medium. Different orientations of the optic axis of the uniaxial medium are considered and the wave transmission and modal behaviors are investigated. When the optic axis is aligned with one of the coordinate axes, i. e., x, y, or z axis, the method of wave decomposition with respect to the optic axis orientation is proposed and the complete analytic solutions are presented and compared with conventional transverse-to-z solutions. When the optic axis is tilted but lying in one of the side wall planes,  $TE_{0n}$  or  $TE_{m0}$  (transverse to z) modes are shown to be supported. Furthermore, the supported hybrid wave modes in these cases are numerically found from calculations using the proposed boundary condition matrix (BCM) method. Different from the conventional spectral domain calculation methods, the numerically found hybrid wave modes are expressed as a linear combination of ordinary and extraordinary waves. The algorithm is illustrated and numerical examples are given. The validity of the solution is verified by comparing its results with those of the aligned cases that are analytically solved.

The second wave-guiding structure is focused on a type of metamaterial realization. Analyses and experimental results of the negative resistance enhanced composite right/left-handed (NR-CRLH) transmission line are presented. As a demonstration of its unique amplitude and phase behaviors and its application, the detailed analysis of the structure is followed by an example of high-directivity leaky-wave antenna (LWA). In contrast to the conventional CRLH unit cell with via terminated stubs, the NR-CRLH unit cell is designed with negative-resistance (NR) terminated stub that compensates the power loss from the orthogonal direction with respect to the direction of guided-wave propagation. The NR is realized using the inverted common collector (ICC)

configuration of an RF transistor, a common commercial product often seen for RF amplifier and oscillator applications. This implementation topology allows the active unit cell (AUC) to preserve all the CRLH properties including the unique dispersion relations, constant Bloch impedance in a broad operating frequency range, and bilateral operation. To highlight the advantages of the active metamaterial transmission line (TL), the NR-CRLH TL based LWA that permits the manipulation of the current distributions over the antenna surface is demonstrated. The NR-CRLH based active antenna allows the control of radiation performances including the patterns, beamwidth, and directivity. The measured results of the LWA prototype demonstrate enhanced directivity compared to the conventional CRLH LWA of the same lengths while minimally influencing all the preferable characteristics of full frequency scanning LWA.

**Rectangular Waveguide Filled with Uniaxial Medium  
and  
Negative Resistance Enhanced Composite Right/Left-Handed  
Transmission Line**

By  
Kepei Sun

B.E., North China University of Technology, 2006

M.S., Syracuse University, 2012

Dissertation

Submitted in partial fulfillment of the requirement for the Degree of Doctor of Philosophy in  
Electrical and Computer Engineering.

Syracuse University

December 2017

Copyright © 2017 Kepei Sun  
All Rights Reserved

## **Acknowledgement**

First, I would like to thank my advisor, Professor Jay Kyoon Lee, and my co-advisor, Professor Jun Hwan (Brandon) Choi. Professor Lee has been my mentor and provided considerable valuable guidance that will not only help me complete my study but also benefit many aspects of my future career. I thank Professor Lee for encouraging and guiding me through my entire research and study in graduate school at Syracuse University. I also would like to express my gratitude to Professor Lee for allowing great flexibility when I was exploring different fields of study. Professor Choi guided me during the second half of my whole PhD study. His creativity and enthusiasm in the broad and fast paced field of microwave technologies always inspired and impassioned me. Sometimes, my family (and my work, particularly in the last year of my study) needed my full attention. I truly appreciate Professor Lee's patience in those least productive periods of time.

Secondly, I would like to thank the professors on my defense committee, including Professor Thong Quoc Dang who chaired the committee, Professor Qiwang Song, Professor M. Cenk Gursoy, and Professor Jennifer Warzala Graham. Reading this work and giving meaningful comments can consume excessive amount of time. I appreciate all the feedback from the committee members.

Last but not the least, I would like to thank my beloved wife, Chonghui Huang, and my lovely daughter Isabella for their patience and support. I owe Chonghui, Isabella and my little son, Johnathan so much time of company. I also wholeheartedly appreciate my parents' patience and support, without which I could not have finished my study.

# Contents

List of Figures .....	xi
List of Tables .....	xxii
Chapter 1 Introduction .....	1
Chapter 2 Rectangular Waveguide Filled with Uniaxial Medium – Aligned Cases .....	9
2.1. Formulation.....	10
2.1.1. Isotropic Case – Formulation.....	11
2.1.2. Isotropic Case – Field Solutions .....	15
2.1.3. Tensors for Uniaxial Media .....	16
2.1.4. Uniaxial-z Case – Formulation .....	18
2.1.5. Uniaxial-z Case – Solution .....	19
2.2. Generalized Cases .....	23
2.2.1. Uniaxial-x and Uniaxial-y Cases .....	24
2.2.2. General Formulation .....	26
2.3. Results.....	29
2.3.1. Mode Decomposition in Uniaxial-x Case.....	29
2.3.2. Mode Decomposition in Uniaxial-y Case.....	32
2.3.3. Dominant Modes.....	34
2.3.4. Guided Wave Impedance .....	38

2.3.5. Field Distributions .....	39
2.3.6. Attenuation Constants .....	45
2.4. Summary .....	46
Chapter 3 Rectangular Waveguide Filled with Uniaxial Medium – Tilted Cases.....	47
3.1. Constitutive Relations .....	48
3.1.1. Rotation in Cross-Section Plane .....	50
3.1.2. Rotation in Side Wall Plane .....	51
3.2. Analytical Solution .....	53
3.3. Hybrid Mode Solutions.....	56
3.3.1. Free Space Wave Formulation.....	57
3.3.2. Reflection Behaviors.....	60
3.3.3. Travelling Wave Formulation.....	64
3.3.4. Computational Process.....	69
3.4. Solution Example.....	70
3.4.1. Analytical Solution .....	71
3.4.2. Hybrid Solution Preparation .....	71
3.4.3. Matrix Solutions.....	76
3.4.4. Finding Dominant Mode.....	83
3.5. Verification .....	84



3.5.1. Comparison with the Uniaxial-z Case .....	84
3.5.2. Comparison with the Uniaxial-y Case .....	87
3.6. Modal Behaviors .....	89
3.6.1. The Effect of Relative Permittivity.....	90
3.6.2. The Effect of the Tilting Angle.....	91
3.6.3. The Effect of the Dimension.....	93
3.7. Field Distributions .....	94
3.8. Summary .....	98
Chapter 4 NR-CRLH Transmission Line Metamaterial .....	100
4.1. A Brief History of the CRLH Structure.....	102
4.2. Fundamentals of CRLH Transmission Line .....	103
4.2.1. Conventional TL and LH TL .....	104
4.2.2. CRLH TLs .....	105
4.2.3. CRLH Unit Cell Layout.....	107
4.2.4. IDC Simulations.....	113
4.2.5. Short-Stub Simulations .....	115
4.2.6. CRLH Unit Cell ECM .....	117
4.2.7. Symmetric CRLH Unit Cell ECM.....	120
4.2.8. Calculation Example.....	122

4.3. Negative Resistance .....	126
4.3.1. Negative Resistance and Typical Applications in Amplifiers .....	126
4.4. ICC NR Circuit .....	129
4.4.1. Active Inductors .....	131
4.4.2. Mathematical Models.....	132
4.4.3. Circuit Analysis and Simulations.....	135
4.4.4. Post Layout Simulations .....	141
4.4.5. Circuit Prototype.....	143
4.5. NR-CRLH Unit Cell .....	146
4.5.1. Short Stub Revisit .....	146
4.5.2. The NR Terminated Stub .....	148
4.5.3. Equivalent Circuit Model.....	151
4.5.4. Active ECM Calculation Example.....	152
4.6. Simulation, Fabrication and Measurement .....	157
4.6.1. Simulation .....	158
4.6.2. Fabrication and Measurement.....	160
4.7. Summary .....	162
Chapter 5 NR-CRLH TL Based Leaky-Wave Antenna .....	163
5.1. Leaky-Wave Antenna .....	164

5.2. LWA Analysis .....	165
5.2.1. Travelling Wave Antenna .....	167
5.2.2. Arbitrary Decaying Current Distribution .....	168
5.3. CRLH LWA .....	171
5.3.1. Simulated Radiation Performances .....	173
5.3.2. Effect of Loss .....	175
5.3.3. Array Method .....	176
5.4. Mixed Design .....	179
5.4.1. An 11-Unit-Cell Design Example .....	182
5.4.2. Explanations .....	189
5.5. Summary .....	190
Chapter 6 Conclusions .....	192
Bibliography .....	196
Vita .....	210

## List of Figures

Figure 2-1	A rectangular waveguide and its dimensions.....	11
Figure 2-2	A rectangular waveguide in the uniaxial-z case.....	18
Figure 2-3	Dominant mode changes when the degree of anisotropy changes.....	36
Figure 2-4	Dominant mode changes as the degree of anisotropy ( $\epsilon_x / \epsilon_t$ ) changes in uniaxial-x case.....	37
Figure 2-5	Dominant mode changes as the degree of anisotropy ( $\epsilon_y / \epsilon_t$ ) changes in uniaxial-y case.....	38
Figure 2-6	Field distributions of the $TM_{31}$ mode in the uniaxial-z case and the isotropic case. Dimension ratio is $a/b = 2$ . The uniaxial-Z case has $\epsilon_z / \epsilon_t = 2.5$ .....	40
Figure 2-7	Field distribution of the $TM_{Z31}$ Modes in the isotropic case.....	41
Figure 2-8	Contours showing the equal-magnitude curves in the isotropic case. ....	41
Figure 2-9	Field distribution of the $TM_{X31}$ Modes in the uniaxial-x case. ....	42
Figure 2-10	Contours showing the equal-magnitude curves in the uniaxial-x case. ....	42
Figure 2-11	Field distribution of the $TM_{X31}$ Modes in the uniaxial-x case. ....	43
Figure 2-12	Contours showing the equal-magnitude curves in the uniaxial-y case. ....	43
Figure 2-13	Field distribution of the $TM_{Y31}$ Modes in the uniaxial-y case. ....	44
Figure 2-14	Contours showing the equal-magnitude curves in the uniaxial-y case. ....	44

Figure 3-1 Demonstration of Euler Angles in transformation matrices. The most general transformation takes three rotations but may use two or three rotation matrices. .... 49

Figure 3-2 Optic axis tilts from x axis and lies in the cross section plane..... 50

Figure 3-3 Optic axis tilts from the z axis and lies in the y-z plane. .... 52

Figure 3-4 Reflection on  $x=0$  plane is a simple case in which the incidence angle and the reflection angle are same,  $\theta_i=\theta_r$  ..... 62

Figure 3-5 Reflection on  $y=0$  plane causes double reflection. Birefringence phenomenon is observed. .... 63

Figure 3-6 (Color) The curves of  $k_y$  values corresponding to the Table 3-4 min and max values. The yellow curve shows the set of  $k_y$  values at the index  $m=6$  (top left curve). Magenta  $m=5$ , red  $m=4$ , cyan  $m=3$ , green  $m=2$ , and blue  $m=1$  (bottom right curve). .... 74

Figure 3-7 (Color) The curves of  $k_y$  values corresponding to the Table 3-5 min and max values. The yellow curve shows the set of  $k_y$  values at the index  $m=6$  (bottom left curve) while the blue shows  $m=1$ (top right curve). Magenta  $m=5$ , red  $m=4$ , cyan  $m=3$ , and green  $m=2$ . .... 75

Figure 3-8 (Color) The curves of  $k_y$  values corresponding to the Table 3-7 min and max values. The yellow curve shows the set of  $k_y$  values at the index  $m=6$  (top left curve) while the blue shows  $m=1$  (bottom right curve). Magenta  $m=5$ , red  $m=4$ , cyan  $m=3$ , and green  $m=2$ . ..... 75

Figure 3-9 (Color) The curves of  $k_y$  values corresponding to the Table 3-6 min and max values. The yellow curve shows the set of  $k_y$  values at the index  $m=6$  (bottom left curve) while the blue shows  $m=1$  (top right curve). Magenta  $m=5$ , red  $m=4$ , cyan  $m=3$ , and green  $m=2$ . .... 76

Figure 3-10 BCM determinant curves versus  $k_z$  values with  $m=1$ , taking absolute value, real part, imaginary part and phase.  $f=10\text{GHz}$ . .... 77

Figure 3-11	BCM determinant curves versus $k_z$ values with $m=2$ , taking absolute value, real part, imaginary part and phase. $f=10$ GHz. ....	78
Figure 3-12	BCM determinant curves versus $k_z$ values with $m=3$ , taking absolute value, real part, imaginary part and phase. $f=10$ GHz. ....	79
Figure 3-13	BCM determinant curves versus $k_z$ values with $m=4$ , taking absolute value, real part, imaginary part and phase. $f=10$ GHz. ....	80
Figure 3-14	BCM determinant curves versus $k_z$ values with $m=5$ , taking absolute value, real part, imaginary part and phase. $f=10$ GHz. ....	81
Figure 3-15	BCM determinant curves versus $k_z$ values with $m=6$ , taking absolute value, real part, imaginary part and phase. $f=10$ GHz. ....	82
Figure 3-16	The change of the cutoff frequency of the lowest hybrid mode as the relative permittivity along the optic axis increases. $\epsilon_t = 3$ . ....	91
Figure 3-17	The change of the cutoff frequency of the lowest hybrid mode as the tilting angle increases. $\epsilon_t = 3$ , $\epsilon_z = 4$ . ....	92
Figure 3-18	The change of the cutoff frequency of the lowest hybrid mode as the waveguide dimension $a$ changes while dimension $b$ remains at $b=2.7945$ cm. $\epsilon_t = 3$ , $\epsilon_z = 4$ . ....	94
Figure 3-19	Field distribution of the first example over the cross-section of the waveguide filled with uniaxial medium with tilted optic axis. ( $\alpha=30^\circ$ ).....	95
Figure 3-20	Contour plot of the field distribution of the first example over the cross-section of the waveguide filled with uniaxial medium with tilted optic axis ( $\alpha=30^\circ$ ).....	96

Figure 3-21	Field distribution of the second example over the cross-section of the waveguide filled with uniaxial medium with tilted optic axis. ( $\alpha=30^\circ$ ) .....	96
Figure 3-22	Contour plot of the field distribution of the second example over the cross-section of the waveguide filled with uniaxial medium with tilted optic axis. ( $\alpha=30^\circ$ ).....	97
Figure 3-23	Contour plot of the limiting case field distribution of the second example over the cross-section of the waveguide filled with uniaxial medium with almost aligned optic axis. ( $\alpha=0.1^\circ$ ).....	97
Figure 4-1	Unit cell of the conventional CRLH periodic structure (with regular input/output transmission lines). The number of pair of fingers shown in the figure is 3. ....	103
Figure 4-2	Voltage and current definitions and the equivalent circuit for an incremental length of a conventional transmission line.....	104
Figure 4-3	Voltage and current definitions and the equivalent circuit for an incremental length of a left-handed transmission line. ....	105
Figure 4-4	Demonstration of three unit cells in an infinitely long periodic structure (between semi-infinite section on the left and semi-infinite section on the right). ....	106
Figure 4-5	A 10-unit-cell CRLH TL transitioned to a 50 Ohm microstrip line without tapering. ....	106
Figure 4-6	(Figure 9(a) in [80]) Presence of a 24-unit-cell CRLH TL with normal transmission lines and SMA connections. Tapering can be observed on both terminals of the CRLH TL.....	107
Figure 4-7	The 3-D model drawn in HFSS simulation software with feeding lines 20 mm. ....	108

Figure 4-8	Return loss of the simulated unit cell with stub length as 8.8 mm, 9 mm, 9.1 mm, and 9.2 mm.....	109
Figure 4-9	Insertion loss of the simulated unit cell with stub length as 8.8 mm, 9 mm, 9.1 mm, and 9.2 mm. ....	110
Figure 4-10	Dispersion diagram calculated from the simulated unit-cell S-parameters with stub length as 8.8 mm, 9 mm, 9.1 mm, and 9.2 mm. ....	111
Figure 4-11	Bloch impedance (real part) of the unit cell calculated from the simulated S-parameters with stub length as 8.8 mm, 9.0 mm, 9.1 mm, 9.2 mm. ....	112
Figure 4-12	IDC model (top view) in HFSS simulation software. The substrate is the 62 mil thick Rogers RT/duroid 5880 with dielectric constant equal to 2.2 and loss tangent 0.0009. The IDC figure width is 0.3 mm and the gaps measure 0.2 mm.....	114
Figure 4-13	a) The ECM of an IDC. b) The $\pi$ -network of the IDC ECM. ....	114
Figure 4-14	The short-stub model (top view) in HFSS simulation software. The small circle on the end of the stub is the via connecting to the ground plane of the microstrip line stack-up. ....	116
Figure 4-15	a) The ECM of a short stub. b) The T-network of the short-stub ECM.....	116
Figure 4-16	ECM of CRLH unit cell including lossy elements. Ideal loss-free unit cell ECM has no $R_{se}$ and $G_{sh}$ components. ....	118
Figure 4-17	ECM of CRLH unit cell in the symmetric form including lossy elements. Ideal loss-free unit cell ECM has no $R_{se}$ and $G_{sh}$ components.....	120



Figure 4-18 Combining the ECMs of IDC and short-stub to form an asymmetric unit cell model.....	122
Figure 4-19 Matlab plotted return loss (left) and insertion loss (right) of the unit cell ECM with $Z_0$ terminated on both ports. ....	123
Figure 4-20 Matlab plotted the calculated dispersion relation (left) and the phase propagation (right) across the unit cell ECM.....	124
Figure 4-21 Bloch impedance calculation based on the symmetric model (left) and the asymmetric model (right). The asymmetric model results in less resistance. ....	125
Figure 4-22 A schematic of the two-port amplifier using one-port amplification mechanism and a circulator to isolate the input and output signals. Figure is a duplicate of Fig. 6 in [41] in the year of 1979. ....	127
Figure 4-23 A photo of the two-port waveguide amplifier with one-port amplification and a circulator. Figure is a duplicate of Fig. 4 in [91] in the year of 1977. ....	128
Figure 4-24 A schematic of terminating one port of a two-port circuit and use the other port as the NR. The realized NR is used in an amplifier circuit incorporating a circulator. Figure is a duplicate of Fig. 1 in [93]. ....	128
Figure 4-25 Negative resistance circuit and its equivalent model. a) Negative resistance circuit based on a bi-polar junction transistor. b) The equivalent circuit model with an inductor and a negative resistor in series. c) The equivalent circuit model of the via-hole termination at the ends of the short stubs in the CRLH structure. ....	130

Figure 4-26	Schematic of the ICC NR circuit. The dashed line indicates the simplified configuration of grounding the collector terminal directly. $V_{CC}$ is a positive biasing voltage and $V_{EE}$ is negative for NPN transistors. ....	131
Figure 4-27	Duplicate of Fig. 1 in [104]. The input admittance is inductive and minimally lossy. ....	132
Figure 4-28	Conventional common base amplifier circuit schematic. a) Circuit schematic. b) Equivalent circuit model schematic. ....	133
Figure 4-29	ICC circuit and its high-frequency equivalent circuit model. a) ICC circuit used in the BJT-based design. b) The small-signal equivalent circuit model. ....	136
Figure 4-30	ECM with controlled source modeling the current delay. ....	137
Figure 4-31	Simulation results of the transistor model with delayed conductivity. Solid line: input resistance. Dashed curve: input reactance. ....	138
Figure 4-32	Circuit simulation using the SPICE model of the BFG425W from NXP semiconductor. ....	139
Figure 4-33	ICC NR circuit response. The solid curves represent the case when $V_{CC}$ is turned off. The dashed curves represent the case when $V_{CC}$ is turned on at 1 V. a) The simulated S-parameters. b) The simulated input impedance. ....	140
Figure 4-34	(Colored) Layout and post layout simulations. a) Board layout of the circuit (without matching stub). The picture has black background and orange copper feature. b) Mixed simulation with EM results and schematic components. The picture has white background. ....	141
Figure 4-35	Layout design of the circuit with TRL calibration kit on the same board. ....	143

Figure 4-36	NR circuit board with TRL calibration kit built on the same board. ....	144
Figure 4-37	The simulated and measured NR circuit responses without the matching short-stub. The obtained reflection coefficients are converted to input impedance for the observation of negative resistance values. ....	144
Figure 4-38	Layout design and the fabricated NR circuit with matching shorted-stub. ....	145
Figure 4-39	The simulated and measured NR circuit responses with the matching short-stub. The obtained reflection coefficients are converted to input impedance for the observation of negative resistance values. ....	146
Figure 4-40	A normal CRLH unit cell in a) and an NR-CRLH unit cell in b). ....	147
Figure 4-41	The equivalent circuit model of a NR-CRLH unit cell with NR-terminated stub. ....	151
Figure 4-42	The symmetric ECM of an active NR-CRLH unit cell including lossy elements and possibly negative effective resistor $R_e$ . ....	152
Figure 4-43	The exponential $R_e$ model used in the ECM calculations. ....	153
Figure 4-44	Return loss of the ECM model with different $R_e$ values. ....	154
Figure 4-45	Insertion loss or gain of the four ECM models with different $R_e$ values. ....	155
Figure 4-46	Dispersion relation curves of the ECM models with different $R_e$ values. In the left figure the solid red curve and the dotted red curves are almost overlapping, and the difference can only be seen in the zoomed-in view (on the right) in proximity of the transition frequency on the right. ....	156

Figure 4-47	The real (resistance) and imaginary parts (reactance) of the Bloch impedance curves with different $R_e$ values. ....	157
Figure 4-48	The unit cell layout simulation with the stub terminated with a port. In schematic simulation the stub end can be connected to a NR circuit through a piece of transmission line.	158
Figure 4-49	a) ADS schematic simulation incorporating the port-terminated unit cell, NR circuit simulation (post-layout) and the tuning/matching shorted stub in between. b) A schematic view of the post-layout simulation with complete copper features. ....	159
Figure 4-50	a) The layout simulation consists of all the unit cell copper features. b) Diagram that demonstrates the post layout simulation of a complete NR-CRLH unit cell including the lumped elements and transistor.....	160
Figure 4-51	Photo of the fabricated NR-CRLH unit cell. The length of the unit cell is 11.4 mm, and the length of the entire board is 21.4 mm. ....	161
Figure 4-52	The measured and simulated results of the active unit cell. LH below 2.3 GHz. RH above 2.3 GHz. a) S parameters. b) Magnified zoom-in view of the insertion loss/gain. ...	161
Figure 5-1	Duplicate of Fig. 1 in [113]. Classification of metamaterials by the real parts of their constitutive parameters, $\epsilon$ and $\mu$ . ....	163
Figure 5-2	The direction of the main beam of a leaky wave antenna [117]. The beam angle $\Phi$ is defined as the complementary angle of $\theta_0$ here.....	166
Figure 5-3	Duplicate of Figure 7-2 in Stutzman and Thiele's antenna textbook [115], demonstrating the travelling wave antenna.....	167
Figure 5-4	Duplicated Fig. 15 in [121]. The slot is engineered to obtain a Gaussian amplitude distribution along the propagation of the slotted waveguide. ....	169

Figure 5-5 Radiation patterns of the LWAs in [121]. a) The radiation pattern of a uniform slot. b) The radiation pattern at different frequencies of a iris slot. .... 170

Figure 5-6 Duplicate of Fig. 1 in [26] describing the relation between radiation and propagation constant. In the cross-section view the wave number is decomposed into the direction of guided wave and the direction of the substrate thickness ( $k_y$ ). .... 172

Figure 5-7 Figure of the LWA with conventional dimensions as described in Chapter 4. The LWA presented in this figure is denoted as LWA-1. .... 173

Figure 5-8 Photo of the LWA with optimized dimensions for consistent radiation performance and lumped element matching capacitor. .... 173

Figure 5-9 HFSS model of a CRLH LWA consists of 11 unit cells. The positive Y direction is toward the right side of the structure. Port-1 is on the left side of the structure ( $y=0$ ). .... 174

Figure 5-10 Simulation LWA radiation pattern in E- plane co-polarization. .... 174

Figure 5-11 Theoretically calculated radiation pattern of multiple current distributions characterized by different attenuation constants. .... 175

Figure 5-12 Calculated radiation patterns of a periodic structure LWA consisted of fifty one unit cells, yet the electrical length is less than  $\lambda$ . The antenna is assigned with different attenuation constants. The antenna is assumed lying along the bottom horizontal line and the wave is excited to travel toward right side (0 degree). Same as the proposed prototype, at 2.1GHz the main beam tilts backward and the phase constant is approximately -10 Radian/m. .... 178

Figure 5-13 An example of LWA with all the unit cells having the same forward gain. The input to termination gain is realized thus the increasing ramp of current distribution. .... 179

Figure 5-14	An example of LWA with alternative passive unit cell and active unit cell. The unit cells having the same forward gain. The antenna has narrower beamwidth. ....	180
Figure 5-15	A diagram of the LWA containing both active unit cells and passive unit cells in the alternating fashion.....	181
Figure 5-16	Photo of the fabricated mixed-design LWA with active unit cells and passive unit cells. Rectangle-A (dashed line) shows the ICC NR circuit; rectangular-B (dashed line) shows a normal unit cell; rectangle-C (dashed line) encloses a matching IDC which makes the periodic structure a symmetric structure. ....	182
Figure 5-17	Measured return losses and insertion losses of the fabricated NRCRLH LWA prototype with biasing voltage turned on and off. The transition frequency is 2.2GHz.....	183
Figure 5-18	Photo of the active LWA mounted in the anechoic chamber. Wires connect DC biasing voltage form the voltage regulator, powered by a lithium-ion battery.....	184
Figure 5-19	Coordinate axes definition diagram. ....	184
Figure 5-20	Measured E-cut radiation patterns of the passive and the active antennas in an anechoic chamber. The patterns are normalized in each frequency for comparison. ....	187
Figure 5-21	Calculated radiation pattern from an 11-unit-cell LWA. ....	189
Figure 5-22	Calculated radiation pattern from a 51-unit-cell LWA. ....	190

## List of Tables

Table 2-1	Modes and Cutoff Frequencies of Uniaxial-z Case.....	23
Table 2-2	Modes and Cutoff Frequencies of Uniaxial-x Case .....	29
Table 2-3	Modes and Cutoff Frequencies of Uniaxial-y Case .....	32
Table 3-1	Analytically obtained wavenumbers for $TE_{z0n}$ modes when the optic axis is tilted but lying in the y-z plane. $f=10$ GHz. $\epsilon_t=3.0$ , $b=27.94$ mm, $k=362.76$ , $k_x=0$ ( $m=0$ ). The $k_y$ values in different modes are listed in the table. The calculated $k_z$ values at 10 GHz are calculated and put in this table.....	71
Table 3-2	Numerical solution starts from calculating the possible $k_x$ values. The possible values in this particular example is listed. ....	72
Table 3-3	Numerical solution need to know the maximum $k_z$ values for each $k_x$ value. ....	72
Table 3-4	The minimum and maximum values of $k_y$ of the extraordinary wave propagating in negative Y direction.....	73
Table 3-5	The minimum and maximum values of $k_y$ of the extraordinary wave propagating in positive Y direction.....	73
Table 3-6	The minimum and maximum values of $k_y$ of the ordinary wave propagating in positive Y direction.....	73
Table 3-7	The minimum and maximum values of $k_y$ of the ordinary wave propagating in negative Y direction.....	73
Table 3-8	Wavenumbers of Hybrid Modes $CM_{1S}$ with $m=1$ at $f=10$ GHz. ....	78

Table 3-9	Wavenumbers of Hybrid Modes $CM_{2S}$ with $m=2$ at $f=10\text{GHz}$ . .....	79
Table 3-10	Wavenumbers of Hybrid Modes $CM_{3S}$ with $m=3$ at $f=10\text{ GHz}$ . .....	80
Table 3-11	Wavenumbers of Hybrid Modes $CM_{4S}$ with $m=4$ at $f=10\text{ GHz}$ . .....	81
Table 3-12	Wavenumbers of Hybrid Modes $CM_{5S}$ with $m=5$ at $f=10\text{ GHz}$ . .....	82
Table 3-13	Analytically calculated propagation constants ( $k_z$ ) of $TE_Z$ modes in the uniaxial-z case. $f=10\text{GHz}$ . $a=57.5\text{mm}$ , $b=27.97\text{mm}$ , $\epsilon_z=4$ , $\epsilon_t=3$ . .....	85
Table 3-14	Analytically calculated propagation constants ( $k_z$ ) of $TM_Z$ modes in the uniaxial-z case. $f=10\text{GHz}$ . $a=57.5\text{mm}$ , $b=27.97\text{mm}$ , $\epsilon_z=4$ , $\epsilon_t=3$ . .....	85
Table 3-15	Numerically calculated propagation constants ( $k_z$ ) when $\alpha=0.1^\circ$ . The results are approaching the analytical solutions in uniaxial-z case. ....	86
Table 3-16	Modes found from the limiting case calculations (Table 3-15) and mapping to Uniaxial-z Modes (Table 3-13 and Table 3-14). .....	86
Table 3-17	Analytically calculated propagation constants ( $k_z$ ) of $TE_Y$ modes in the uniaxial-y case. $f=10\text{GHz}$ . $a=57.5\text{mm}$ , $b=27.97\text{mm}$ , $\epsilon_y=4$ , $\epsilon_t=3$ . ....	87
Table 3-18	Analytically calculated propagation constants ( $k_z$ ) of $TM_Y$ modes in the uniaxial-y case. $f=10\text{GHz}$ . $a=57.5\text{mm}$ , $b=27.97\text{mm}$ , $\epsilon_y=4$ , $\epsilon_t=3$ . ....	87
Table 3-19	Numerically calculated propagation constants when $\alpha=89.9^\circ$ . The results are approaching the analytical solutions in uniaxial-y case. ....	88
Table 3-20	Modes found from the limiting case calculations (Table 3-19) and mapping to uniaxial-y Modes (Table 3-17 and Table 3-18). ....	88



Table 5-1 The measured directivity at different frequencies of the passive antenna (CRLH) and the active antenna (NR-CRLH)..... 188

# Chapter 1 Introduction

Wave-guiding structures are broadly used in all the microwave circuits and systems. They include metallic rectangular/circular waveguides, coaxial cables, microstrip/strip lines, dielectric slab waveguides, optic fibers, and many others. These wave guiding structures form the fundamental elements of various optical and microwave systems. Their propagation characteristics and field distributions must be thoroughly studied so that the guided-wave behaviors can be predicted and used in analysis and synthesis of the systems. With the development of differential equations, homogeneous and isotropic waveguide problems are usually less difficult in solving for the guided-wave characteristics, and in reality these problems provide sufficiently accurate results for fabricated microwave components. However, engineers sometimes find discrepancies between the predicted and measured wave behaviors. Some of these discrepancies are due to the complexity of the dielectric materials. In order to obtain better estimation, engineers came up with various ideas to measure the electrical properties of the materials and adjust the prediction in microwave design process. Both the measurement of the properties and the prediction of the microwave behaviors demand the knowledge of wave propagation in complex media.

Rectangular waveguide (RWG) is a cylindrical wave guiding structure that is comprised of four metallic side walls forming a rectangular cross-section. The properties of a hollow RWG are determined by the dimensions denoted by  $a$  and  $b$  in  $x$  and  $y$  directions, respectively. Marcuvitz's [1] and Collin's [2] books are dedicated to the pertinent waveguide topics. By insertion of various types of media, a third degree of freedom in design of a RWG is introduced. Among many types of anisotropic media, gyromagnetic media were thoroughly studied (fully or partially filled in waveguides), because of the ease of controlling the magnetic property by adjusting the strength of

the external biasing field [3]. For example, ferrite materials are used in RWG to make phase shifters, isolators and other devices mostly documented in [4] and [5]. In recent decades waveguide problems still receive a lot of interest. For example, the rise of so called left-handed materials spurred the plasma simulation using waveguides [6], which then became one of the major implantations of metamaterials by means of negative permeability insertion. One way to model the unusual transmission phenomenon is to consider a waveguide homogeneously loaded with anisotropic media with artificial electric properties.

Uniaxially anisotropic or uniaxial media are often incorporated in various microwave and optical applications. For example, single crystal sapphire was used in microstrip line structures [7] because of its consistent electrical properties, and iron-doped rutile was used to fill a rectangular waveguide [8] because of its paramagnetic property. Except for intentional uses, it is common to see the anisotropy in dielectric substrates and superstrates treated as undesirable, existing naturally or as the byproduct of modern fabrication process [9], though in some instances they may also benefit the circuit design [10]. Due to its broad existence, the uniaxial anisotropy must be accounted for to avoid errors, including but not limited to the resonant-frequency shift of the patch antennas [11] and the dispersive-characteristics change of the transmission lines [12]. The other major application of RWGs filled with dielectric media and other magnetic media is to measure the properties of materials [13], e.g., the biaxial medium [14]. These inverse engineering problems also require ascertaining the transmitting wave modes with the anisotropic insertion before establishing experiments and processing the obtained data.

Birefringent dielectrics also drew considerable attention in the field of integrated optical devices. The  $4 \times 4$  matrix method [15] was widely acknowledged and powerful in addressing problems with layered anisotropic dielectrics. However, this method is not appropriate for an RWG

problem because it ignores one of the transverse derivatives, e.g., the partial derivative with  $y$  is always assumed zero when  $z$  is the direction of guidance.

In the microwave regime, a different  $4 \times 4$  matrix method in spectral domain [16] [17] is of great importance for the analysis of microstrip and strip lines embedded in layered anisotropic superstrates and substrates. This spectral domain analysis (SDA) adopts Fourier transformations to simplify the convolution relations between planar sources and field components parallel to the planar boundaries [18]. The reduced number of field components suffices to construct planar boundary conditions for microstrip and stripline structures that have no side boundaries. However, in a closed waveguide problem the SDA is less efficient. It is justified in [19] that the SDA is not advantageous for certain enclosed waveguide problems. In this dissertation we present a method that neither needs Fourier transformations nor requires the method of moments for numerical calculations. The wave fields are formulated in terms of wavenumbers and the wave propagation characteristics are evaluated in the spectral domain.

It is the objective of this work to analyze the field and mode solutions of the RWGs filled with uniaxial media. Similar to the significance of the biasing field direction for gyrotropic media, the role of the optic axis for uniaxial media is equally critical. It is convenient to categorize the problems as follows.

- 1) Optic axis is aligned to one of the principle axes, namely  $x$ ,  $y$  or  $z$  axis (aligned problems subdivided into uniaxial- $x$ , uniaxial- $y$  and uniaxial- $z$  cases).
- 2) Optic axis is tilted but lying in the cross section plane.
- 3) Optic axis is tilted but lying in the side wall plane (to be discussed in details).

4) Optic axis is tilted but lying in an arbitrary direction and not parallel to any axis or plane (not to be addressed).

The new mode decomposition which leads to complete solutions to all the aligned cases is to be detailed in this work. Part of the solutions to the second type is presented in Davis' work [8] which concerns the computation of phase constant using the variational method. This approach provides the phase constants at different frequencies, but lacks further information on wave modes and field distributions. Type-three will be discussed in this work where the boundary condition matrix (BCM) method is discussed in detail. Numerical examples will be demonstrated along with the explanation to the algorithm. To the author's best knowledge, when the optic axis is arbitrarily oriented (type-four), the problem has not been solved and is also beyond the scope of this work. The conventional spectral domain analysis also encounters computational difficulty. In the RWG chapters, the time harmonic dependence  $e^{-i\omega t}$  is assumed through the mathematical derivations.

The uniaxial medium, although complex, exists in nature. The concept of the negative permittivity and negative permeability medium has been of great interest since the year of 2000 [20]. The concept and fundamental mathematical treatment of the medium with negative permittivity and negative permeability were first proposed by Veselago [21] nearly 50 years ago. However, it had not found massive applications until the first practical negative refractive-index medium (NIM) [22] was predicted in [23] and experimentally demonstrated in 2001 by Shelby, Smith and Schultz [24].

Negative refractive-index materials have held considerable interests since they were experimentally demonstrated in both microwave spectrum and in optic regime. Unprecedented demonstrations of wave controllability have stemmed from these dielectric-and-metal-based

metamaterials. Researchers have found successful implementations in bulk medium and planar circuits, thus the metamaterials have attracted significant interests in broad applications. However, since the constituent metals are of finite conductivity, and the dielectrics are never ideally lossless, the artificial material which is often built with dense use of metal and dielectrics, suffers from inherent losses that are detrimental in most applications. For instance, the resolution of the slab lens [25] is severely limited, and the radiation performances of the leaky-wave antenna (LWA) [26] is degraded. The reason why the LWA performance is degraded will be analyzed. Moreover, although the planar circuit loss is finite, it is still surprisingly high when longer metamaterial transmission lines (TLs) are to be used.

To address the loss problem, active media were suggested to incorporate for energy compensation [27]. Although the theory of combining NIM and active media were studied in [28] from a physics and mathematical perspective, there had been theoretical debate whether NIMs with low-loss or even gain violate causality in principle [29] [30]. However, considering that all the artificial NIMs are of limited bandwidth, the simultaneous negative refractive index and zero loss or gain is, at least in certain frequency range, proven acceptable [31]. In spite of the theoretical dispute, there has been considerable effort drawn to alleviate the issue, confirming the mathematical correctness. Among many, the spaser introduced by Bergman and Stockman [32] has proved to be a practical solution to provide optical gain [33]. The optical parametric amplification based on higher order harmonic energy generation was also predicted capable of alleviating the loss issue, and the experiment has been reported in [34]. Based on the same harmonic energy generation concept, in microwave frequency the use of parametric amplification utilizing nonlinear active components was proposed even earlier, and it has been demonstrated in an active bulk metamaterial [35] and a left-handed transmission line metamaterial [36]. However,

the parametric amplifications are usually narrow band, which limits their usage in broadband applications.

Recently, the energy compensation in the microwave composite right/left-handed (CRLH) structure has been further investigated [37], where the tunnel diode is adopted to realize bi-directional amplification by effectively functioning as a negative resistance (NR). Simultaneous negative propagation constant and net gain is achieved in a limited bandwidth within the left-hand frequency region. In terms of the reciprocity, it is advantageous over a previous paper [38] which allows only forward amplification by inserting quasi-unilateral microwave amplifiers between CRLH unit cells. However, due to the common alternating active-and-passive arrangement resembling the stack-up of the near field lens [27], the phase propagation of these active structures can hardly behave similarly to the composite right-handed (RH) and left-handed (LH) response across the transition frequency in a reasonably wide bandwidth. Furthermore, the amplification of the biased tunnel diode is highly frequency-dependent, thus impractical to maintain a consistent gain over a certain bandwidth which is important for system stability and most microwave applications including the leaky-wave antenna with backward-broadside-endfire scanning capability. Last but not the least, the series connection extends the unit cell length and breaks the metamaterialistic periodicity of the CRLH structure, resulting in the deteriorated return loss at the input and output ports. Nevertheless, it is enlightening to use NR for energy regeneration.

In radio frequency, NR has been known since it was first introduced by Hull [39], disclosing the dynatron. Modern NR circuits often appear as two-terminal (one port) circuits that is usually made of active components and biasing circuits [40]. The impedance looking into the two terminal network presents less-than-zero values in some frequency band depending on the active component characteristics. When operated as one-port devices, the circuits amplify and reflect

more power than the incident power injected from the input port. This enables the design of the reflection-type amplifiers that use the nonlinearities of transistors [41] or diodes [42] associated with circulators to separate input and output ports and avoid instability.

In this dissertation, we take advantage of the NR technique to demonstrate an active CRLH unit cell with compensated loss or even provide net gain covering both the RH and LH frequency bands. The loss is addressed by replacing the shorted (grounded by vias) stubs with the negative-resistance-terminated energy-regeneration stubs, thus the compensated-energy injection is not (in series) between the CRLH unit cells as the previously reported experiments [33] [38] did. The analysis and experiments of the new CRLH unit cell show that the loss can be completely compensated and the unit cell can even have forward gain. More importantly, the original CRLH phase characteristics and broad-band Bloch-impedance matching are preserved. The new structure is given the name as the negative resistance enhanced composite right/left-handed structure, abbreviated as NR-CRLH.

One of the major applications of CRLH structure is the leaky-wave antenna (LWA) that exhibits frequency scanning capability covering from backward to end-fire angles including the broadside radiation [26]. The frequency scanning phenomenon perfectly manifests the phase propagation characteristics of LH and RH behaviors in different frequency bands, and this phenomenon has not been seen with any previous metallic-waveguide-based or microstrip-line-based LWAs. In order to demonstrate the NR-CRLH structure, an LWA is designed, fabricated and measured. Both analysis and experimental results show that the NR-CRLH LWA has not only the similar frequency scanning capability but also higher directivity and narrower beamwidth in most working frequency band. In order to avoid confusion, in Chapter 4 and Chapter 5, the



harmonic time dependence is assumed to be  $e^{j\omega t}$  since this is the common assumption in most of the pioneering publications and heavily cited literature in this field of study.

## **Chapter 2 Rectangular Waveguide Filled with Uniaxial Medium – Aligned Cases**

Rectangular waveguide (RWG) filled with various anisotropic media has been receiving considerable interests for decades. In some cases the complex medium is intentionally inserted in waveguide for particular purposes, but sometimes the introduction of the complex media is unintentional. In either situations, the wave behaviors need to be studied prior to applications. For example, most modern commercial PCB substrates are unintentionally made uniaxial because of their mixing ingredients, but gyromagnetic media are still indispensable in microwave circulator and phase shifter design.

An extensive discussion on guided waves in magneto-plasma medium can be found in Wait's book [43], and the analysis of RWG filled with warm plasma is treated in [44]. The computation of dominant mode for a RWG filled with uniaxially anisotropic or uniaxial medium whose optic axis is arbitrarily tilted in the cross-section plane is presented in [8], by making use of the variational approach. In optics, a landmark paper by Berreman [15] for the anisotropic slab waveguide introduced the  $4 \times 4$  matrix method, which is applicable to the stratified uniaxial case presented by Knoesen et al. [45]. Microwave substrate anisotropy drew attention because in practice many types of substrate materials were revealed to be anisotropic by accurate characterization, and the effect of uniaxial anisotropy was discussed by Pozar in [11] on the study of a patch antenna affected by uniaxial substrate. The anisotropic substrate, in current commercial products, are still common, among various low-cost FR-4 and FR-4 compatible woven fiber-glass materials [46] and high-performance PTFE-based ceramic-filled Roger materials [47]. In recent years, with the emerging enthusiasm in left-hand material, backward wave phenomenon in RWG

due to negative permeability and permittivity has been investigated [48]. In the other category of study, the RWG structure is employed to examine the constitutive parameters [14]. Liu et al. [49] obtained the dyadic Green's functions for RWG using the eigenfunction expansion method. Their analysis is limited to when the optic axis is parallel to the direction of propagation.

However, there has not been any published work on the complete mode (beyond the dominant mode) and field solutions when the optic axis of the uniaxial medium in the RWG is not along the direction of propagation. No previous work has shown that the dominant mode can change when the optic axis is aligned in different directions. It is the purpose of this chapter to obtain the complete mode solutions, derived by employing the method of wave decomposition with respect to the direction of the optic axis. Specifically, we are concerned with the cases when the optic axis is aligned with one of the coordinate axes, namely  $x$ ,  $y$  or  $z$  axis. These cases are named as the aligned problems, and we give them unique names: uniaxial- $x$ , uniaxial- $y$  and uniaxial- $z$ . For three different orientations of the optic axis, the method of wave decomposition with respect to the optic axis is proposed.

## 2.1. Formulation

The RWG is assumed to have width  $b$  in  $y$  direction and height  $a$  in  $x$  direction, with the  $z$  direction as the direction of propagation as shown in Figure 2-1.

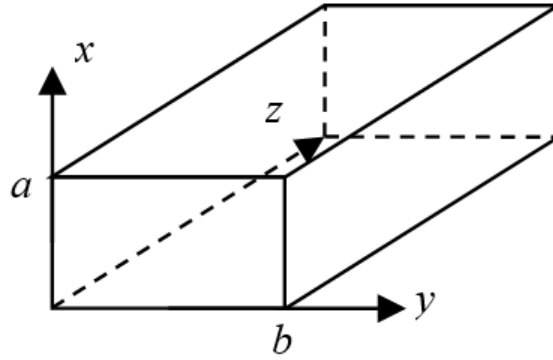


Figure 2-1 A rectangular waveguide and its dimensions.

Conventionally for a hollow waveguide, only the dimensions  $a$  and  $b$  determine the propagation characteristics. If size  $a$  is greater than  $b$ , the dominant mode is  $TE_{10}$  mode; if size  $b$  is greater than  $a$ , the dominant mode is  $TE_{01}$  mode. TM mode does not contribute to dominant modes.

The aforementioned TE and TM modes are given the name in accordance with the nature of the field components. The TE mode has no electrical field along  $z$  axis, and the TM mode has no magnetic field along  $z$  axis. The insertion of an isotropic medium with relative permittivity  $\epsilon_r$  and relative permeability  $\mu_r$  inside the waveguide would not alter these fundamental characteristics. However, in the case of a waveguide filled with uniaxial medium, the mode decomposition and dominant mode behaviors will both change. The mode decomposition is a natural result of the following mathematical derivations.

### ***2.1.1. Isotropic Case – Formulation***

When the medium in RWG is isotropic, travelling waves are usually decomposed into TE-to- $Z$  and TM-to- $Z$  modes, of which  $E_z$  and  $H_z$  components are zeros, respectively. Typical treatment

can be found in many textbooks. It all comes down to solving the Maxwell equations in a source-free region as follows, assuming the  $e^{-i\omega t}$  time dependence.

$$\nabla \times \vec{E} = i\omega \vec{B} \quad (2-1)$$

$$\nabla \times \vec{H} = -i\omega \vec{D} \quad (2-2)$$

$$\nabla \cdot \vec{D} = 0 \quad (2-3)$$

$$\nabla \cdot \vec{B} = 0 \quad (2-4)$$

In the equations above the media are assumed to be isotropic. The constitution relations are thus given by

$$\epsilon_0 \epsilon_r \vec{E} = \vec{D} \quad (2-5)$$

$$\mu_0 \mu_r \vec{H} = \vec{B} \quad (2-6)$$

Conventionally, the modes supported in a waveguide with homogeneous and isotropic interior space is decomposed into TE and TM modes. Guided wave solutions can be found in many textbooks. TE mode wave contains no E field component in Z direction, and TM mode wave has no H field component in Z direction. The decomposition of the wave modes with respect to Z axis was convenient and unique because the Z direction is the direction of propagation, while the two transverse directions are mathematically symmetrical thus interchangeable.

Harrington uses wave potential scalars to formulate a group of scalar solutions [50]. In Kong's book it starts from  $E_z$  and  $H_z$  then find vector formulas for transverse components [51]. What is in common between those two methods is the purpose to obtain the longitudinal components before the transverse components. In the following, Kong's formulation is reviewed and modified for uniaxial-x problem, as an example of applying the revised formulation.

In the isotropic case, Maxwell's equations can be split into transverse-to-Z and parallel-to-Z components.

$$(\nabla_s + \nabla_z) \times (\vec{E}_s + \vec{E}_z) = i\omega\mu_0\mu_r (\vec{H}_s + \vec{H}_z) \quad (2-7)$$

$$(\nabla_s + \nabla_z) \times (\vec{H}_s + \vec{H}_z) = -i\omega\varepsilon_0\varepsilon_r (\vec{E}_s + \vec{E}_z) \quad (2-8)$$

The Laplace operators with subscripts “s” or “z” are defined as follows.

$$\nabla_s = \hat{a}_x \frac{\partial}{\partial x} + \hat{a}_y \frac{\partial}{\partial y} \quad (2-9)$$

$$\nabla_z = \hat{a}_z \frac{\partial}{\partial z} \quad (2-10)$$

Thus the general ‘del’ operator is the sum of the above two definitions. Each of equations (2-7) and (2-8) could be separated into two parts. One of the two parts contains all the transverse-to-z direction terms, the other part contains all the z directional terms. Specifically, (2-7) could be separated into (2-11) and (2-12) representing the transverse components and the Z components, respectively, and similarly (2-8) can be separated into (2-13) and (2-14).

$$i\omega\mu_0\mu_r \vec{H}_s = \nabla_s \times \vec{E}_z + \nabla_z \times \vec{E}_s \quad (2-11)$$

$$i\omega\mu_0\mu_r \vec{H}_z = \nabla_s \times \vec{E}_s \quad (2-12)$$

$$-i\omega\varepsilon_0\varepsilon_r \vec{E}_s = \nabla_s \times \vec{H}_z + \nabla_z \times \vec{H}_s \quad (2-13)$$

$$-i\omega\varepsilon_0\varepsilon_r \vec{E}_z = \nabla_s \times \vec{H}_s \quad (2-14)$$

To further reform the equation (2-11) to equation (2-14), there are several vector product identities need to be used. These identities can be found in electromagnetics textbooks and will be briefed when the identities are used..

First, we use the z unit vector to cross-product (2-11) and (2-13) to obtain the following results.

$$\hat{a}_z \times i\omega\mu_0\mu_r \vec{H}_s = \hat{a}_z \times \nabla_s \times \vec{E}_z + \hat{a}_z \times \nabla_z \times \vec{E}_s = \nabla_s E_z - \frac{\partial}{\partial z} \vec{E}_s \quad (2-15)$$

$$\hat{a}_z \times (-i\omega\epsilon_0\epsilon_r \vec{E}_s) = \hat{a}_z \times \nabla_s \times \vec{H}_z + \hat{a}_z \times \nabla_z \times \vec{H}_s = \nabla_s H_z - \frac{\partial}{\partial z} \vec{H}_s \quad (2-16)$$

Then, we use the z unit vector to cross product (2-15), and that is equivalent to cross product (2-11) twice. Therefore, the following two equations have to be equal with the left-hand side as

$$\hat{a}_z \times \hat{a}_z \times i\omega\mu \vec{H}_s = -i\omega\mu \vec{H}_s, \quad (2-17)$$

and the right-hand side as

$$\hat{a}_z \times \left( \nabla_s E_z - \frac{\partial}{\partial z} \vec{E}_s \right) = -\nabla_s \times \vec{E}_z - \frac{\partial}{\partial z} \hat{a}_z \times \vec{E}_s = -\nabla_s \times \vec{E}_z - (ik_z) \hat{a}_z \times \vec{E}_s. \quad (2-18)$$

Now that we have obtained the left hand side of (2-16) to be (2-18). Since (2-17) and (2-18) are equal, we can find  $E_s$  vector in terms of  $E_z$  and  $H_s$  and put that back into (2-16). By doing so, the transverse magnetic field components in  $H_s$  vector are in terms of  $E_z$  and  $H_z$  only as follows.

$$\vec{H}_s = \frac{1}{\omega^2 \mu_0 \epsilon_0 \epsilon_r - k_z^2} \left[ \nabla_s \frac{\partial H_z}{\partial z} - i\omega \epsilon_0 \epsilon_r \nabla_s \times \vec{E}_z \right] \quad (2-19)$$

Following the similar derivations, the transverse electric field components are also found in terms of  $H_z$  and  $E_z$  as follows.

$$\vec{E}_s = \frac{1}{\omega^2 \mu_0 \epsilon_0 \epsilon_r - k_z^2} \left[ \nabla_s \frac{\partial E_z}{\partial z} + i\omega \mu_0 \nabla_s \times \vec{H}_z \right] \quad (2-20)$$

The equations (2-19) and (2-20) indicate that the transverse components are all ready to be obtained if  $E_z$  and  $H_z$  are solved.

### 2.1.2. Isotropic Case – Field Solutions

The  $z$  components could be solved from their Helmholtz's equations which are derived from Maxwell's equations. From (2-1) and (2-2) we have

$$\frac{\partial^2 E_x}{\partial x \partial z} + \frac{\partial^2 E_y}{\partial y \partial z} + \left( \frac{\partial^2 E_z}{\partial z \partial z} - \frac{\partial^2 E_z}{\partial z \partial z} \right) - \frac{\partial^2 E_z}{\partial x^2} - \frac{\partial^2 E_z}{\partial y^2} - \omega^2 \mu_0 \epsilon_0 \epsilon_r E_z = 0 . \quad (2-21)$$

The above is Helmholtz's equation whose solution in rectangular waveguide can be analytically solved using separation of variables. The final solutions can be found in many textbooks and are not listed here.

Taking advantage of the vanished divergence of electrical field vector from Gauss' law we have the following equation holding for electrically isotropic media

$$\frac{\partial E_x}{\partial x} + \frac{\partial E_y}{\partial y} + \frac{\partial E_z}{\partial z} = 0 . \quad (2-22)$$

Then (2-21) becomes

$$\nabla^2 E_z + \omega^2 \mu_0 \epsilon_0 \epsilon_r E_z = 0 , \quad (2-23)$$

where

$$k_0^2 = \omega^2 \mu_0 \epsilon_0 . \quad (2-24)$$

From (2-23), the dispersion relation could be derived as

$$k_z^2 + k_x^2 + k_y^2 = \omega^2 \mu_0 \epsilon_0 \epsilon_r . \quad (2-25)$$

The above dispersion relation governs the guided wave behaviors. The transverse wave numbers are determined by the dimensions and take discrete values as given by

$$k_x = m \frac{\pi}{a} \quad (2-26)$$

$$k_y = n \frac{\pi}{b} \quad (2-27)$$



In Chapter 2 and Chapter 3, the index  $m$  is associated with the wavenumber along X axis, and the index  $n$  is associated with the wavenumber along Y axis. With the values of  $k_x$  and  $k_y$  limited because of the boundary conditions, the wavenumber  $k_z$  (propagation constant) is only derivable through the dispersion relation as follows.

$$k_z = \pm \sqrt{\omega^2 \mu_0 \varepsilon_0 \varepsilon_r - \left(m \frac{\pi}{a}\right)^2 - \left(n \frac{\pi}{b}\right)^2} \quad (2-28)$$

The propagation constant, or  $k_z$ , takes either positive or negative values, corresponding to the wave travelling in positive Z direction or negative Z direction, respectively. When the excitation frequency is less than the cutoff frequency,  $k_z$  takes imaginary value and the wave attenuations while propagating along the waveguide. Thus the frequency of a supported travelling wave has to be greater than the lowest cutoff frequency of the waveguide. In general, the cutoff frequency is given by

$$f_c = \frac{c}{2\sqrt{\varepsilon_r}} \sqrt{\left(\frac{m}{a}\right)^2 + \left(\frac{n}{b}\right)^2} \quad (2-29)$$

where the lower case letter  $c$  represents the speed of light in vacuum.

### ***2.1.3. Tensors for Uniaxial Media***

The solutions to the RWG problems involving uniaxial media with aligned optic axis can be obtained analytically. Plenty of mathematical methods developed for isotropic media could be adopted handily. The fundamental reason is that the relative permittivity tensors are always diagonal, namely, the off-diagonal elements are all zeros. The aligned cases include three difference alignments. When the optic axis is parallel to x axis, the tensor of the relative permittivity is given by

$$\varepsilon_{rx} = \begin{pmatrix} \varepsilon_x & 0 & 0 \\ 0 & \varepsilon_t & 0 \\ 0 & 0 & \varepsilon_t \end{pmatrix}. \quad (2-30)$$

When the optic axis is aligned with y axis, the tensor of the relative permittivity is as follows.

$$\varepsilon_{ry} = \begin{pmatrix} \varepsilon_t & 0 & 0 \\ 0 & \varepsilon_y & 0 \\ 0 & 0 & \varepsilon_t \end{pmatrix} \quad (2-31)$$

Thirdly, when the optic axis is along the direction of propagation, the tensor of the relative permittivity is

$$\varepsilon_{rz} = \begin{pmatrix} \varepsilon_t & 0 & 0 \\ 0 & \varepsilon_t & 0 \\ 0 & 0 & \varepsilon_z \end{pmatrix}. \quad (2-32)$$

With the above relative permittivity tensor defined, the constitution relations are given as follows.

$$\varepsilon_0 \varepsilon_r \cdot E = D \quad (2-33)$$

Notice that the scalar relative permittivity in (2-5) is changed to be a tensor, in the form of a 3-by-3 matrix as shown in equations (2-30) to (2-32). In the rest of this work on rectangular waveguides, for simplicity of discussion, the media are all assumed to be non-magnetic. Thus the constitution (2-6) can be simply written as

$$\mu_0 \mu_r H = B \quad (2-34)$$

### 2.1.4. Uniaxial-z Case – Formulation

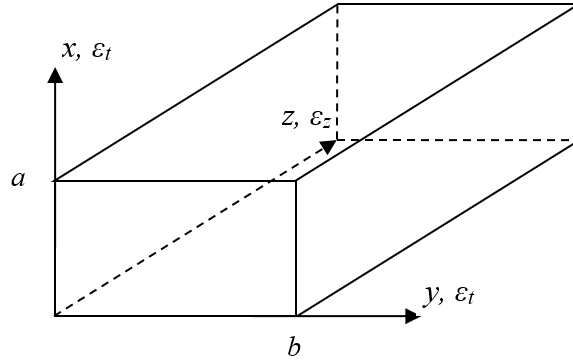


Figure 2-2 A rectangular waveguide in the uniaxial-z case.

In RWG with isotropic and homogeneous internal space, conventionally the travelling waves are decomposed into TE-to-Z and TM-to-Z modes. Solutions to such waveguides can be found in numerous electromagnetics and microwave textbooks and have been understood. They form the foundation of a large portion of microwave technologies. Among various solutions, the common procedure is to obtain the longitudinal components before the transverse components. This methodology works well for uniaxial-z case as we will show in the following procedure.

First, the transverse field components are expressed in terms of  $E_z$  and  $H_z$ , the longitudinal components. If we define  $\nabla_s$  as the transverse part of Laplace operator in Cartesian coordinate system, Maxwell's equations can be explicitly split into transverse-to-Z and parallel-to-Z groups as follows.

$$(\nabla_s + \nabla_z) \times (\vec{E}_s + \vec{E}_z) = i\omega\mu_0 (\vec{H}_s + \vec{H}_z) \quad (2-35)$$

$$(\nabla_s + \nabla_z) \times (\vec{H}_s + \vec{H}_z) = -i\omega\varepsilon_0 (\varepsilon_t \vec{E}_s + \varepsilon_z \vec{E}_z) \quad (2-36)$$

The subscript s denotes the directions transverse to Z axis. Note the difference between the pair of equations (2-7) and (2-8) and the pair of equations (2-35) and (2-36). The only difference is the relative permittivity  $\varepsilon_z$  which is the relative permittivity along the optic axis with  $E_z$

component. This difference is the result of applying the constitutive relation of matrix tensor (2-32) in Maxwell's equations.

It can be directly verified that the derivation process applied for the isotropic case can be applied to this uniaxial-z case as well. There is no modification to the vector operators and identities. Following the described mathematical manipulations, we have the expressions for transverse components in terms of the  $E_z$  and  $H_z$  components as follows.

$$\vec{H}_s = \frac{1}{\omega^2 \mu_0 \varepsilon_0 \varepsilon_t - k_z^2} \left[ \nabla_s \frac{\partial H_z}{\partial z} - i\omega \varepsilon_0 \varepsilon_t \nabla_s \times \vec{E}_z \right] \quad (2-37)$$

$$\vec{E}_s = \frac{1}{\omega^2 \mu_0 \varepsilon_0 \varepsilon_t - k_z^2} \left[ \nabla_s \frac{\partial E_z}{\partial z} + i\omega \mu_0 \nabla_s \times \vec{H}_z \right] \quad (2-38)$$

Compared with the isotropic equations, the equations (2-37) and (2-38) are only different by employing  $\varepsilon_t$  instead of  $\varepsilon_r$ . Here the subscript 's' also designates the components transverse to Z-axis. Note that the above two equations contain no  $\varepsilon_z$  which is the relative permittivity along Z-axis. Thus on the first sight the solutions are not affected by the presence of the anisotropy. However, the answer will be revealed by the examination of dispersion relation.

### 2.1.5. Uniaxial-z Case – Solution

Analytical solutions of uniaxial-z case can be obtained by solving PDEs similar to an isotropic case. First, the Maxwell equations are listed as follows.

$$\frac{\partial E_z}{\partial y} - \frac{\partial E_y}{\partial z} = i\omega \mu_0 H_x \quad (2-39)$$

$$\frac{\partial E_x}{\partial z} - \frac{\partial E_z}{\partial x} = i\omega \mu_0 H_y \quad (2-40)$$

$$\frac{\partial E_y}{\partial x} - \frac{\partial E_x}{\partial y} = i\omega\mu_0 H_z \quad (2-41)$$

$$\frac{\partial H_z}{\partial y} - \frac{\partial H_y}{\partial z} = -i\omega\epsilon_0\epsilon_t E_x \quad (2-42)$$

$$\frac{\partial H_x}{\partial z} - \frac{\partial H_z}{\partial x} = -i\omega\epsilon_0\epsilon_t E_y \quad (2-43)$$

$$\frac{\partial H_y}{\partial x} - \frac{\partial H_x}{\partial y} = -i\omega\epsilon_0\epsilon_z E_z \quad (2-44)$$

It has been summarized in [49] that the modal decomposition results in TE-to-z and TM-to-z modes, corresponding to the o-wave and e-wave, respectively. Here we derive the analytical TM solutions first.

TM modes solutions should contain no  $H_z$  component which is thus assumed to be zero. From (2-39) to (2-44) and with the help of Gauss' law

$$\epsilon_t \frac{\partial E_x}{\partial x} + \epsilon_t \frac{\partial E_y}{\partial y} + \epsilon_z \frac{\partial E_z}{\partial z} = 0 , \quad (2-45)$$

we can find the second order PDEs for  $E_z$  given by

$$\frac{\epsilon_z}{\epsilon_t} \frac{\partial^2 E_z}{\partial z^2} + \frac{\partial^2 E_z}{\partial x^2} + \frac{\partial^2 E_z}{\partial y^2} + \omega^2 \mu_0 \epsilon_0 \epsilon_z E_z = 0 . \quad (2-46)$$

The first direct result of the above PDE is the *dispersion relation* of an extraordinary wave

$$\frac{\epsilon_z}{\epsilon_t} k_z^2 + k_x^2 + k_y^2 = \omega^2 \mu_0 \epsilon_0 \epsilon_z \quad (2-47)$$

The solutions to the second order differential equations reflect standing wave along X-direction and Y-direction, and travelling wave on the Z-direction. The boundary conditions are the same as the isotropic case. The  $E_z$  magnitude has to vanish on the side-walls of the waveguide. Therefore the  $E_z$  solutions is found as follows.

$$E_z = E_0 \sin k_x x \cdot \sin k_y y \cdot e^{ik_z z} \quad (2-48)$$

The magnitude  $E_0$  is an unknown value which will be determined when excitation is known. This solution serves as the first solved component in TM modes, whose  $H_z$  components are assumed to be zero. Hence the other components transverse to Z-axis can be all obtained through (2-37) and (2-38). The obtained solutions are listed and interested readers can compare the results with the isotropic results in Kong's book [51]. For TMz wave the solutions are given as follows with  $H_z$  equal to zero.

$$E_x = E_0 \frac{ik_x k_z}{\omega^2 \mu \epsilon_t - k_z^2} \cos k_x x \cdot \sin k_y y \cdot e^{ik_z z} \quad (2-49)$$

$$E_y = E_0 \frac{ik_y k_z}{\omega^2 \mu \epsilon_t - k_z^2} \sin k_x x \cdot \cos k_y y \cdot e^{ik_z z} \quad (2-50)$$

$$E_z = E_0 \sin k_x x \cdot \sin k_y y \cdot e^{ik_z z} \quad (2-51)$$

$$H_x = E_0 \frac{-i\omega \epsilon k_y}{\omega^2 \mu \epsilon_t - k_z^2} \sin k_x x \cdot \cos k_y y \cdot e^{ik_z z} \quad (2-52)$$

$$H_y = E_0 \frac{i\omega \epsilon k_x}{\omega^2 \mu \epsilon_t - k_z^2} \cos k_x x \cdot \sin k_y y \cdot e^{ik_z z} \quad (2-53)$$

Similarly, the TE solution which contains no  $E_z$  component will require first to solve for  $H_z$  component. Its PDE can also be derived from Maxwell's equations with the help of the Gauss' law for magnetic fields as

$$\frac{\partial H_x}{\partial x} + \frac{\partial H_y}{\partial y} + \frac{\partial H_z}{\partial z} = 0 \quad (2-54)$$

The resultant PDE is given by

$$\frac{\partial^2 H_z}{\partial z^2} + \frac{\partial^2 H_z}{\partial x^2} + \frac{\partial^2 H_z}{\partial y^2} + \omega^2 \mu_0 \epsilon_0 \epsilon_t H_z = 0, \quad (2-55)$$

which is identical in a isotropic case, except that the isotropic case uses  $\epsilon_r$  and the uniaxial-z TE mode solution employs  $\epsilon_t$ . The lack of  $\epsilon_z$  is because of  $E_z$  is assumed to be zero and indicates an ordinary wave dispersion relation known as

$$k_z^2 + k_x^2 + k_y^2 = \omega^2 \mu_0 \epsilon_0 \epsilon_t . \quad (2-56)$$

From (2-55) and the boundary conditions for  $E_x$  and  $E_y$  components the  $H_z$  can be solved as

$$H_z = H_0 \cos k_x x \cdot \cos k_y y \cdot e^{ik_z z} \quad (2-57)$$

The derived solutions are given as follows with  $E_z$  components equal to zero.

$$E_x = H_0 \frac{-i\omega \mu k_y}{\omega^2 \mu \epsilon_t - k_z^2} \cos k_x x \cdot \sin k_y y \cdot e^{ik_z z} \quad (2-58)$$

$$E_y = H_0 \frac{i\omega \mu k_x}{\omega^2 \mu \epsilon_t - k_z^2} \sin k_x x \cdot \cos k_y y \cdot e^{ik_z z} \quad (2-59)$$

$$H_x = H_0 \frac{-ik_x k_z}{\omega^2 \mu \epsilon_t - k_z^2} \sin k_x x \cdot \cos k_y y \cdot e^{ik_z z} \quad (2-60)$$

$$H_y = H_0 \frac{-ik_y k_z}{\omega^2 \mu \epsilon_t - k_z^2} \cos k_x x \cdot \sin k_y y \cdot e^{ik_z z} \quad (2-61)$$

$$H_z = H_0 \cos k_x x \cdot \cos k_y y \cdot e^{ik_z z} \quad (2-62)$$

The modes and corresponding cutoff frequencies are tabulated in Table 2-1. The values of  $k_x$  and  $k_y$  are given by the equations (2-26) and (2-27).

Table 2-1 Modes and Cutoff Frequencies of Uniaxial-z Case.

Mode	Exist	Cutoff Frequency	Compare
$TM_{Zm0}$	No	N/A	No
$TM_{Z0n}$	No	N/A	No
$TM_{Zmn}$	Yes	$f_{cZ}^{TM_{mn}} = \frac{c}{2\epsilon_z} \sqrt{\left(\frac{m}{a}\right)^2 + \left(\frac{n}{b}\right)^2}$	$TM_{mn}$
$TE_{Z0n}$	Yes	$f_{cZ}^{TE_{0n}} = \frac{nc}{b2\sqrt{\epsilon_t}}$	$TE_{0n}$
$TE_{Zm0}$	Yes	$f_{cZ}^{TE_{m0}} = \frac{mc}{a2\sqrt{\epsilon_t}}$	$TE_{m0}$
$TE_{Zmn}$	Yes	$f_{cZ}^{TE_{mn}} = \frac{c}{2\sqrt{\epsilon_t}} \sqrt{\left(\frac{m}{a}\right)^2 + \left(\frac{n}{b}\right)^2}$	$TE_{mn}$

## 2.2. Generalized Cases

In the previous isotropic case and uniaxial-z case,  $E_z$  and  $H_z$  components are decoupled. The mathematical manifest is seen from the existence of the second order partial differential equations for  $E_z$  and  $H_z$ , separately. Consequently, the modes in the previous cases can be categorized into TE modes whose  $E_z$  component is zero and TM modes whose  $H_z$  component is zero. To be more specific, the conventional TE modes and TM modes are interchangeable with the mode denotation  $TE_Z$  and  $TM_Z$  modes, respectively. The necessity of this clarification is due to the proposed general formulation and mode decompositions with respect to the optic axis, which can be parallel to any one of the coordinate axes.



Even for the isotropic case, the mode decomposition can also be done with respect to other coordinate axes, too. Harrington briefly mentioned the feasibility of TE/TM to X axis modes and TE/TM to Y axis modes in his book [50]. In this section the formulation applying to all the aligned uniaxial waveguide cases are detailed. The resultant decomposed modes are discussed in next section.

### ***2.2.1. Uniaxial-x and Uniaxial-y Cases***

The aforementioned separable PDEs of  $E_z$  and  $H_z$  manifest the convenience of decomposing the modes into TE and TM modes. However, in uniaxial-x and uniaxial-y cases,  $E_z$  and  $H_z$  are not always decoupled. In other words, partial differential equations (PDE) exclusively having  $E_z$  or  $H_z$  component as the only unknown cannot be derived from Maxwell's equations. Therefore the TE/TM mode decomposition is not convenient to obtain the full solutions.

However, decomposition with respect to the optic axis is always practical. Mathematically, in any uniaxial medium where the optic axis is aligned with one of the coordinate axes, Maxwell's equations can be concisely organized to obtain the PDE exclusively with unknown field components that are parallel to the direction of optic axis. This fact allows the decomposition with respect to the direction of the components that are parallel to the optic axis.

To be distinguished from previous TE/TM modes, TE-to-X ( $TE_x$ ) mode, and similarly  $TE_y$ ,  $TM_x$ ,  $TM_y$  modes are defined. In order to eliminate confusion, terms TE/TM will imply transverse-to-Z modes only, so are the  $TE_z$  and  $TM_z$ , while other decompositions will always be identified by subscripts. The analyses of uniaxial-x case and uniaxial-y case are naturally similar in terms of mathematical treatment because of the rotational geometry between x and y coordinates

in the study of RWG, but the decomposition is not symmetric as in an isotropic waveguide because of the presence of the optic axis.

To clarify the existence of the PDEs mentioned previously, we start the analysis with particular cases and lay down the necessary derivation procedures. For example, in uniaxial-x case, Faraday's law remains the same, and the differential equations that are different from the uniaxial-Z case are listed as follows.

$$\frac{\partial H_z}{\partial y} - \frac{\partial H_y}{\partial z} = -i\omega \epsilon_0 \epsilon_x E_x \quad (2-63)$$

$$\frac{\partial H_x}{\partial z} - \frac{\partial H_z}{\partial x} = -i\omega \epsilon_0 \epsilon_y E_y \quad (2-64)$$

$$\frac{\partial H_y}{\partial x} - \frac{\partial H_x}{\partial y} = -i\omega \epsilon_0 \epsilon_z E_z \quad (2-65)$$

Note that the Gauss' law is also changed to be

$$\epsilon_x \frac{\partial E_x}{\partial x} + \epsilon_y \frac{\partial E_y}{\partial y} + \epsilon_z \frac{\partial E_z}{\partial z} = 0 \quad (2-66)$$

First we consider TM modes with  $H_z$  equal to zero. Conventionally one may attempt to solve for  $E_z$  prior to other components. However, due to the different relative permittivity in (2-63) from the other two Faraday's law equations, and the inhomogeneity among the coefficients of the first order derivatives in Gauss' law, solving for  $E_z$  is impractical because there is no separated second order PDE can be obtained. Therefore, conventional TM-to-Z modes are not supported in such a waveguide.

Secondly we consider TE modes with  $E_z$  equal to zero. In this case, the separated second order PDE with neither  $k_x$  nor  $k_y$  being zero is not possible, too. Nevertheless, with one of the transverse wavenumber being zero, the solutions are approachable.

When  $k_x = 0$ , the second order PDE for  $H_z$  component is

$$\frac{\partial^2 H_z}{\partial z^2} + \frac{\partial^2 H_z}{\partial y^2} + \omega^2 \mu_0 \epsilon_0 \epsilon_x H_z = 0 \quad (2-67)$$

And the dispersion relation is derived as

$$k_z^2 + k_y^2 = \omega^2 \mu_0 \epsilon_0 \epsilon_x \quad (2-68)$$

It can be verified that this mode contains only  $E_x$  component, and this is the reason why in the dispersion relation there is only  $\epsilon_x$  but not the relative permittivity in the transverse directions.

When  $k_y = 0$ , the second order PDE for  $H_z$  component is obtained as

$$\frac{\partial^2 H_z}{\partial z^2} + \frac{\partial^2 H_z}{\partial x^2} + \omega^2 \mu_0 \epsilon_0 \epsilon_t H_z = 0 \quad (2-69)$$

And the dispersion relation is derived as

$$k_z^2 + k_x^2 = \omega^2 \mu_0 \epsilon_0 \epsilon_t \quad (2-70)$$

It can be verified that this mode contains only  $E_y$  component, and this is the reason why in the dispersion relation there is only  $\epsilon_t$  but not  $\epsilon_x$ . In uniaxial-y cases, the derivation of solutions is similar to the uniaxial-x case, thus the processes and details are omitted.

Now the question arises: Are these two modes the only supported modes in such a rectangular waveguide? Next section we describe another method to solve for the complete wave modes.

### ***2.2.2. General Formulation***

The analyses of the uniaxial-x and uniaxial-y cases are naturally the same because of the rotational geometry between x and y coordinates in the study of RWG. We formulate the solution for broader generality, using the Laplace operators

$$\nabla_c = \hat{a}_c \frac{\partial}{\partial c} \quad (2-71)$$

$$\nabla_t = \hat{a}_u \frac{\partial}{\partial u} + \hat{a}_v \frac{\partial}{\partial v} \quad (2-72)$$

The subscript c denotes the direction of optic axis, and the subscript t (u, v) designates the directions transverse to c. For example, if the c stands for x, then u and v represent y and z. If the c designates y, then u and v represent x and z.

Then Faraday's law can be rewritten and separated as follows.

$$\nabla_t \times \vec{E}_c + \nabla_c \times \vec{E}_t = i\omega\mu_0 \vec{H}_t \quad (2-73)$$

$$\nabla_t \times \vec{E}_t = i\omega\mu_0 \vec{H}_c \quad (2-74)$$

And Ampere's law can be separated as follows.

$$\nabla_t \times \vec{H}_c + \nabla_c \times \vec{H}_t = -i\omega\varepsilon_0\varepsilon_t \vec{E}_t \quad (2-75)$$

$$\nabla_t \times \vec{H}_t = -i\omega\varepsilon_0\varepsilon_c \vec{E}_c \quad (2-76)$$

The unit vector  $\hat{a}_c$  is defined as the unit vector in the direction parallel to the optic axis. It applies in all the three aligned uniaxial cases. Applying anterior cross-product on the above equations, and using the general operators defined in (2-71) and (2-72), a similar derivation can be done following the same procedure described in Section 2.1.1 and Section 2.1.4. We can obtain the most general equations for all three uniaxial cases given by

$$\vec{E}_t = \frac{1}{\omega^2\mu_0\varepsilon_0\varepsilon_t - k_c^2} \left[ \nabla_t \frac{\partial \vec{E}_c}{\partial c} + i\omega\mu \nabla_t \times \vec{H}_c \right], \quad (2-77)$$

$$\vec{H}_t = \frac{1}{\omega^2\mu_0\varepsilon_0\varepsilon_t - k_c^2} \left[ \nabla_t \frac{\partial \vec{H}_c}{\partial c} - i\omega\varepsilon_0\varepsilon_t \nabla_t \times \vec{E}_c \right]. \quad (2-78)$$

Inspired by the mode decompositions with respect to the orientation of the optic axis, it is better to obtain the  $E_c$  and  $H_c$  components, or  $E_x$  and  $H_x$  in this particular case, prior to other components. It can be easily verified that  $E_c$  and  $H_c$  components are always decoupled in PDEs and thus can be solved independently. Again, we first take the uniaxial-x case as the example and details the derivations.

For  $TE_x$  modes, assume  $E_x = 0$ , and the second order PDE for  $H_x$  is given by

$$\frac{\partial^2 H_x}{\partial z^2} + \frac{\partial^2 H_x}{\partial x^2} + \frac{\partial^2 H_x}{\partial y^2} + \omega^2 \mu_0 \varepsilon_0 \varepsilon_t H_x = 0 \quad (2-79)$$

And this second order PDE bears the solutions to  $H_x$  component with assistance from the boundary conditions. The dispersion relation is the same as (2-56), which is  $TE_z$  mode dispersion relation in the uniaxial-z case. It represents an ordinary wave. Other components can be derived once  $H_x$  is obtained.

For  $TM_x$  modes, assume  $H_x = 0$ , and the PDE is derived as follows.

$$k_z^2 + \frac{\varepsilon_x}{\varepsilon_t} k_x^2 + k_y^2 = \omega^2 \mu_0 \varepsilon_0 \varepsilon_x \quad (2-80)$$

The above result is comparable to (2-47), which is the  $TM_z$  mode dispersion relation in the uniaxial-z case. This represents an extraordinary wave.

Similarly,  $TM_y$  modes have the dispersion relation as

$$k_z^2 + k_x^2 + \frac{\varepsilon_y}{\varepsilon_t} k_y^2 = \omega^2 \mu_0 \varepsilon_0 \varepsilon_y \quad (2-81)$$

Utilizing the general operators and unit vectors, we can conclude that for all the  $TE_c$  modes, all the modal waves are ordinary waves, and they are all governed by the same dispersion relation

(2-56). Moreover, all the  $TM_C$  mode waves are extraordinary waves, the they all have particular dispersion relation for each case that has been discussed before. One general form can be written as follows.

$$\varepsilon_c k_c^2 + \varepsilon_t k_u^2 + \varepsilon_t k_v^2 = \omega^2 \mu_0 \varepsilon_0 \varepsilon_t \varepsilon_c \quad (2-82)$$

The modal decomposition results are discussed in the following section.

## 2.3. Results

This section discusses the wave modes,, dominant modes, field distributions, and other results with the solution from the previous section.

### 2.3.1. Mode Decomposition in Uniaxial-x Case

The decomposed modes in uniaxial-x case are summarized in Table 2-2.

Table 2-2 Modes and Cutoff Frequencies of Uniaxial-x Case

Mode	Exist	Cutoff Frequency	Compare*
$TM_{Xm0}$	No	N/A	N/A
$TM_{X0n}$	Yes	$f_{cX}^{TM_{0n}} = \frac{nc}{b 2 \sqrt{\varepsilon_x}}$	$TE_{0n}$
$TM_{Xmn}$	Yes	$f_{cX}^{TM_{mn}} = \frac{c}{2} \sqrt{\frac{1}{\varepsilon_t} \left(\frac{m}{a}\right)^2 + \frac{1}{\varepsilon_x} \left(\frac{n}{b}\right)^2}$	$E_z \neq 0; H_z \neq 0.$
$TE_{X0n}$	No	N/A	N/A
$TE_{Xm0}$	Yes	$f_{cX}^{TE_{m0}} = \frac{mc}{a 2 \sqrt{\varepsilon_t}}$	$TE_{m0}$
$TE_{Xmn}$	Yes	$f_{cX}^{TE_{mn}} = \frac{c}{2 \sqrt{\varepsilon_t}} \sqrt{\left(\frac{m}{a}\right)^2 + \left(\frac{n}{b}\right)^2}$	$E_z \neq 0; H_z \neq 0.$

\* Compare with conventional transverse-to-z modes.

In uniaxial-x case, the  $TM_X$  modes are extraordinary waves and the  $TE_X$  modes are all ordinary modes.  $TM_{Xm0}$  modes with  $k_y = 0$  do not exist because the solution would become trivial with  $E_x = 0$ .  $TM_{X0n}$  modes correspond to the  $TE_{0n}$  (transverse to Z) modes with  $k_x = 0$ .  $TE_{Xm0}$  modes correspond to the  $TE_{m0}$  (transverse to Z) modes with  $k_y = 0$ . Note that  $TE_{mn}$  (transverse to Z) modes with neither  $k_x$  nor  $k_y$  being zero are not supported in such waveguides. In agreement with the previous theoretical examination and prediction, the TM to Z modes are not supported at all.

It is worth mentioning that the supported  $TM_{Xmn}$  modes and  $TE_{Xmn}$  modes do not find matched modes in conventional TE/TM (transverse to Z) mode set. Note that without using the proposed general formulation and mode decomposition with respect to optic axis, the  $TM_{Xmn}$  and  $TE_{Xmn}$  would be difficult to find from the conventional TE/TM mode (transverse to Z) decompositions.

Essentially both  $TM_{Xmn}$  mode and  $TE_{Xmn}$  mode would contain both  $E_z$  and  $H_z$  components. Therefore, again, the conventional method of separating  $E_z$  and  $H_z$  components from Maxwell's equations would encounter difficulties. Similarly,  $TM_{Xmn}$  mode has no  $H_x$  component and  $TE_{Xmn}$  mode has no  $E_x$  component, but they are both comparable to conventional transverse-to-z modes as shown in the last column in Table 2-2.

With the transverse wavenumbers defined in (2-26) and (2-27) which are valid in all the aligned uniaxial cases, the complete wave field component solutions of  $TM_X$  modes are given as follows in the uniaxial-x case.

$$E_x = E_0 \cos k_x x \cdot \sin k_y y \cdot e^{ik_z z} \quad (2-83)$$

$$E_y = E_0 \frac{-k_x k_y}{\omega^2 \mu \epsilon_0 \epsilon_t - k_x^2} \sin k_x x \cdot \cos k_y y \cdot e^{ik_z z} \quad (2-84)$$

$$E_z = E_0 \frac{-ik_x k_z}{\omega^2 \mu \varepsilon_0 \varepsilon_t - k_x^2} \sin k_x x \cdot \sin k_y y \cdot e^{ik_z z} \quad (2-85)$$

$$H_x = 0 \quad (2-86)$$

$$H_y = E_0 \frac{\omega \varepsilon_0 \varepsilon_t k_z}{\omega^2 \mu \varepsilon_0 \varepsilon_t - k_x^2} \cos k_x x \cdot \sin k_y y \cdot e^{ik_z z} \quad (2-87)$$

$$H_z = E_0 \frac{i\omega \varepsilon_0 \varepsilon_t k_y}{\omega^2 \mu \varepsilon_0 \varepsilon_t - k_x^2} \cos k_x x \cdot \cos k_y y \cdot e^{ik_z z} \quad (2-88)$$

$$k_z^2 = \omega^2 \mu \varepsilon_0 \varepsilon_t - k_y^2 - (\varepsilon_x / \varepsilon_t) k_x^2 \quad (2-89)$$

The complete wave field component solutions in the uniaxial-x case are given as follows for TE<sub>x</sub> modes. Note that the relation of the three wavenumber components follows the form of the conventional isotropic case with no uniaxiality involved.

$$E_x = 0 \quad (2-90)$$

$$E_y = H_0 \frac{-\omega \mu k_z}{\omega^2 \mu \varepsilon_0 \varepsilon_t - k_x^2} \sin k_x x \cdot \cos k_y y \cdot e^{ik_z z} \quad (2-91)$$

$$E_z = H_0 \frac{i\omega \mu k_y}{\omega^2 \mu \varepsilon_0 \varepsilon_t - k_x^2} \sin k_x x \cdot \sin k_y y \cdot e^{ik_z z} \quad (2-92)$$

$$H_x = H_0 \sin k_x x \cdot \cos k_y y \cdot e^{ik_z z} \quad (2-93)$$

$$H_y = H_0 \frac{-k_y k_x}{\omega^2 \mu \varepsilon_0 \varepsilon_t - k_x^2} \cos k_x x \cdot \sin k_y y \cdot e^{ik_z z} \quad (2-94)$$

$$H_z = H_0 \frac{ik_z k_x}{\omega^2 \mu \varepsilon_0 \varepsilon_t - k_x^2} \cos k_x x \cdot \cos k_y y \cdot e^{ik_z z} \quad (2-95)$$

$$k_z^2 = \omega^2 \mu \varepsilon_0 \varepsilon_t - k_y^2 - k_x^2 \quad (2-96)$$



Apparently they have the same sinusoidal functional dependence as the conventional TE and TM waves because the boundary conditions never changed. The dominant mode will be discussed in Section 2.3.3.

### 2.3.2. Mode Decomposition in Uniaxial-y Case

The decomposed modes in uniaxial-y case are summarized in Table 2-3.

Table 2-3 Modes and Cutoff Frequencies of Uniaxial-y Case.

Mode	Exist	Cutoff Frequency	Compr*
TM <sub>Y0n</sub>	No	N/A	N/A
TM <sub>Ym0</sub>	Yes	$f_{cY}^{TM_{m0}} = \frac{m c}{2 a \sqrt{\epsilon_y}}$	TE <sub>m0</sub>
TM <sub>Ymn</sub>	Yes	$f_{cY}^{TM_{mn}} = \frac{c}{2} \sqrt{\frac{1}{\epsilon_y} \left(\frac{m}{a}\right)^2 + \frac{1}{\epsilon_t} \left(\frac{n}{b}\right)^2}$	$E_z \neq 0; H_z \neq 0.$
TE <sub>Ym0</sub>	No	N/A	N/A
TE <sub>Y0n</sub>	Yes	$f_{cY}^{TE_{0n}} = \frac{n c}{2 b \sqrt{\epsilon_t}}$	TE <sub>0n</sub>
TE <sub>Ymn</sub>	Yes	$f_{cY}^{TE_{mn}} = \frac{c}{2 \sqrt{\epsilon_t}} \sqrt{\left(\frac{m}{a}\right)^2 + \left(\frac{n}{b}\right)^2}$	$E_z \neq 0; H_z \neq 0.$

\* Compare with conventional transverse-to-z modes.

In uniaxial-y case, TM<sub>Ym0</sub> modes with  $k_x = 0$  do not exist because the solution would become trivial with  $E_y = 0$ . TM<sub>Y0n</sub> modes correspond to the TE<sub>0n</sub> (transverse to Z) modes with  $k_x = 0$ . TE<sub>Ym0</sub> modes correspond to the TE<sub>m0</sub> (transverse to Z) modes with  $k_y = 0$ . Note that TE<sub>mn</sub> (transverse to Z) modes with neither  $k_x$  nor  $k_y$  being zero are not supported in such waveguides. In agreement with the previous theoretical examination and prediction, the TM-to-Z modes are not supported at all.

It is worth mentioning that the supported  $\text{TM}_{Ymn}$  modes and  $\text{TE}_{Ymn}$  modes do not find matched modes in conventional TE/TM mode set. Note that without using the proposed general formulation and mode decomposition with respect to optic axis, the  $\text{TM}_{Ymn}$  and  $\text{TE}_{Ymn}$  would be difficult to find from the conventional TE/TM mode decompositions. Essentially both  $\text{TM}_{Xmn}$  mode and  $\text{TE}_{Xmn}$  mode wave solutions would contain both  $E_z$  and  $H_z$  components, whereas  $\text{TM}_{Xmn}$  mode has no  $H_x$  component and  $\text{TE}_{Xmn}$  mode wave has no  $E_x$  component.

The complete wave field component solutions for  $\text{TM}_Y$  modes are given as follows in the uniaxial-y case.

$$E_x = E_0 \frac{-k_x k_y}{\omega^2 \mu \varepsilon_0 \varepsilon_t - k_y^2} \cos k_x x \cdot \sin k_y y \cdot e^{ik_z z} \quad (2-97)$$

$$E_y = E_0 \sin k_x x \cdot \cos k_y y \cdot e^{ik_z z} \quad (2-98)$$

$$E_z = E_0 \frac{-ik_y k_z}{\omega^2 \mu \varepsilon_0 \varepsilon_t - k_y^2} \sin k_x x \cdot \sin k_y y \cdot e^{ik_z z} \quad (2-99)$$

$$H_x = E_0 \frac{-\omega \varepsilon_0 \varepsilon_t k_z}{\omega^2 \mu \varepsilon_0 \varepsilon_t - k_y^2} \sin k_x x \cdot \cos k_y y \cdot e^{ik_z z} \quad (2-100)$$

$$H_y = 0 \quad (2-101)$$

$$H_z = E_0 \frac{-i\omega \varepsilon_0 \varepsilon_t k_x}{\omega^2 \mu \varepsilon_0 \varepsilon_t - k_y^2} \cos k_x x \cdot \cos k_y y \cdot e^{ik_z z} \quad (2-102)$$

$$k_z^2 = \omega^2 \mu \varepsilon_0 \varepsilon_t - k_x^2 - (\varepsilon_y / \varepsilon_t) k_y^2 \quad (2-103)$$

The complete wave field component solutions for  $\text{TE}_Y$  modes are given as follows in the uniaxial-y case. Note that the relation of the three wavenumber components follows the form of the conventional isotropic case with no uniaxial permittivity involved.

$$E_x = H_0 \frac{\omega \mu k_z}{\omega^2 \mu \epsilon_0 \epsilon_t - k_x^2} \cos k_x x \cdot \sin k_y y \cdot e^{ik_z z} \quad (2-104)$$

$$E_y = 0 \quad (2-105)$$

$$E_z = H_0 \frac{-i\omega \mu k_x}{\omega^2 \mu \epsilon_0 \epsilon_t - k_y^2} \sin k_x x \cdot \sin k_y y \cdot e^{ik_z z} \quad (2-106)$$

$$H_x = H_0 \frac{-k_x k_y}{\omega^2 \mu \epsilon_0 \epsilon_t - k_y^2} \sin k_x x \cdot \cos k_y y \cdot e^{ik_z z} \quad (2-107)$$

$$H_y = H_0 \cos k_x x \cdot \sin k_y y \cdot e^{ik_z z} \quad (2-108)$$

$$H_z = H_0 \frac{ik_z k_y}{\omega^2 \mu \epsilon_0 \epsilon_t - k_y^2} \cos k_x x \cdot \cos k_y y \cdot e^{ik_z z} \quad (2-109)$$

The expression for calculating  $k_z$  is the same as (2-96).

### 2.3.3. Dominant Modes

A waveguide is always characterized by the dominant mode and the corresponding cutoff frequency ( $f_c$ ). The cutoff frequency of a hollow waveguide's dominant mode is determined by the waveguide dimensions,  $a$  and  $b$ . When a waveguide is homogeneously filled by an isotropic medium, for example, an isotropic dielectric, the cut off frequencies of all the modes are scaled down by the relative permittivity, so is that of the dominant mode as well. A recent example is the substrate integrated waveguide built using modern printed circuit board technology [52]. The cutoff frequencies are reduced by the substrates compared to hollow metallic waveguides.

However, the situation changes in a different fashion due to the anisotropy of its internal medium. First, the cutoff frequencies of different modes are shifted at different levels. Secondly, the waveguide may be intrinsically changed due to the alternation of the dominant mode. Thirdly,

the field distributions, guided wave impedances and attenuation constants will all be affected. Details on each uniaxial case are provided in the following discussion.

### Uniaxial-Z Case

For the uniaxial-z case, where the conventional  $TE_{z10}$  and  $TE_{z01}$  modes are supported, their cutoff frequencies are as follows.

$$f_{cZ}^{TE_{mn}} = \frac{c}{2\sqrt{\epsilon_t}} \sqrt{\left(\frac{m}{a}\right)^2 + \left(\frac{n}{b}\right)^2} \quad m, n = 0, 1, 2, \dots \quad (2-110)$$

$$f_{cZ}^{TM_{mn}} = \frac{c}{2\sqrt{\epsilon_z}} \sqrt{\left(\frac{m}{a}\right)^2 + \left(\frac{n}{b}\right)^2} \quad m, n = 1, 2, 3, \dots \quad (2-111)$$

The subscript  $c$  at the foot of  $f$  implies cutoff frequency, and symbol  $c$  in numerators denotes the velocity of light in vacuum. The above two cutoff frequency equations are different between TE and TM modes. The same set of equations fit for an isotropic case if the  $\epsilon_z$  is replaced by  $\epsilon_t$ , assuming the later relative permittivity characterizes the isotropic medium's relative permittivity. No matter how great or small  $\epsilon_t$  will be, the dominant mode would not change for isotropic case. Assuming  $a$  is greater than  $b$ , the dominant mode is always  $f_{cZ}^{TE_{10}}$ . However, in the uniaxial-z case, the difference in the permittivities in (2-110) and (2-111) changes the order of lowest modes. The change can be demonstrated in Figure 2-3.

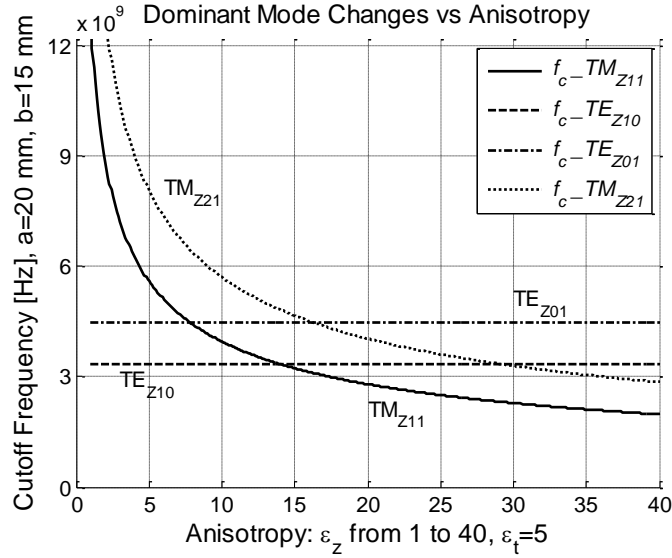


Figure 2-3 Dominant mode changes when the degree of anisotropy changes.

In the example illustrated in Figure 2-3, the cutoff frequency of the  $TM_{Z11}$  is always the lowest among all  $TM_z$  modes due to the lowest order. The cutoff frequency is derived from the dispersion relation and letting  $m$  of  $k_x$  and  $n$  of  $k_y$  to be the minimum values, namely  $m=1$  and  $n=1$ . Stunningly, the  $TM_{Z11}$  mode also becomes the dominant mode including the lowest order TE modes when the relative permittivity along Z axis ( $\epsilon_z$ ) exceeds certain value which is around 14 in this example.

### Uniaxial-X Case

In the uniaxial-x case, although the decomposition method has been changed, the way to pursue the dominant mode remains unaltered. In Table 2-2 where cutoff frequencies are tabulated the subscript  $cX$  is denoting that the cutoff frequency is formulated for the uniaxial-x case. Once again, it is observed that the dominant mode is determined not only by the dimensions of the waveguide, but also by the degree of anisotropy as shown in Figure 2-4. It is also worth mentioning that, of all the conventional transverse-to-Z modes, only the  $TE_{Zm0}$  or  $TE_{Z0n}$  modes coincide with  $TE_{Xm0}$  and  $TM_{X0n}$  modes of the uniaxial-x case, respectively.  $E_z$  and  $H_z$  are coupled in other modes.

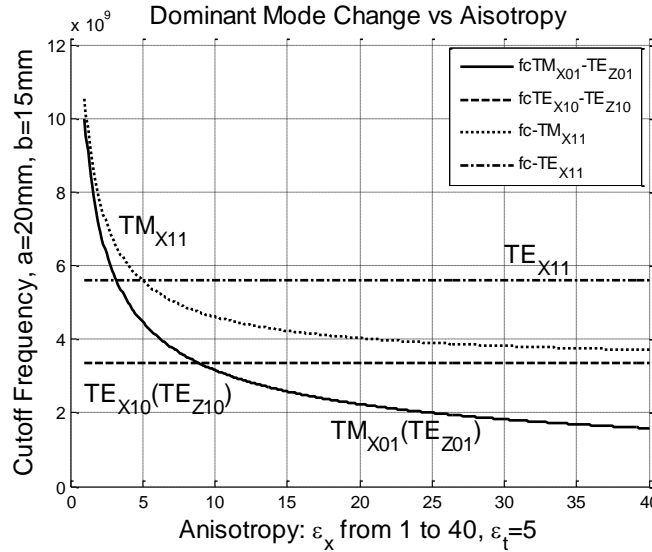


Figure 2-4 Dominant mode changes as the degree of anisotropy ( $\epsilon_x / \epsilon_t$ ) changes in uniaxial-x case.

In this example, although the dimension  $a$  is greater than  $b$ , the  $TM_{X01}$  mode which corresponds to the conventional  $TE_{Z01}$  mode becomes the dominant mode when the degree of anisotropy is strong enough, or when  $\epsilon_x$  exceeds the value of 8. Clearly, the dominant mode is not exclusively determined by the waveguide dimensions. The anisotropy also affects which mode has the lowest cutoff frequency.

### Uniaxial-Y Case

Last but not the least, from the supported modes and their cutoff frequencies tabulated in Table 2-3 the uniaxial-y case mode shift is also studied. The analysis and wave mode change due to the varying degree of anisotropy is similar to the previous uniaxial-x case. It was found that the dominant mode shift (between  $TE_{Y01}$  mode and  $TM_{Y10}$  mode) occurs when the medium is negatively uniaxial ( $\epsilon_y < \epsilon_t$ ), as shown in Figure 2-5. Specifically, the dominant mode is the  $TE_{Y01}$  mode when  $\epsilon_y$  is smaller than 2.5, and the dominant mode is the  $TM_{Y10}$  mode (corresponding to  $TE_{Z10}$ ) when  $\epsilon_y$  is greater than 2.5. Again the anisotropy affects which mode is the dominant mode.

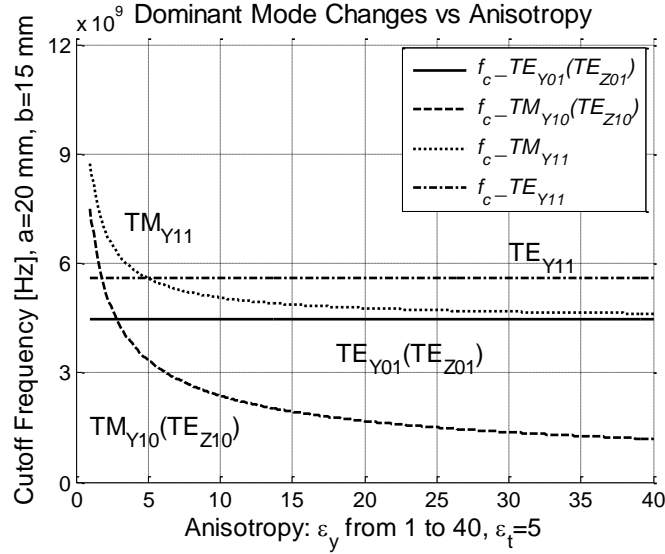


Figure 2-5 Dominant mode changes as the degree of anisotropy ( $\epsilon_y / \epsilon_t$ ) changes in uniaxial-y case.

### 2.3.4. Guided Wave Impedance

Last but not least, attenuation constants due to conductor loss are also subject to change. Physically, these variances can be attributed to the change of field distributions that intensify the dissimilarities of the modes of the same indices. The wave impedance formulas are different between the ordinary waves and the extraordinary waves. Only the possible dominant modes are considered. The definitions of the impedances follow the regular RWG (isotropic) conventions.

The  $TE_{Xm0}$ ,  $TE_{Y0n}$ ,  $TE_{Zm0}$  and  $TE_{Z0n}$  modes which are all o-waves have the same guided impedances given by

$$Z_0 = \frac{\eta_t}{\sqrt{1 - f_c^2 / f^2}}, \quad (2-112)$$

where

$$\eta_t = \sqrt{\frac{\mu_0}{\epsilon_0 \epsilon_t}}. \quad (2-113)$$

They are different from the isotropic dielectric filled waveguide by using the transverse relative permittivity other than the isotropic relative permittivity. Note that the optic axis is not involved because they are all ordinary waves with no E field component in the optic axis direction.

And the guided wave impedances of  $TM_{X0n}$  and  $TM_{Ym0}$  modes whose electric fields are non-zero in the optic axis direction are given by

$$Z_0 = \frac{\eta_{x,y}}{\sqrt{1 - f_c^2 / f^2}}, \quad (2-114)$$

where the subscripts of the impedance  $\eta$  and permittivity  $\epsilon$  represent the directions of the optic axis and the intrinsic impedances are given by

$$\eta_{x,y} = \sqrt{\frac{\mu_0}{\epsilon_0 \epsilon_{x,y}}}. \quad (2-115)$$

Equations (2-112) and (2-114) appear in the identical form because essentially they both describe how electrically transverse-to-z modes ( $TE_z$ ) behave. They include all the possible dominant modes except the  $TM_z$  modes in uniaxial-z case. In contrast, the  $TM_z$  modes in uniaxial-z case are the only magnetically transverse-to-z modes among all the supported modes, and the formula of the characteristic impedance is in the unique form as

$$Z_0 = \eta_t \sqrt{1 - f_c^2 / f^2} \quad (2-116)$$

### 2.3.5. Field Distributions

In isotropic and uniaxial-z cases, plots of field distributions of  $TM_{Z31}$  modes are provided in [49] and duplicated in Figure 2-6. In those figures, the  $E_z$  magnitudes are assumed same, and dimensions and relative permittivities are not specified except the relative ratios. Details are given in the figure caption. The fields are calculated from the obtained dyadic Green's functions over



the cross-section of the waveguide. In this work more field distributions are plotted using the analytical solutions.

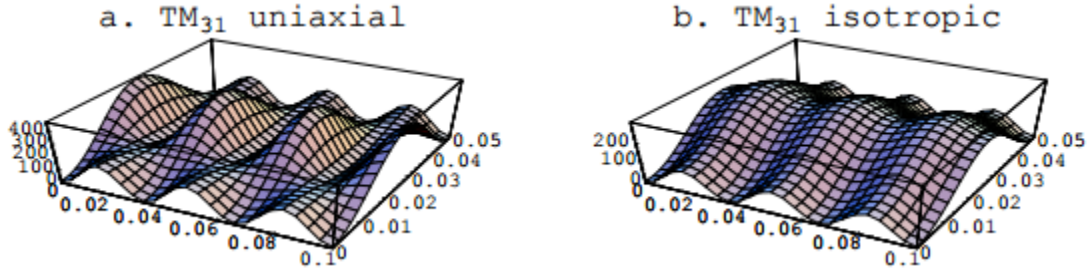


Figure 2-6 Field distributions of the  $TM_{31}$  mode in the uniaxial-z case and the isotropic case. Dimension ratio is  $a/b = 2$ . The uniaxial-Z case has  $\epsilon_z / \epsilon_t = 2.5$ .

Plots of field distributions of  $TM_{C31}$  modes (the subscript ‘C’ stands for X or Y) for uniaxial- $x$  and uniaxial- $y$  cases are shown in Figure 2-7 through Figure 2-14, along with the plots of the contours of the equal-field-strength curves. The equal strength contour is given by  $|E|^2 = E_x^2 + E_y^2 + E_z^2 = Constant$ .

In all the three-D plots, the amplitudes of  $E_z$  are all normalized to be 1 V/m for comparisons. The relative permittivity values are specified in the figures. Note that the relative relations among the E-field components are also calculated and included with the figures. The waveguide dimensions are all same as  $a=10$  cm and  $b=5$ cm.

Across all the field plots, although all the peaks and valleys are at the same locations in the cross-section plane (XY plane), their peak magnitudes are different. Although field distributions all follow the sinusoidal functional dependence, the field strength over the cross-section plane are quite different. In guided wave structures or microwave component design, the difference may affect the result of insertion loss or the performances at the discontinuities. In radiative unit design,

the field distribution may result in the changes in far field radiation pattern and antenna performances [11].

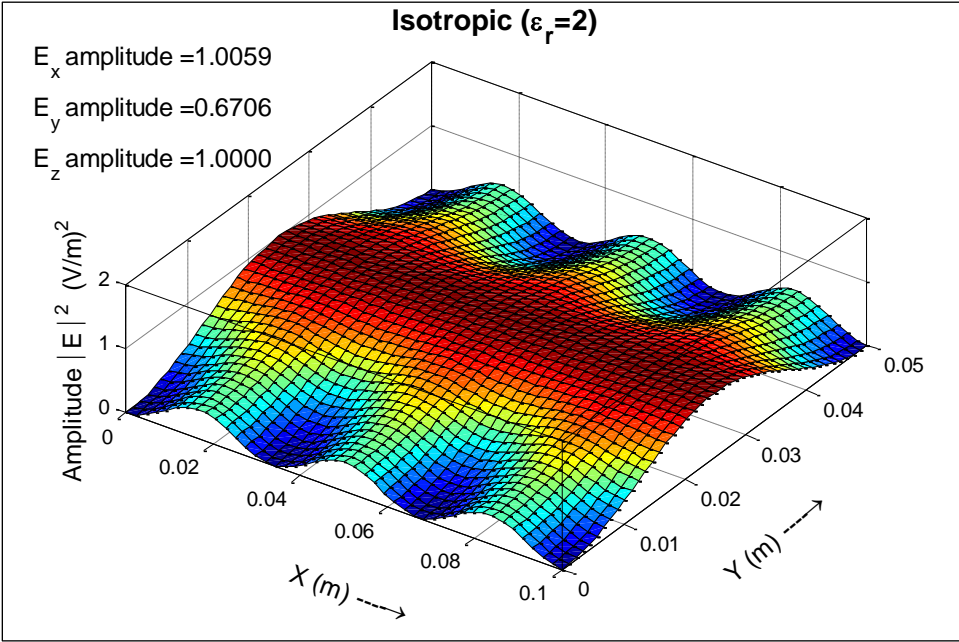


Figure 2-7 Field distribution of the  $TM_{z31}$  Modes in the isotropic case.

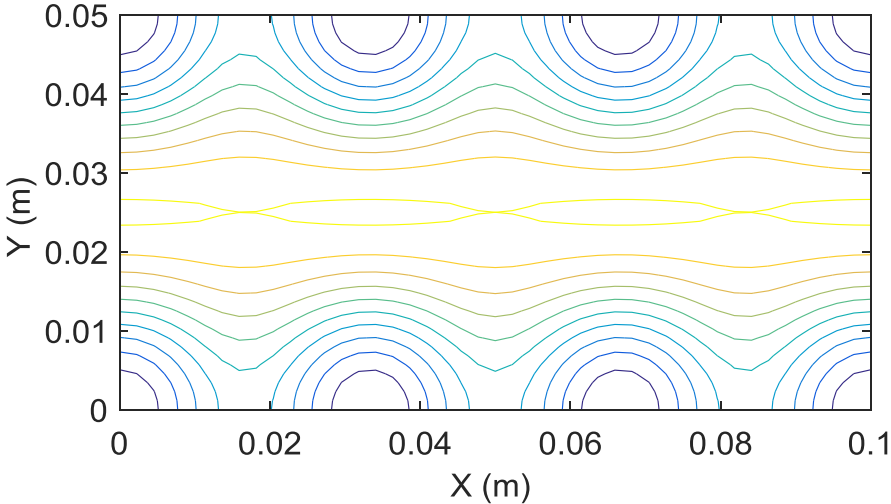


Figure 2-8 Contours showing the equal-magnitude curves in the isotropic case.

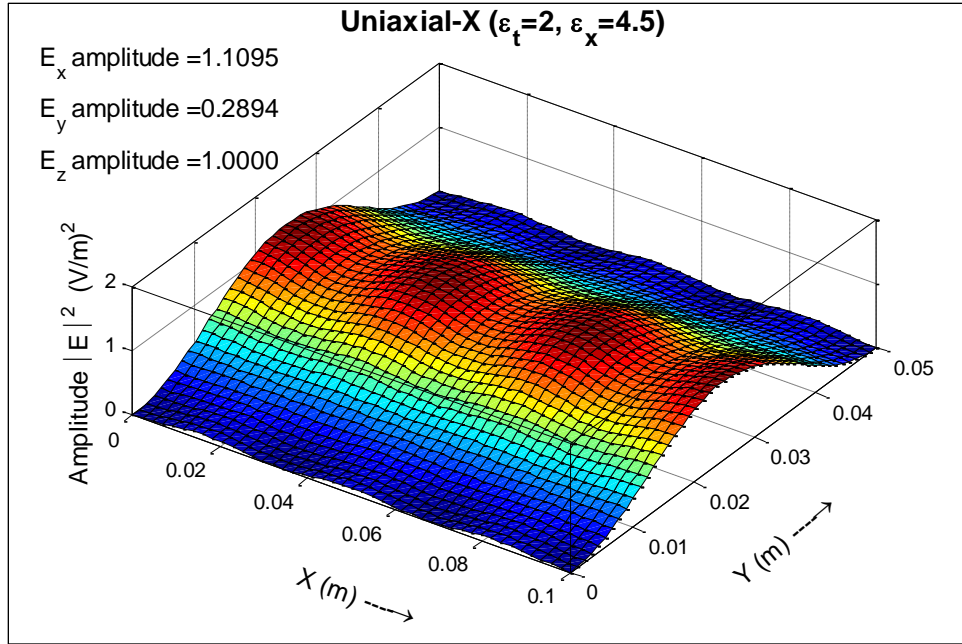


Figure 2-9 Field distribution of the  $TM_{x31}$  Modes in the uniaxial-x case.

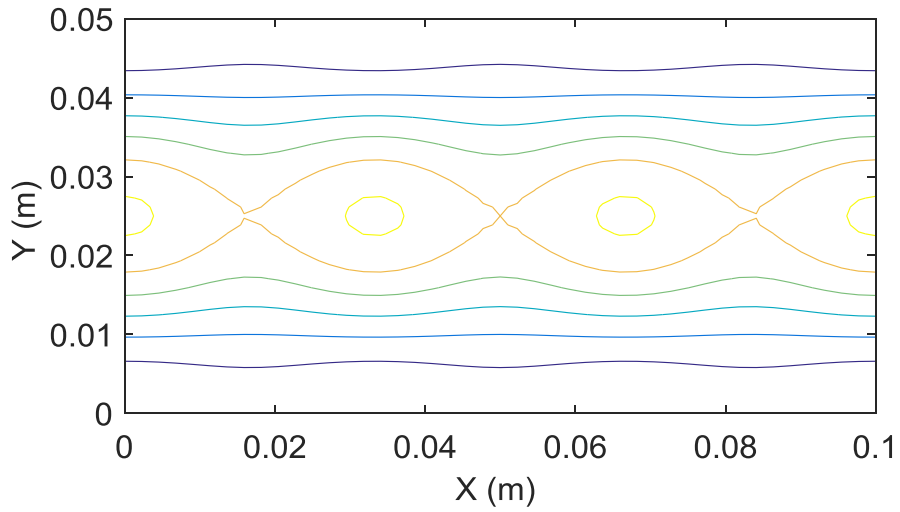


Figure 2-10 Contours showing the equal-magnitude curves in the uniaxial-x case.

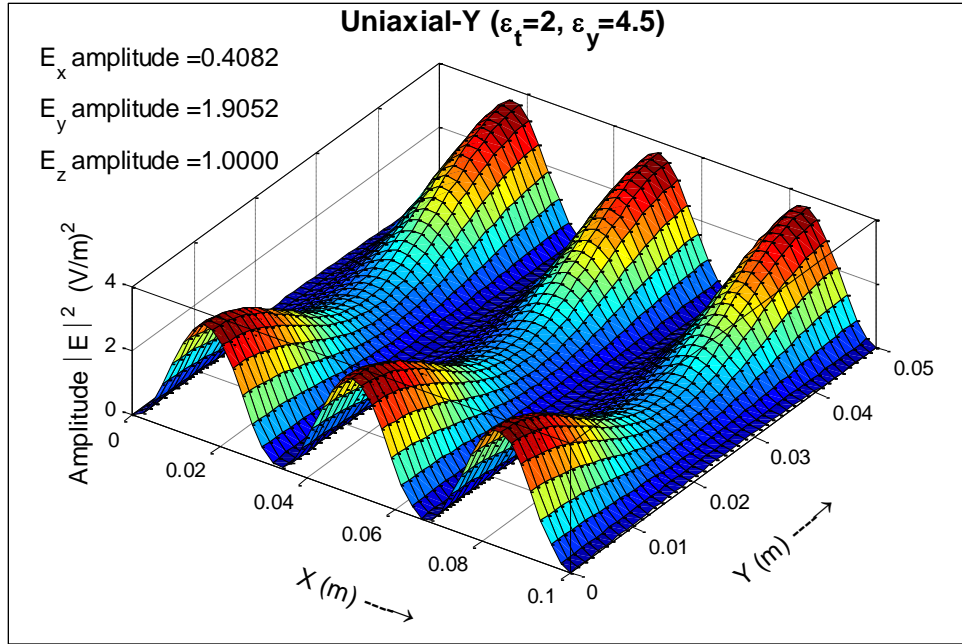


Figure 2-11 Field distribution of the  $TM_{X31}$  Modes in the uniaxial-x case.

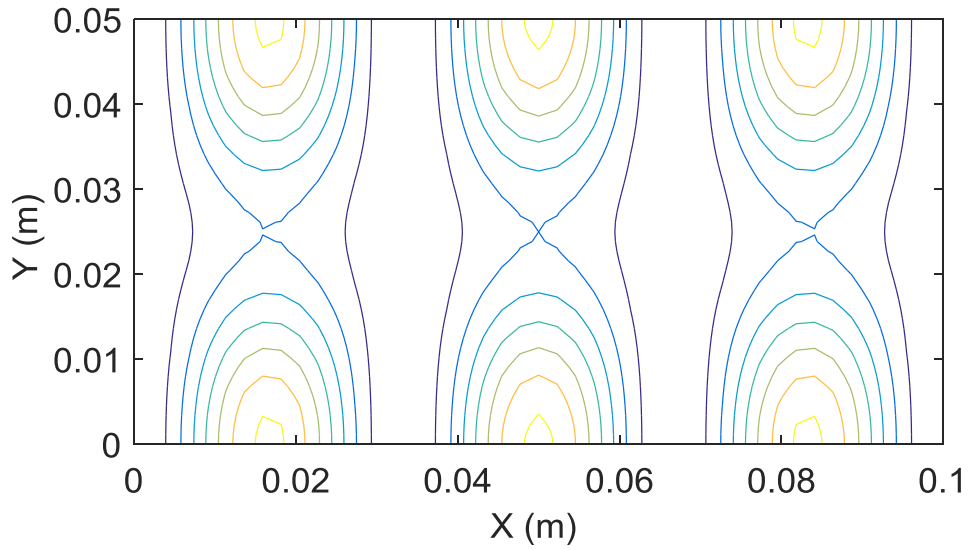


Figure 2-12 Contours showing the equal-magnitude curves in the uniaxial-y case.

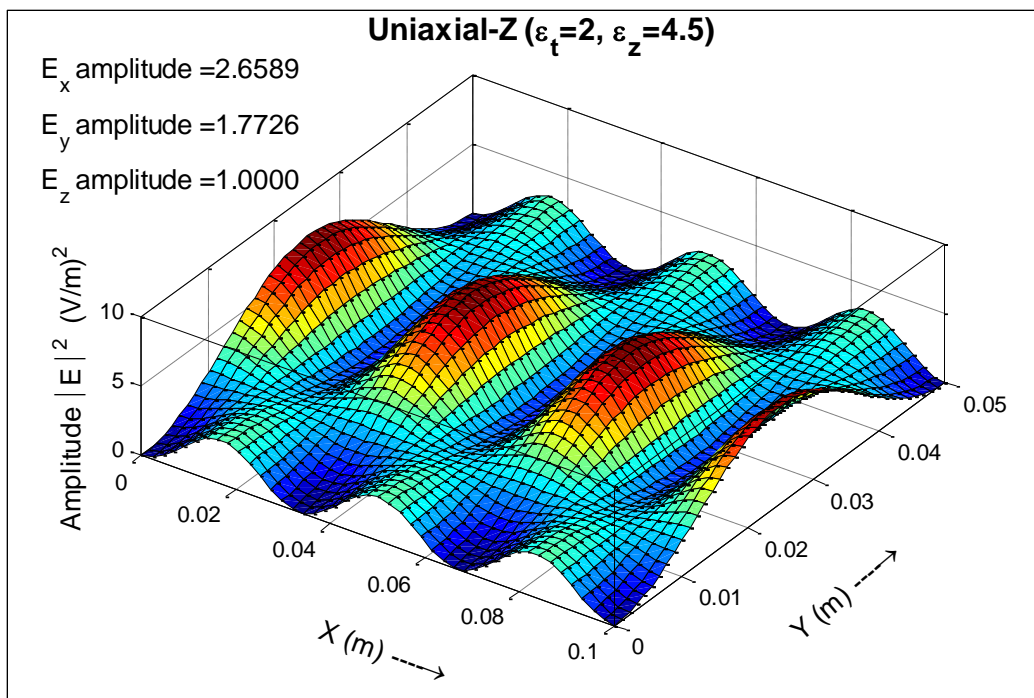


Figure 2-13 Field distribution of the  $TM_{Y31}$  Modes in the uniaxial-y case.

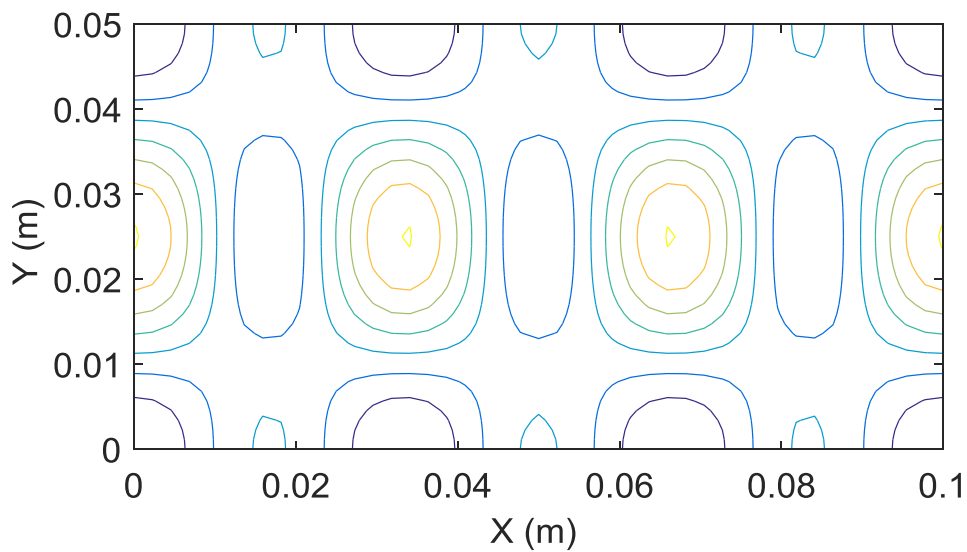


Figure 2-14 Contours showing the equal-magnitude curves in the uniaxial-y case.

All the contour plots exhibit one period along Y axis and three period over X axis. This is due to the mode chosen.

### 2.3.6. Attenuation Constants

The attenuation constants due to finite conductor loss are derived using the perturbation method and presented as follows with  $R_s$  representing the metal surface resistance, which is the real part of a lossy (highly conductive) medium's intrinsic impedance [53].

$$R_s = \text{Re}(\hat{\eta}) = \sqrt{\frac{\omega \mu}{2\sigma}} \quad (2-117)$$

Note that the intrinsic impedance has the same real part and imaginary part. Then the attenuation constants can be found as follows for  $\text{TM}_{X0n}$  ( $\text{TE}_{Z0n}$ ) modes

$$\alpha_c = \frac{R_s}{\eta_x \sqrt{1 - f_c^2/f^2}} \left[ \frac{2 f_c^2}{b f^2} + \frac{1}{a} \right], \quad (2-118)$$

and for  $\text{TE}_{Xm0}$  ( $\text{TE}_{Zm0}$ ) modes

$$\alpha_c = \frac{R_s}{\eta_t \sqrt{1 - f_c^2/f^2}} \left[ \frac{2 f_c^2}{a f^2} + \frac{1}{b} \right]. \quad (2-119)$$

For  $\text{TE}_{Y0n}$  ( $\text{TE}_{Z0n}$ ) modes the attenuation constant is given by

$$\alpha_c = \frac{R_s}{\eta_t \sqrt{1 - f_c^2/f^2}} \left[ \frac{2 f_c^2}{b f^2} + \frac{1}{a} \right], \quad (2-120)$$

and for  $\text{TM}_{Ym0}$  ( $\text{TE}_{Zm0}$ ) modes the result is

$$\alpha_c = \frac{R_s}{\eta_y \sqrt{1 - f_c^2/f^2}} \left[ \frac{2 f_c^2}{a f^2} + \frac{1}{b} \right]. \quad (2-121)$$

The cutoff frequency expressions for uniaxial-x and uniaxial-y cases can be found in Table 2-2 and Table 2-3, respectively. Finally for TM<sub>Z</sub> modes in the uniaxial-z case the attenuation constant is derived as follows.

$$\alpha_{c,mn}^{TM_z} = \frac{2R_s}{\eta_t \sqrt{1 - f_c^2/f^2}} \left( \frac{b^3 m^2 + a^3 n^2}{ab^3 m^2 + a^3 b n^2} \right) \quad (2-122)$$

The  $f_c$  expression for TM<sub>Z</sub> modes can be found in (2-111).

## 2.4. Summary

In this chapter we have shown the mathematical derivation and mode decomposition method developed for the RWGs filled with uniaxial medium whose optic axis is aligned with one of the coordinate axes. Dominant mode change was found through the calculations using the analytical solutions. Field distributions revealed the change due to the incorporation of the uniaxial medium. Complete fields and wave mode solutions are provided, along with the impedance and attenuation constants.

## Chapter 3 Rectangular Waveguide Filled with Uniaxial Medium – Tilted Cases

Tilting of the optic axis elevates the complexity of the problem substantially. The aligned problems are only slightly distinctive from the isotropic problem in terms of formulation, wave modes and standing wave conditions. However, the birefringence that induces the double reflection phenomenon significantly complicates waveguide problems. Relevant electromagnetic problems on reflection and transmission were thoroughly investigated in [54], which enlightened the study of the reflection behaviors on the waveguide's inner side walls (uniaxial-metal interfaces). Furthermore, the approach to solve the side wall problem depends heavily on the aforementioned study of reflections. The following discussion will be organized by directions of optic axis orientations.

When the optic axis is tilted but lying in the cross-section plane, namely the x-y plane according to Figure 2-1 in Chapter 2, the research into this type of problem was first reported in [8] using the variational method. The vectorial variational formula of guided propagation constant in an inhomogeneous and/or anisotropic waveguide was first derived by Berk [55], and since detailed in several textbooks, e.g., [4] and [56]. Although certain restrictions apply, the method has proved successful in treating resonators and waveguides enclosing anisotropic media. By employing the so-called Rayleigh-Ritz procedure, asymptotic numerical results can be obtained.

Although it is considered concise and conceives unified formulation, the variational method solutions lack adequate information to model all of the travelling waves. The method provides only the propagation constant of dominant mode, but other quantities of interests including  $k_x$ ,  $k_y$  and field distributions are, at least in Davis' paper, not available. Moreover, its convergence and



accuracy depend on structural configurations and modal approximations [57], or the selected test functions. The trial solutions of the field components in [8] need to be modified in order to be used for other uniaxial waveguide problems. Although it has these disadvantages, the variational method can still be applied in future work to verify the correctness of the computed results presented here. In Chapter 3, we consider the problem when the optic axis is tilted but lying in the side wall plane, i.e., either the X-Z plane or the Y-Z plane. The first following section will review the constitutive relation with complex matrix forms. The second section will brief the analytical solutions, followed by the hybrid numerical solutions in the third section. The fourth section presents a detailed example for readers to understand how the computation routine works.

### 3.1. Constitutive Relations

The constitutive relations in the aligned cases have been discussed in the previous chapter. The relative permittivity tensors are in diagonal form with off-diagonal elements all zeros. This changes in the tilted cases. In general, the tensor can be obtained using the transformation matrix [56]. The transformation matrix can be obtained as the combination of two of the three matrices as follows.

$${}^{\Rightarrow\gamma} R_z(\theta) = \begin{pmatrix} \cos \gamma & \sin \gamma & 0 \\ -\sin \gamma & \cos \gamma & 0 \\ 0 & 0 & 1 \end{pmatrix} \quad (3-1)$$

$${}^{\Rightarrow\beta} R_y(\theta) = \begin{pmatrix} \cos \beta & 0 & -\sin \beta \\ 0 & 1 & 0 \\ \sin \beta & 0 & \cos \beta \end{pmatrix} \quad (3-2)$$

$$R_x(\alpha) = \begin{pmatrix} 1 & 0 & 0 \\ 0 & \cos \alpha & \sin \alpha \\ 0 & -\sin \alpha & \cos \alpha \end{pmatrix} \quad (3-3)$$

The above transformation matrices are defined to be used with the rotation with respect to Z, Y, and X axis, respectively. The rotating angles are called Euler Angles which are shown in Figure 3-1.

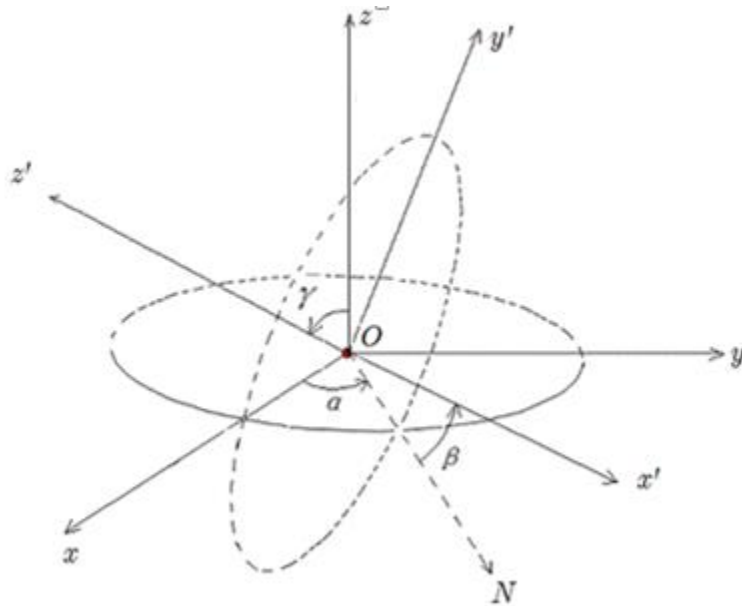


Figure 3-1 Demonstration of Euler Angles in transformation matrices. The most general transformation takes three rotations but may use two or three rotation matrices.

Although the rotation matrix is defined in three forms, a general rotating process requires only two out of the three. More details can be found in many other mathematics books like [56]. In this chapter, the relative permittivity matrices will be rotated only once along one of the coordinate axes.

### 3.1.1. Rotation in Cross-Section Plane

Assume originally the optic axis is aligned with one of the axes in the cross section plane, namely the X-Y plane. If the medium is rotated around the axial direction with an angle  $\gamma$  as depicted in Figure 3-2 the permittivity tensors will have non-zero off-diagonal elements.

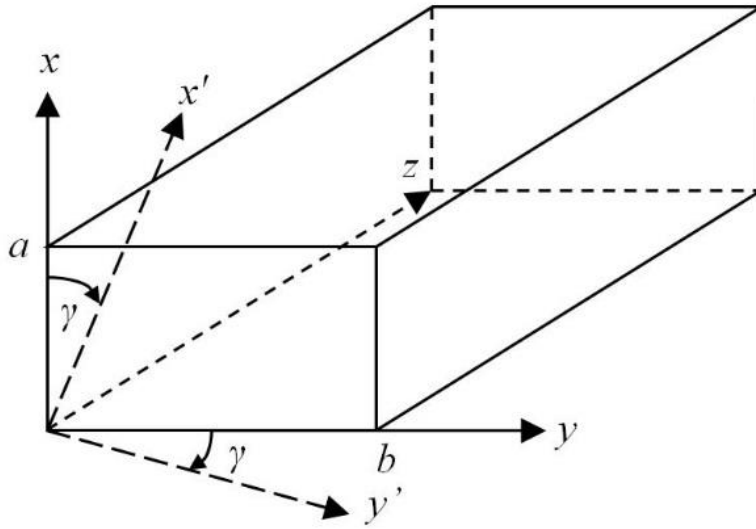


Figure 3-2 Optic axis tilts from x axis and lies in the cross section plane.

Taking uniaxial-x as the initial configuration and applying Euler's angle rotation, the rotated tensor can be obtained by

$$\overline{\overline{\varepsilon}}_r^\gamma = \left( \overline{\overline{R}}_z^\gamma \right)^{-1} \cdot \begin{pmatrix} \varepsilon_x & 0 & 0 \\ 0 & \varepsilon_t & 0 \\ 0 & 0 & \varepsilon_t \end{pmatrix} \cdot \left( \overline{\overline{R}}_z^\gamma \right) \quad (3-4)$$

which results in the following form.

$$\overline{\overline{\varepsilon}}_r^\gamma = \begin{pmatrix} \varepsilon_{11} & \varepsilon_{12} & 0 \\ \varepsilon_{21} & \varepsilon_{22} & 0 \\ 0 & 0 & \varepsilon_t \end{pmatrix} \quad (3-5)$$

The rotated matrix elements are given by

$$\varepsilon_{11} = \varepsilon_x \cos^2 \gamma + \varepsilon_t \sin^2 \gamma \quad (3-6)$$

$$\varepsilon_{22} = \varepsilon_x \sin^2 \gamma + \varepsilon_t \cos^2 \gamma \quad (3-7)$$

$$\varepsilon_{12} = \varepsilon_{21} = (\varepsilon_x - \varepsilon_t) \cos \gamma \sin \gamma \quad (3-8)$$

Note that for a positive uniaxial medium whose  $\varepsilon_x$  is greater than  $\varepsilon_t$ , the off diagonal elements are positive, and they are negative for a negative uniaxial medium.

### ***3.1.2. Rotation in Side Wall Plane***

An RWG has two orthogonal side wall planes, both of which are parallel to the direction of propagation. The structural characteristic, sometimes referred to as *rotational symmetry*, allows us to demonstrate the solution to one type of problem and the method is automatically applicable to the other, the symmetric problem. Accordingly, the tilted case with the optic axis lying in Y-Z plane and the tilted case with the optic axis lying in X-Z plane are considered as symmetric problems, and here we use the former one as the example.

Assume the optic axis is originally along z-axis, and it is tilted by an angle  $\alpha$  in the y-z plane as shown in Figure 3-3.

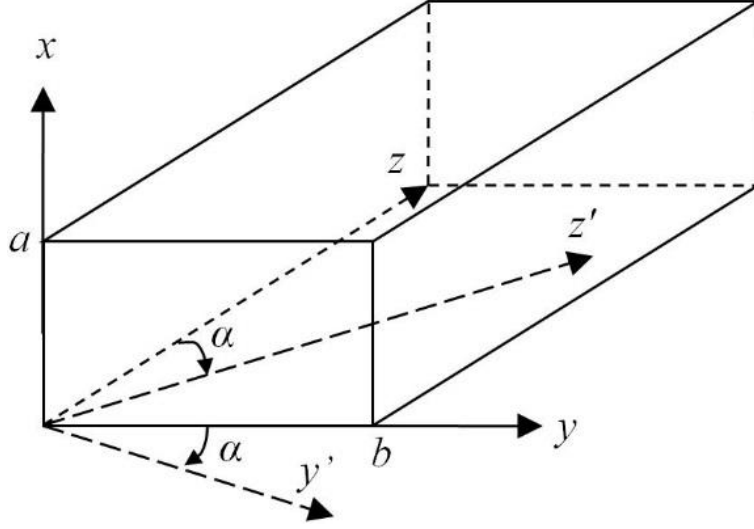


Figure 3-3 Optic axis tilts from the  $z$  axis and lies in the  $y$ - $z$  plane.

Then we have five non-zero elements in the tensor can be obtained by

$$\overset{=}{\varepsilon}_r^\alpha = \left( \overset{=}{R}_x^\alpha \right)^{-1} \cdot \begin{pmatrix} \varepsilon_t & 0 & 0 \\ 0 & \varepsilon_t & 0 \\ 0 & 0 & \varepsilon_z \end{pmatrix} \cdot \left( \overset{=}{R}_x^\alpha \right) \quad (3-9)$$

which results in the following form

$$\overset{=}{\varepsilon}_r^\alpha = \begin{pmatrix} \varepsilon_t & 0 & 0 \\ 0 & \varepsilon_{22} & \varepsilon_{23} \\ 0 & \varepsilon_{32} & \varepsilon_{33} \end{pmatrix} \quad (3-10)$$

The matrix entries are derived as follows.

$$\varepsilon_{22} = \varepsilon_t \cos^2 \alpha + \varepsilon_z \sin^2 \alpha \quad (3-11)$$

$$\varepsilon_{33} = \varepsilon_t \sin^2 \alpha + \varepsilon_z \cos^2 \alpha \quad (3-12)$$

$$\varepsilon_{23} = \varepsilon_{32} = (\varepsilon_z - \varepsilon_t) \cos \alpha \sin \alpha \quad (3-13)$$

Those who are familiar with gyrotropic media may easily recognize the similarity between the tensors in (3-5) and (3-10) and the permeability tensor of a ferrite with biasing magnetic field in  $z$

and x directions [3], respectively. Moreover, the guided wave problem with tensor (3-10) is exactly rotationally symmetric with the configuration in [58], where the permittivity matrix was given by

$$\bar{\varepsilon} = \begin{pmatrix} \varepsilon_1 & 0 & \varepsilon_3 \\ 0 & \varepsilon_2 & 0 \\ -\varepsilon_3 & 0 & \varepsilon_1 \end{pmatrix}. \quad (3-14)$$

The matrix elements are defined in [58]. The matrix in (3-14) is the same form as a uniaxial side-wall case with optic axis lying in X-Z plane. Because of the similarity in the tensor forms, it seems advisable to import those methods developed for gyrotropic RWGs. However, differences between tensorial terms restrict the direct usage, and additional complexity is encountered when determining the wave modes for tilted uniaxial problems. Hence we will address this uniaxial RWG problem in a different approach.

In the following discussion, we take the side-wall plane case with the optic axis in Y-Z plane as the example to conduct derivation and computation. The method and principles all apply to the other side-wall plane case as well, due to the rotational symmetry of the rectangular waveguide geometry.

### 3.2. Analytical Solution

First we consider the case that can be solved analytically by following a conventional method of manipulating separated PDEs of Maxwell's equations in the source-free region.

$$\nabla \times \vec{E} = i\omega\mu_0\vec{H} \quad (3-15)$$

$$\nabla \times \vec{H} = -i\omega\varepsilon_0\overline{\varepsilon_r} \cdot \vec{E} \quad (3-16)$$

$$\nabla \cdot \vec{D} = 0 \quad (3-17)$$

Gauss' law for magnetic flux density remains the same as the non-magnetic aligned cases since the tilted medium is again assumed non-magnetic. The relative permittivity tensor is defined in (3-10) whose elements are given in (3-11) to (3-13).

The separated PDEs of the two curl equations are listed as follows.

$$\frac{\partial E_z}{\partial y} - \frac{\partial E_y}{\partial z} = i\omega\mu_0 H_x \quad (3-18)$$

$$\frac{\partial E_x}{\partial z} - \frac{\partial E_z}{\partial x} = i\omega\mu_0 H_y \quad (3-19)$$

$$\frac{\partial E_y}{\partial x} - \frac{\partial E_x}{\partial y} = i\omega\mu_0 H_z \quad (3-20)$$

$$\frac{\partial H_z}{\partial y} - \frac{\partial H_y}{\partial z} = -i\omega\varepsilon_0\varepsilon_t E_x \quad (3-21)$$

$$\frac{\partial H_x}{\partial z} - \frac{\partial H_z}{\partial x} = -i\omega\varepsilon_0\varepsilon_{22} E_y - i\omega\varepsilon_0\varepsilon_{23} E_z \quad (3-22)$$

$$\frac{\partial H_y}{\partial x} - \frac{\partial H_x}{\partial y} = -i\omega\varepsilon_0\varepsilon_{32} E_y - i\omega\varepsilon_0\varepsilon_{33} E_z \quad (3-23)$$

Compared to the isotropic or the aligned cases, the fifth and the sixth PDEs share the coupled  $E_y$  and  $E_z$  components due to the existence of the  $\varepsilon_{23}$  element, which, as will be demonstrated, lead to the existence of the hybrid modes. The electric field Gauss' law can be written as

$$\varepsilon_t \frac{\partial}{\partial x} E_x + \varepsilon_{22} \frac{\partial}{\partial y} E_y - \varepsilon_{23} \frac{\partial}{\partial y} E_z + \varepsilon_{23} \frac{\partial}{\partial z} E_y - \varepsilon_{33} \frac{\partial}{\partial z} E_z = 0 \quad (3-24)$$

The above equation comes from the sum of partial derivative of  $D_x$  with  $x$ , partial derivative of  $D_y$  with  $y$  and partial derivative of  $D_z$  with  $z$ . Both  $D_y$  and  $D_z$  are combinations of  $E_y$  and  $E_z$  due to the non-zero  $\varepsilon_{23}$  entry.

Although  $E_y$  and  $E_z$  components are coupled and are impractical to separate, the mode that has only  $E_x$  component might still be supported. This inspired the process of seeking the analytical mode. One may also follow the conventional fashion to find the analytical modes as explained in numerous previous papers that address the anisotropy in waveguides. The conventional fashion directly verifies the support of TE and TM modes by arbitrarily letting  $E_z$  and  $H_z$  components vanish, respectively. Moreover, the TE modes can have one of the transverse wavenumbers being zero and need to have less number of wave components, thus are even easier for mathematical verification.

From the separated PDEs, direct verification confirms that when the x dependence is gone the TE waves are described by the following reduced number of PDEs.

$$\frac{\partial E_x}{\partial z} = i\omega\mu_0 H_y \quad (3-25)$$

$$-\frac{\partial E_x}{\partial y} = i\omega\mu_0 H_z \quad (3-26)$$

$$\frac{\partial H_z}{\partial y} - \frac{\partial H_y}{\partial z} = -i\omega\varepsilon_0\varepsilon_t E_x \quad (3-27)$$

The resultant equations above contain no permittivity along the optic axis. Applying boundary conditions, these first order PDEs lead to ordinary wave (o-wave) solutions given in the following equations.

$$H_z = H_0 \cos k_y y \cdot e^{-jk_z z} \quad (3-28)$$

$$H_y = H_0 \frac{-ik_y k_z}{\omega^2 \mu_0 \varepsilon_t - k_z^2} \sin k_y y \cdot e^{-jk_z z} \quad (3-29)$$

$$E_x = H_0 \frac{-i\omega\mu_0 k_y}{\omega^2 \mu_0 \varepsilon_t - k_z^2} \sin k_y y \cdot e^{jk_z z} \quad (3-30)$$



where  $H_0$  can be solved once the excitation is known and  $k_y$  satisfies the following condition to form standing waves between the planes separated by the distance  $b$ .

$$k_y b = n\pi, \quad n = 1, 2, 3 \dots \quad (3-31)$$

The above solution shows that the conventional  $TE_{0n}$  modes are supported in the case when the optic axis is tilted and lying in  $y$ - $z$  plane. The supported analytical mode contains only  $E_x$  component with electric field. This fact eliminated the need to involve the off-diagonal relative permittivities. It can also be easily verified that there is no other conventional modes supported in such waveguide.

Due to the rotational symmetry, when the optic axis is tilted and lying in the  $x$ - $z$  plane, the  $TE_{zm0}$  modes of o-waves are supported. In these side wall problems, no other travelling modes of exclusively o-waves or exclusively extraordinary waves (e-wave) can be found. Therefore, as has been established by numerous former researchers, we must resort to hybrid modes that are combinations of o-waves and e-waves. The coupled waves are connected in that they share the identical propagation constant along the guided direction.

Since our objective is to obtain the full solution of all the propagating modes, field distributions and wavenumbers, we choose a method that includes and relates every aspect of the final solutions. To this end, the total wave formulation using wavenumbers is distinguished from other approaches.

### 3.3. Hybrid Mode Solutions

The hybrid mode will be solved using the combined wave formulation as a combination of ordinary wave and extraordinary wave. The coupling of the two types of modes can be either seen from the previous description in the analytical mode solutions or the wave reflection behaviors.

### 3.3.1. Free Space Wave Formulation

Taking curl on both sides of (3-15) and making the use of the equation (3-16), we can find a general wave equation for the electric field in source-free region filled by uniaxial media as follows.

$$\nabla \times \nabla \times \vec{E} - \omega^2 \mu_0 \varepsilon_0 \varepsilon_r \cdot \vec{E} = 0 \quad (3-32)$$

The above equation leads to three scalar partial differential equations which are the x, y and z components in the vectorial equation. For general anisotropic media in unbounded space, the electric field components can be solved using dyadic Green's functions [59]. However in a waveguide problem where the boundary conditions are much more complex, the dyadic Green's functions are difficult to use. Therefore in solving this problem we use vectorial wave formulation and solve matrix problems.

Making use of the tensor operation [54] and assuming plane wave solution  $e^{i\vec{k} \cdot \vec{r}} = e^{i(k_x x + k_y y + k_z z)}$ , the wave equation (3-32) can be rewritten as

$$\vec{k} \cdot \vec{k} \cdot \vec{E} + k_0^2 \varepsilon_r \cdot \vec{E} = 0, \quad (3-33)$$

where  $k_0^2 = \omega^2 \mu_0 \varepsilon_0$  and the 3-by-3 matrix  $\vec{k}$  is defined as [54]

$$\vec{k} = \begin{pmatrix} 0 & -k_z & k_y \\ k_z & 0 & -k_x \\ -k_y & k_x & 0 \end{pmatrix}. \quad (3-34)$$

Subsequently the wave equation for electric fields can be found in the matrix form as

$$\begin{pmatrix} k_y^2 + k_z^2 - k_0^2 \varepsilon_{11} & -k_x k_y & -k_x k_z \\ -k_y k_x & k_x^2 + k_z^2 - k_0^2 \varepsilon_{22} & -k_y k_z - k_0^2 \varepsilon_{23} \\ -k_z k_x & -k_z k_y - k_0^2 \varepsilon_{32} & k_x^2 + k_y^2 - k_0^2 \varepsilon_{33} \end{pmatrix} \cdot \vec{E} = 0. \quad (3-35)$$

by transforming the double-curl equation of the E field. Hence the problem of partial differential equations is turned into an eigenvalue problem. The E-field vector solution can be easily found with boundary condition after the hybrid mode wave is formulated.

The determinant of the coefficient matrix in (3-35) can be written in the form of the multiplication of three polynomials as follows.

$$(k_x^2 + k_y^2 + k_z^2 - k_0^2 \epsilon_t)(k_x^2 \epsilon_t + k_y^2 \epsilon_{22} + 2k_y k_z \epsilon_{23} + k_z^2 \epsilon_{33} - k_0^2 \epsilon_t \epsilon_z) k_0^2 \quad (3-36)$$

Letting the determinant of the coefficient matrix vanish [60], the dispersion relations for o-wave and e-wave are obtained as follows.

$$k_x^2 + k_y^2 + k_z^2 = k_0^2 \epsilon_t \quad (3-37)$$

$$k_x^2 \epsilon_t + k_y^2 \epsilon_{22} + 2k_y k_z \epsilon_{23} + k_z^2 \epsilon_{33} = k_0^2 \epsilon_t \epsilon_z \quad (3-38)$$

Equation (3-37) is the dispersion relation for the o-wave and (3-38) is that for the e-wave. Then the eigenvectors representing the characteristic wave fields can be calculated numerically [61] or symbolically [56] [62]. The general numerical solutions have been explored in [63] for radiation problems. The symbolical solutions are explored here and used in further formulation.

Consider the eigenvalue problem in the matrix operation in (3-35). It is to seek eigenvector solutions with eigenvalues of zeors, or equivalently, the solution to the homogeneous linear equations with three unknowns ( $E_x, E_y, E_z$ ). The three unknowns form a valid wave solution only when the determinant is zero.

When the determinant is zero, the rank of the coefficient matrix is not full. When the three wavenumbers satisfy one of the dispersion relations, the coefficient matrix leads to two vector

solutions. The two vector solutions are obtained when the three wavenumbers satisfy either the ordinary wave dispersion relation or the extraordinary wave dispersion relation.

Homogeneous equations do not have unique solution but ratios among elements in each solutions is fixed [56]. For example, in the matrix problem below

$$A \cdot x = \begin{bmatrix} a_{11} & a_{12} & a_{13} \\ a_{21} & a_{22} & a_{23} \\ a_{31} & a_{32} & a_{33} \end{bmatrix} \begin{bmatrix} x_1 \\ x_2 \\ x_3 \end{bmatrix} = \begin{bmatrix} 0 \\ 0 \\ 0 \end{bmatrix}, \quad (3-39)$$

if the determinant of the matrix A is zero, then the solution to the vector x can be formulated as

$$\frac{x_1}{x_3} = \frac{M_{31}}{M_{33}}, \quad (3-40)$$

$$\frac{x_2}{x_3} = \frac{M_{32}}{M_{33}}, \quad (3-41)$$

$$x_3 = 1, \quad (3-42)$$

if  $M_{33}$  is not zero. The  $M_{ij}$  represent the minor of the matrix with the subscripts i and j denoting the row-position and column position of the entry in the matrix. The above solution uses the minors of the third row in the coefficient matrix assuming the  $M_{33}$  is non-zero. If  $M_{33}$  is zero, then one can use either the minors of the second row or the first row. They all yield the same answer when normalized. Another formulation gives  $x_1=M_{31}$ ,  $x_2=M_{32}$  and  $x_3=M_{33}$  which is used in subsequent eigenvector solution formulation.

Consequently, for o-wave vector and e-wave vector, the obtained solutions are normalized when used in calculations. Using the solution formulated using the minors of the coefficient matrix, the two vector solutions can be found as follows.

$$\vec{E}^{or} = \begin{Bmatrix} k_z \sin \alpha - k_y \cos \alpha \\ k_x \cos \alpha \\ -k_x \sin \alpha \end{Bmatrix} \quad (3-43)$$

$$\vec{E}^{ex} = \begin{Bmatrix} -k_x k_y \varepsilon_z \sin \alpha - k_x k_z \varepsilon_z \cos \alpha \\ k_x^2 \varepsilon_t \sin \alpha + (k_z \sin \alpha - k_y \cos \alpha)(k_z \varepsilon_{33} + k_y \varepsilon_{23}) \\ k_x^2 \varepsilon_t \cos \alpha + (k_y \cos \alpha - k_z \sin \alpha)(k_y \varepsilon_{22} + k_z \varepsilon_{23}) \end{Bmatrix} \quad (3-44)$$

The superscripts *or* and *ex* designate the characteristic types of o-wave and e-wave, respectively. The dispersion relations (3-37) and (3-38) apply to the vectors (3-43) and (3-44), respectively. The above results agree with those presented in [54].

Another set of symbolic vector solutions that will be used in the future is given by

$$\vec{E}_i^{or} = E_i \begin{Bmatrix} C_{xi}^{or} \\ C_{yi}^{or} \\ C_{zi}^{or} \end{Bmatrix}, \quad (3-45)$$

$$\vec{E}_i^{ex} = E_i \begin{Bmatrix} C_{xi}^{ex} \\ C_{yi}^{ex} \\ C_{zi}^{ex} \end{Bmatrix}. \quad (3-46)$$

The vectors are the characteristic wave vectors solved previously. The subscript *i* represents the incident wave. The notation is useful in wave reflection behavior studies.

### 3.3.2. Reflection Behaviors

The birefringence effect in anisotropic media has been studied broadly. What birefringence effect suggests is that on the boundary with anisotropic media involved, the incident wave of a single characteristic mode may produce reflected wave(s) as a combination of different characteristic waves. In order to formulate a complete travelling wave that contains all the possible

waves travelling simultaneously, we need to first study wave reflection behaviors at the uniaxial and metal boundaries of the RWG inner walls. For simplicity we assume the metal walls are perfect conductors (PECs).

The investigations are based on the characteristic vectors. In general, the ordinary incident wave would be reflected with two characteristic waves thus

$$\vec{E}_r^{io} = R^{oo} E_i \begin{Bmatrix} C_{xr}^{or} \\ C_{yr}^{or} \\ C_{zr}^{or} \end{Bmatrix} + R^{oe} E_i \begin{Bmatrix} C_{xr}^{ex} \\ C_{yr}^{ex} \\ C_{zr}^{ex} \end{Bmatrix}. \quad (3-47)$$

Similarly, generally the incident e-wave would have the reflected waves as

$$\vec{E}_r^{ie} = R^{eo} E_i \begin{Bmatrix} C_{xr}^{or} \\ C_{yr}^{or} \\ C_{zr}^{or} \end{Bmatrix} + R^{ee} E_i \begin{Bmatrix} C_{xr}^{ex} \\ C_{yr}^{ex} \\ C_{zr}^{ex} \end{Bmatrix}. \quad (3-48)$$

In the above formulation, the subscript  $r$  denotes the reflected wave. The superscript  $io$  denotes the reflection from an ordinary incident wave, and the superscript  $ie$  denotes the reflection from an extraordinary incident wave. The superscript with reflection coefficients  $R$ 's denotes the co-type and cross-type reflection coefficients.

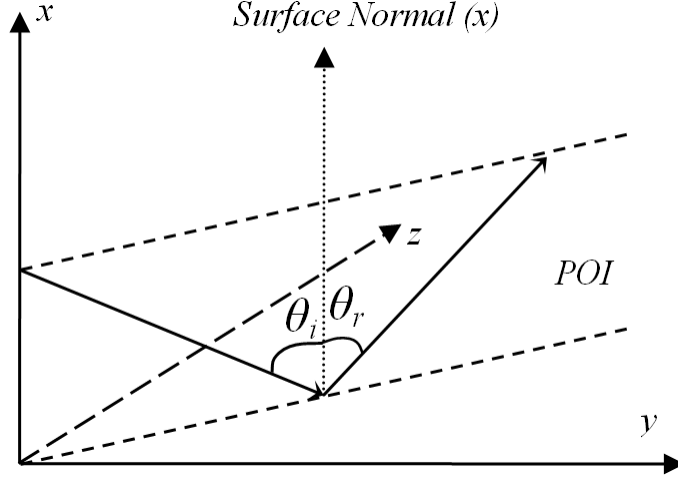


Figure 3-4 Reflection on  $x=0$  plane is a simple case in which the incidence angle and the reflection angle are same,  $\theta_i=\theta_r$ .

Figure 3-4 shows the wave reflection on the boundary parallel to  $y-z$  plane, or with more generality, the plane in which the optic axis is lying. In other words, the plane of incidence (POI) is perpendicular to the plane in which the optic axis is lying. While the wavenumbers  $k_y$  and  $k_z$  retain their values in the reflected waves due to phase matching, birefringence generally induces two vertical (normal to the boundary) wavenumbers for two different types of characteristics waves [33]. The two vertical wavenumber formulas are given by

$$k_x^{or} = \pm \sqrt{k_0^2 \epsilon_t - k_y^2 - k_z^2} \quad (3-49)$$

$$k_x^{ex} = \pm \frac{1}{\sqrt{\epsilon_t}} \sqrt{k_0^2 \epsilon_t \epsilon_z - k_y^2 \epsilon_{22} - 2k_y k_z \epsilon_{23} - k_z^2 \epsilon_{33}} \quad (3-50)$$

However, since  $k_x$  appears only in quadratic terms in both ordinary and extraordinary dispersion relations above, the reflected wave actually retains the same normal wavenumber magnitude (although with flipped signs) and is of the same characteristic type with the incident wave. This behavior can also be confirmed using the field vectors to satisfy the BCs. Similar reflection from gyrotropic-PEC boundary was also observed and mentioned as *reflection symmetry*

in [64] addressing a gyromagnetic-medium-filled rectangular waveguide, and it is later reused in [58] addressing a gyroelectric-medium-filled rectangular waveguide. If the second medium is other isotropic dielectric instead of PEC, the transmitted waves will possess both a parallel polarized wave and a perpendicular polarized wave unless the POI is aligned with the tilted optic axis. But PEC boundary considers no transmitted waves.

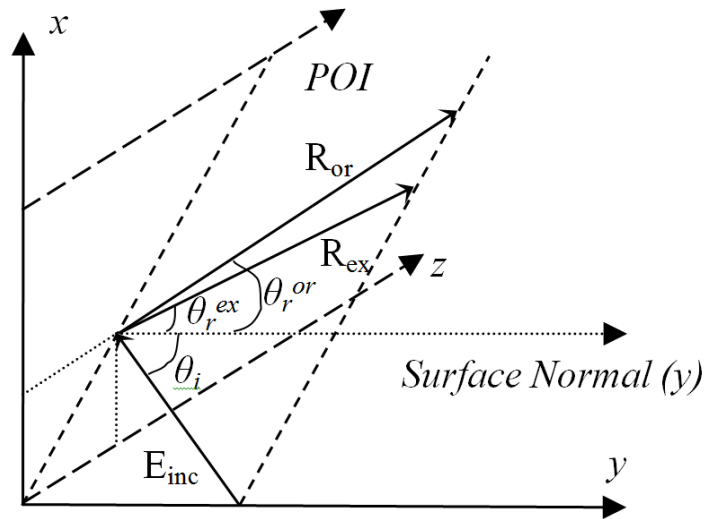


Figure 3-5 Reflection on  $y=0$  plane causes double reflection. Birefringence phenomenon is observed.

Figure 3-5 illustrates the wave reflection on the  $x$ - $z$  plane which is a more representative birefringence case, in which one incident beam causes two reflected beams of distinct characteristic types, regardless of the incident wave type. For an arbitrary incident o-wave, the reflected o-wave retains the same  $k_y$  (normal to the boundary) magnitude but flips the sign, while the reflected e-wave has a different  $k_y$  which can possibly be negative and/or having an imaginary part as seen in the following equations.

$$k_y^{or} = \pm \sqrt{k_0^2 \epsilon_t - k_x^2 - k_z^2} \quad (3-51)$$



$$k_y^{ex} = -k_z \frac{\epsilon_{23}}{\epsilon_{22}} \pm \frac{1}{\epsilon_{22}} \sqrt{k_0^2 \epsilon_t \epsilon_z \epsilon_{22} - k_x^2 \epsilon_t \epsilon_{22} - k_z^2 \epsilon_t \epsilon_z} \quad (3-52)$$

As a consequence, at some incidence angles incident o-waves may be reflected with attenuating e-waves and vice versa. In those cases the excited signals can be seriously distorted. In order to support a lossless guided mode, all the wavenumbers must be real with proper signs.

Herein lies the most significant dissimilarity between the aligned problems and the tilted problems (the isotropic RWG problem is same as the former). The aligned problems have travelling wave that can be characterized by discrete transverse wavenumbers with indices m, n, resulting in no more than two non-zero magnitudes for transverse phase constant. However, this tilted case has possibly three different  $k_y$  magnitudes along with one  $k_x$  magnitude. This fact complicates the wave formulation and functional dependence of the field components.

### 3.3.3. Travelling Wave Formulation

The travelling wave inside the waveguide can be formulated as the combination of the ordinary wave and extraordinary wave sharing the same propagation constant along the direction of propagation. Making use of the eigenvector solutions (3-43) and (3-44), we can first formulate all the possible wave beams as follows. With full understanding of the wave behaviors in the guided uniaxial region, we can formulate the total travelling wave as follows.

$$\begin{aligned} \vec{E} = & \vec{E}_{up}^{or} (k_z, k_{xu}, k_{yp}^{or}) + \vec{E}_{dp}^{or} (k_z, k_{xd}, k_{yp}^{or}) \\ & + \vec{E}_{un}^{or} (k_z, k_{xu}, k_{yn}^{or}) + \vec{E}_{dn}^{or} (k_z, k_{xd}, k_{yn}^{or}) \\ & + \vec{E}_{up}^{ex} (k_z, k_{xu}, k_{yp}^{ex}) + \vec{E}_{dp}^{ex} (k_z, k_{xd}, k_{yp}^{ex}) \\ & + \vec{E}_{un}^{ex} (k_z, k_{xu}, k_{yn}^{ex}) + \vec{E}_{dn}^{ex} (k_z, k_{xd}, k_{yn}^{ex}) \end{aligned} \quad (3-53)$$

The total wave is the hybrid of attenuation-free o-waves and e-waves propagating in all the four transverse directions. The subscripts u (up) and d (down) denote the signs of  $k_x$  to be positive and negative, respectively. Similarly,  $k_y$  is positive when it appears with subscript p and negative when it is with n. The vector types are indicated by superscripts *or* and *ex*, for o-waves and e-waves, respectively.

The vector expressions are all in terms of wavenumbers whose numerical domains are determined based on the previous studies of reflections and dispersion relations. *All terms must share the same propagation constant along the guided direction ( $k_z$ ).* Each field vector has a unique magnitude, thus there are eight unknowns.

On each inner face of the four side walls of the RWG, there are two BCs. Thus a total of eight BCs are available, sufficient to solve for the eight unknowns. The boundary conditions can be expressed as

$$\left\{ \overline{E} (x = 0 \text{ or } a, y, z) \right\}_{y,z} = 0, \quad (3-54)$$

$$\left\{ \overline{E} (x, y = 0 \text{ or } b, z) \right\}_{x,z} = 0. \quad (3-55)$$

We can treat the problem of eight linear equations as another problem of eigenvalues even though some terms are complex, and the eigenvectors contain the magnitude information. An  $8 \times 8$  boundary condition matrix (BCM) is expected and formulated as follows.

$$\begin{bmatrix}
C_{yup}^{or} e^{ik_{yp}^{or}y} & C_{yun}^{or} e^{ik_{yn}^{or}y} & C_{yup}^{ex} e^{ik_{yp}^{ex}y} & C_{yun}^{ex} e^{ik_{yn}^{ex}y} & C_{ydp}^{or} e^{ik_{yp}^{or}y} & C_{ydn}^{or} e^{ik_{yn}^{or}y} & C_{ydp}^{ex} e^{ik_{yp}^{ex}y} & C_{ydn}^{ex} e^{ik_{yn}^{ex}y} \\
C_{zup}^{or} e^{ik_{zp}^{or}y} & C_{zun}^{or} e^{ik_{zn}^{or}y} & C_{zup}^{ex} e^{ik_{zp}^{ex}y} & C_{zun}^{ex} e^{ik_{zn}^{ex}y} & C_{zdp}^{or} e^{ik_{zp}^{or}y} & C_{zdn}^{or} e^{ik_{zn}^{or}y} & C_{zdp}^{ex} e^{ik_{zp}^{ex}y} & C_{zdn}^{ex} e^{ik_{zn}^{ex}y} \\
C_{yup}^{or} e^{ik_{yp}^{or}y} e^{ik_{xa}a} & C_{yun}^{or} e^{ik_{yn}^{or}y} e^{ik_{xa}a} & C_{yup}^{ex} e^{ik_{yp}^{ex}y} e^{ik_{xa}a} & C_{yun}^{ex} e^{ik_{yn}^{ex}y} e^{ik_{xa}a} & C_{ydp}^{or} e^{ik_{yp}^{or}y} e^{ik_{xa}a} & C_{ydn}^{or} e^{ik_{yn}^{or}y} e^{ik_{xa}a} & C_{ydp}^{ex} e^{ik_{yp}^{ex}y} e^{ik_{xa}a} & C_{ydn}^{ex} e^{ik_{yn}^{ex}y} e^{ik_{xa}a} \\
C_{zup}^{or} e^{ik_{zp}^{or}y} e^{ik_{xa}a} & C_{zun}^{or} e^{ik_{zn}^{or}y} e^{ik_{xa}a} & C_{zup}^{ex} e^{ik_{zp}^{ex}y} e^{ik_{xa}a} & C_{zun}^{ex} e^{ik_{zn}^{ex}y} e^{ik_{xa}a} & C_{zdp}^{or} e^{ik_{zp}^{or}y} e^{ik_{xa}a} & C_{zdn}^{or} e^{ik_{zn}^{or}y} e^{ik_{xa}a} & C_{zdp}^{ex} e^{ik_{zp}^{ex}y} e^{ik_{xa}a} & C_{zdn}^{ex} e^{ik_{zn}^{ex}y} e^{ik_{xa}a} \\
C_{xup}^{or} e^{ik_u^x} & C_{xun}^{or} e^{ik_u^x} & C_{xup}^{ex} e^{ik_u^x} & C_{xun}^{ex} e^{ik_u^x} & C_{xdp}^{or} e^{ik_d^x} & C_{xdn}^{or} e^{ik_d^x} & C_{xdp}^{ex} e^{ik_d^x} & C_{xdn}^{ex} e^{ik_d^x} \\
C_{zup}^{or} e^{ik_z^x} & C_{zun}^{or} e^{ik_z^x} & C_{zup}^{ex} e^{ik_z^x} & C_{zun}^{ex} e^{ik_z^x} & C_{zdp}^{or} e^{ik_d^x} & C_{zdn}^{or} e^{ik_d^x} & C_{zdp}^{ex} e^{ik_d^x} & C_{zdn}^{ex} e^{ik_d^x} \\
C_{xup}^{or} e^{ik_u^x} e^{ik_{yb}b} & C_{xun}^{or} e^{ik_u^x} e^{ik_{yb}b} & C_{xup}^{ex} e^{ik_u^x} e^{ik_{yb}b} & C_{xun}^{ex} e^{ik_u^x} e^{ik_{yb}b} & C_{xdp}^{or} e^{ik_d^x} e^{ik_{yb}b} & C_{xdn}^{or} e^{ik_d^x} e^{ik_{yb}b} & C_{xdp}^{ex} e^{ik_d^x} e^{ik_{yb}b} & C_{xdn}^{ex} e^{ik_d^x} e^{ik_{yb}b} \\
C_{zup}^{or} e^{ik_z^x} e^{ik_{yb}b} & C_{zun}^{or} e^{ik_z^x} e^{ik_{yb}b} & C_{zup}^{ex} e^{ik_z^x} e^{ik_{yb}b} & C_{zun}^{ex} e^{ik_z^x} e^{ik_{yb}b} & C_{zdp}^{or} e^{ik_d^x} e^{ik_{yb}b} & C_{zdn}^{or} e^{ik_d^x} e^{ik_{yb}b} & C_{zdp}^{ex} e^{ik_d^x} e^{ik_{yb}b} & C_{zdn}^{ex} e^{ik_d^x} e^{ik_{yb}b}
\end{bmatrix}$$

$$\begin{bmatrix}
E_{up}^{or} \\
E_{un}^{or} \\
E_{up}^{ex} \\
E_{un}^{ex} \\
E_{dp}^{or} \\
E_{dn}^{or} \\
E_{dp}^{ex} \\
E_{dn}^{ex}
\end{bmatrix} \cdot = 0 \quad (3-56)$$

Due to the same mathematical reason, in order to have a non-trivial solution of the E vector, the matrix coefficient has to vanish at the four boundaries. However, the coefficient matrix is not practical to manipulate because some of the entries are functions of spatial coordinates.

To address this issue, we take advantage of the results from the first case on  $x=0$  and  $x=a$  planes in the reflection investigation. Basically, the issue is created when we assume the birefringence effect on all the four side walls. However, since the independence between o-waves and e-waves on these boundaries is known, we claim that the full set of boundary conditions could be satisfied as long as each pair of incident and reflected waves can meet the boundary conditions.

Equivalently, from (3-43) we can tell that, when  $k_x$  flips its sign, it corresponds to a wave reflected on  $x=0$  or  $x=a$  plane. The reflection coefficients can be determined quickly as  $+1$ , because

the y and z components also flip their signs and the incident wave vector and reflected wave vector sum to have zero y and z components.

Similarly, from (3-44) we can tell that the reflection coefficient for incident e-wave is  $-1$ , because the y and z components would not flip their sign. Thus the  $-1$  reflection coefficient is needed to satisfy the boundary conditions.

A similar strategy was adopted in the gyrotropic guide analyses in [64] and [58]. The simplified relations could be described by the following formulas.

$$\vec{E}_{or}(k_z, k_{xu}, k_{yp}^{or}) + \vec{E}_{or}(k_z, k_{xd}, k_{yp}^{or}) = 0 \quad (3-57)$$

$$\vec{E}_{or}(k_z, k_{xu}, k_{yn}^{or}) + \vec{E}_{or}(k_z, k_{xd}, k_{yn}^{or}) = 0 \quad (3-58)$$

$$\vec{E}_{ex}(k_z, k_{xu}, k_{yp}^{ex}) + \vec{E}_{ex}(k_z, k_{xd}, k_{yp}^{ex}) = 0 \quad (3-59)$$

$$\vec{E}_{ex}(k_z, k_{xu}, k_{yn}^{ex}) + \vec{E}_{ex}(k_z, k_{xd}, k_{yn}^{ex}) = 0 \quad (3-60)$$

where

$$k_x a = m\pi, \quad m = 1, 2, 3, \dots \quad (3-61)$$

Accordingly, each pair of waves that are only differentiated by equal and opposite  $k_x$  values has the identical magnitude since the reflection coefficient is of unit magnitude. As a consequence, the  $E_y$  and  $E_z$  components can pose sinusoidal dependence on x direction as

$$E_{y,z} \propto \sin\left(\frac{m\pi x}{a}\right) \exp(-jk_z z) \quad (3-62)$$

Hence the number of unknowns reduces to half and the  $8 \times 8$  matrix is to be replaced by a  $4 \times 4$  matrix as

$$\begin{bmatrix} E_{xup}^{or} & E_{xun}^{or} & E_{xup}^{ex} & E_{xun}^{ex} \\ E_{zup}^{or} & E_{zun}^{or} & E_{zup}^{ex} & E_{zun}^{ex} \\ E_{xup}^{or} e^{-jk_{yp}^{or}b} & E_{xun}^{or} e^{-jk_{yn}^{or}b} & E_{xup}^{ex} e^{-jk_{yp}^{ex}b} & E_{xun}^{ex} e^{-jk_{yn}^{ex}b} \\ E_{zup}^{or} e^{-jk_{yp}^{or}b} & E_{zun}^{or} e^{-jk_{yn}^{or}b} & E_{zup}^{ex} e^{-jk_{yp}^{ex}b} & E_{zun}^{ex} e^{-jk_{yn}^{ex}b} \end{bmatrix} \begin{bmatrix} E_p^{or} \\ E_n^{or} \\ E_p^{ex} \\ E_n^{ex} \end{bmatrix} = 0 \quad (3-63)$$

So far the x-dependence has been addressed and the complex coefficient matrix depends only on y coordinate which takes values 0 and b. So far the mathematical procedure and its complexity are hardly distinctive from those of an RWG filled with a ferrite biased in a transverse direction. However, for a gyromagnetic problem one can proceed and find the transcendental function (TF) by making the determinant of the coefficient matrix zero.

This is due to the fact that the dispersion relations of unbounded gyromagnetic media magnetized along one of the coordinate axes yield wavenumbers with even orders only, and the TFs may eventually be found having sinusoidal functions of equal and opposite wavenumbers, consequently the waveguides are reciprocal [64]. This is different from the non-reciprocity observed when the guides are partially filled [65] [66].

In contrast, from (3-52) we can see that the two  $k_y$  roots differ by both sign and magnitude. As a consequence the TF found from the determinant of the matrix should not have sinusoidal function of  $k_y$ , but complex exponential functions instead. Of course complex exponential functions could be converted in terms of sinusoidal functions according to Euler's equation, however, if that was done, the TF would have imaginary part and real part, and eventually two TFs to solve simultaneously. These factors increase the difficulty in solving TFs in an asymptotic approach. Thus we introduce the following graphical method with high automation.

### 3.3.4. Computational Process

The problem now comes to solving the matrix problem (3-63) as another eigenvector problem. The numerical computations exploring cutoff modes at particular frequency proceeds in steps as listed below.

1) Since  $k_x$  takes known discrete values as in (3-61), the given frequency should be higher than the value below which any other wavenumber is complex when  $m$  is set equal to one. On the other hand, when the frequency is high enough,  $m$  may take multiple values but cannot grow beyond the point below which other wavenumbers are real and with proper signs.

2) The propagation constant  $k_z$  is the main loop variable discretized at a reasonably fine resolution. In accordance with each  $m$  index,  $k_z$  is discretized in its domain, whose upper bound is set such that the four  $k_y$  values are real and with proper physical meaning. The resolution may affect the number of modes the program can identify and the accuracy of the final outcome.

3) After  $k_z$  and  $k_x$  are ready, the four values of  $k_y$  are determined from the dispersion relations, including e-wave roots and o-wave roots. When a set of wave numbers satisfying dispersion relations are used, the electric field vectors could be computed directly using the eigenvectors. The electric field vectors are better to be normalized before their components are taken in determinant calculations.

4) Once the waves and fields are prepared, the program traverses all the valid combinations of the wavenumbers and computes the determinant values. For each possible  $m$  value in (3-61), as  $k_z$  changes, curves of determinant values are to be recorded. Plots of the curves can help improve understanding of their functional behaviors.

5) At the points where BCM determinant is zero the supported modes are identified and the corresponding sets of wavenumbers are saved. Visual recognition on the plotted curves is not reliable; instead, it can be executed automatically to locate the desired  $k_z$  values using curve fitting and Newton-Raphson method in the program. This procedure yields higher accuracy beyond the resolution of discretization and significantly saves computational time.

6) After mode-related wavenumbers are obtained, the BCM eigenvalue equation (3-63) is reconstructed to calculate the four wave magnitudes in the column vector, which is an eigenvector associated with eigenvalue zero. The general method using singular value decomposition [39] is used and compared with the results obtained from using cofactors to formulate vectors orthogonal to the BCM's row space [34]. The program ends with both the wave modes and field components obtained.

To find the lowest frequency where there exists at least one propagating hybrid mode, the program may start from a reasonably low frequency, go up gradually by fine increments, and stop at the frequency at which one or more propagating hybrid modes are found. The starting low frequency should be determined from the greater one of the two original relative permittivities and the larger size of the two dimensions, assuming TE modes of an aligned problem to be treated. Note that  $TM_{11}$  mode needs also to be taken into account if the tilted problem could originate from a uniaxial-z case. The example given in the following section demonstrates how the computation routine works. The Matlab script code is programmed for computation.

### 3.4. Solution Example

In the example through this whole section, the dimensions of the rectangular waveguide are set  $a=57.5$  mm and  $b=27.94$  mm. The anisotropic relative permittivities are originally  $\epsilon_z=4$  and

$\epsilon_t=3$ . Then the clockwise rotation angle is 30 degrees, i.e., the angle  $\alpha$  in Figure 3-3 is  $30^\circ$ . The script runs at 10 GHz, under which frequency  $k_x$  can take up to seven values before other wavenumbers become complex, but not all of them support propagating hybrid modes.

### 3.4.1. Analytical Solution

The wavenumbers of the four lowest order  $TE_{Z0n}$  modes are calculated and tabulated in Table 3-1. Again, omitting the hybrid modes may result in tremendous design errors. For example, if the  $TE_{Z01}$  mode is taken as the dominant mode which is to be assumed as the only propagating mode up to the  $TE_{Z02}$  mode cutoff frequency, this design should not be considered reliable. The following subsection shows that hybrid mode also exist below 6.2 GHz.

Table 3-1 Analytically obtained wavenumbers for  $TE_{Z0n}$  modes when the optic axis is tilted but lying in the y-z plane.  $f=10$  GHz.  $\epsilon_t=3.0$ ,  $b=27.94$  mm,  $k=362.76$ ,  $k_x=0$  ( $m=0$ ). The  $k_y$  values in different modes are listed in the table. The calculated  $k_z$  values at 10 GHz are calculated and put in this table.

n	1	2	3	4
$k_y$	112.42	224.84	337.26	449.68
$k_z$	344.90	284.68	133.60	265.74j
Mode	$TE_{01}$	$TE_{02}$	$TE_{03}$	NA
$f_c$	3.099 GHz	6.198 GHz	9.297 GHz	NA

### 3.4.2. Hybrid Solution Preparation

The hybrid mode calculation starts from determining the vector for all the possible  $k_x$  values which take the known values starting from  $m=1$ . In this particular case, the  $k_x$  is found that it can take up to 6 values listed in the following table.



Table 3-2 Numerical solution starts from calculating the possible  $k_x$  values. The possible values in this particular example is listed.

m	1	2	3	4	5	6
$k_x$	54.636	109.273	163.909	218.546	273.182	327.818

The process to find the possible  $k_x$  values has been stated in Section 3.3.4. Clearly that the  $k_x$  values are dependent on the waveguide dimension  $a$ . The index  $m$  cannot go beyond the point where all the  $k_y$  values are imaginary even  $k_z$  is assumed zero.

Secondly, the maximum  $k_z$  values for each  $k_x$  value is calculated. Again, the domain of  $k_z$  values are confined in the region where all the  $k_y$  values, for both o-wave and e-wave, are real and having correct signs.

Table 3-3 Numerical solution need to know the maximum  $k_z$  values for each  $k_x$  value.

m	1	2	3	4	5	6
$k_z$ Max	358.62	345.9	323.6	289.52	238.66	155.32

The resolution of the solution depends on the resolution of  $k_z$  increment, which is set as 0.01 in this example. Finer resolution takes more computational time but the process can be parallelized once all the wavenumbers are obtained, thus utilizing modern computational technology the calculation process can be accelerated significantly.

Once the  $k_x$  values and  $k_z$  max values are determined, all the  $k_y$  values can be obtained from the dispersion relations. The sampled values are tabulated in the following tables.

Table 3-4 The minimum and maximum values of  $k_y$  of the extraordinary wave propagating in negative Y direction.

m	1	2	3	4	5	6
Max	-162.09	-168.665	-178.05	-189.06	-200.216	-208.73
Min	-399.01	-388.51	-370.36	-343.33	-305.08	-205.53

Table 3-5 The minimum and maximum values of  $k_y$  of the extraordinary wave propagating in positive Y direction.

m	1	2	3	4	5	6
Max	399.005	388.51	370.35	343.33	305.08	250.526
Min	66.73	76.5	91.83	111.91	136.62	167.34

Table 3-6 The minimum and maximum values of  $k_y$  of the ordinary wave propagating in positive Y direction.

m	1	2	3	4	5	6
Max	358.62	345.91	323.62	289.54	238.68	155.34
Min	3.95	4.605	4.95	3.275	2.78	2.354

Table 3-7 The minimum and maximum values of  $k_y$  of the ordinary wave propagating in negative Y direction.

m	1	2	3	4	5	6
Min	-358.62	-345.91	-323.62	-289.54	-238.68	-155.34
Max	-3.95	-4.605	-4.95	-3.275	-2.78	-2.354

Table 3-4 and Table 3-5 tabulate the minimum and maximum values of the e-wave's  $k_y$  values. Note that they are usually not opposite of each other. In contrast, Table 3-6 and Table 3-7 values

are opposite of each other because the ordinary dispersion relations end up have  $k_y$  values equal and opposite. A more important observation is that the ordinary wave  $k_y$  values always reach zeros faster than those of the e-wave.

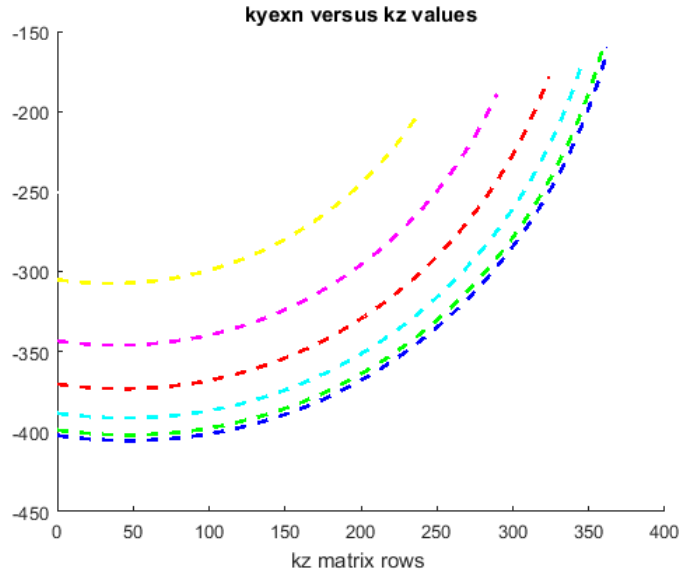


Figure 3-6 (Color) The curves of  $k_y$  values corresponding to the Table 3-4 min and max values. The yellow curve shows the set of  $k_y$  values at the index  $m=6$  (top left curve). Magenta  $m=5$ , red  $m=4$ , cyan  $m=3$ , green  $m=2$ , and blue  $m=1$  (bottom right curve).

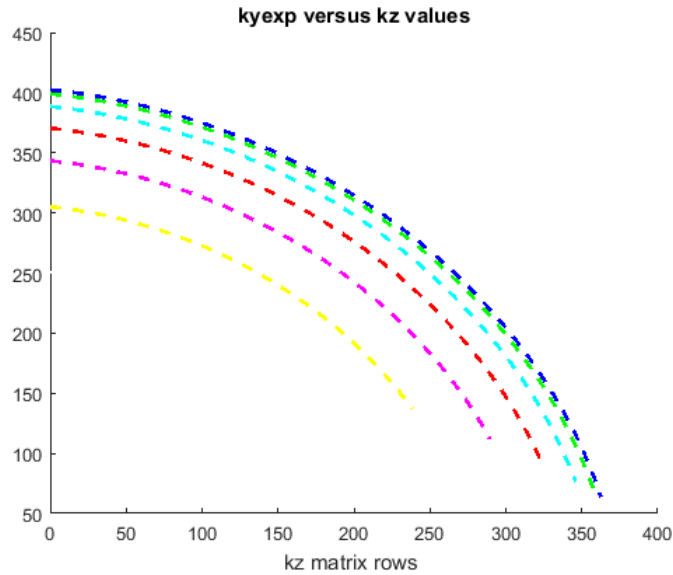


Figure 3-7 (Color) The curves of  $k_y$  values corresponding to the Table 3-5 min and max values. The yellow curve shows the set of  $k_y$  values at the index  $m=6$  (bottom left curve) while the blue shows  $m=1$  (top right curve). Magenta  $m=5$ , red  $m=4$ , cyan  $m=3$ , and green  $m=2$ .

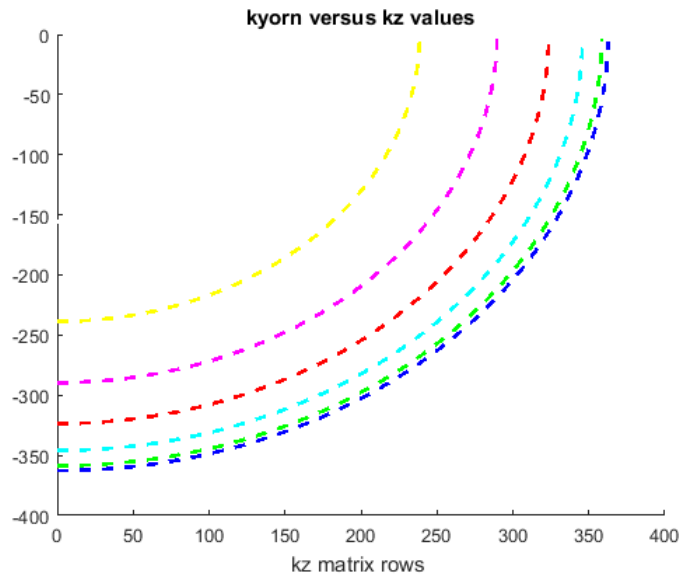


Figure 3-8 (Color) The curves of  $k_y$  values corresponding to the Table 3-7 min and max values. The yellow curve shows the set of  $k_y$  values at the index  $m=6$  (top left curve) while the blue shows  $m=1$  (bottom right curve). Magenta  $m=5$ , red  $m=4$ , cyan  $m=3$ , and green  $m=2$ .

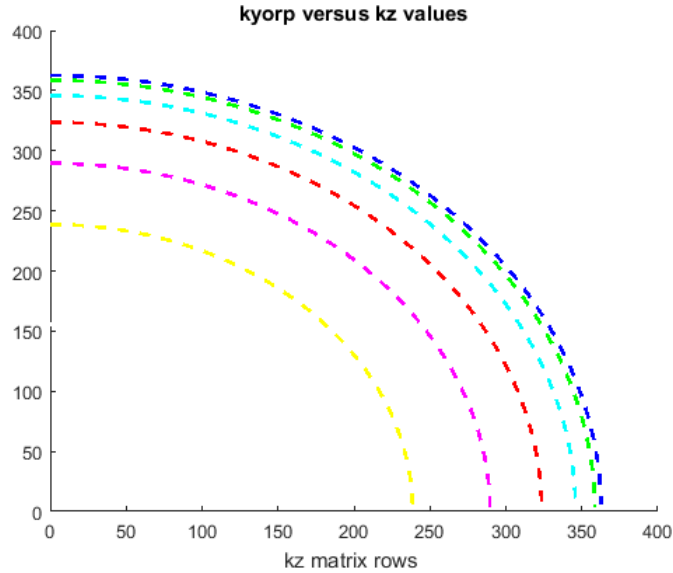


Figure 3-9 (Color) The curves of  $k_y$  values corresponding to the Table 3-6 min and max values. The yellow curve shows the set of  $k_y$  values at the index  $m=6$  (bottom left curve) while the blue shows  $m=1$  (top right curve). Magenta  $m=5$ , red  $m=4$ , cyan  $m=3$ , and green  $m=2$ .

### 3.4.3. Matrix Solutions

With all the wavenumbers discretized numerically, the calculation process then goes through all the combinations that satisfy either e-wave or o-wave dispersion relations and plots all the determinant values versus  $k_z$ 's. The valid solutions that makes the determinant of (3-63) equal to zero can be captured through looking for the points where the determinant curves (absolute value, real part, and imaginary part). An example of the plots of the coefficient matrix determinant are shown in the following figures, with  $m=1$  up to  $m=6$ . The tables that present the captured solutions of wavenumbers are given after each figure. These curves demonstrate how the determinant of the coefficient matrix varies as  $k_z$  traverses its domains. It is interesting to observe that each phase curve jumps drastically  $\pm\pi$  and flips its sign at those locations where the other three curves go to zero. This feature can be used to identify the zero points in a computer program which provides a clear means of automation.

In the tables that present the obtained solutions, the index  $m$  has the meaning of the conventional waveguide solutions. However the index  $S$  does not determine any deterministic values like  $m$  does (e.g.,  $k_x = m\pi/a$ ), but rather denotes the order that the mode is found. Arbitrarily defined, among the modes with the same  $m$  index, the  $k_z$  grows greater as the  $S$  index increases.

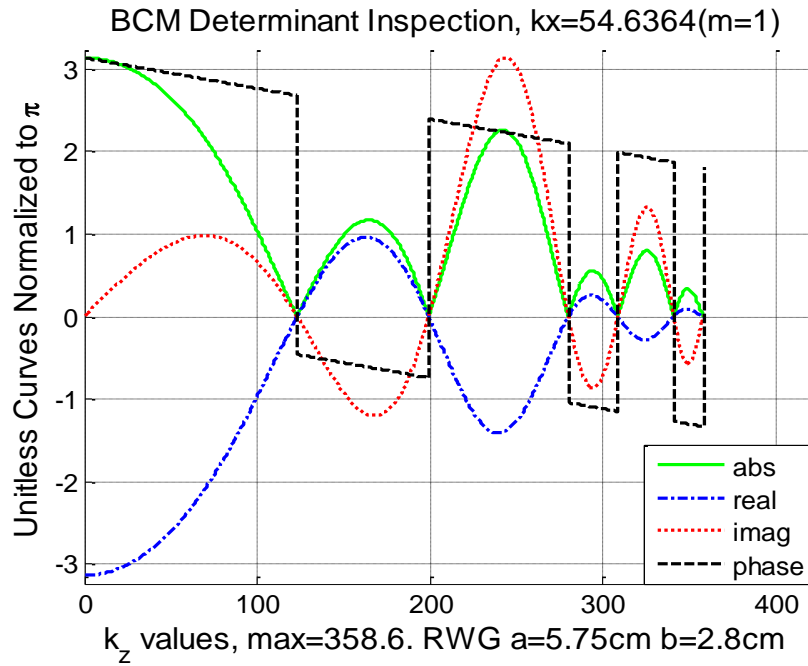


Figure 3-10 BCM determinant curves versus  $k_z$  values with  $m=1$ , taking absolute value, real part, imaginary part and phase.  $f=10\text{GHz}$ .

Table 3-8 Wavenumbers of Hybrid Modes  $CM_{1S}$  with  $m=1$  at  $f=10\text{GHz}$ .

S	1	2	3	4	5
$k_x (m=1)$	54.64	54.64	54.64	54.64	54.64
$k_z$	123.07	199.28	280.01	308.60	341.07
$k_{yp}^{or}$	336.84	298.16	224.06	182.68	110.81
$k_{yn}^{or}$	-336.84	-298.16	-224.06	-182.68	-110.81
$k_{yp}^{ex}$	360.43	311.22	227.51	184.73	119.01
$k_{yn}^{ex}$	-393.23	-364.32	-302.13	-266.97	-209.90
Mode	$CM_{11}$	$CM_{12}$	$CM_{13}$	$CM_{14}$	$CM_{15}$

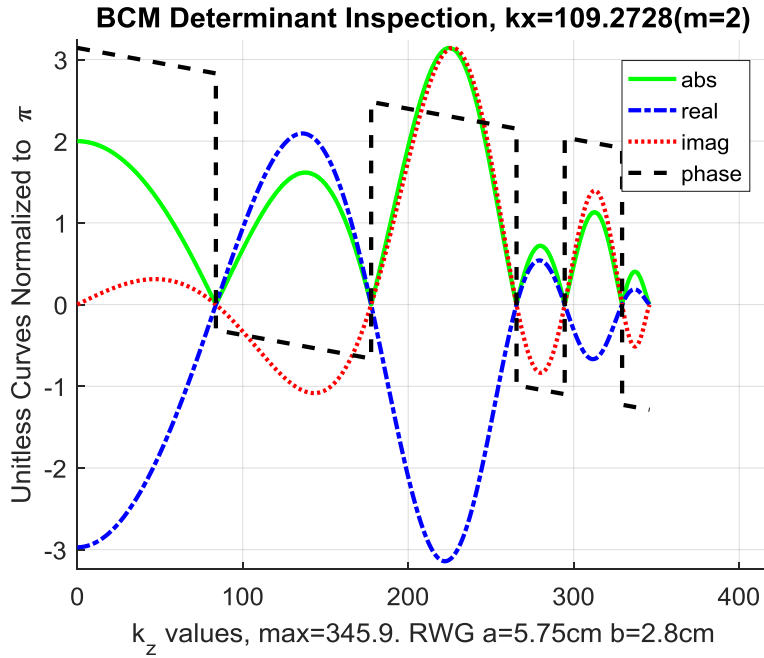


Figure 3-11 BCM determinant curves versus  $k_z$  values with  $m=2$ , taking absolute value, real part, imaginary part and phase.  $f=10\text{ GHz}$ .

Table 3-9 Wavenumbers of Hybrid Modes CM<sub>2S</sub> with m=2 at f=10GHz.

S	1	2	3	4	5
$k_x$ (m=2)	109.27	109.27	109.27	109.27	109.27
$k_z$	83.78	239.13	269.70	308.42	329.27
Mode	CM <sub>21</sub>	CM <sub>22</sub>	CM <sub>23</sub>	CM <sub>24</sub>	CM <sub>25</sub>

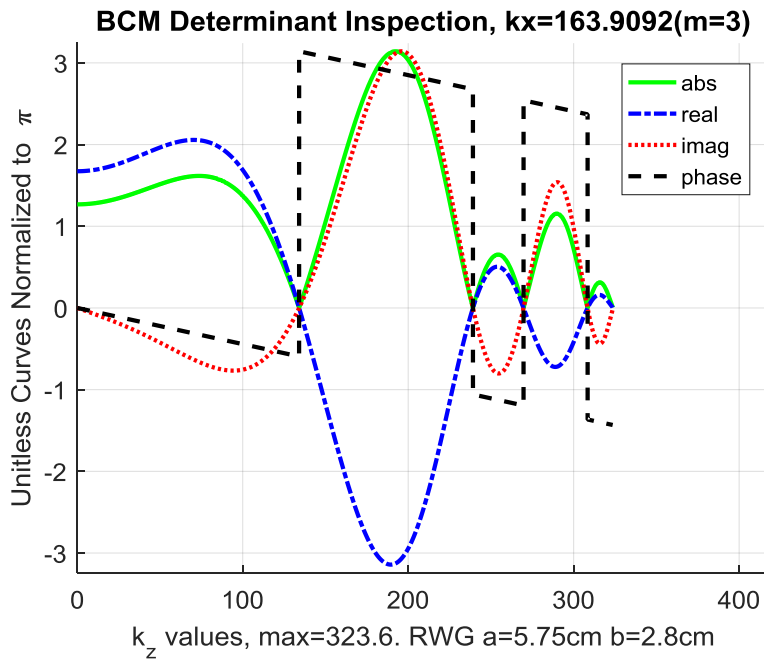


Figure 3-12 BCM determinant curves versus  $k_z$  values with  $m=3$ , taking absolute value, real part, imaginary part and phase.  $f=10$  GHz.



Table 3-10 Wavenumbers of Hybrid Modes  $CM_{3S}$  with  $m=3$  at  $f=10$  GHz.

S	1	2	3	4
$k_x$ (m=3)	163.9	163.9	163.9	163.9
$k_z$	134.08	239.13	269.7	308.42
Mode	$CM_{31}$	$CM_{32}$	$CM_{33}$	$CM_{34}$

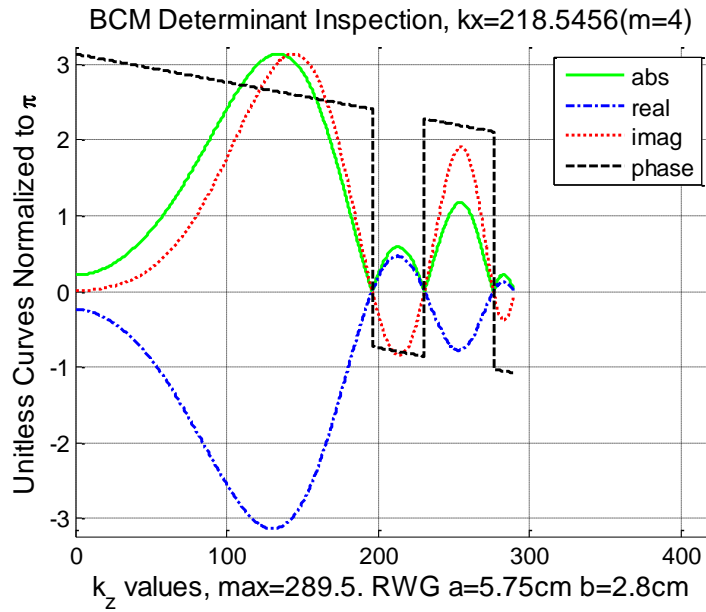


Figure 3-13 BCM determinant curves versus  $k_z$  values with  $m=4$ , taking absolute value, real part, imaginary part and phase.  $f=10$  GHz.

In Table 3-11, the solutions are presented with complete sets of wavenumbers, though the  $k_y$ 's can be obtained from the dispersion relations once the  $k_x$  and  $k_z$  are given.

Table 3-11 Wavenumbers of Hybrid Modes CM<sub>4S</sub> with  $m=4$  at  $f=10$  GHz.

S	1	2	3
$k_x$	218.55	218.55	218.55
$k_z$	196.04	230.59	276.25
$k_{yp}^{or}$	213.08	175.10	86.71
$k_{yn}^{or}$	-213.08	-175.10	-86.71
$k_{yp}^{ex}$	246.30	209.00	139.75
$k_{yn}^{ex}$	-298.54	-270.45	-213.37
Mode	CM <sub>41</sub>	CM <sub>42</sub>	CM <sub>43</sub>

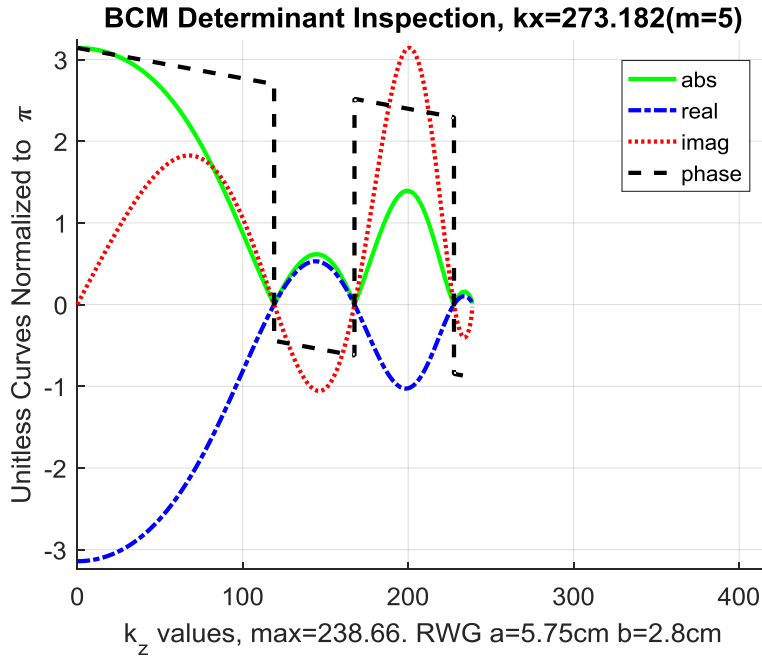


Figure 3-14 BCM determinant curves versus  $k_z$  values with  $m=5$ , taking absolute value, real part, imaginary part and phase.  $f=10$  GHz.

The obtained solutions pertaining Figure 3-14 curves are given in the following table.

Table 3-12 Wavenumbers of Hybrid Modes  $CM_{5S}$  with  $m=5$  at  $f=10$  GHz.

S	1	2	3
$k_x$	273.18	273.18	273.18
$k_z$	118.97	167.52	227.66
$k_{yp}^{or}$	206.91	170.01	71.66
$k_{yn}^{or}$	-206.91	-170.01	-71.66
$k_{yp}^{ex}$	261.63	225.05	154.57
$k_{yn}^{ex}$	-293.33	-269.69	-215.24
Mode	$CM_{51}$	$CM_{52}$	$CM_{53}$

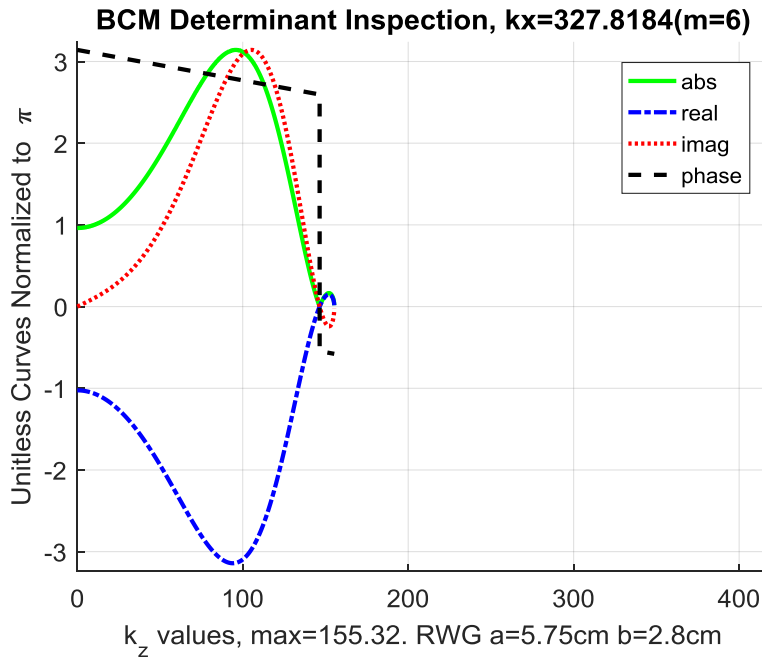


Figure 3-15 BCM determinant curves versus  $k_z$  values with  $m=6$ , taking absolute value, real part, imaginary part and phase.  $f=10$  GHz.

With  $m=6$ , the only captured solution is having  $k_x = 327.82$ ,  $k_z = 146.47$ , ordinary  $k_y$ 's with magnitude 51.74, and e-wave  $k_y$ 's as 176.42 (positive direction) and -215.45 (negative direction). The resultant hybrid modes are tabulated in Table 3-8 through Table 3-12, presenting the hybrid modes with  $m=1$  through  $m=5$  as labeled in mode numbers and titles.

Again, the S index does not directly relate to any wavenumber, and this is apparently different from the n index in isotropic waveguide modes. It is hard to abstract the relations analytically due to the complex nature of the BCM determinant. The mode names are arbitrarily assigned as  $CM_{mS}$  modes. The nomenclature implies 'the *Coupled Modes*', in contrast with the pure o-wave modes and pure e-wave modes found in aligned problems. The first subscript 'm' is the  $k_x$  index, and the second subscript S merely accounts for the sequence of the mode found in the aforementioned algorithm under a certain m value. The first found mode is assigned  $S=1$ , with the smallest  $k_z$  value among all those who share the same m index.

The most prominent difference between S and n is that the former corresponds to three magnitudes while the latter maps to only one. Actually, n directly relates to the  $k_y$  expression regardless of temporal frequency, while without frequency and m specified a solitary S is nonsensical. In the given example, not surprisingly, there is no obvious correlation between the  $k_y$  values in Table 3-1 and the  $k_y$  values in Table 3-8 through Table 3-12.

#### ***3.4.4. Finding Dominant Mode***

In this particular configuration, the dominant mode is found to be the  $TE_{z01}$  mode, meaning that the lowest hybrid mode cutoff frequency is greater than 3.1GHz.

To find the lowest hybrid mode, namely the hybrid mode of the lowest operating frequency, the code starts from the lowest possible cutoff frequency of the isotropic RWG, 1.3GHz, taking the  $TE_{Z10}$  mode with the larger dimension  $a$  and the greater relative permittivity 4. This rule applies to all the tilted cases. At each frequency, the calculation process first determines if  $k_x$  and  $k_y$  can be assigned with valid values. The method to mesh wavenumbers has been described previously. If valid wavenumbers are discretized, then the code scans through all the possible  $m$  indices and look for supported modes. If no modes are found, then the code will proceed with next higher frequency until a hybrid mode is found.

In this example, the first frequency at which a hybrid mode found is 3.2 GHz, marginally (3%) higher than that of the  $TE_{Z01}$  mode but much lower than that of  $TE_{Z02}$  mode.

We tried another configuration with  $\epsilon_z$  changed to be 6, and the first hybrid mode is found at 2.76 GHz, lower than that of the  $TE_{Z01}$  mode which is not affected by  $\epsilon_z$  at all. This computation clearly shows that the hybrid mode could possibly be the dominant mode depending on the properties of the uniaxial medium.

## 3.5. Verification

### 3.5.1. Comparison with the Uniaxial-z Case

The validity of the method can be verified by comparisons with limiting cases whose solutions were obtained in Chapter 2. This can be done by changing the optic axis orientations. By setting the rotation angle  $\alpha$  very close to  $0^\circ$  or  $90^\circ$ , the problems approach the uniaxial-z or uniaxial-y case, respectively.

For uniaxial-z case ( $\alpha=0$ ), the  $TE_z$  and  $TM_z$  mode propagation constants of lower order modes are calculated from the analytical solutions in the previous chapter and summarized in Table 3-13 and Table 3-14. In the cells where imaginary numbers appear the  $m$  and  $n$  indices correspond to the modes attenuating at the frequency.

Table 3-13 Analytically calculated propagation constants ( $k_z$ ) of  $TE_z$  modes in the uniaxial-z case.  $f=10\text{GHz}$ .  $a=57.5\text{mm}$ ,  $b=27.97\text{mm}$ ,  $\epsilon_z=4$ ,  $\epsilon_t=3$ .

$TE_z$	n=0	n=1	n=2	n=3	n=4
m=0	NA	<u>344.90</u>	<u>284.68</u>	<u>133.60</u>	265.74j
m=1	358.6218	340.55	279.39	121.92	271.30j
m=2	345.9107	327.13	262.87	76.87	287.33j
m=3	323.6178	303.46	232.76	94.96j	312.23j
m=4	289.5385	266.82	182.43	172.95j	344.07j
m=5	238.6762	210.54	80.08	238.28j	381.11j
m=6	155.3378	107.20	162.55j	299.35j	422.00j

Table 3-14 Analytically calculated propagation constants ( $k_z$ ) of  $TM_z$  modes in the uniaxial-z case.  $f=10\text{GHz}$ .  $a=57.5\text{mm}$ ,  $b=27.97\text{mm}$ ,  $\epsilon_z=4$ ,  $\epsilon_t=3$ .

$TM_z$	n=0	n=1	n=2	n=3	n=4
m=0	NA	NA	NA	NA	NA
m=1	NA	346.23	302.39	209.87	149.35j
m=2	NA	336.39	291.07	193.21	170.36j
m=3	NA	319.32	271.16	161.67	200.54j
m=4	NA	293.76	240.54	102.29	236.41j
m=5	NA	257.19	194.19	98.42j	275.75j
m=6	NA	203.76	114.37	185.24j	317.28j

Results from the hybrid mode algorithm are laid out in Table 3-15, where the imaginary  $k_z$  values corresponding to attenuating modes are not calculated and thus not presented. The comparison and mapping results are shown in Table 3-16. When  $m=0$  the analytical solutions are found in Table 3-1 to which the  $TE_{z0n}$  modes in Table 3-13 can be mapped.

Table 3-15 Numerically calculated propagation constants ( $k_z$ ) when  $\alpha=0.1^\circ$ . The results are approaching the analytical solutions in uniaxial-z case.

Index	Values of $k_z$					
m=0	(Use Analytical Results from Table 3-1)					
m=1	121.92	209.87	279.39	302.39	340.55	346.23
m=2	76.87	193.21	262.87	291.07	327.13	336.39
m=3		161.67	232.76	271.16	303.46	319.32
m=4		102.29	182.43	240.54	266.82	
m=5			80.08	194.19	210.54	
m=6				114.38	107.19	

Table 3-16 Modes found from the limiting case calculations (Table 3-15) and mapping to Uniaxial-z Modes (Table 3-13 and Table 3-14).

Index	Mapped Modes					
m=0	(Map to $TE_{z01}$ , $TE_{z02}$ and $TE_{z03}$ modes in Table 3-1)					
m=1	$TE_{z13}$	$TM_{z13}$	$TE_{z12}$	$TM_{z12}$	$TE_{z11}$	$TM_{z11}$
m=2	$TE_{z23}$	$TM_{z23}$	$TE_{z22}$	$TM_{z22}$	$TE_{z21}$	$TM_{z21}$
m=3		$TM_{z33}$	$TE_{z32}$	$TM_{z32}$	$TE_{z31}$	$TM_{z31}$
m=4		$TM_{z43}$	$TE_{z42}$	$TM_{z42}$	$TE_{z41}$	
m=5			$TE_{z52}$	$TM_{z52}$	$TE_{z51}$	
m=6				$TM_{z62}$	$TE_{z61}$	

### 3.5.2. Comparison with the Uniaxial-y Case

A similar comparison is made with the uniaxial-y case as well by letting the rotation angle be  $89.9^\circ$ . The calculated propagation constants from the analytical solutions in Chapter 2 are put in Table 3-17 and Table 3-18 for  $TE_Y$  modes and  $TM_Y$  modes, respectively.

Table 3-17 Analytically calculated propagation constants ( $k_z$ ) of  $TE_Y$  modes in the uniaxial-y case.  $f=10\text{GHz}$ .  $a=57.5\text{mm}$ ,  $b=27.97\text{mm}$ ,  $\epsilon_y=4$ ,  $\epsilon_t=3$ .

$TE_y$	n=0	n=1	n=2	n=3	n=4
m=0	NA	<u>344.90</u>	<u>284.67</u>	<u>133.60</u>	265.74j
m=1	NA	340.55	279.38	121.92	271.30j
m=2	NA	327.13	262.87	76.87	287.33j
m=3	NA	303.46	232.75	94.96j	312.23j
m=4	NA	266.82	182.43	172.95j	344.07j
m=5	NA	210.54	80.08	238.28j	381.11j
m=6	NA	107.19	162.55j	299.36j	422.00j

Table 3-18 Analytically calculated propagation constants ( $k_z$ ) of  $TM_Y$  modes in the uniaxial-y case.  $f=10\text{GHz}$ .  $a=57.5\text{mm}$ ,  $b=27.97\text{mm}$ ,  $\epsilon_y=4$ ,  $\epsilon_t=3$ .

$TM_y$	n=0	n=1	n=2	n=3	n=4
m=0	NA	NA	NA	NA	NA
m=1	415.3005	394.49	324.14	144.27	311.68j
m=2	404.3749	382.97	310.02	108.9	325.73j
m=3	385.4782	362.96	284.94	55.38j	347.89j
m=4	357.3478	332.93	245.55	154.80j	376.72j
m=5	317.5394	289.79	182.83	225.45j	410.84j
m=6	260.758	226.15	24.29	289.25j	449.03j



The proposed algorithm results are in Table 3-19 and their mode mapping results are in Table 3-20. Note that when  $m=0$  we again use Table 3-1 to which the  $TE_{Y0n}$  modes in Table 3-17 can be mapped.

Table 3-19 Numerically calculated propagation constants when  $\alpha=89.9^\circ$ . The results are approaching the analytical solutions in uniaxial-y case.

Index	$k_z$ values				
m=0	(Use Analytical Results from Table 3-1)				
m=1	121.92	144.27	279.39	324.14	340.55
m=2	76.87	108.90	262.87	310.02	327.13
m=3			232.76	284.94	303.46
m=4			182.43	245.55	266.82
m=5			80.08	182.83	210.54
m=6				24.29	107.20

Table 3-20 Modes found from the limiting case calculations (Table 3-19) and mapping to uniaxial-y Modes (Table 3-17 and Table 3-18).

Index	Mapped Modes				
m=0	(Map to $TE_{Z01}$ , $TE_{Z02}$ and $TE_{Z03}$ modes in Table 3-1)				
m=1	$TE_{Y13}$	$TM_{Y13}$	$TE_{Y12}$	$TM_{Y12}$	$TE_{Y11}$
m=2	$TE_{Y23}$	$TM_{Y23}$	$TE_{Y22}$	$TM_{Y22}$	$TE_{Y21}$
m=3			$TE_{Y32}$	$TM_{Y32}$	$TE_{Y31}$
m=4			$TE_{Y42}$	$TM_{Y42}$	$TE_{Y41}$
m=5			$TE_{Y52}$	$TM_{Y52}$	$TE_{Y51}$
m=6				$TM_{Y62}$	$TE_{Y61}$

The tables that present the aligned results provide more interesting insight worth mentioning. First, for isotropic waveguides, the TE and TM to Z modes with the same m and n indices would share the same cutoff frequency and the same propagation constant at any frequency. However, this does not occur for the aligned uniaxial cases. Secondly, for isotropic waveguides, if the size a is designed as multiple of b then there must be repeated values in cutoff frequency or propagation constant. While this is not seen in the examples, in general the probability is very small because it occurs only when the dimensions and permittivities satisfy certain conditions. These two remarks also provide justification for mode-mapping based on matching propagation constants.

### 3.6. Modal Behaviors

In this section we investigate the effect of uniaxial permittivity, tilting angle, and RWG dimension on the cutoff frequency of the calculated hybrid modes. To recap the conditions, the waveguide dimensions take the same waveguide dimensions and constitutive parameters as the example illustrated in [8]. The waveguide dimensions are  $a=5.75$  cm and  $b=2.7945$  cm. The inserted anisotropic medium is assumed to have relative permittivities  $\epsilon_t = 3$  and  $\epsilon_z = 4$  unless otherwise specified.  $\epsilon_z$  is the relative permittivity along the optic axis and  $\epsilon_t$  is that along the other two transverse-to-optic-axis directions. In the previous demonstration the optic axis tilting angle was set  $30^\circ$  but is to be changed in this section. The  $TE_{0n}$  modes have been analytically obtained and the lowest cutoff frequency belongs to the  $TE_{01}$  mode with cutoff frequency  $f_{c,10} = 3.1$  GHz. In the following we discuss three particular phenomena of interest.

### 3.6.1. The Effect of Relative Permittivity

Generally, the cutoff frequencies of all the wave modes in a waveguide homogeneously filled with isotropic dielectric medium would be decreased by the ratio of refractive index, which is calculated from the relative permittivity as  $1 / \sqrt{\epsilon_r}$ . This has been a practical method in waveguide miniaturization. Oftentimes, fabricated waveguides on dielectric substrates cannot avoid having internal space filled by dielectrics, and the wave and field behaviors in such waveguides must be studied in order to fully understand the propagation characteristics. Similar reasons motivate the study of wave mode behaviors when the internal uniaxial medium varies.

The cutoff frequencies of the lowest hybrid modes as the relative permittivity  $\epsilon_z$  increases are plotted in Table 3-16. In the calculation the other relative permittivity  $\epsilon_t$  remains the same value 3. Thus the change of  $\epsilon_z$  also means the change of the degree of positive uniaxial anisotropy. Obviously the negative-slope curve implies lower cutoff frequency as  $\epsilon_z$  gets larger. Intuitively this reminds the result shown in [67] and Chapter 2, where the cutoff frequency of the  $TM_{11}$  mode in the uniaxial-z case becomes lower than that of the  $TE_{10}$  mode ( $a > b$ ) as  $\epsilon_z$  becomes large enough.

Note that if the medium is isotropic with relative permittivity  $\epsilon_t=3$ , the cutoff frequency of the  $TM_{11}$  mode is 3.446 GHz, which is what the curve approaches as  $\epsilon_z$  decreases to the left. In this limiting case, the medium is approaching its isotropic appearance, and the supported modes should also approach those of the isotropic waveguide with dielectric constant 3. This turns out to be another evidence of the connection between the hybrid mode and the aforementioned TM-to-z mode in the uniaxial-z case.

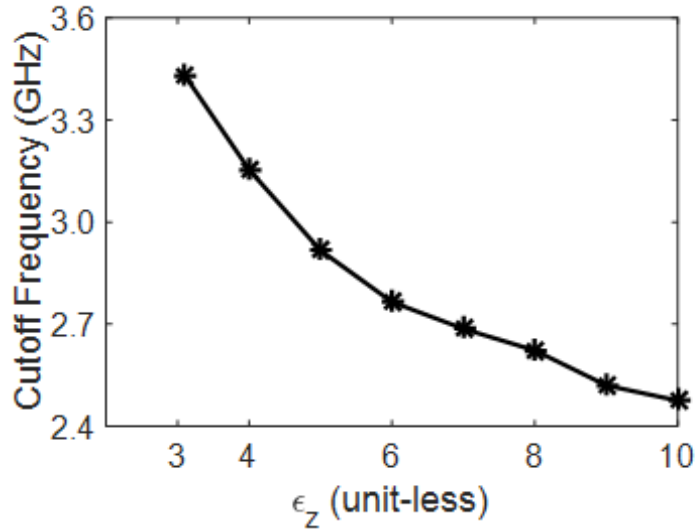


Figure 3-16 The change of the cutoff frequency of the lowest hybrid mode as the relative permittivity along the optic axis increases.  $\epsilon_t = 3$ .

### 3.6.2. The Effect of the Tilting Angle

It has been well known that the tilted uniaxial medium cause reflection and refraction differently when the optic axis varies [54]. The same phenomena have also been seen with other media, e.g., biaxial media [68]. In this section the effect of the tilting angle on the propagating modes are studied.

The plot in Figure 3-17 demonstrates how the cutoff frequency changes as the optic axis tilts to larger angles. Apparently as the tilting angle increases from the lower value 5 degrees up to 85 degrees, the cutoff frequency of the lowest hybrid mode shifts up in general, however, a peak appears around 65 degree, which is believed to be dependent on the waveguide dimensions and constitutive parameters.

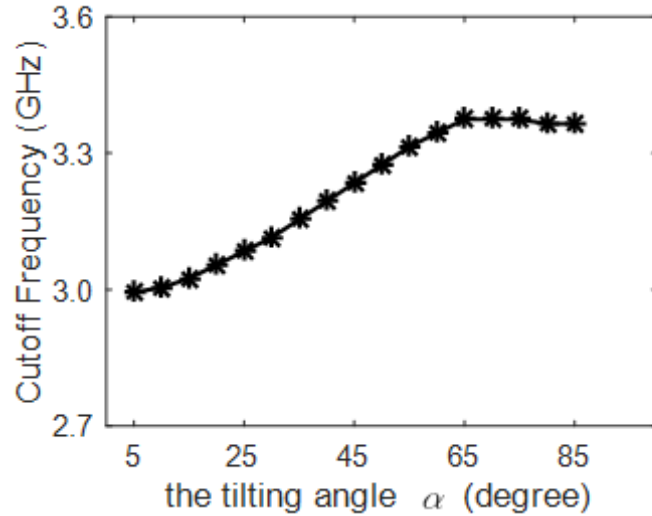


Figure 3-17 The change of the cutoff frequency of the lowest hybrid mode as the tilting angle increases.  $\epsilon_t = 3$ ,  $\epsilon_z = 4$ .

The algorithm does not calculate the case when one of the transverse wavenumbers is zero, since those cases correspond to the de-coupled modes in aligned cases. Therefore, in limiting cases, the curve must approach the lowest cutoff frequency of either  $TE_{11}$  or  $TM_{11}$  mode.

When the tilting angle is close to zero (equivalently uniaxial-z case), the analytical solutions presented in the previous chapter can be used. The waveguide dominant mode is the  $TE_{10}$  mode with cutoff frequency about 1.506 GHz. However, this mode is not examined by the hybrid mode calculation process because it does not process the case when  $k_x$  or  $k_y$  is zero. Nevertheless, the calculation process does capture the lowest mode with neither of the transverse wavenumbers being zero. Actually, the  $TM_{11}$  mode has the cutoff frequency 2.984 GHz, close to the plotted value when the angle  $\alpha$  is small, and it is supposed to be what the curve approaches when the tilting approaches zero.

When the tilting angle is close to 90 degree (eventually uniaxial-y case), the analytical solutions can be used again. The dominant mode is the  $TM_{Y10}$  ( $TE_{Z10}$ ) mode with cutoff frequency

about 1.304 GHz. Note that although the  $TM_{Y10}$  mode is actually also  $TE_{Z10}$  mode, its cutoff frequency is different from the  $TE_{10}$  mode (also  $TE_{Z10}$  mode) mentioned in the previous paragraph. The reason is the orientation of the optic axis. Former case has only  $E_y$  component in the electric field and that is in the direction perpendicular to the orientation of the optic axis. In contrast, the  $TM_{Y10}$  mode that also has only  $E_y$  component in the electric field has its only E field component parallel to the direction of optic axis. This causes the difference in this dominant mode cutoff frequency. To prove it, we show that  $1.506/\sqrt{4} \approx 1.304/\sqrt{3}$ .

In this particular waveguide dimension,  $TM_{Y10}$  is lower than that of the  $TE_{Y0n}$  mode. The sole e-wave mode  $TM_{Y11}$  (no transverse-to-z mode corresponding) mode has the lowest  $f_c$  with neither of the transverse wavenumbers being zero. It can be calculated as 3.362 GHz, which is what the curve approaching to when  $\alpha$  grows large in Figure 3-17. It is worth mentioning that this comparison with the results from the aligned-case solutions verifies the correctness of the computation process.

### ***3.6.3. The Effect of the Dimension***

Last but not the least, we shall demonstrate how the waveguide dimension  $a$  influences the hybrid mode cutoff frequency. Figure 3-18 shows the calculation results with the dimension  $a$  being from the same as the dimension  $b$  (square cross-section) up to about 20 percent greater than the original value (5.75 cm). The dimension  $b$  is kept the same because the analytical  $TE_{0n}$  modes depends exclusively on  $b$  and their cutoff frequencies do not change as these computations run. It is observed that the cutoff frequency of the lowest hybrid mode decreases monotonically as the waveguide cross-section ratio  $a/b$  increases.

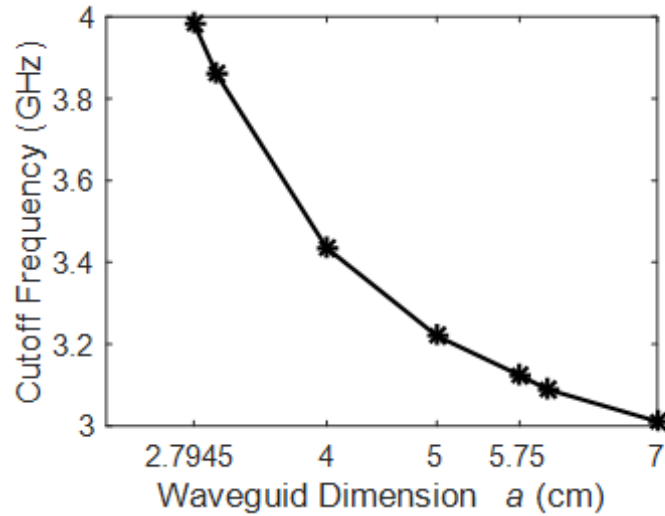


Figure 3-18 The change of the cutoff frequency of the lowest hybrid mode as the waveguide dimension  $a$  changes while dimension  $b$  remains at  $b=2.7945$  cm.  $\epsilon_t = 3$ ,  $\epsilon_z = 4$ .

### 3.7. Field Distributions

In the study of aligned cases, the field distributions were plotted in Section 2.3.5. The common phenomenon among all the aligned uniaxial cases and the isotropic cases is that all the field distributions are symmetrical. The distributions are symmetrical to the middle lines and the geometric center of the cross-section. This symmetry feature is due to the sinusoidal functional dependence of the solutions. However, the symmetry is broken in the titled case.

The same sample waveguide is used to demonstrate the field distributions of various propagating hybrid modes. Specifically, the first example is when the tilting angle is  $30^\circ$  in  $y$ - $z$  plane, the field distributions of the hybrid mode with  $m=2$ , namely  $k_x=109.27$ . Ordinary  $k_y=\pm 106$ , extraordinary  $k_{yp}=122.76$  and  $k_{yn}=-210.5$ . Compare the above results with that  $\pi/b \approx 112.42$ , which is different from all the ordinary and extraordinary  $k_y$ 's. The obtained field solutions are plotted in 3-D form in Figure 3-19.

Again, note that the ordinary wave  $k_y$  value is close to but not equal to  $\pi/b$ , partially explaining why the variation of the field amplitude along y-axis shows no duplication but the variation along x-axis repeats.

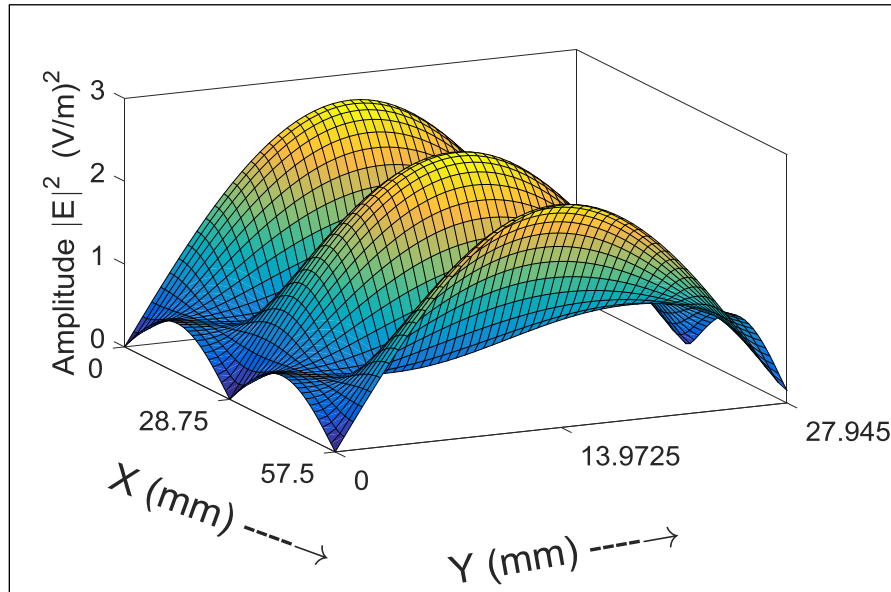


Figure 3-19 Field distribution of the first example over the cross-section of the waveguide filled with uniaxial medium with tilted optic axis. ( $\alpha=30^\circ$ )

Figure 3-20 shows the equal-magnitude contours of the electric field magnitude distributions, which provide better means of comparing with the electric field distribution contours in the aligned uniaxial cases and the isotropic case plotted in Chapter 2. The symmetry that can be observed in the figures from Figure 2-7 through Figure 2-14 are not seen with the tilted cases. It is obvious in Figure 3-20 that there exists no perfect symmetry with respect to the geometric center of the cross-section rectangle in field distributions. The asymmetry is primarily due to the simultaneous presence of o-wave and e-wave which the hybrid modes are comprised of, while in the aligned cases the o-wave and e-wave are separated and travel as TE and TM (transverse to the optic axis) modes, respectively.



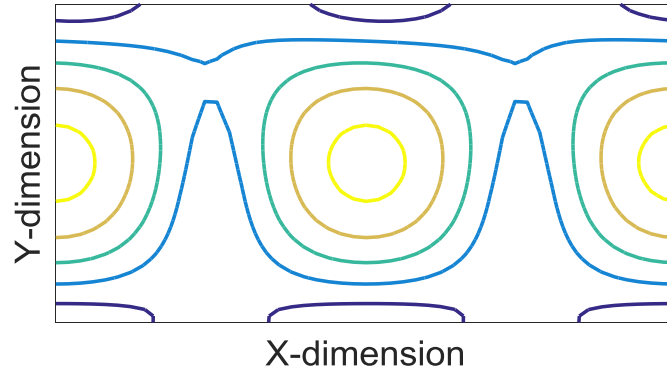


Figure 3-20 Contour plot of the field distribution of the first example over the cross-section of the waveguide filled with uniaxial medium with tilted optic axis ( $\alpha=30^\circ$ ).

Another example is shown in Figure 3-21 and Figure 3-22 with field distribution and contour curves presented, respectively. In this example  $m=3$  ( $k_x=163.91$ ), ordinary  $k_y=\pm 178.86$ , extraordinary  $k_{yp}=197.57$  and  $k_{yn}=-269.44$ . Note that  $2\pi/b \approx 224.84$ .

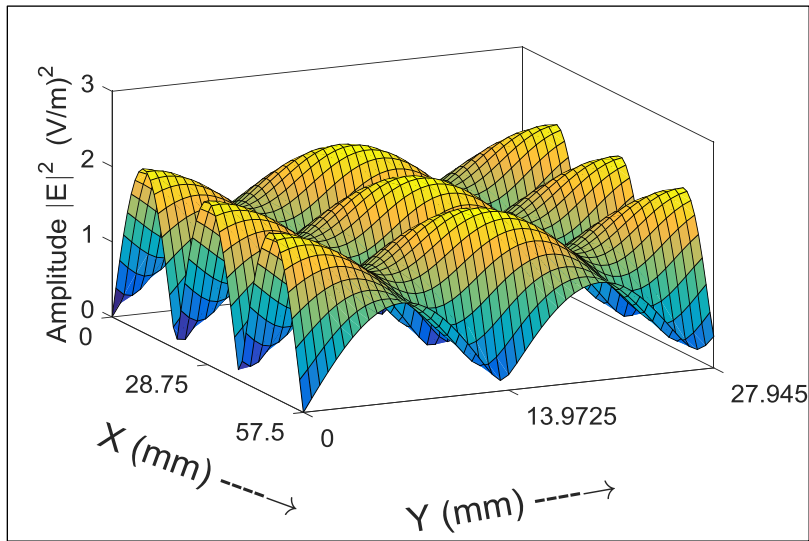


Figure 3-21 Field distribution of the second example over the cross-section of the waveguide filled with uniaxial medium with tilted optic axis. ( $\alpha=30^\circ$ )

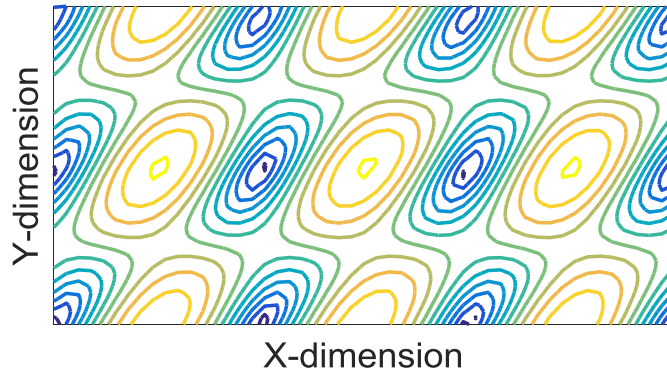


Figure 3-22 Contour plot of the field distribution of the second example over the cross-section of the waveguide filled with uniaxial medium with tilted optic axis. ( $\alpha=30^\circ$ )

Once again, the validation of the results could be conducted by comparing the field distributions. Figure 3-23 shows the field plots from the same computational algorithm but with a limiting configuration as the tilting angle is only  $0.1^\circ$  off the z-axis. Almost perfect symmetry is found in this limiting case, which is close to the aligned uniaxial-z case. The field distribution of the presented mode is approaching the  $TM_{z31}$  mode in uniaxial-z case, whose field contours approximately reflect the distributions in the uniaxial aligned case.

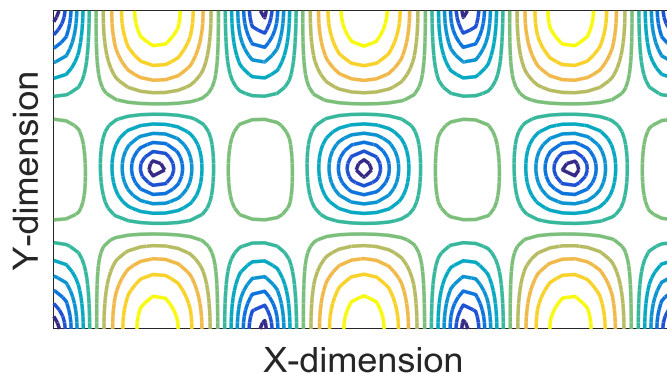


Figure 3-23 Contour plot of the limiting case field distribution of the second example over the cross-section of the waveguide filled with uniaxial medium with almost aligned optic axis. ( $\alpha=0.1^\circ$ )

In summary, the field distributions of various uniaxial cases in rectangular waveguides are demonstrated. The field distributions of all the aligned cases are obtained analytically and show perfect symmetry. The field distributions of the hybrid modes in the tilted cases do not show symmetry due to the coupled e-wave and o-wave that have different wave numbers along y-axis (x-axis if tilted in the x-z plane). It can thus be concluded that the tilting angle not only changes the mode behaviors but also affect the symmetry of the electric field amplitude distributions. The presented field distributions provide a useful means of helping to physically understand the modal behaviors and waveguide characteristics.

### 3.8. Summary

The problem of the waveguide filled with uniaxial media are addressed in Chapter 2 and Chapter 3. The aligned problems are analytically solved and the new mode decomposition with respect to the optic axis direction is presented. Analytical field solutions are derived and wave impedances are formulated in Chapter 2.

The tilted problems are solved using the proposed numerical technique. The computational routine is explained in detail and an example was used to illustrate the usage of the algorithm. In particular, the hybrid modes are analyzed in detail. In the example the calculated wavenumbers are presented and used for defining the wave modes. The validity of the calculation process was verified by comparing the calculated results with the results analytically obtained from the aligned cases, since the results of slight tilting and close to 90 degree tilting should be similar to the results of the 0 degree tilting and 90 degree tilting which are the aligned cases. Except for the calculated wavenumbers, the validity of the calculation process was also demonstrated by comparing the obtained field results with the limiting cases. At these limiting cases, the hybrid modes also exhibit

close to periodic and sinusoidal field magnitude distributions like the isotropic and the aligned cases.

Again, characterizing the dominant mode is important for waveguide structures. It was found that the hybrid mode may also become the dominant mode, or the lowest hybrid mode can have a cutoff frequency lower than that of the supported TE modes. Therefore care must be taken when this type of waveguide structure is used in a RF system because out-of-band signal may be transmitted undesirably in the form of hybrid mode. Last but not the least, we investigated how certain parameters would affect the dominant mode, particularly the hybrid dominant mode.

## Chapter 4 NR-CRLH Transmission Line Metamaterial

Postulated decades ago [21], negative refractive-index materials (NIM) have held considerable interests since the experimental verifications in microwave frequency range [24] and optic regime [69]. Since modern fabrication techniques allow broad usage of planar structures, the metamaterial reported in [70] and [71] and the CRLH structure reported in [72] and [73] have recently received considerable attention. However, for over a decade the inherent loss has been one of the major problem that has plagued establishing metamaterial as a mainstream waveguide technology. Although there had been theoretical debate on the existence of loss-free NIMs which may violate the law of causality [29], the argument soon ended with the validity of the energy-compensating NIMs justified in [30] and [31]. After the problem of loss was first revealed in [25], the layered structure with alternatively stacking lossy NIM layers and gain-medium layers was suggested [27] and later experimentally validated by loss-free photonic NIM [33]. Notwithstanding the success in optic frequency, that topology has not proven prevailing in microwave bands.

In the planar metamaterials, the loss is mainly attributed to the non-ideal lossy materials, lumped component imperfection, and leaky-wave radiation. Although the amount of loss from unit cells may be negligible, metamaterial transmission lines typically consist of multiple cascaded unit cells which can lead to significant insertion loss. Even in the applications where the metamaterial structures are made of only a handful of unit cells, the loss can still cause notable negative impact. For instance, the metamaterial based resonators are often found with lower quality factor than conventional microstrip TL based resonators [74]. Radiating metamaterial leaky-wave antennas (LWAs), however, take advantage of the radiative loss to produce full frequency scanning beams [26]. Yet several performance limitations remain to be solved. The most critical problem is the exponentially decaying current amplitude profile that causes degradation of spatial resolution.

Therefore, it is desirable to develop metamaterial TLs that are capable of controlling the amplitude of the guided waves, not only to compensate the loss but also to control the radiation characteristics of the LWAs.

Few have explored loss compensation and amplitude control along metamaterial transmission lines and LWAs. In [38], the quasi-unilateral amplifiers are incorporated to compensate for the current amplitude attenuation. Near the transition frequency the improved directivity and gain were demonstrated. However, the involved amplifiers not only compromise the reciprocity, but may also affect the phase response in the LH and/or RH frequency bands, and thus the capability of frequency beam scanning. The unilateral amplifiers were later replaced by the tunnel diodes [37] which permit bi-directional operation. Although the reciprocity is retained, the amplification behavior is highly frequency-dispersive in the range of less than 1 dB to greater than 10 dB, with an undesirable peak (in the amplification versus frequency curve) in the LH region. In addition, it can be shown that the input reflection coefficients may be greater than one in magnitude thus leading to system instability and oscillation between adjacent unit cells. Inevitably, in both of the previous attempts, loss-compensation occurs at the expenses of risking the unit-cell length and trading off the desired consistent Bloch impedance in broad bandwidth. These compromises are due to their design topology inherited from [27] where NIMs and gain units are serially cascaded in an alternating fashion.

This work presents a new energy regenerating technology developed to not only compensate the loss but also to control the amplitude of the guided wave. The loss-compensating power is pumped-in from the orthogonal direction with respect to the propagating waves. This energy regeneration is realized by terminating the inductive stubs of the passive CRLH unit-cell with NR circuits. As will be discussed, the length of these stubs are not necessarily same as the NR

terminated stub. Furthermore, the proposed topology fundamentally changed the principle of loss compensation by creating an active unit cell (AUC), effectively combining the vital metamaterial characteristics of the conventional passive unit cell (PUC) and bi-directional gain without physically breaking guide discontinuities along the transmission line.

An improved set of equivalent circuit model (ECM) compared with the conventional ECM will be introduced to inspire physical interpretation of the AUC. Conventionally the CRLH unit cells are comprehended from the ideal loss-free ECM and in most low-loss applications the ideal ECM is sufficient for evaluation/prediction purposes as well. However, it is advantageous to understand the functionality of the incorporated negative resistance from the proposed ECM model which is a variation of the conventional lossy model.

#### **4.1. A Brief History of the CRLH Structure**

The original CRLH structure was first introduced in [72] in 2002 as the “left-handed” transmission line, known as one of the practical planar realization of the emerging metamaterial. The other well-known metamaterial transmission loaded with lumped L-C components was also introduced in the same year and can be found in [70]. More details about the lumped component loaded metamaterial transmission line can be found in [71].

Regarding the CRLH TL only, its left-handed characteristic of the CRLH structure was discussed in depth for the first time in [75]. However, as its name suggested, it was better known for possessing both right-handed (positive propagation constant) and left-handed (negative propagation constant) frequency bands on its spectrum. The composite feature of both LH and RH performances was first taken advantage of in [26] as a leaky-wave antenna capable of backfire-to-endfire (including broadside) frequency scanning. Analyses on the support of LH and RH

characteristics was first seen in 2003 [73], and in and after the year of 2004 a number of articles from the original group of UCLA demonstrated complete theory and broad applications of the CRLH structure including the transmission line characteristics [76] [77], design of dual-band couplers [78] [79], and implementation of resonators [74]. A comprehensive review of the relevant fundamentals can be found in [80]. Among various applications, we are focused on the leaky-wave antenna applications. Sufficient survey material on metamaterial antennas can be found in [81].

#### 4.2. Fundamentals of CRLH Transmission Line

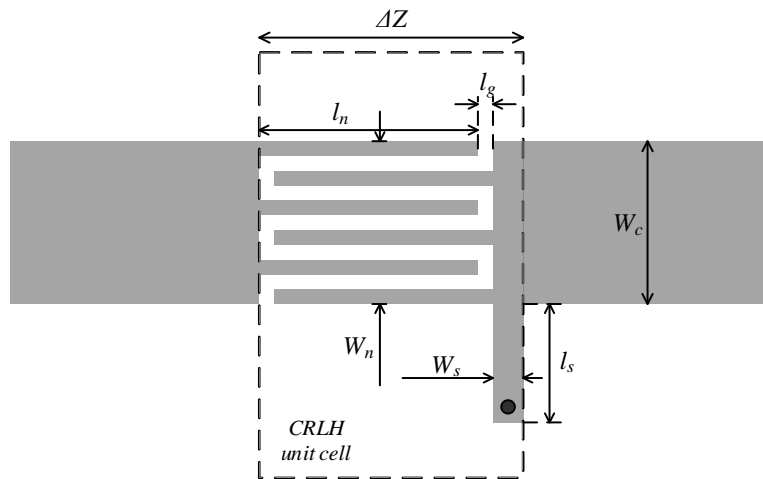


Figure 4-1 Unit cell of the conventional CRLH periodic structure (with regular input/output transmission lines). The number of pair of fingers shown in the figure is 3.

The CRLH transmission lines (TL) consisting of CRLH unit cells shown in Figure 4-1 can be analyzed using the theory of periodic structure (a thorough explanation can be found in Collin's Book [4]). The theory analyzes the cascaded structure by first analyzing each unit-cell behaviors and then utilizing network parameters to calculate and evaluate the behaviors of the entire structure. The method treats the structure of finite length based on the infinitely cascaded structures.



### 4.2.1. Conventional TL and LH TL

The conventional transmission line, for example, a microstrip line, a strip line, a coaxial cable or a rectangular waveguide, can also be analyzed using the theory of periodic structure as shown in Figure 4-2. Typically, transmission lines are analyzed using the telegraph function as demonstrated in many textbooks (e.g., see [4] and [5]).

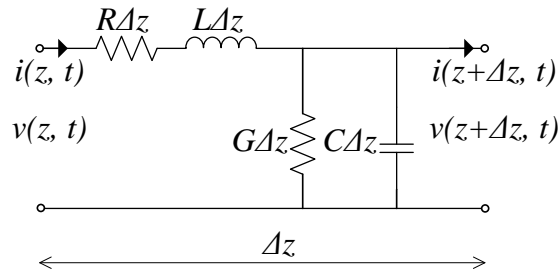


Figure 4-2 Voltage and current definitions and the equivalent circuit for an incremental length of a conventional transmission line.

The conventional TL can be considered as right-handed material, whose refractive index is a positive number. In terms of guided waves, the direction of phase propagation and power flow are parallel. The solutions to the propagating waves always have phase delay across the unit cell. However, the metamaterial TLs, or sometimes called negative-refractive-index material TL, are considered as left-handed material, whose refractive index is a negative number. Consequently, the direction of phase propagation and power flow are anti-parallel. The solutions to the propagating waves always have negative delay (phase advance) across the unit cell. Ideally, the CRLH structure seamlessly combines the two phase propagation characteristics and thus provide more flexibility than single LH or RH TLs.

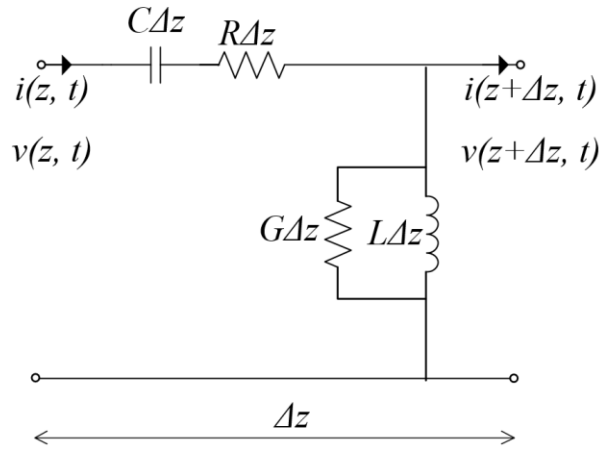


Figure 4-3 Voltage and current definitions and the equivalent circuit for an incremental length of a left-handed transmission line.

The diagram shown in Figure 4-3 is designed such that it is complementary to the conventional structure as shown in Figure 4-2. The diagrams in these two figures scan illustrate the differences between a RH that produces phase day and a LH TL that produces phase advance. Note that the notations and circuit structure are not necessarily same for other LH TLs. Combining the RH TL and LH TL makes a composite right-handed and left-handed transmission line.

#### 4.2.2. CRLH TLs

A CRLH TL can consist of an arbitrary number of unit cells. Consider a CRLH TL consisting of over ten unit cells, of which the three consecutive unit cells are shown in Figure 4-4. The figure shows three unit cells between the section on their left and the section on their right. In other words, the CRLH TL is not terminated at either the leftmost unit cell or the rightmost unit cell in Figure 4-4. Note that the terminating unit cells are usually different from the regular unit cells.

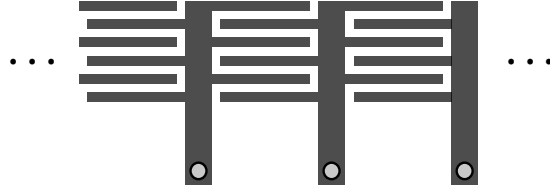


Figure 4-4 Demonstration of three unit cells in an infinitely long periodic structure (between semi-infinite section on the left and semi-infinite section on the right).

When designed properly, the input impedance of a properly terminated CRLH TL can be approximately 50 Ohm, and the transition between a normal TL and a CRLH TL is simply a direct connection as Figure 4-5 shows. When the characteristic impedance of a CRLH TL is designed to be other than the standard value of 50 Ohm, an impedance transformer can be used for the transition as shown in Figure 4-6. If the width of the unit cell or TL, which is usually the width of the inter-digit capacitor, is not the same as the width of a conventional TL which is matched to the CRLH TL, care should be taken and the transition may be done with tapering.



Figure 4-5 A 10-unit-cell CRLH TL transitioned to a 50 Ohm microstrip line without tapering.

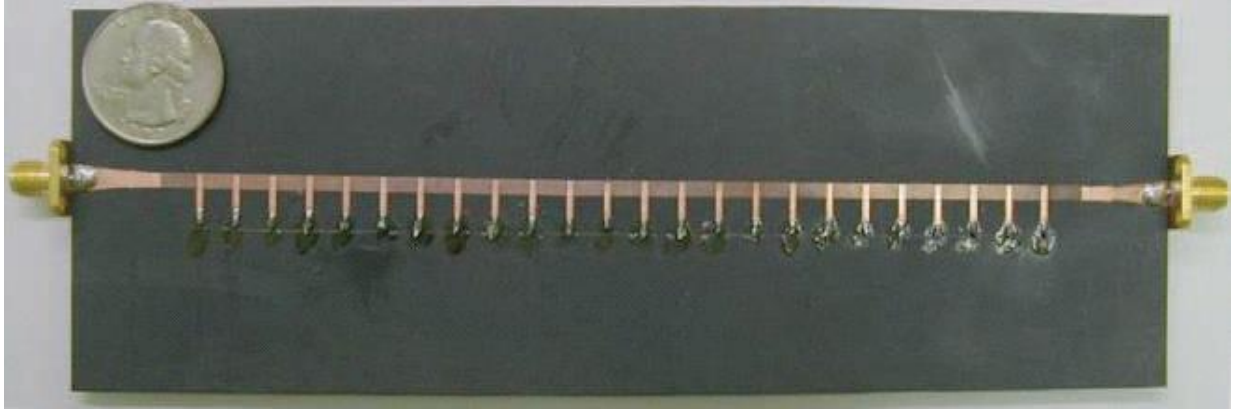


Figure 4-6 (Figure 9(a) in [80]) Presence of a 24-unit-cell CRLH TL with normal transmission lines and SMA connections. Tapering can be observed on both terminals of the CRLH TL.

One may notice that the TLs in Figure 4-5 and Figure 4-6 are symmetric but the unit cells in Figure 4-4 are not. This will be explained after the unit cell study.

#### 4.2.3. CRLH Unit Cell Layout

The layout of a CRLH unit cell is shown in Figure 4-1. The unit cell is composed of an interdigit capacitor (IDC) and a shorted stub. The total length of the unit cell is the sum of the IDC finger length ( $l_n$ ), IDC finger gap ( $l_g$ ) and the width of the shorted stub ( $W_s$ ). The edge-to-edge width ( $W_n$ ) of the IDC determines the widths of the metamaterial TL. Usually it is preferable to have  $W_n$  equal to the width ( $W_c$ ) of the desired microstrip transmission line. If  $W_n$  cannot be made equal to  $W_c$ , again, tapering can be used to realize a smooth transition. The total length of the unit cell follows the conventional notation given by  $\Delta z$ .

The length of the unit cell is assume to be  $\Delta z$ , or  $d$  in the analysis of periodic structure. The equivalent circuit model is valid when  $\Delta z$  is much smaller than the wavelength corresponding to the highest frequency in the desired band. A commonly accepted rule for  $\Delta z$  is  $\Delta z < \lambda_g/4$ , where

$\lambda_g$  is the wavelength of the guided wave. A more conservative criterion is known as  $\Delta z < \lambda_g/10$  which provides better approximation.

There are various EM simulation commercial software tools that can be used to simulate the unit cell behaviors as shown in Figure 4-1. For example, method of moments [82] based planar 2-D simulation tools like Ansys Designer, Keysight ADS and Sonnet, finite element based 3-D simulation tool Ansys HFSS, and finite-element based CST. The primary tools used in this work are HFSS and ADS.

A simulation model in HFSS is shown in Figure 4-7. The number of finger pairs is 5, the finger length  $l_n$  is 10.2 mm, the finger gap  $l_g$  is 0.2 mm, and the finger width is 0.3 mm, thus the total width  $\underline{W}_n$  is 4.8 mm, about the same as the 50 Ohm microstrip line on the RO/duroid 5880 substrate of 62 mil (1.57 mm) thickness. The width of the stub is 1 mm.

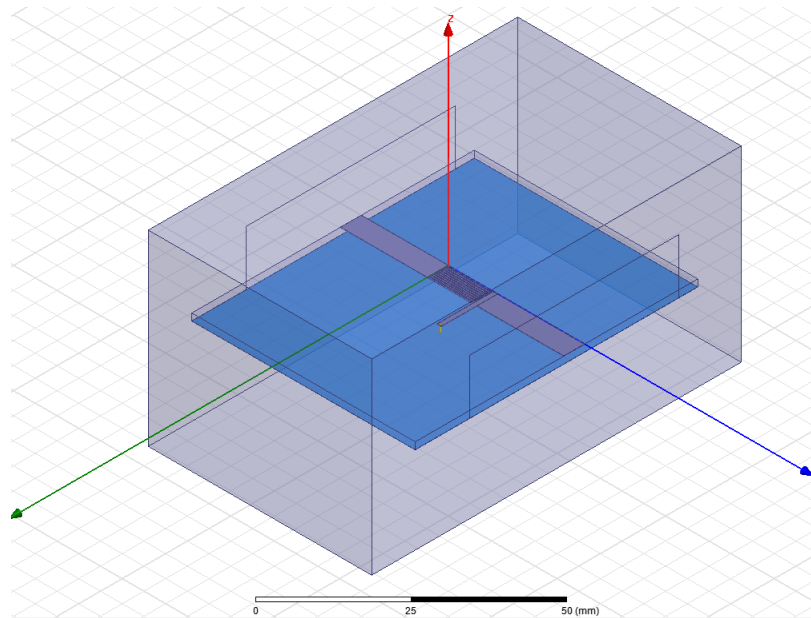


Figure 4-7 The 3-D model drawn in HFSS simulation software with feeding lines 20 mm.

The unit-cell simulation results are presented in this section. In each figure there are four curves plotted representing different stub length  $l_s$ 's. The systematic design method of a CRLH unit cell has been detailed in many literature, particularly useful guide can be found in a textbook written by Caloz and Itoh [83]. In a simpler yet practical manner, the design can start from the ideal circuit model and IDC and stub parameters, then tune the stub length  $l_s$  to find the optimum design. The design methodology will be detailed in the analysis of the equivalent circuit model (ECM).

The return loss plots are presented in Figure 4-8. The desired null that occurs near 2.05 GHz implies the approximate locus of the transition frequency. The spurious narrow peak and drop that occurs near 2.75 GHz is primarily due to the self-resonance of the IDC [84]. The simulation of the IDC alone will be presented elsewhere. The peak (nearly total reflection) right after 3.5 GHz confines the upper limit of the fundamental working band, which can also be identified in the dispersion relation.

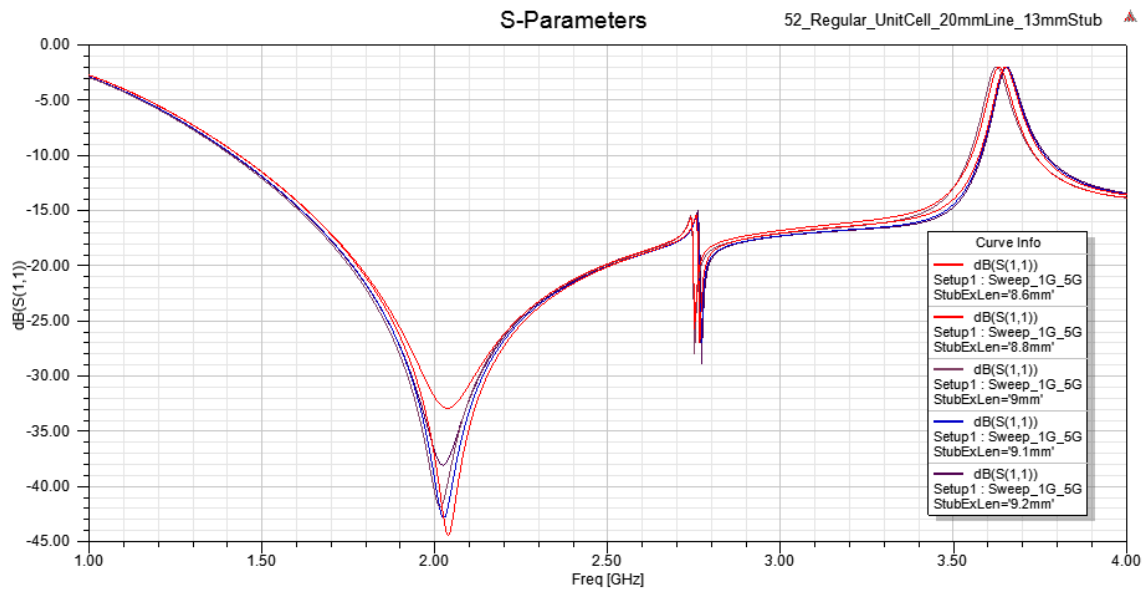


Figure 4-8 Return loss of the simulated unit cell with stub length as 8.8 mm, 9 mm, 9.1 mm, and 9.2 mm.

The insertion loss curves are plotted in Figure 4-9. It can be observed that for a such a short structure, the insertion loss is comparable to a common transmission line near the transition frequency, if we consider the common transmission line can have below -20 dB return loss in a very broad frequency range. The substrate is the industrial well-known low-loss material with loss tangent only 0.0009. The reason that causes the loss is primarily due to the leaky-wave radiation from the apertures. The radiative characteristics will be discussed in the section describing the leaky-wave antenna.

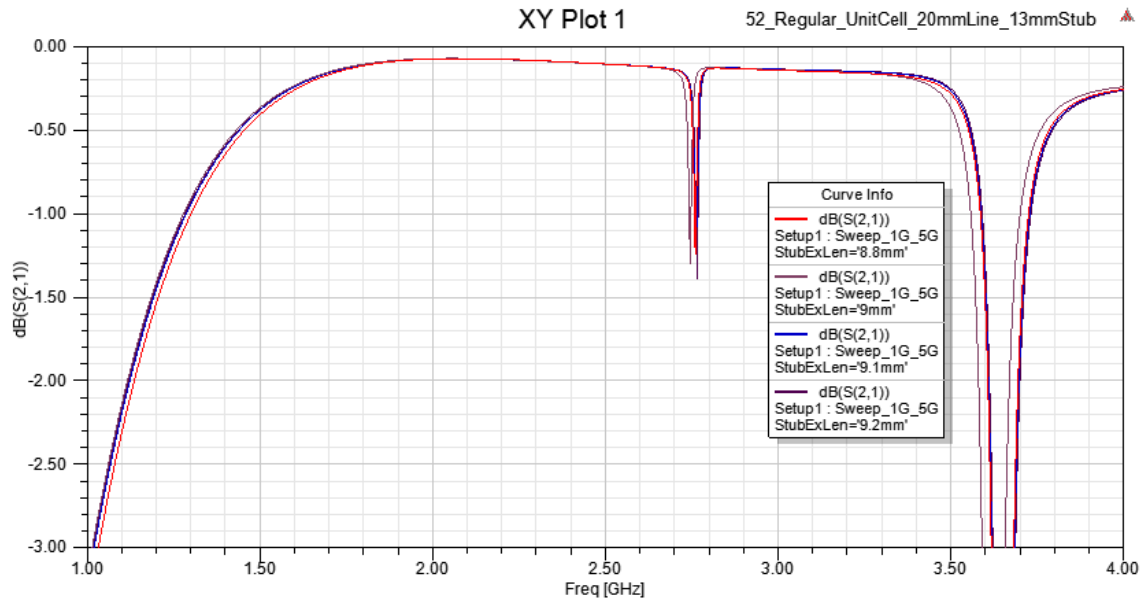


Figure 4-9 Insertion loss of the simulated unit cell with stub length as 8.8 mm, 9 mm, 9.1 mm, and 9.2 mm.

From the regular S parameters in dB, the left-handed properties of the unit cell cannot be revealed. But one can plot the insertion phase from which interesting phase advance phenomenon will be discovered. Moreover, one can plot and examine the dispersion diagram, or Brillouin diagram, to find the phase behavior of the unit cell. The dispersion diagram of the simulated unit is shown in Figure 4-10. The horizontal axis Beta<sub>p</sub> is calculated from the simulated S parameters using the equation given by [4]

$$\beta_d d = \cos^{-1} \left( \frac{1 - S_{11} S_{22} + S_{12} S_{21}}{2 S_{21}} \right). \quad (4-1)$$

The transition frequency is found near 2.05 GHz, and the band-gap is found minimum with stub length to be 9.1 mm. The straight line represents the dispersion of the free-space propagation constant with frequency. The curves appear as frequency versus the phase delay over the unit-cell physical length calculated from

$$\beta_0 d = \frac{2\pi f}{c} d. \quad (4-2)$$

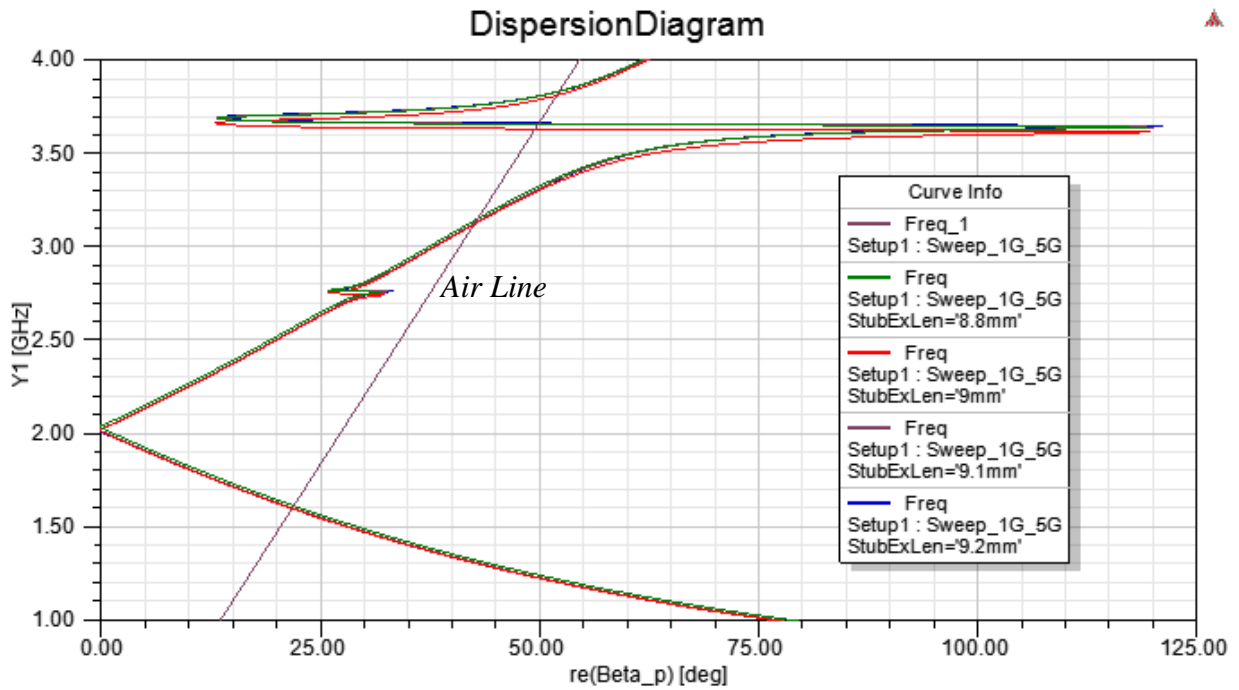


Figure 4-10 Dispersion diagram calculated from the simulated unit-cell S-parameters with stub length as 8.8 mm, 9 mm, 9.1 mm, and 9.2 mm.

The dispersion relation in Figure 4-10 also demonstrates the leaky-wave region, or radiation region and the non-radiation region, divided by the straight air line. The radiative characteristics will be discussed in Chapter 5.



A set of plots for the Bloch impedance over the frequency band are shown in Figure 4-11. The Bloch impedance is calculated from the S-parameters as follows.

$$Z_B = Z_0 \frac{2j \sin(\beta_d) S_{21}}{(1 - S_{11})(1 - S_{22}) - S_{21}S_{12}} \quad (4-3)$$

The Bloch impedance is represented as one impedance value if the unit cell of a periodic structure is symmetric, and when the unit cell is asymmetric two  $Z_B$ 's are required to describe the impedance seeing from left port and right port, or port-1 and port-2 of the unit cell's two port network. Although the unit cell shown in Figure 4-1 is not a symmetric structure, note that the antenna or transmission line in Figure 4-5 and Figure 4-6 are symmetric. Therefore here the unit cell's parameters are used to calculate the symmetric Bloch impedance. Details will be given in the ECM subsection.

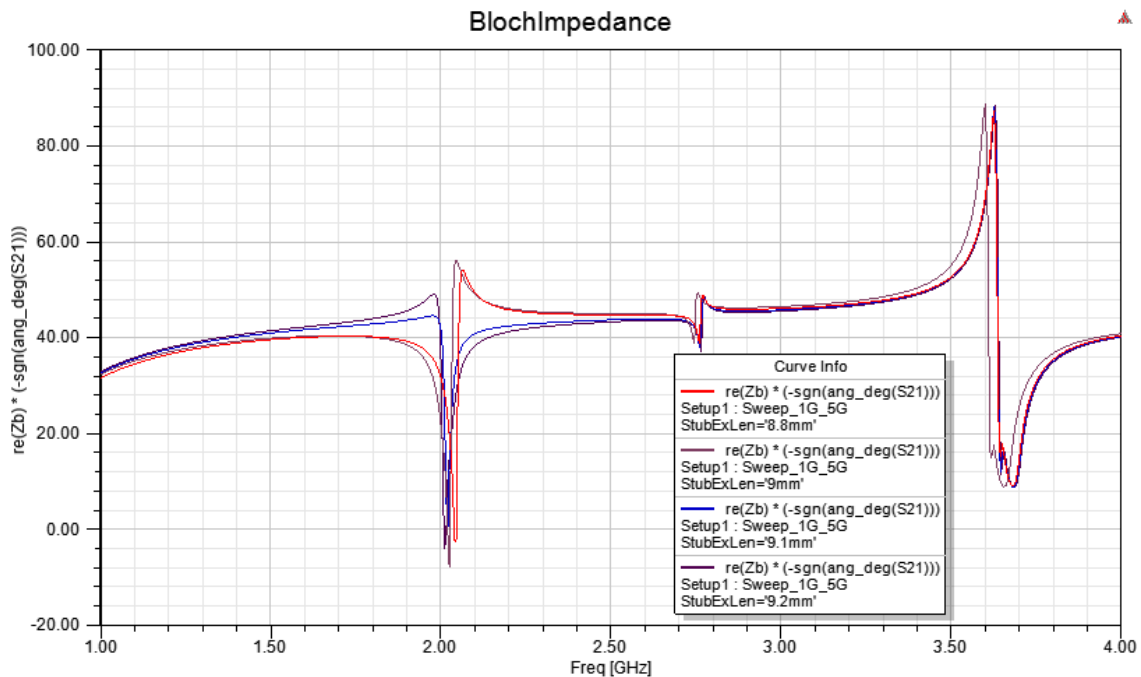


Figure 4-11 Bloch impedance (real part) of the unit cell calculated from the simulated S-parameters with stub length as 8.8 mm, 9.0 mm, 9.1 mm, 9.2 mm.

It is worth mentioning that the dispersion diagram and the Bloch impedance curves both reveal the existence of band-gap, a narrow frequency range over which the unit cell theoretically behaves as an unmatched, extraneous phase delay unit. It is hard to completely avoid the band-gap in simulations and calculation, however near the transition frequency the constituted TLs/LWAs usually behave well.

The above presented simulation results find the optimum design with stub length 9.1 mm by tuning the stub length [85]. It demonstrates a design process that seeks the optimum design by repeatedly simulating the entire structure. The following sections demonstrate another type of design flow and the derivations of the equations used in the periodic structure analysis.

#### ***4.2.4. IDC Simulations***

In order to estimate the final TL behavior, the ECM of each single unit cell is usually obtained prior to evaluating the TL design. In an ideal loss-free CRLH unit cell ECM, the series capacitance and inductance are primarily contributed from the IDC, and the shunt inductance resides in the grounded short stub. Therefore, we can simulate and extract the ECM's lumped component values from separate IDC and shorted stub simulations [78]. The procedure of parameter extraction for an IDC design is as follows.

In HFSS 3-D model simulation software, a microstrip line inter-digital capacitor (IDC) is drawn as shown in Figure 4-12. The microwave circuits will all be simulated and built on the low-loss 62 mil thick Rogers RT/duroid 5880 substrates with dielectric constant 2.2.

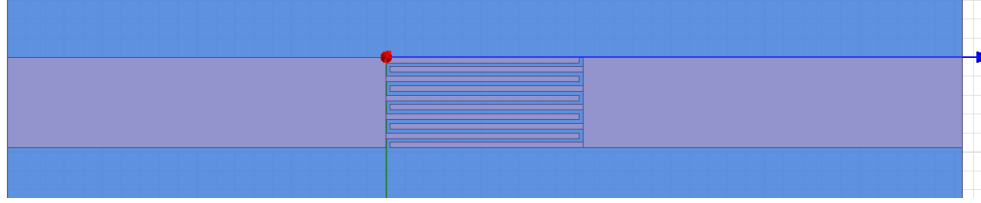


Figure 4-12 IDC model (top view) in HFSS simulation software. The substrate is the 62 mil thick Rogers RT/duroid 5880 with dielectric constant equal to 2.2 and loss tangent 0.0009. The IDC figure width is 0.3 mm and the gaps measure 0.2 mm.

The microstrip lines connected to the IDC can be de-embedded using wave ports at their terminals, so that the simulated S-parameters or Z-parameters or Y-parameters are nearly just the responses of the IDC. Using lumped circuit elements, the IDC can be modeled as shown in Figure 4-13a), which is a loss-free version of the model presented in [86]. The ECM can also be abstracted as a  $\pi$ -network as shown in Figure 4-13b).

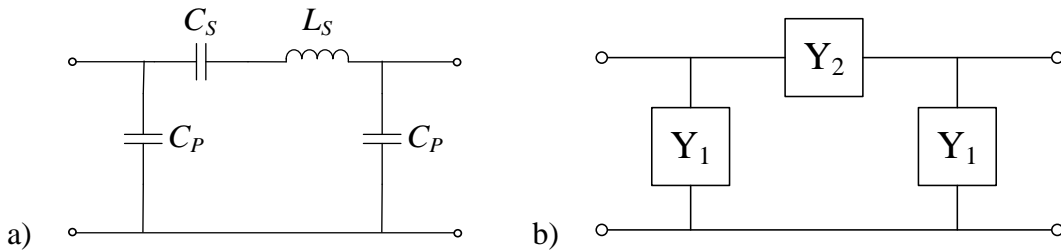


Figure 4-13 a) The ECM of an IDC. b) The  $\pi$ -network of the IDC ECM.

The Y matrix of the  $\pi$ -network is given by [5]

$$\begin{bmatrix} Y_{11} & Y_{12} \\ Y_{21} & Y_{22} \end{bmatrix} = \begin{bmatrix} Y_1 + Y_2 & -Y_2 \\ -Y_2 & Y_1 + Y_2 \end{bmatrix}, \quad (4-4)$$

where the matrix elements are defined as follows.

$$Y_1 = j\omega C_P \quad (4-5)$$

$$Y_2 = \frac{1}{j\omega L_s + \frac{1}{j\omega C_s}} = \frac{1}{Z_2} \quad (4-6)$$

The Y matrix can be obtained through simulations thus  $Y_{ij}$ 's are known after simulation. Note that  $Y_2 = -Y_{12}$ . Then the lumped elements can be derived using the  $Y_{ij}$ 's as given by

$$C_p^{IDC} = \frac{Y_1}{j\omega} = \frac{Y_{11} + Y_{12}}{j\omega} \quad (4-7)$$

$$L_s^{IDC} = \frac{1}{2j\omega} \left( \omega \frac{\partial Z_2}{\partial \omega} + Z_2 \right) \quad (4-8)$$

$$C_s^{IDC} = \frac{2j}{\omega} \left( \omega \frac{\partial Z_2}{\partial \omega} - Z_2 \right)^{-1} \quad (4-9)$$

Using the given dimensions, the calculated results are  $L_s = 2.9$  nH,  $C_p = 0.52$  pF, and  $C_s = 2$  pF. The simulated S-parameters may have spurious spikes where the calculated component values are extraneous [84]. The presence of the spurious spikes may prohibit the use of the CRLH unit cell to be used near the frequencies where the spikes appear. A solution has been proposed [84] to improve the bandwidth utilization of the microstrip IDC based CRLH unit cell.

The spurious spikes do not appear in the L-C loaded CRLH transmission lines, but the limited Q values of the capacitor components prohibits the use of L-C loaded CRLH TL in frequency bands higher than, typically, 2-3 GHz.

#### **4.2.5. Short-Stub Simulations**

Short stubs along with open stubs have been used broadly in impedance matching network [4], multiband filter design [87] [88], diplexer design [89], and many other resonance/non-resonance

based implementations. A typical short stub layout between connecting transmission lines are shown in Figure 4-14.

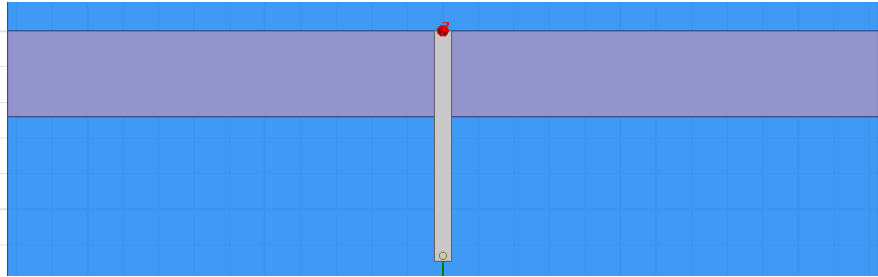


Figure 4-14 The short-stub model (top view) in HFSS simulation software. The small circle on the end of the stub is the via connecting to the ground plane of the microstrip line stack-up.

The microstrip line connecting to the short stub is de-embedded to look through into the stub directly. The behavior of a short stub can be understood from the ECM as shown in Figure 4-15. Although the notations are same as the IDC ECM, the physical functionality of the notations are different between the two sub-sections.

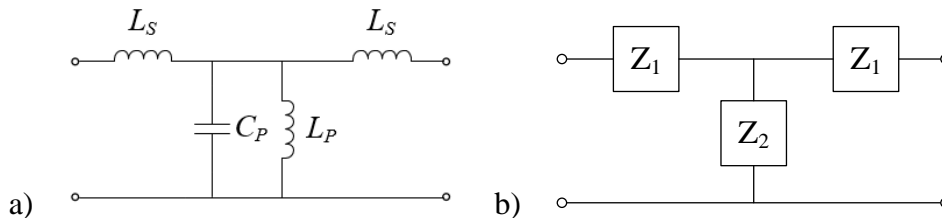


Figure 4-15 a) The ECM of a short stub. b) The T-network of the short-stub ECM.

The Z-matrix of the T-network is expressed as follows.

$$Z = \begin{bmatrix} Z_{11} & Z_{12} \\ Z_{21} & Z_{22} \end{bmatrix} = \begin{bmatrix} Z_1 + Z_2 & Z_2 \\ Z_2 & Z_1 + Z_2 \end{bmatrix} \quad (4-10)$$

The  $Z_1$  and  $Z_2$  in (4-10) are given by

$$Z_1 = j\omega L_S \quad (4-11)$$

$$Z_2 = \frac{1}{j\omega C_p + \frac{1}{j\omega L_p}} = \frac{1}{Y_2} \quad (4-12)$$

The Z matrix can be obtained through simulations thus  $Z_{ij}$ 's are known after simulation. Note that  $Z_2 = Z_{12}$ . Then the lumped elements can be derived using the  $Z_{ij}$ 's as given by

$$L_s = \frac{1}{j\omega} (Z_{11} - Z_{12}) \quad (4-13)$$

$$C_p = \frac{1}{2j\omega} \left( \omega \frac{\partial Y_{12}}{\partial \omega} + Y_{12} \right) \quad (4-14)$$

$$L_p = \frac{2j}{\omega} \left( \omega \frac{\partial Y_{12}}{\partial \omega} - Y_{12} \right)^{-1} \quad (4-15)$$

where  $Y_{12} = 1/Z_{12}$ . Using the given dimensions with stub length 8.1mm and feeding line width 4.8 mm, the calculated results are  $L_s = 0.15$  nH,  $C_p = 0.22$  pF, and  $L_p = 4.7$  nH. Parameter extraction for a shorted stub encounters no spurious behaviors. The L-C loaded CRLH transmission line uses inductors loaded to ground to realize  $L_p$ , however, the finite Q of the lumped elements disqualifies the use of them in higher frequency bands.

#### **4.2.6. CRLH Unit Cell ECM**

The analysis of the CRLH unit cell can be conveniently performed using the equivalent circuit model as shown in Figure 4-16.

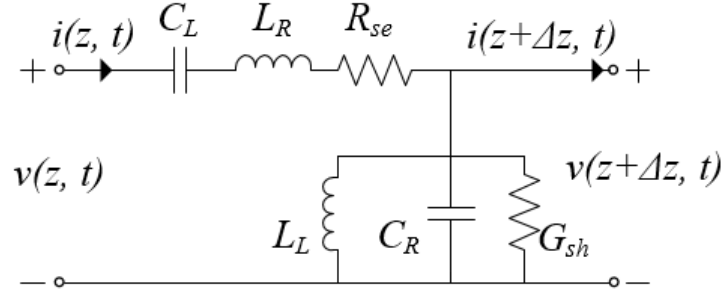


Figure 4-16 ECM of CRLH unit cell including lossy elements. Ideal loss-free unit cell ECM has no  $R_{se}$  and  $G_{sh}$  components.

The two port network can be analyzed to obtain its ABCD matrix and S parameters assuming 50 Ohm characteristic impedance in the system. Then the ABCD matrix can be used in the periodic structure calculations to find the dispersion relations and the Bloch impedances.

First, define two resonance frequencies (in radian) as follows.

$$\omega_{sh} = \frac{1}{\sqrt{C_R L_L}} \quad (4-16)$$

$$\omega_{se} = \frac{1}{\sqrt{C_L L_R}} \quad (4-17)$$

The subscript ‘sh’ indicate the resonant frequency in the shunt circuit, and the subscript ‘se’ implies the resonant frequency in the series circuit. Following the same style, the two quantities of impedance and admittance are defined as follows.

$$Z_{sh} = \frac{1}{Y_{sh}} \quad (4-18)$$

$$Z_{se} = \frac{1}{Y_{se}} \quad (4-19)$$

In terms of the lumped elements in the ECM, the following equations can also be found.

$$Y_{sh} = G_{sh} + j\omega C_R + \frac{1}{j\omega L_L} = G_{sh} + \frac{1 - \omega^2 / \omega_{sh}^2}{j\omega L_L} \quad (4-20)$$

$$Z_{se} = R_{se} + j\omega L_R + \frac{1}{j\omega C_L} = R_{se} + \frac{1 - \omega^2 / \omega_{se}^2}{j\omega C_L} \quad (4-21)$$

A balanced design has two resonance frequencies equal to each other in order to have a balanced unit cell design. The condition also leads to the matched results [76] with the line impedances related by

$$\sqrt{\frac{L_R}{C_R}} = \sqrt{\frac{L_L}{C_L}} = Z_0. \quad (4-22)$$

The condition (4-22) represents a balanced design with the left-handed line impedance equal to the right-handed line impedance.

With the defined impedances and admittances, the ABCD matrix of the two-port network is given by

$$A_P = \begin{bmatrix} A & B \\ C & D \end{bmatrix} = \begin{bmatrix} \frac{Z_{se} + Z_{sh}}{Z_{sh}} & Z_{se} \\ \frac{1}{Z_{sh}} & 1 \end{bmatrix}. \quad (4-23)$$

The theory of periodic structure [4] indicates that the forward phase delay of the two-port network can be calculated from the ABCD matrix as follows.

$$\beta_d d = \cos^{-1} \left( \frac{A + D}{2} \right) = \cos^{-1} \left( \frac{Z_{se} + Z_{sh}}{2Z_{sh}} + \frac{1}{2} \right) \quad (4-24)$$

Using the conversion equations presented in [5], we have from ABCD matrix entries to S-parameters as follows.



$$\frac{A + D}{2} = \frac{1 - S_{11}S_{22} + S_{12}S_{21}}{2S_{21}} \quad (4-25)$$

The equation (4-1) used in unit cell simulation is obtained in terms of simulated S parameters. Again, the notation  $\beta_d$  represents the equivalent propagation phase constant when the periodic structure is treated as a continuous regular wave guiding structure. The subscript  $d$  distinguishes the equivalent propagation constant from the conventional phase constant  $\beta$  (or  $k_0$ ). The variable  $d$  denotes the physical length of the two-port network which serves as a unit cell in the periodic structure.

In order to find the symmetric model Bloch impedance, the standard ECM must be modified assuming that the periodic structure consists of the symmetric unit cells.

#### 4.2.7. Symmetric CRLH Unit Cell ECM

In practice, the unit cell shown in Figure 4-1 which can be modeled as in Figure 4-16 is often used with matching network. The objective of the matching network is usually to achieve double the capacitance in the asymmetric layout. If the CRLH structure consisting of multiple unit cells is well matched, the asymmetric unit cell ECM can be reorganized to obtain a symmetric ECM as shown in Figure 4-17.

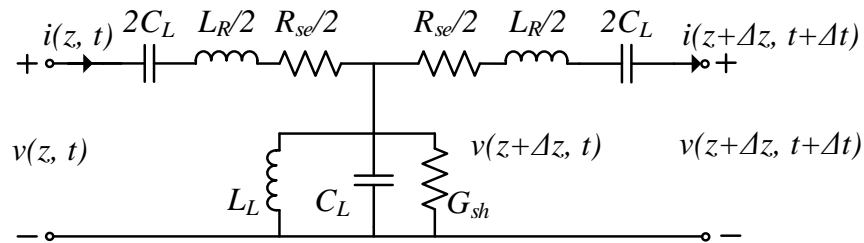


Figure 4-17 ECM of CRLH unit cell in the symmetric form including lossy elements. Ideal loss-free unit cell ECM has no  $R_{se}$  and  $G_{sh}$  components.

The symmetric ECM is basically a T-network, with two series impedances denoted by  $Z_{se}^T$ . The series impedance (4-21) applies here for the symmetric model as well. The series impedance can be calculated from the equation given by

$$Z_{se}^T = \frac{R_{se}}{2} + j\omega \frac{L_L}{2} + \frac{1}{j\omega 2C_R} = \frac{1}{2} Z_{se} \quad (4-26)$$

The symmetric ECM would lead to symmetric ABCD matrix, which is given by

$$A_P^T = \begin{bmatrix} A_T & B_T \\ C_T & D_T \end{bmatrix}, \quad (4-27)$$

where  $A_T = D_T$ . The matrix entries are expressed in terms of the previously defined impedances and admittance as follows.

$$A_T = 1 + \frac{Z_{se}^T}{Z_{sh}^T} = 1 + \frac{1}{2} Z_{se} Y_{sh} \quad (4-28)$$

$$B_T = Z_{se} + \left( \frac{Z_{se}}{2} \right)^2 Y_{sh} \quad (4-29)$$

$$C_T = Y_{sh} \quad (4-30)$$

From the ABCD matrix of the symmetric model, the propagation constant and Bloch impedance can be formulated using the theory of periodic structure. Note that the propagation constant is calculated from

$$\beta_d d = \cos^{-1} \left( \frac{A_T + D_T}{2} \right) = \cos^{-1} \left( \frac{Z_{se} Y_{sh}}{2} + 1 \right), \quad (4-31)$$

which is exactly same as (4-24) formulated based on the asymmetric model. The Bloch impedance can be derived as follows.

$$Z_B^T = \frac{B_T}{\sqrt{A_T^2 - 1}} = Z_{se} \sqrt{Z_{se} Y_{sh} + \frac{1}{4}} \quad (4-32)$$

With (4-20) and (4-21) plugged in, the Bloch impedance can be calculated from the lumped elements in the ECMs.

#### 4.2.8. Calculation Example

Using the aforementioned dimensions of the IDC and the short-stub and the simulation results, we can combine the  $\pi$ -network of IDC and T-network of short-stub and obtain an asymmetric model. The combination is shown in Figure 4-18.

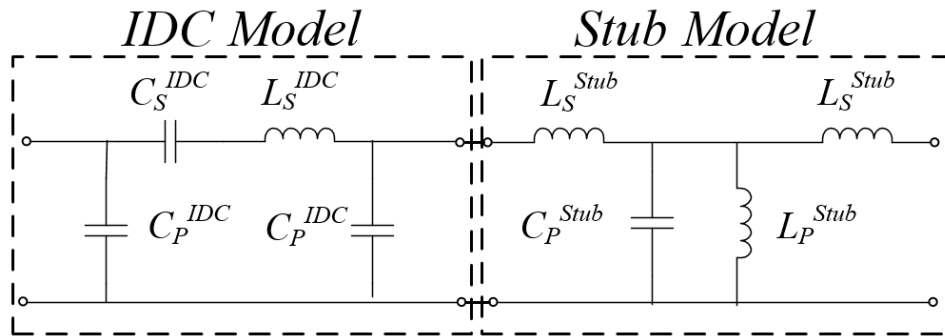


Figure 4-18 Combining the ECMs of IDC and short-stub to form an asymmetric unit cell model.

The circuit model in the above figure is much less complicated if  $L_S$  of the short-stub is ignored. The given dimensions result in the stub's  $L_S$  about 0.15 nH which is small enough to be ignored. Moreover, the left-most  $C_P$  of the IDC's model can be assumed to contribute in  $Y_{sh}$  for the adjacent unit cell on the left. Therefore, we have  $Z_{se}$  comprised of IDC's  $C_S$  and  $L_S$  and  $Y_{sh}$  comprised of IDC's two  $C_P$ 's, stub's  $C_P$  and  $L_S$ .

In conclusion, the asymmetric model has the following reactive elements as follows.

$$C_L = C_S^{IDC} \quad (4-33)$$

$$L_R = L_S^{IDC} \quad (4-34)$$

$$C_R = 2 * C_P^{IDC} + C_P^{Stub} \quad (4-35)$$

$$L_L = L_S^{Stub} \quad (4-36)$$

From the given dimensions, the resultant model has  $C_L$  as 1.88 pF,  $L_R$  as 2.9 nH,  $C_R$  as 1.18 pF, and  $L_L$  as 4.65 nH. A Matlab code was written for the analysis of the unit cell ECM. The plotted curves can be compared with the simulated results in Figure 4-8 to Figure 4-11.

First, the return loss is shown in Figure 4-19.

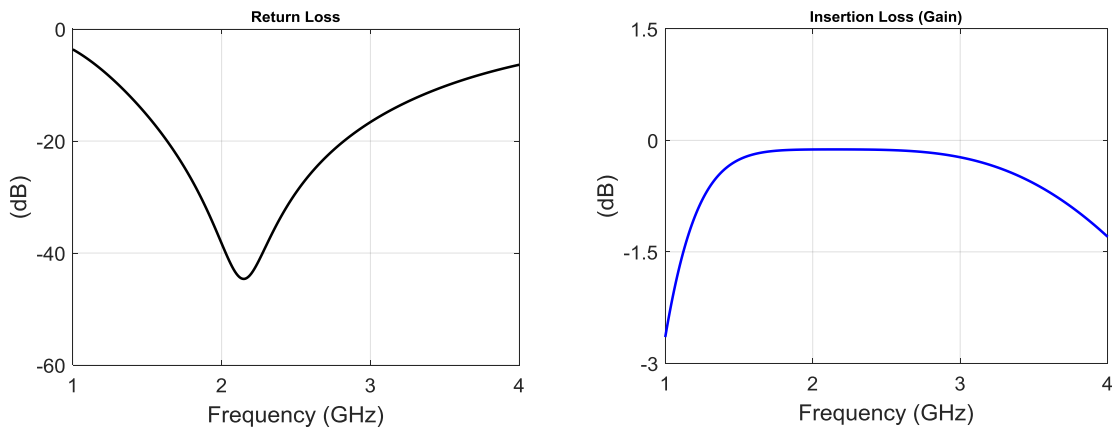


Figure 4-19 Matlab plotted return loss (left) and insertion loss (right) of the unit cell ECM with  $Z_0$  terminated on both ports.

The null in the return loss curve shows where the transition frequency is in proximity. The loss revealed in the insertion loss plots is much greater compared to a conventional right-handed transmission line. However, in such an ideal ECM analysis the components are considered lossless, and the unit cell losses are not accounted for.

Secondly, the insertion loss (or gain, in the active unit cell demonstration) is also plotted in Figure 4-19. Note that the return loss and insertion loss are not plotted in the same scale. Actually,

close to reality, the unit cell is of loss that is not much more significant than a piece of microstrip line or strip line. However, this is only the loss of one single unit cell. When multiple unit cells are cascaded to be used as transmission lines, the insertion loss usually causes undesired degradation in signal or power transmissions.

On the other hand, the loss which is desired in an LWA application environment is not great enough, indicating that the radiation efficiency is very poor.

The dispersion relation and the phase delay of the unit cell ECM is plotted in Figure 4-20. From the dispersion diagram it is clear that below the transition frequency the phase propagation constant is a negative value. The curves in Figure 4-10 have their lower sections (below transition frequency, with negative phase values) flipped with respect to the vertical axis for a concise view of the radiation region. The dispersion curve in Figure 4-20 is not treated in the same way but plotted with two air-lines showing the dispersion relation of the electromagnetic wave in air. The curves in Figure 4-20 are plotted based on the constant ECM model which has been usually considered as an effective help with physical interpretation.

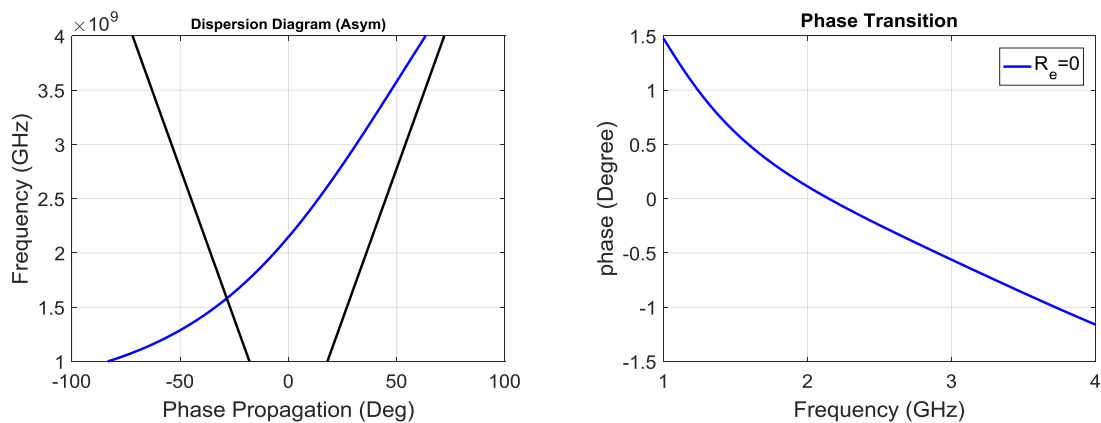


Figure 4-20 Matlab plotted the calculated dispersion relation (left) and the phase propagation (right) across the unit cell ECM.

Since the lumped element values are intentionally adjusted to reflect a balanced ECM design [72], there is no band-gap, or transition gap in the dispersion diagram. A dispersion diagram containing band-gap near the transition frequency can be found in the demonstration of the active ECM and simulations. The frequency range where the phase delay is positive reflect a left handed region, while the frequency range where the phase delay is negative reflect a right handed region. It has been proven that the dispersion relation can be calculated from the asymmetric model, whereas the Bloch impedance must be calculated from the symmetric model. The calculation using the symmetric model and the asymmetric model are shown in Figure 4-21.

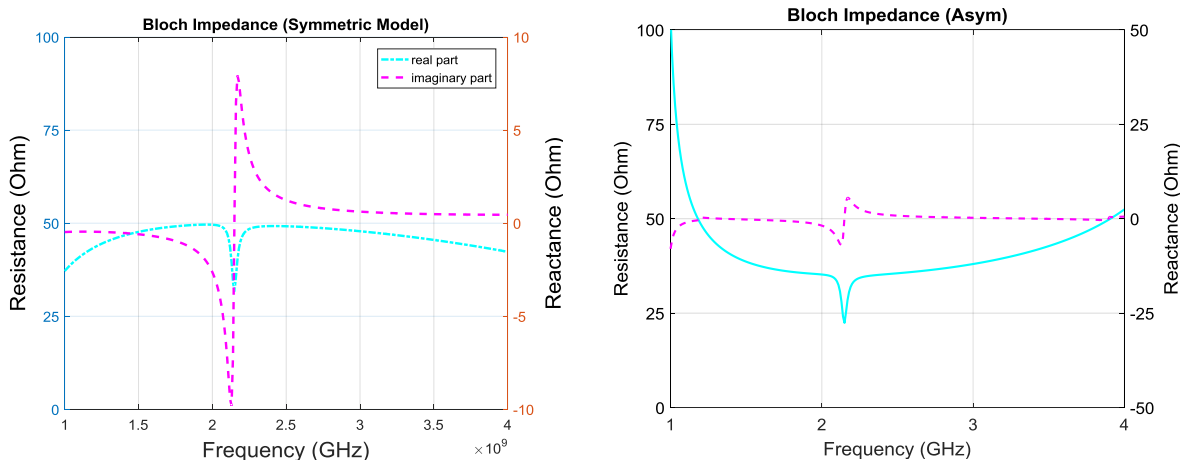


Figure 4-21 Bloch impedance calculation based on the symmetric model (left) and the asymmetric model (right). The asymmetric model results in less resistance.

The difference between the ECM calculation and the full-wave simulation is more significant further away from the transition frequency, because in reality the distribution elements in models are strongly dispersive (frequency dependent) and the picked values are intentionally from near the transition frequency. Note that the ECM is found with the transition frequency about 2.1 GHz, while the unit cell full wave simulation finds its transition frequency at about 2.05 GHz. The difference is primarily due to the neglected inter-coupling between the short-stub and the IDC, and

this inter-coupling is not incorporated in the separated IDC and stub simulations but certainly accounted for in the unit cell full wave simulation.

Moreover, the unit cell simulation is not the most accurate either, as can be found in transmission line and leak-wave antenna design and analysis in [85]. The behavior of the TLs and LWAs is usually different from the prediction from the unit cell behaviors.

Last but not the least, the insufficient accuracy of the modelling methods using unit cell is also because the theory of periodic structure is based on the infinite series but in practice almost all the structures are of finite length or consisted of finite number of unit cells. The corrected theory of terminated periodic structure [4] can help but usually this category of inaccuracy is small enough for long structures.

### **4.3. Negative Resistance**

#### ***4.3.1. Negative Resistance and Typical Applications in Amplifiers***

In radio frequency, negative resistance (NR) has been known since it was first introduced by Hull [39], disclosing the dynatron, the vacuum tube. Modern NR circuits often appear as two-terminal circuits (one port device) that consist of active devices and biasing circuits [40]. When operated as a one-port device, the NR circuits amplify and reflect the incident power, enabling the design of reflection-type amplifier that uses a circulator to separate the input and output ports of the amplifier [42]. A typical schematic of a RF amplifier employing one-port amplification is shown as in Figure 4-22, and a photo of a prototyped waveguide amplifier utilizing the reflection-type amplifier is presented in Figure 4-23.

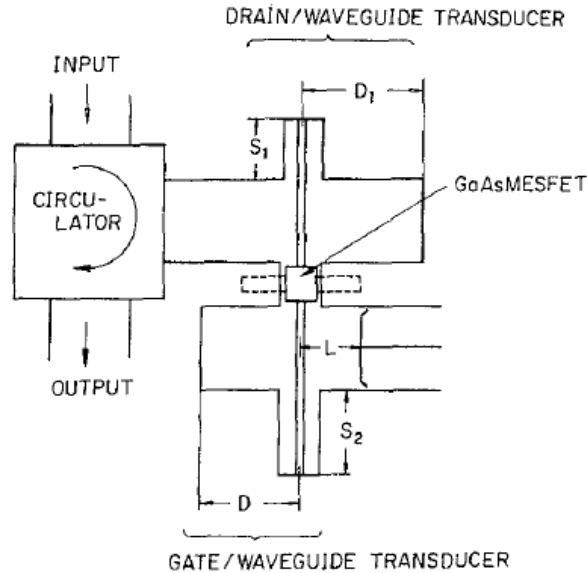


Figure 4-22 A schematic of the two-port amplifier using one-port amplification mechanism and a circulator to isolate the input and output signals. Figure is a duplicate of Fig. 6 in [41] in the year of 1979.

The schematic of the two port amplifier utilize a microwave circulator to isolate the input and output port. The incident power delivered toward the MESFET (denoted as the GaAsMESFET in the figure) is amplified and returned back to the circulator. The reflected power is then guided to its output port, isolated from the input port by the circulator. Therefore there is nearly zero reflected power leaking backward to the input power if the circulator is highly directional. Tohyama and H. Mizuno prototyped the amplifier using the rectangular waveguide technology. It has also been presented that implementing microwave circulating circuit and amplification circuit using microstrip technology [90] in W-band is feasible as well.



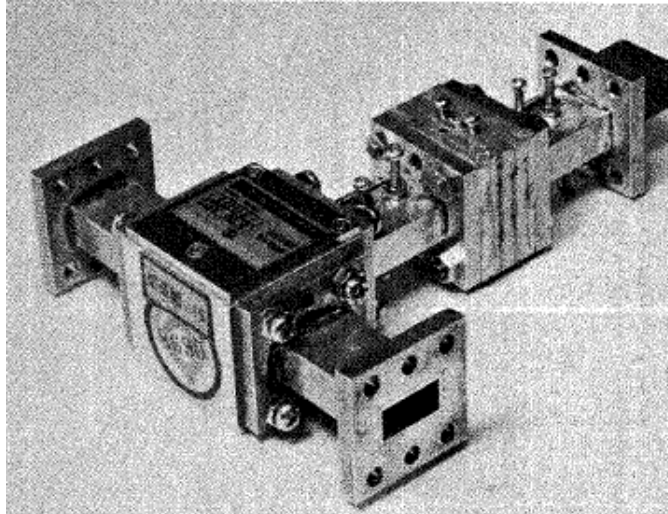


Figure 4-23 A photo of the two-port waveguide amplifier with one-port amplification and a circulator. Figure is a duplicate of Fig. 4 in [91] in the year of 1977.

Generally, except for the intrinsic two-port devices like diodes [92], other NRs realized using three terminal components including all types of BJTs and FETs are essentially to terminate one of the two port circuits and leave the other port for NR response. For illustration, an abstracted amplifier schematic that demonstrates this category of implementations is shown in Figure 4-24, which provides more details on the functionality of the amplifying semiconductor.

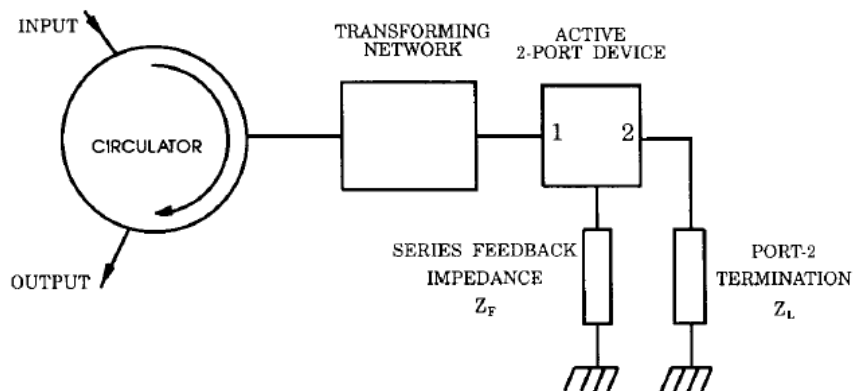


Figure 4-24 A schematic of terminating one port of a two-port circuit and use the other port as the NR. The realized NR is used in an amplifier circuit incorporating a circulator. Figure is a duplicate of Fig. 1 in [93].

However, the diagram in Figure 4-24 does not include the other class of intrinsic 2-port device, typically diode. More specifically, tunnel-diode has found a lot of applications in single amplification since it was discovered by Esaki [94] in 1958. The use of tunnel-diode based negative resistance have been reported in the application of amplifier [42] as well, and extensive analysis regarding different types of negative resistance diodes can be found in [92].

There is another active CRLH unit cell that incorporates tunnel diodes and realizes forward gain [37]. The NR-CRLH unit cell that will be described in the following sections will be compared with the tunnel-diode CRLH unit cell side by side.

Among various NR circuits, the inverted common collector (ICC) is of particular interests to us. This circuit was one of the well-known circuit to simulate high-Q inductance in history. The circuit originated from the study of the active-circuit simulated inductance and capacitance. During the long and evolutionary history of semiconductor technology, the general trend toward microminiaturization had made it desirable to fabricate inductive and capacitive elements by a pure semiconductor approach [95]. The following sections are focused on the ICC circuit and its application in NR-CRLH structure.

#### **4.4. ICC NR Circuit**

The simplified schematic and the equivalent simple circuit model of the inverted common collector model is shown in Figure 4-25. The input impedance of the active circuit can be modeled as an inductor in series with a negative resistor as shown in Figure 4-25b). The circuit has caused considerable interests due to its combination of inductance and negative resistance.

The name inverted common collector (ICC) was first given in [96] in 1968, because the input terminal (base) of the conventional common-collector circuit is loaded and grounded while the output port is inverted as the input port and output since it is a one-port network (basics of common BJT transistor circuits can be found in numerous textbooks, e.g., in [97], [98] and [99] and is not in the scope of this work). The analysis of the circuit can be found in [100]. However, the accuracy of the approximated equations is not good enough to guide the actual circuit design, and the simulation tool will be the primary source to evaluate and predict circuit behaviors.

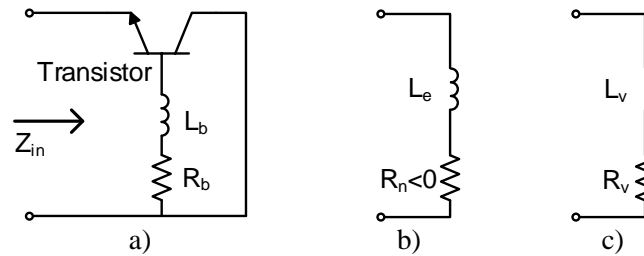


Figure 4-25 Negative resistance circuit and its equivalent model. a) Negative resistance circuit based on a bi-polar junction transistor. b) The equivalent circuit model with an inductor and a negative resistor in series. c) The equivalent circuit model of the via-hole termination at the ends of the short stubs in the CRLH structure.

Another circuit schematic with more details is shown in Figure 4-26 using a NPN type bi-polar junction transistor. The circuit can be implemented using a PNP transistor as well, provided that the circuits are properly biased using different class of BJTs. MOSFETs are potential substitutes in the same or different frequency bands, in particular higher frequency bands. The dashed line in Figure 4-26 indicates a simpler circuit eliminating the biasing network connected to the collector terminal, but experiments show that dual-biasing improves the NR response at higher frequency by increasing  $V_{CE}$  with constant  $I_C$ . Therefore in this schematic both configurations are presented. In the NPN-based circuit, the  $V_{EE}$  is negative voltage and  $V_{CC}$  is positive.

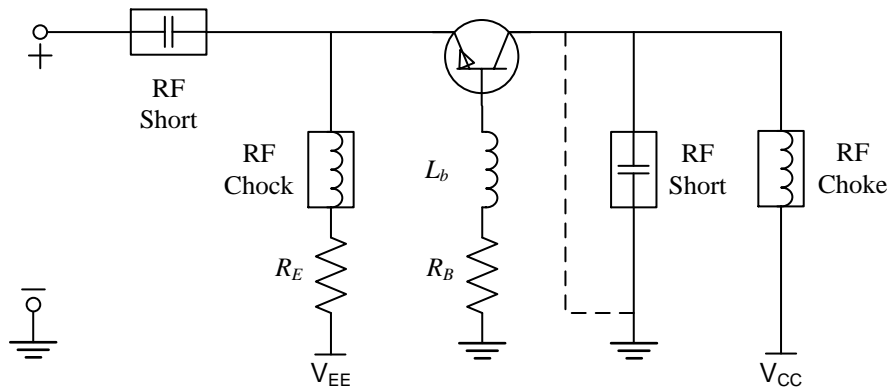


Figure 4-26 Schematic of the ICC NR circuit. The dashed line indicates the simplified configuration of grounding the collector terminal directly.  $V_{CC}$  is a positive biasing voltage and  $V_{EE}$  is negative for NPN transistors.

The ICC NR circuits have been advised to realize the oscillator by Gibbons [101] and zero insertion-loss filters [102] as a practical replacement of the low-Q microstrip or lumped inductors in microwave circuits, and different types of filters have been designed using the ICC-simulated inductance and negative resistance. For example, the active direct-coupled filter was demonstrated by Chang and Itoh in [103].

#### 4.4.1. Active Inductors

If the illustrated ICC circuit was changed with the  $L_b$  removed (or  $L_b=0$ ), the resultant circuit was used to realize active inductor. Before the ICC NR circuit was proposed in filter applications by Adams and Ho in 1968, a similar circuit was developed to realize active inductance. A broad survey of the active inductor realization utilizing various semiconductor technologies can be found in [95] by Dill. Pertinent analysis particularly addressing the ICC active inductor circuit was given by Lindmayer and Worth in 1965 [104] and by Dutta Roy in 1963 [105]. This analysis laid foundations for the ICC NR circuit application [102] and analysis in [100]. The diagram showing

the active inductor circuit is shown in Figure 4-27, which only differs from the ICC NR circuit by the absence of  $L_b$  loading at the base terminal.

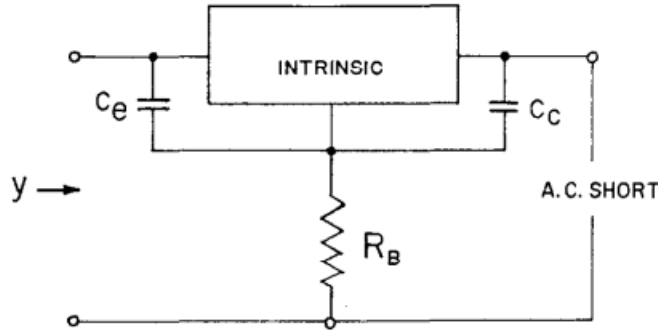


Figure 4-27 Duplicate of Fig. 1 in [104]. The input admittance is inductive and minimally lossy.

When used to build active filters, the transistor based elements can either function as coupling elements (e.g., inverters) [106], or to strengthen the passive resonators by compensating the loss thereby boosting the overall quality factor [103].

The semiconductor simulated inductors drew considerable attention because of its high quality factor, smaller area, operation in high frequency where spiral inductors fail, miniaturized and consistent dimensions that permit high density integration, and broad-band tunability that is not seen with semiconductor capacitive elements [107]. Broad range of applications have been reported using various semiconductor three-terminal devices (BJT or MOSFET).

#### **4.4.2. Mathematical Models**

Although the analytical models have been found not accurate enough the desired frequency bands, they certainly help with establishing the fundamental concepts and physical insights. Several previously recognized models will be discussed in this section.

The name of the circuit, inverted common collector, is given because the regular input port of a common-collector circuit is used for the loading port while the output port of it is used for the input port. A regular common-collector configuration can be found from many textbooks, for example, [97]. Its input voltage is applied to base terminal, and the output voltage is taken from the emitter terminal. A typical circuit can be found in Figure 4-28a), and the equivalent circuit model (ECM) is also given in Figure 4-28b) using T-model and high frequency model of the transistor. This circuit is better known as emitter follower [97].

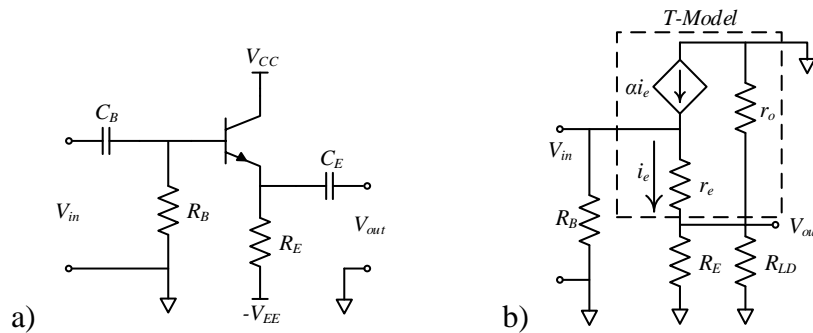


Figure 4-28 Conventional common base amplifier circuit schematic. a) Circuit schematic. b) Equivalent circuit model schematic.

The ECM shown in Figure 4-28 might not be reliable at high frequency, where parasitic parameters cause significant deviation in performance. The high-frequency model will be detailed in the following section. The most important parameter in the circuit analysis is finding a proper common base current gain, commonly denoted by  $\alpha$  as shown in [97].

Dill [95] summarized an approximate mathematical model for the common-base current gain denoted by  $\alpha$  as given by

$$\alpha = \frac{1}{1 + j \frac{f}{f_b}} \alpha_0, \quad (4-37)$$

where  $\alpha_0$  is the DC common-base current gain and  $f_b$  is the  $\alpha$  cutoff frequency which can be calculated from

$$f_b = \frac{1.22 D}{\pi b_{eff}}. \quad (4-38)$$

The notation  $D$  in the above equation is diffusion coefficient, and  $b_{eff}$  is called effective base width. Consequently the input impedance  $Z_{in}$  as shown in Figure 4-25 can be calculated as follows.

$$Z_{in} = r_e + r_{bs} [1 - \alpha] \quad (4-39)$$

The note  $r_e$  represents the resistance at emitter terminal of the transistor, and  $r_{bs}$  is the sum of  $R_b$  as shown in Figure 4-25 and resistance at base terminal of the transistor. Note that  $L_b$  is not involved (or, equivalently  $L_b=0$ ) because in [95] the author was primarily interested in the inductive reactance of the input impedance. In this case the real part of the input impedance is the smaller the better in order to achieve higher Q value. Notice that if  $\alpha$  is decomposed into its real part ( $\alpha_r$ ) and imaginary part ( $\alpha_i$ ) and both assumed to be greater than zero,  $Z_{in}$  can be rewritten as follows.

$$Z_{in} = r_e + r_{bs} (1 - \alpha_r) + jr_{bs} \alpha_i \quad (4-40)$$

Apparently the major problem that degrades the Q value is the emitter terminal resistance  $r_e$ , and the achievable inductance value depends on  $R_B$ , although not exclusively. Therefore in the active inductor circuit, increasing  $R_B$  in Figure 4-26 was preferred to increase inductance.

A more accurate model also introduced in [95] is given as

$$Z_{in} = r_e + r_b \frac{1 - \alpha}{1 + j \frac{f}{f_0}}, \quad (4-41)$$

where a more accurate model for  $\alpha$  is given by

$$\alpha = \frac{e^{-jm(f/f_b)}}{1 + j \frac{f}{f_b}} \alpha_0, \quad (4-42)$$

The new involved notation  $m$  is correction factor. The resultant imaginary part of  $Z_{in}$  is positive and the circuit functions as an inductor. The quality factor of the simulated inductor is analyzed in the paper.

Dutta-Roy proposed a more complex solution but with higher accuracy in [105] using the theory of exponentially tapered resistance capacitance transmission line [108]. In a similar form, the real and imaginary parts of the input impedance are given by

$$R_{in} = r_e + r_b [1 - A] \quad (4-43)$$

$$X_{in} = -r_b B \quad (4-44)$$

The notations  $A$  and  $B$  are given as follows.

$$A = \frac{\cosh \lambda' \cos \mu'}{\cos^2 \mu' + \sinh^2 \lambda'} \quad (4-45)$$

$$B = -\frac{\sinh \lambda' \sin \mu'}{\cos^2 \mu' + \sinh^2 \lambda'} \quad (4-46)$$

The notations  $\lambda'$  and  $\mu'$  are detailed in [105] and omitted here. With the real part and imaginary part separated, the quality factor of the simulated inductor is readily to calculate from  $Q = X / R$ .

#### ***4.4.3. Circuit Analysis and Simulations***

The ICC circuit shown in Figure 4-26 used in this design is further simplified and presented in Figure 4-29a. The collector terminal is not directly grounded but the bypass capacitor  $C_C$  ensures RF shorting at the collector terminal. One single biasing voltage  $-V_{EE}$  suffices to bias the transistor



properly, however, dual biasing voltages offer more flexibility in tuning the transistor behavior. This is difficult to manifest in calculation but easy to demonstrate in simulation and measurement. The emitter terminal is hooked up to the biasing resistor  $R_E$  and negative voltage source  $-V_{EE}$  through the RF blocking inductor  $L_E$ . The component  $C_E$  is simply DC blocking capacitor at the input. Although it is not necessary to use  $C_E$  in the CRLH transmission line or leaky-wave antenna because the connected stub is in conjunction with two IDCs on both sides (thus the NR circuit is not physically connected to other active circuits with low resistance path), the component is kept for possible phase adjustment or impedance matching in the simulation and layout.

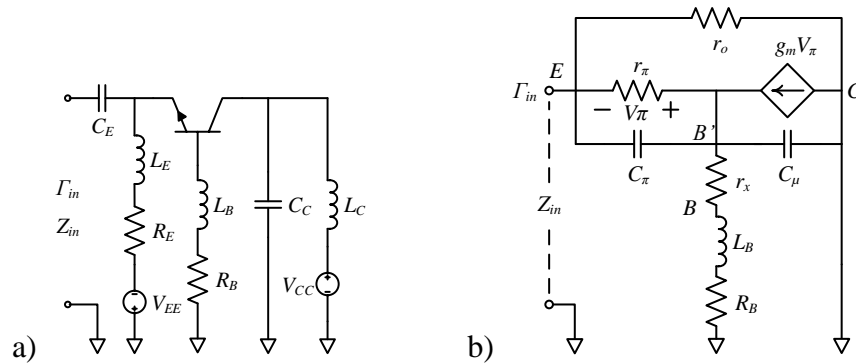


Figure 4-29 ICC circuit and its high-frequency equivalent circuit model. a) ICC circuit used in the BJT-based design. b) The small-signal equivalent circuit model.

The ECM of the AC-circuit is shown in Figure 4-29b), incorporating the high-frequency hybrid- $\pi$  ECM of a BJT. The hybrid- $\pi$  model is different from the low-frequency T-model in Figure 4-28b). Similar models can also be found in other analog and RF circuit books, like the classical analog circuit book by Gray *et. al.* [109] and the popular RF technique book by Lee Thomas [110].

The ECM circuit can be put in a schematic circuit simulator to evaluate the behavior. Normally, a transistor model having constant real-valued transconductance  $g_m$  does not reflect a negative real

part of  $Z_{in}$ . As pointed out by Dill [95], the inductive response of the conventional circuit is caused by delayed conductivity modulation of the base. This time delay is modeled in Figure 4-30 which shows an ADS circuit schematic. The transistor is modeled by a controlled current source with time delay as ‘T’ in the component ‘SRC1’.

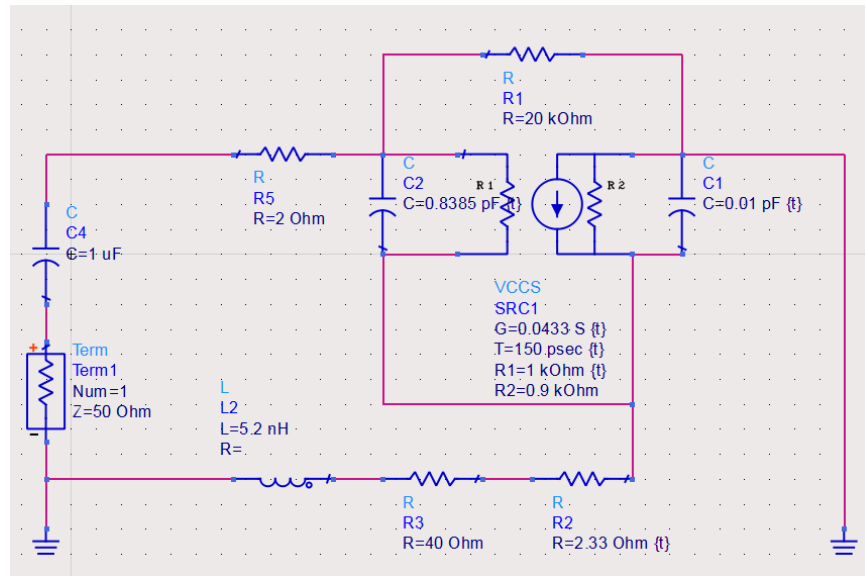


Figure 4-30 ECM with controlled source modeling the current delay.

The simulated results are plotted in Figure 4-31. The input resistance is seen smaller than zero from 200 MHz up to 4.2 GHz, and the inductive response appears at higher frequency band starting from 2.8 GHz all the way up to 6 GHz. It is difficult to reflect the circuit precisely, thus the circuit model results are provided only to illustrate the physical rationale of the existence of the negative resistance.

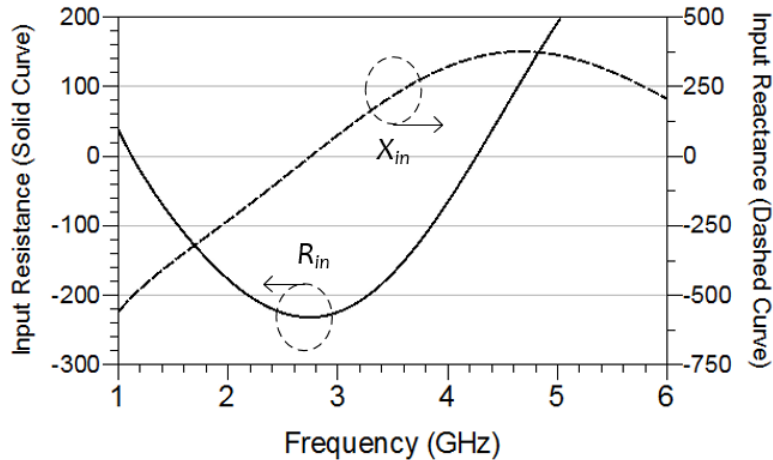


Figure 4-31 Simulation results of the transistor model with delayed conductivity.  
Solid line: input resistance. Dashed curve: input reactance.

In summary, three analyses of the NR circuit response have been briefed. These approximate results can be used in the early phase of the design procedure. However, due to the limited accuracy of the mathematical models, NR response model equations surrenders their credibility to the circuit simulation results incorporating the SPICE models or S-parameter models. Therefore the simulation results will be the primary source of predicting and designing the circuit responses in this work.

In the circuit analysis, most of the lumped elements need to be determined from the very low level device characterization, and are difficult to obtain the accurate values across broad bandwidth. It can be much easier to use the component's measured S-parameters or SPICE models. The S-parameter simulation has limitations that require the circuit layout to mimic the layout of the board on which the S-parameters are tested. Whereas the SPICE model is much more flexible and promises even better accuracy.

The circuit simulation schematic is shown in Figure 4-32. Lumped inductors and capacitors are assumed to give extremely high Q. Voltage sources are assumed to be ideal as well. The

capacitor(s) connecting to the collector terminal (the pin on the left of the square box named bfg425w) is shorting the terminal to ground at RF frequency to perform common-collector configuration. In actuality the collector may be grounded directly using via-holes and only one biasing source is needed, which simplifies the circuit design but sacrifice high frequency performance. Differences will be shown in the simulation results. The resistors are for base terminal loading and biasing.

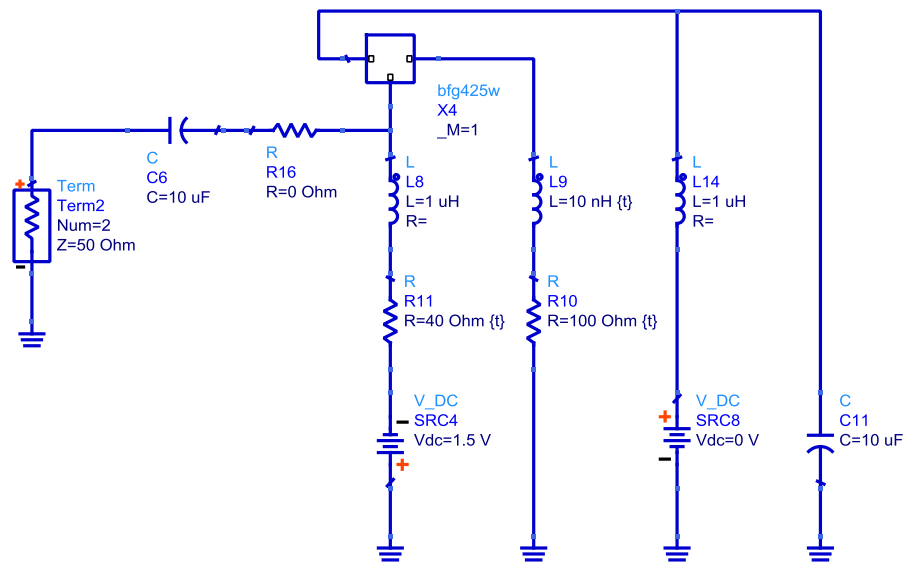


Figure 4-32 Circuit simulation using the SPICE model of the BFG425W from NXP semiconductor.

The simulated results are shown in Figure 4-33 in the format of reflection coefficient and input impedance. Notice that the input resistance goes below 0 Ohm between 1.6 GHz up to about 4GHz. The circuit responds inductively in the entire simulation frequency band. The simulation takes two biasing conditions. The red curves show that when the Vcc voltage is shut off, and blue curves show represent that when the Vcc voltage is set 1 V. The higher the Vcc frequency is, the higher reflection coefficient is at higher frequency region. However the high reflection coefficient indicates great amount of power being reflected and may saturate the transistor. This nonlinearity

is not reflected in the presented curves and it determines the linear region. The high amplification will be suppressed for practicality purposes.

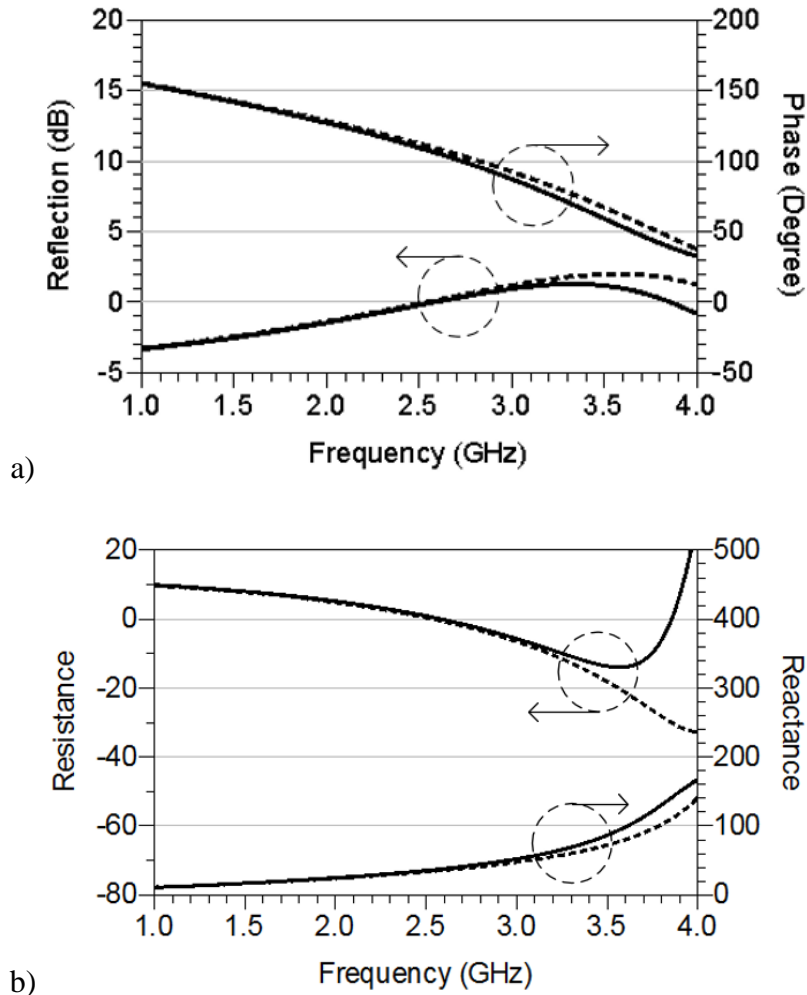


Figure 4-33 ICC NR circuit response. The solid curves represent the case when Vcc is turned off. The dashed curves represent the case when Vcc is turned on at 1 V. a) The simulated S-parameters. b) The simulated input impedance.

The circuit simulation results demonstrate the circuit response in the ideal circuit. However in RF circuit the layout and its parasitic effects produces significant difference. The best way to estimate the actual circuit behaviors on the customized layout is to combine layout and circuit simulations, which will be referred to as post-layout simulation shown in the next section.

#### 4.4.4. Post Layout Simulations

In order to obtain the most accurate predictions, we utilize the layout and post-layout simulation feature in ADS. After the basic circuit is preliminarily determined, we incorporate physical layout to evaluate the RF performances.

The microstrip layout in Keysight® Momentum® simulation software is drawn as demonstrated in Figure 4-34a). Near the north pole of the figure lies the input port, which is the only TML calibration port in Momentum port setting. The rest of all the ports are non-calibration ports as junctions with component pins. The four-pad footprint near the middle of the figure is where the transistor sits, and the larger pad is one of the emitter pins (the other one is the diagonal pad). The bottom two ports are where the biasing DC wires are soldered. Via-hole diameters are 0.6 mm. All surface mount discrete components are of 0603 code size (EIA code).

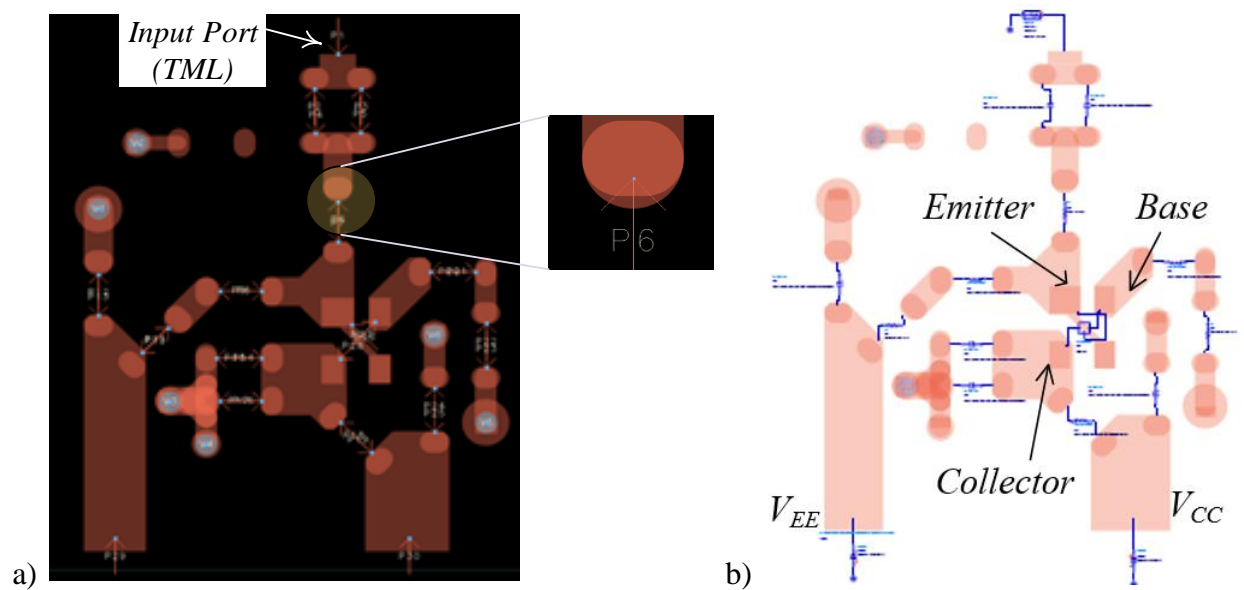


Figure 4-34 (Colored) Layout and post layout simulations. a) Board layout of the circuit (without matching stub). The picture has black background and orange copper feature. b) Mixed simulation with EM results and schematic components. The picture has white background.

The layout simulation is then used in a schematic simulation. Models of lumped elements are filled in between the pads, which are the locus of the ports that are set in the layout simulation. The schematic simulation is shown in Figure 4-34b). Although the schematic components are hardly recognizable due to the limited space (only key voltage points and junctions are marked in black texts), it is given to provide a closer view of the entire circuit with both layout and lumped components. Nevertheless, the circuit can be reconstructed by comparing the post layout simulation with the schematic simulation.

The lumped components are all from Murata, who provide device library based on the measured results. It is known that the lumped elements are barely ideal because of the parasitic effects. For example, inductors come with intrinsic resistance, capacitors come with conductance and parasitic inductance. Therefore the measurement-based library allows the best prediction of the actual circuit behavior by means of taking all the parasitic parameters in components into consideration.

Because the input port of the circuit layout in Figure 4-34 needs to be connected to the CRLH unit cell's stub, its line width has to be same as that of the stub. However this creates difficulty in measuring the reflection coefficient using 50 Ohm based network analyzer. One of the best way to measure the circuit response is to connect to the circuit to the 50 Ohm system using microstrip line and then de-embed the connection line to obtain the circuit port response. The TRL (transmission-reflection-line) calibration feature in network analyzers is dedicated for this purpose. Such a design is shown in Figure 4-35.

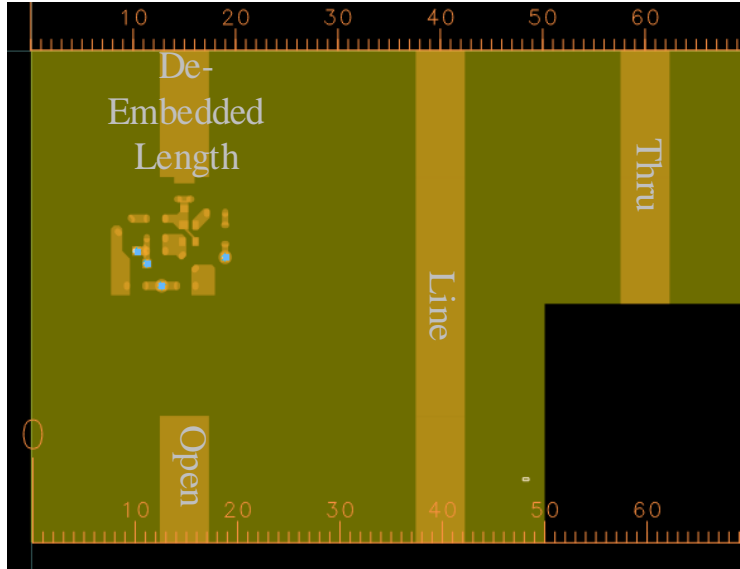


Figure 4-35 Layout design of the circuit with TRL calibration kit on the same board.

Now we have established simulation and measurement methodologies. In order to verify the results, the circuit will be fabricated and measured to compare with the simulation.

#### 4.4.5. Circuit Prototype

The circuit is then fabricated on a 62mil thick Rogers Duroid 5880 substrate with 1 oz. copper clad. Since highly accurate information of phase response is critical, the test equipment must run TRL calibration to de-embed the microstrip transmission line structure. The board on which the TRL calibration kit and the device under test (DUT) are printed is shown in Figure 4-36.

The measured one-port S-parameter is illustrated in Figure 4-37 and compared with the simulation results. The data obtained from the network analyzer are in the form of S-parameters. In the figure they are converted into input impedance curves. Satisfactory agreement can be found below 3 GHz, though the discrepancy in return-loss decibel curves starts to become greater around 2.8 GHz.



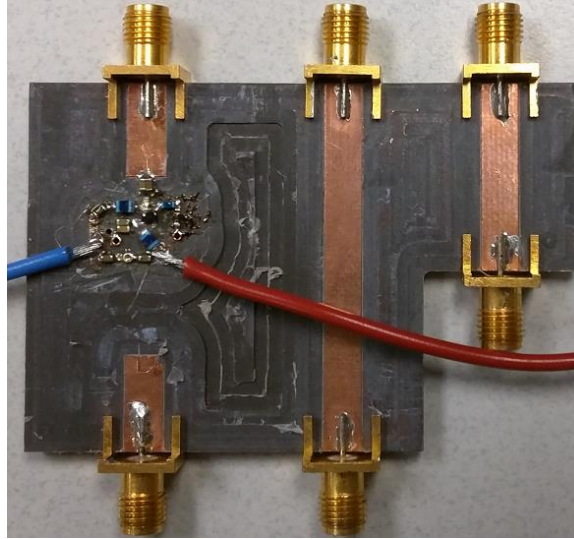


Figure 4-36 NR circuit board with TRL calibration kit built on the same board.

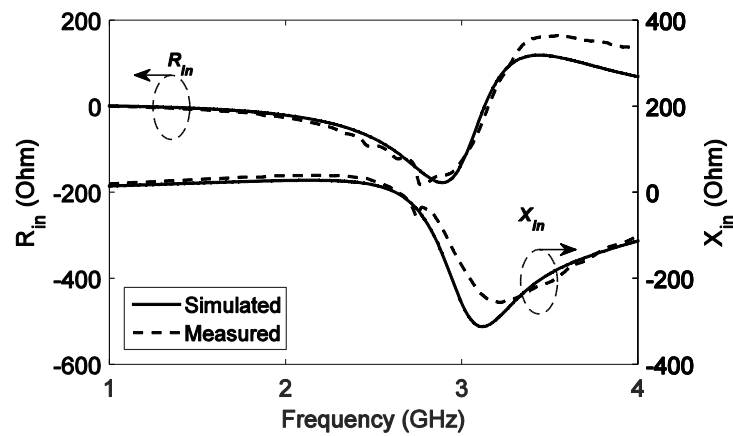


Figure 4-37 The simulated and measured NR circuit responses without the matching short-stub. The obtained reflection coefficients are converted to input impedance for the observation of negative resistance values.

In Figure 4-37, it can be seen that the example NR circuit response is inductive below about 2.7 GHz but becomes capacitive above 2.7 GHz. This transition is specific due to the part chosen and the biasing circuit designed. The capacitive response may affect the unit cell's phase behavior severely. In the unit cell evaluation, it was found that the NR circuit itself is difficult to be used solely to realize CRLH unit cell behaviors. Hence adding a matching shorted-stub helps to

maintain the unit cell's unique metamaterialistic phase behaviors. If the NR circuit response is pure inductive in the entire working frequency, then the matching stub may not be needed. The layout of the NR circuit with short stub is shown in Figure 4-38a), and the fabricated NR circuit with de-embedding line is shown in Figure 4-38b). The matching shorted-stub is between the wide de-embedding line and the junction to the NR circuit.

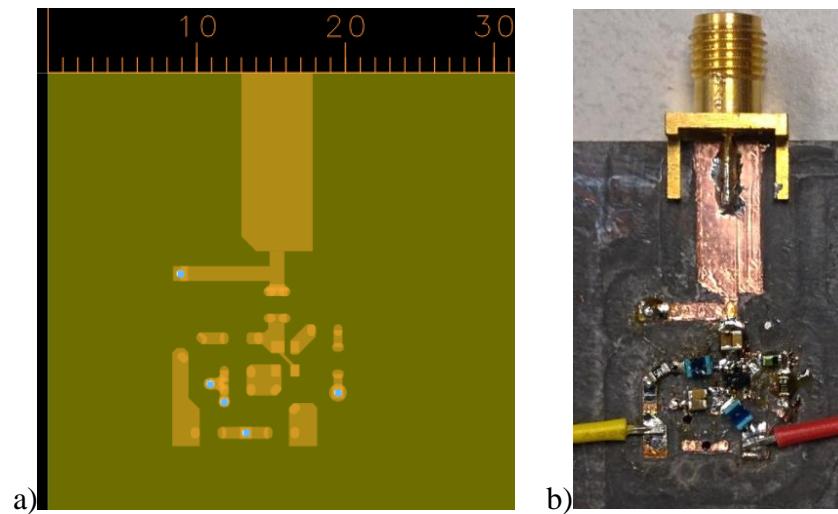


Figure 4-38 Layout design and the fabricated NR circuit with matching shorted-stub.

The measured results are shown in Figure 4-39 and compared with the simulated results. Two major differences between the results in Figure 4-37 and Figure 4-39 are as follows. First, the NR circuit with matching stub consistently exhibit inductive response in the entire simulation and measurement band. This guarantees the CRLH stub to produce inductive response for the unit cell. Secondly, the negative resistance values become controllable and is much smaller in magnitude than the circuit without the matching stub.

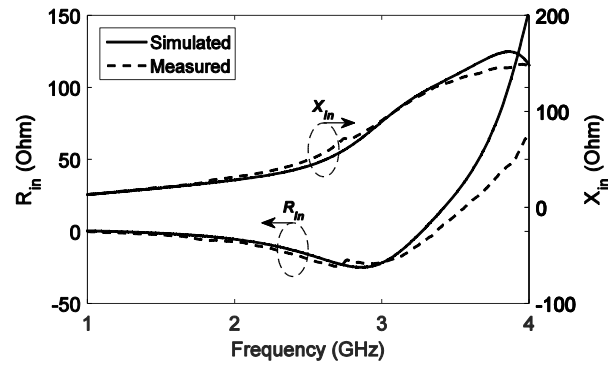


Figure 4-39 The simulated and measured NR circuit responses with the matching short-stub. The obtained reflection coefficients are converted to input impedance for the observation of negative resistance values.

With the circuit well studied thoroughly, it is ready to be combined with CRLH unit cell to realize NR-CRLH unit cell.

## 4.5. NR-CRLH Unit Cell

All the previous efforts that aimed to increase the forward energy propagation add amplification along the direction of wave guiding. The structures consisting of multiple unit cells had to be chopped to add series amplifying elements. In this Section, a novel NR-CLRH unit cell is detailed.

### 4.5.1. Short Stub Revisit

It is evident that adding amplification in series with the CRLH unit cells can interfere the CRLH structure's metamaterialistic phase behaviors. In this dissertation, we propose to incorporate energy compensation circuit at the terminating end of the unit cell stub as shown in Figure 4-40.

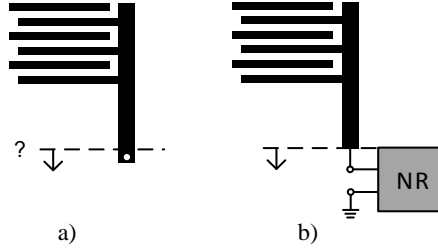


Figure 4-40 A normal CRLH unit cell in a) and an NR-CRLH unit cell in b).

The first question from the audience when a structure shown in Figure 4-40b) is presented is usually if (and how) the structure would work similarly to the passive one. Simulations, fabrication and measurements may be convincing but one can quickly do some derivations and calculations to verify the idea.

First we consider the approximate calculation that gives the left-handed inductance  $L_L$  of the passive unit cell as shown in Figure 4-40a). If we assume the via provides ideal grounding from the stub to ground, then effectively the impedance of the shorted-stub seen from the edge of the transmission line (or the IDC) is given by [5]

$$Z_{in} = Z_{stub} \frac{Z_t + jZ_{stub} \tan \beta_s l_s}{Z_{stub} + jZ_t \tan \beta_s l_s} = jZ_{stub} \tan \beta_s l_s \quad (4-47)$$

The  $Z_t$  represents the termination impedance of the short stub, which is in this ideal case to be zero.  $Z_{stub}$  denotes the characteristic impedance of the stub line, determined by the width and the substrate. The propagation constant of the stub line  $\beta_s$  multiplies the length of the stub  $l_s$  to become the phase delay on the stub. Then the effective left-handed inductance can be obtained from the imaginary part (which is the non-zero part in this case where  $Z_t = 0$ ) of the  $Z_{in}$  as follows.

$$L_L = Z_{stub} \frac{\tan \beta_s l_s}{\omega} \quad (4-48)$$

Because the shorted stub itself is just a piece of regular RH transmission line, the propagation constant and characteristic impedance are easily obtainable through calculations. It is common to adjust the  $l_s$  when tuning the unit cell into a balanced status [85]. The  $L_L$  obtained using the equation (4-48) is usually noticeably different from the simulation results as mentioned in former sections, considering that the via is usually not a perfect shoring path [111] and T-junction effects [112] varies the length of the stub. Nevertheless, it demonstrates the fundamental mechanism of producing effective left handed inductance.

#### 4.5.2. The NR Terminated Stub

To demonstrate the idea of incorporating NR, consider a non-zero  $Z_t$  in (4-47). Actually to be more precise, it is better to assume  $Z_t$  none zero which is common among via terminations [111]. A more accurate model that is used to analyze shorted-stubs uses the inductive model to incorporate the via impedance  $Z_t$  as follows.

$$Z_{t\_via} = R_{via} + j\omega L_{via} \quad (4-49)$$

The resistive part (real part) is given by

$$R_{via} = R_{dc} \sqrt{1 + \frac{f}{f_\delta}}, \quad f_\delta = \frac{1}{\pi \mu_0 \sigma t^2} \quad (4-50)$$

And the inductance is calculated from

$$L_{via} = \frac{\mu_0}{2\pi} \left[ h \cdot \ln \left( \frac{h + \sqrt{r^2 + h^2}}{r} \right) + \frac{3}{2} \left( r - \sqrt{r^2 + h^2} \right) \right] \quad (4-51)$$

The notations are as follows.  $R_{dc}$  represents the DC resistance of the via which can be calculated from the via dimensions and material conductivity  $\sigma$ . The notation  $t$  is the penetration

depth. The letter  $h$  is the thickness of the substrate, or the length of the via, and the letter  $r$  is the radius of the via. These equations are presented in [111].

Replacing  $Z_t$  with  $Z_{t\_via}$  the impedance of the via-shorter-stub  $Z_{in}$  can be calculated using (4-47). For broader generality and convenience to incorporate the negative resistance, we define the general terminated impedance as

$$Z_t = R_t + X_t. \quad (4-52)$$

If the termination impedance is normalized to the characteristic impedance of the stub  $Z_{stub}$  or  $Z_s$ , the normalized impedance is denoted as

$$z_t = Z_t / Z_s = r_t + x_t. \quad (4-53)$$

Using these notations, we can derive the input impedance (4-47) as follows (note that  $Z_{stub}$  disappears in the equation as the equation is normalized to  $Z_s$ )

$$z_{in} = r_{in} + x_{in} = \frac{r_t (1 + \tan^2 \beta l)}{(1 - x_t \tan \beta l)^2 + r_t^2 \tan^2 \beta l} + j \frac{[(1 - x_t \tan \beta l)(x_t + \tan \beta l) - r_t^2 \tan \beta l]}{(1 - x_t \tan \beta l)^2 + r_t^2 \tan^2 \beta l} \quad (4-54)$$

Interesting phenomena can be observed by manipulating the above equation. The real part of  $z_{in}$  can be simplified to

$$r_{in} \approx r_t (1 + \tan^2 \beta l) \quad (4-55)$$

when  $r_t$  is assumed much smaller in magnitude than  $Z_s$ , and  $x_t$  is assumed very small (or  $X_t \ll Z_s$ ). The assumption reflects the case when NR circuit response is very close to the response of an ideal negative resistor. The most inspiring fact is that, the resultant  $r_{in}$  which is the shunt loading of the transmission line caused by the stub is a negative value if  $r_t$  is negative, because its sign is the same

as  $r_t$ . With this said, the model of the CRLH can be changed to what the following section would present.

The imaginary part of  $z_{in}$  has to be greater than zero in order to preserve the shunt inductance  $L_L$  in CRLH model. If the  $x_t$  and the stub length  $l$  can be designed arbitrarily, it is best to have the shunt inductance  $x_{in}$  same as the reactance of a via-shortened stub, thus the phase response of the NR-CRLH unit cell can emulate that of a passive unit cell.

To quantitatively demonstrate the idea, the  $Z_s$  of the passive and active unit cell design both use 1 mm wide stub with short length. The  $Z_s$  can be easily found as  $112 \Omega$ . The length of the NR-terminated stub is restricted to be less than electrically  $\pi/4$ . Therefore the multiplication of  $r_t$  square and  $\tan\beta_s l$  can be considered as a small quantity in (4-54), consequently the requirement of a positive  $x_{in}$  can be met if the following condition is satisfied.

$$X_t < \frac{Z_s}{\tan \beta l} \quad (4-56)$$

Then the inductive response of the terminating NR circuit can be quickly checked using this condition.

These effects of the input impedance results due to stub and NR termination will be demonstrated in the ECM and calculations. Again, the generalized equation (4-54) can quickly compute the  $R_e$  and  $L_L$  values from a given stub and termination configuration, it qualifies to be used in evaluating the phase propagation of the modified structure.

### 4.5.3. Equivalent Circuit Model

From the previously derived equations, it can be justified that the following ECM model of a NR-CRLH unit cell with NR-terminated-stub can be used to evaluate the modal behaviors.

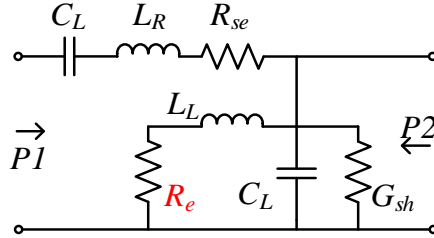


Figure 4-41 The equivalent circuit model of a NR-CRLH unit cell with NR-terminated stub.

Through examinations of the ECM behaviors, the novel unit cell behaviors can be predicted roughly. Moreover, the validity of the ECM also helps establish physical understanding of the active unit cell.

Basically the similar analyses and calculations compared with Section 4.2.6 through Section 4.2.8 will be done. Some of the benefit of using an NR-CRLH unit cell relies heavily on the similarity between the ECMs in Figure 4-41 and Figure 4-16.

The IDC of the active unit cell is the same as the passive cell. Thus the IDC simulation and parameter abstraction explained in Section 4.2.4 can still be used. The NR-terminated-stub cannot be simulated in a 3-D model, because full-wave simulators cannot handle active circuits and copper features at the same time (in the same model). Therefore, the unit cell simulation will be done in ADS schematic simulation, incorporating layout simulation and NR circuit components. This simulation will be detailed later.

In order to calculation the ECM network, we first redefine shunt admittance as follows.



$$Y_{sh} = G_{sh} + j\omega C_R + \frac{1}{R_e + j\omega L_L} = G_{sh} + \frac{j\omega C_R R_e - \omega^2 / \omega_{sh}^2}{R_e + j\omega L_L} \quad (4-57)$$

And the series impedance can take the same form as (4-21). The ABCD matrix defined for the passive network can also be used in this active model as well. Therefore, the propagation constant can be calculated using the same equation, too.

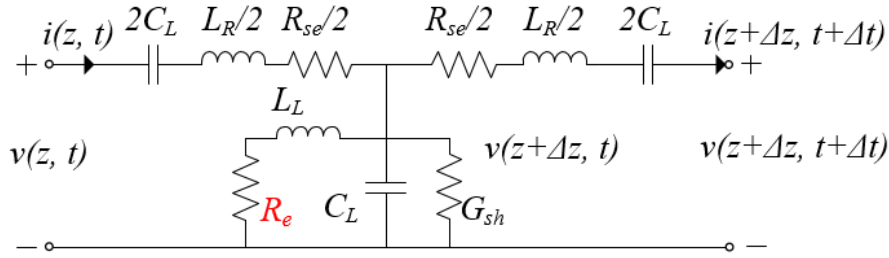


Figure 4-42 The symmetric ECM of an active NR-CRLH unit cell including lossy elements and possibly negative effective resistor  $R_e$ .

The symmetric active model adopts the passive model and add  $R_e$  as shown in Figure 4-42. With the  $Y_{sh}$  redefined in (4-57), the equations defined for the passive unit cell can be used also for this active unit cell, since all the equations are based on the  $Z_{se}$  and  $Y_{sh}$ , for symmetric or asymmetric structures. Notice that we use asymmetric equations for propagation and phase response, but symmetric equations for Bloch impedance and scattering parameter matrix calculations.

#### 4.5.4. Active ECM Calculation Example

It has been shown in Figure 4-41 and Figure 4-42 that the active unit cell (AUC) ECM differs from its passive version in that the AUC contains an effective resistor  $R_e$  in series with the shunt left-handed inductor  $L_L$ . The ECM entails  $R_{se}$  and  $G_{sh}$  to account for the low efficient leaky-wave radiation and they can close the band-gap for the passive unit cells.

In the calculated results of the following example, the components are all given constant values except for the effective resistor, whose value will be varied for the study of the unit-cell behaviors. The fixed values of the lumped components are  $C_R = 1.18$  pF,  $L_R = 2.9$  nH,  $C_L = 1.88$  pF,  $L_L = 4.6$  nH,  $R_{se} = 1.5 \Omega$  and  $G_{sh} = 10e-3$  S. The  $R_e$  values are set 0.5 Ohm, 0 Ohm, -3 Ohm, and an exponential function (denoted as Var Model). The exponential  $R_e$  values which was obtained to mimic the actual measured NR response are plotted in Figure 4-43. It will be shown later where the simulation and measurement are presented that the exponential curve is realistic and close to NR circuit response. Another ECM model that incorporates the realistic circuit measurement data will be presented later, too.

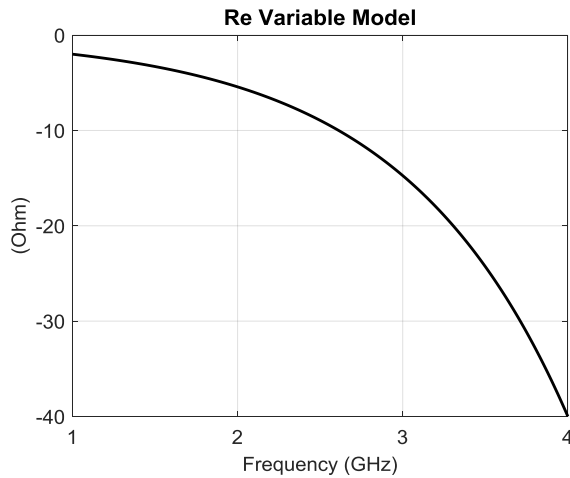


Figure 4-43 The exponential  $R_e$  model used in the ECM calculations.

The reactive component values are abstracted from the full wave simulations of the passive CRLH design to be compared with, utilizing the corrected equations described previously. The values of the resistive components that mainly account for the radiation losses are modeled such that the constant-radiation-rate condition is satisfied. However, it is worth pointing out that due to the nonlinearity of the involved transistor and its resultant effective resistance in the ECM, the constant-radiation-rate condition does not necessarily hold any more and the radiation rate will be

controllable. Once again, the ECM models are provided to demonstrate the concepts and to illuminate the physical insight of the artificial structures.

First, the return loss curves are plotted in Figure 4-44. When  $R_e$  is just slightly greater than zero, the return loss is just slightly different. However, when  $R_e$  reflects a negative resistor, the return loss curves are apparently different. The raised level of return loss is due to that the reflection type amplification would also cause extra power flowing backward. Potentially, if the number of active unit cell is large, the return loss might be too high, or even causing the system in an unstable status. However, for periodic structure, no unit cell is standing alone. The reversely reflected energy from one unit cell may cancel the reflection from another different unit cell which is a certain distance away from the first unit cell. Therefore, as long as the Bloch impedance, which shows the overall behaviors when multiple unit cells are cascaded in series, does not show negative resistance, the entire system should not be unstable.

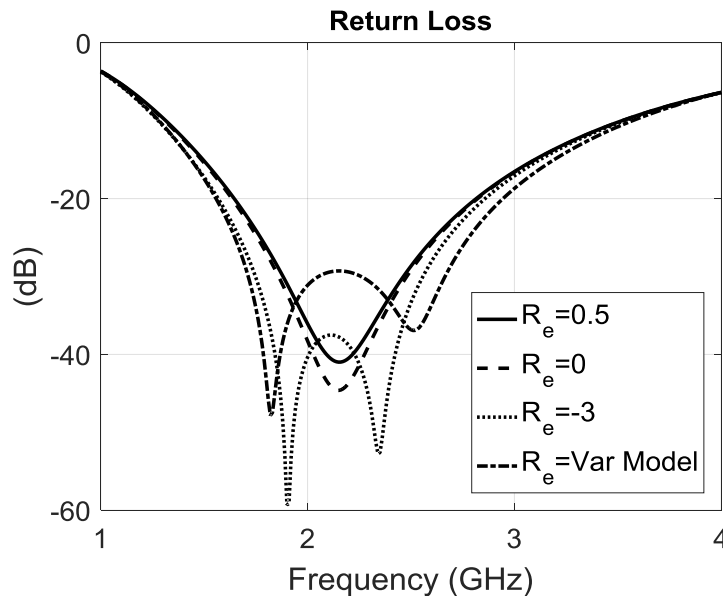


Figure 4-44 Return loss of the ECM model with different  $R_e$  values.

Secondly, the insertion loss curves are plotted in Figure 4-45. Apparently when  $R_e$  is greater than zero, the model becomes more lossy. When  $R_e$  is a negative value, the insertion gain is realized in certain frequency range. From the calculation equation (4-54), it is understood that the stub impedance is not a constant value but frequency dependent. The “Var Model” for  $R_e$  in the plots are designed to reflect the impedance of a NR terminated stub.

It has been found that for constant  $R_e$  models, the insertion gain at higher frequency range is not as high as at the lower frequency range. To conquer this problem, the  $R_e$  model is chosen exponentially as shown in Figure 4-43 such that the negative resistance is stronger at higher frequency but weaker at lower frequency. Thus it leads to a rather flat insertion gain curve in the working frequency band.

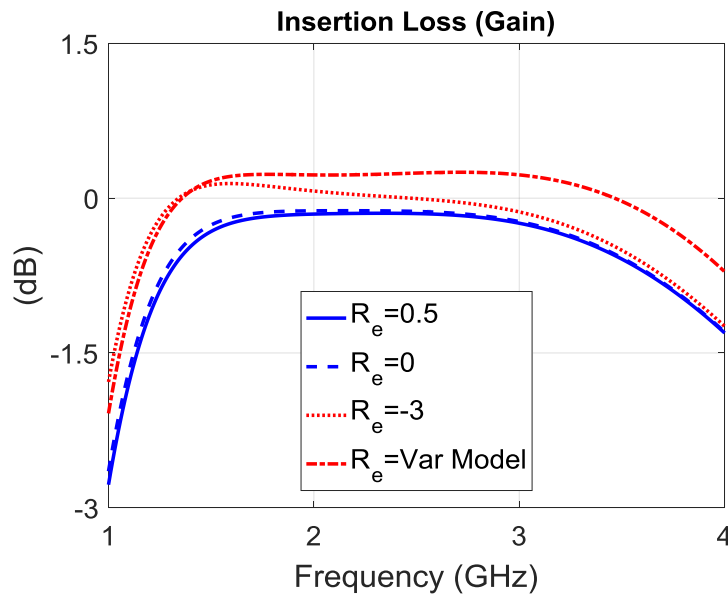


Figure 4-45 Insertion loss or gain of the four ECM models with different  $R_e$  values.

The unique phase properties of a metamaterialistic CRLH unit cell is preserved in a NR-CRLH unit cell. This can be seen in Figure 4-46 where the dispersion diagrams of the ECM models are shown. Notice that the four dispersion relation curves in Figure 4-46 are almost overlapping. This

is an evidence to confirm that the introduced  $R_e$  in the ECM would minimally affect the phase behavior. It is ascertained that the phase propagation of LH and RH regions are both preserved, although a very narrow band-gap is seen when the plot is zoomed in to the proximity of the transition frequency.

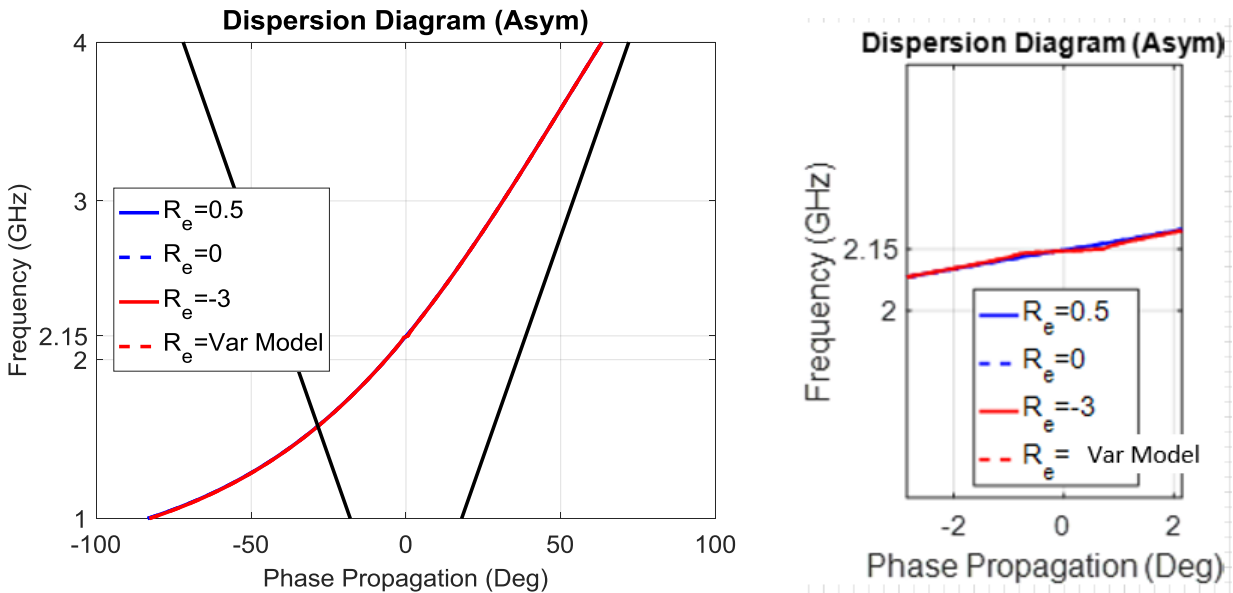


Figure 4-46 Dispersion relation curves of the ECM models with different  $R_e$  values. In the left figure the solid red curve and the dotted red curves are almost overlapping, and the difference can only be seen in the zoomed-in view (on the right) in proximity of the transition frequency on the right.

This similarity between the  $R_e = 0$  case and  $R_e < 0$  cases allows the mixed antenna or transmission line design containing both active and passive unit cells. In LWA applications, such mixed design would also be able to retain the beam scanning capability. This will be demonstrated in the next chapter.

Last but not least, the Bloch impedance of an active unit cell is plotted in Figure 4-47. It is noticed that for  $R_e < 0$  models, the Bloch impedance gap is shown slightly wider, but the measured

data from the fabricated prototype shown that the original performance was maintained. The imaginary part of the Bloch impedance are close to zero in most of the frequency band.

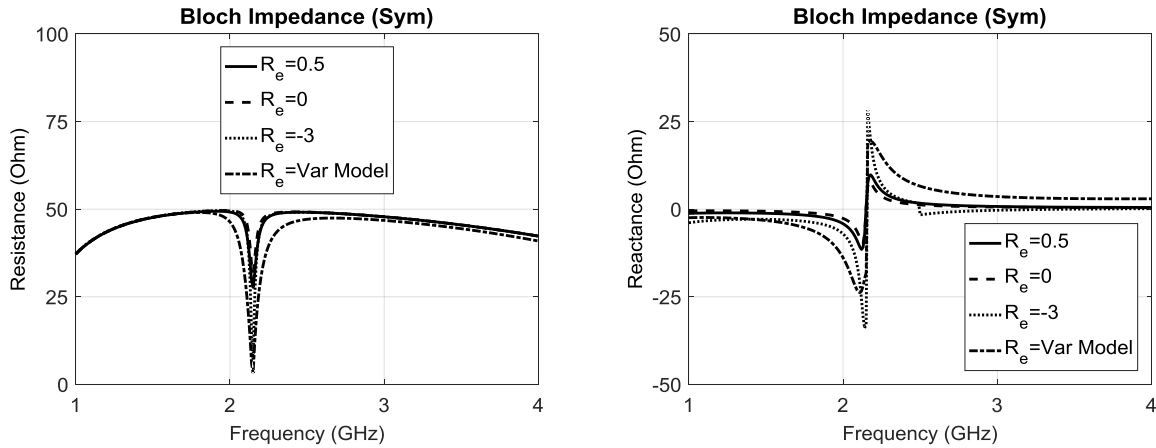


Figure 4-47 The real (resistance) and imaginary parts (reactance) of the Bloch impedance curves with different  $R_e$  values.

It is worth emphasizing that although negative resistance is incorporated in this model, the Bloch impedance does not present negative resistance corresponding to input/output instability.

#### 4.6. Simulation, Fabrication and Measurement

The presented ECM calculations have shown that incorporating a negative resistance in series with the left-handed inductance can maintain the metamaterialistic behaviors of a CRLH unit cell and is able to completely diminish the insertion loss, realizing insertion gain instead. In this section, the simulations and fabrications with measured results will be presented to further prove the idea.

#### 4.6.1. Simulation

The full-wave simulators cannot handle an entire circuit with passive layout and active circuits. There are circuit simulators that are able to analyze the models with known network parameters. We chose ADS post-layout simulation for this task.

From the equation used to evaluate  $R_e$  and  $L_L$  from the given termination impedance  $Z_t$  and stub length, it is clear that these two factors determine how the active unit cell should behave. Therefore the simulation can start with a port terminated stub which is relatively short, and combined the simulated model with circuit simulation through a transmission line in between. The port-terminated unit cell is shown in Figure 4-48, and the simulation topology is shown in Figure 4-49.

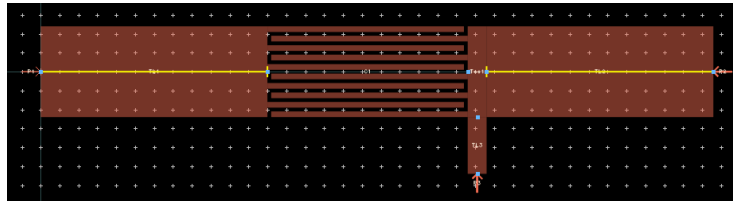


Figure 4-48 The unit cell layout simulation with the stub terminated with a port. In schematic simulation the stub end can be connected to a NR circuit through a piece of transmission line.

The NR circuit simulation has been detailed in the corresponding section. Here the necessity of the tuning/matching stub between the NR circuit and the passive layout simulation is explained as follows.

The chosen NR circuit based on BFG425W can realize negative resistance up to a high frequency sufficient to cover the entire working band of the unit cell. However, in order to make the NR circuit inductive in the same frequency range, an inductive shorted stub needs to be inserted. If a different transistor were used and it provide inductive response when the proper NR is achieved,

the inductive matching stub should be not necessary. It is also possible to have the matching shorted-stub is removed if other circuit and transistors are used, but it has been concluded through experiments and simulations that it is optimum to have the matching stub in this circuit and unit cell design.

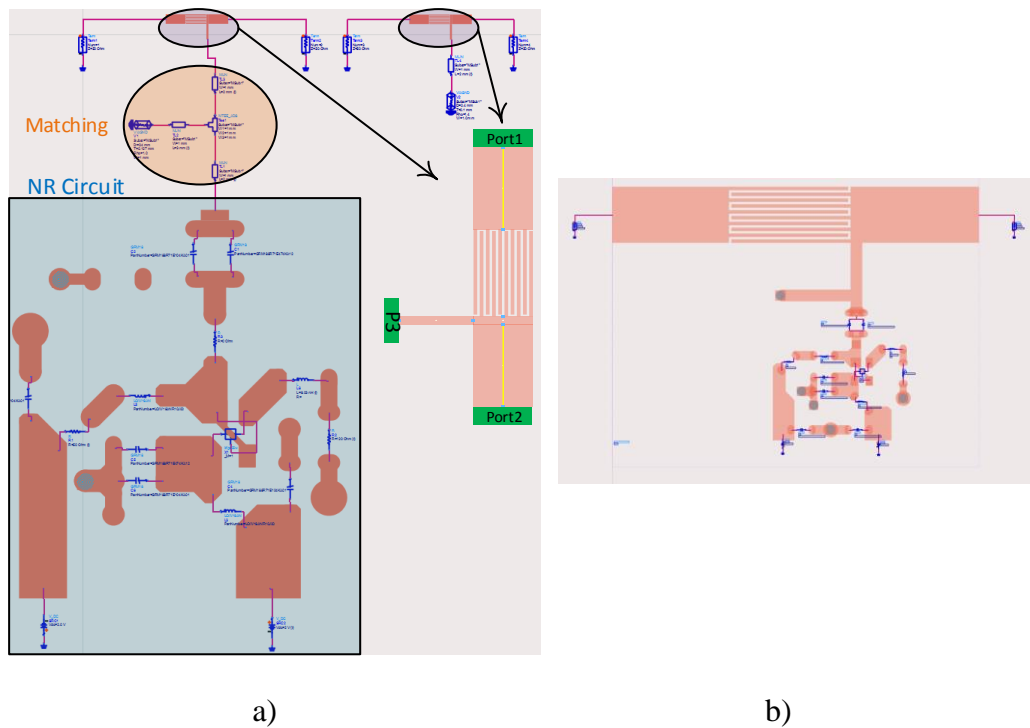


Figure 4-49 a) ADS schematic simulation incorporating the port-terminated unit cell, NR circuit simulation (post-layout) and the tuning/matching shorted stub in between. b) A schematic view of the post-layout simulation with complete copper features.

Notice that in the schematic simulation shown in Figure 4-49a), an active unit cell (on the left) and a passive unit cell (on the right) are put next to each other for comparison. The two simulations use the same unit cell layout with port-terminated stub. This is shown only to demonstrate that this port-terminated stub simulation can give accurate passive unit cell evaluation compared to the hundred percent layout simulation (usually a pure full-wave simulation).



The post layout simulation in a schematic design view can be found in Figure 4-49b). A complete unit cell copper layout simulation and its post-layout simulation diagram can be found in Figure 4-50a) and Figure 4-50b), respectively. A more illustrative diagram of the unit cell post layout simulation is shown in Figure 4-50b). This simulation is used when the matching stub and unit cell stub length are determined in schematic simulation. After all, the simulation containing all the layout would be considered more accurate.

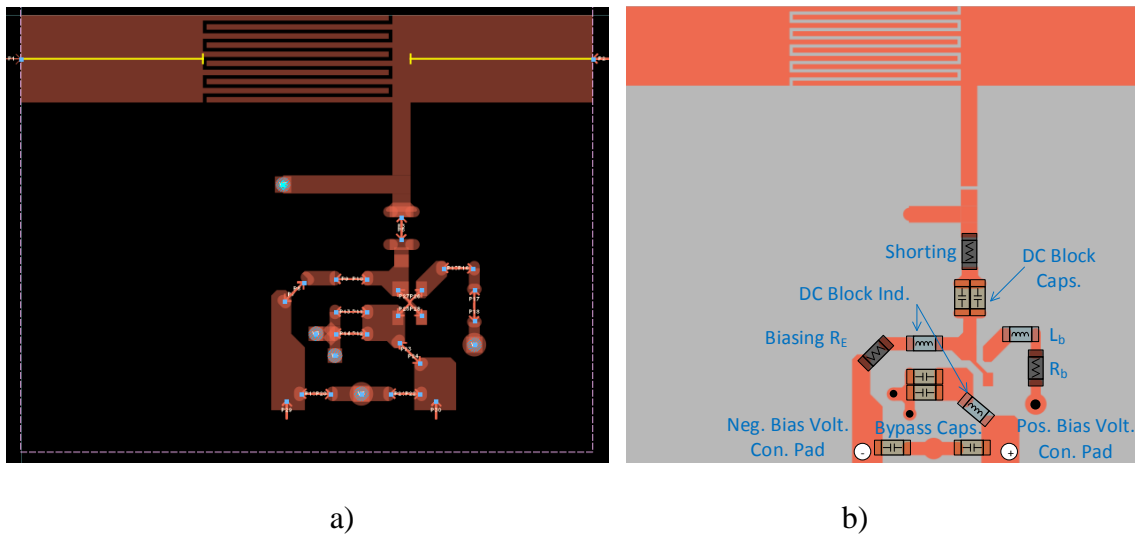


Figure 4-50 a) The layout simulation consists of all the unit cell copper features.  
 b) Diagram that demonstrates the post layout simulation of a complete NR-CRLH unit cell including the lumped elements and transistor.

The result of the above simulation method can be verified through fabrication and measurement.

#### 4.6.2. Fabrication and Measurement

An NR-CRLH unit cell is fabricated at Syracuse University Microwave Laboratory at CASE Center. The unit cell is built on 62 mil thick RO/Duroid 5880 substrate with 1 oz. copper cladding. A photo of the unit cell is shown in Figure 4-51.

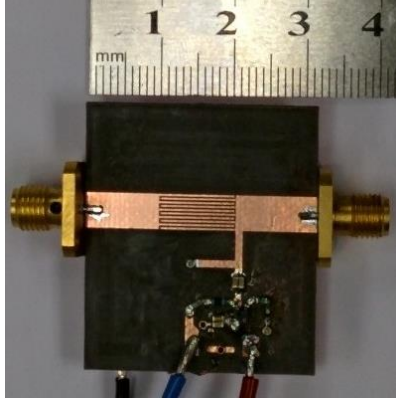


Figure 4-51 Photo of the fabricated NR-CRLH unit cell. The length of the unit cell is 11.4 mm, and the length of the entire board is 21.4 mm.

The unit cell is measured at Syracuse University Microwave Lab. The measured results are shown in Figure 4-52, with magnified view of the insertion gain from 1.8 GHz to 3.4 GHz. In the same figure the measured results and simulated results are presented simultaneously for comparison. The input and output transmission lines are de-embedded in schematic simulation. It can be seen that the simulation gives very accurate results that agree well with the measured results.

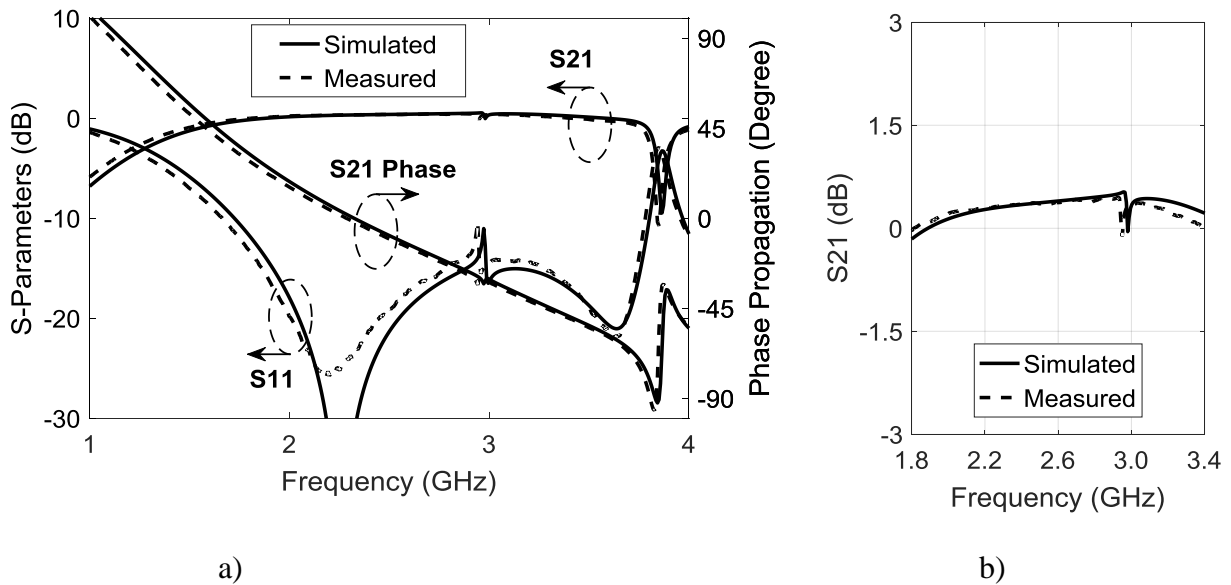


Figure 4-52 The measured and simulated results of the active unit cell. LH below 2.3 GHz. RH above 2.3 GHz. a) S parameters. b) Magnified zoom-in view of the insertion loss/gain.

Through comparison between the simulation and the fabrication and measurement results, we have demonstrated that an NR-CRLH unit cell can be designed using existing simulation techniques, and its behavior inherits the significant features of the metamaterialistic properties of a CRLH unit cell. In the following chapter, the active unit cell is incorporated in a LWA application to further demonstrate the consistency between the passive and active unit cells, and to demonstrate the usefulness of the energy compensation and controllable forward amplification.

#### **4.7. Summary**

In this chapter, the novel NR-CRLH structure is presented with analysis and experiments. The original CRLH structure is analyzed and presented with calculations and curves. It was shown that by adapting a new energy compensating mechanism incorporating the ICC NR circuit the active unit cell can simultaneously preserve the unique phase behaviors and consistent Bloch impedance in a broad bandwidth, while realizing down-to-zero insertion loss or even forward gain. Unit cell analysis and experimental results are provided to prove that the inserted negative resistance minimally perturbs the phase behaviors of the original passive unit cells and does not introduce stability issue. Physically, the novel power compensating mechanism does not prolong the length of each unit cell, therefore the amplification is not in series with the unit cells. Thus this energy compensating mechanism does not interrupt the tight periodicity of the original periodic structure.

## Chapter 5 NR-CRLH TL Based Leaky-Wave Antenna

In 2006, a comprehensive summary of the development of the metamaterial radiative structures was written [113], when the structures gained considerable interest in the microwave field. Various types of metamaterial antennas were discussed including single negative metamaterial antenna with one of permittivity or permeability as zero, double negative metamaterial antenna with both  $\epsilon$  and  $\mu$  being negative, and zero-index metamaterial radiation systems. Along with the conventional-material based antennas, the four types of realizations are depicted in Figure 5-1.

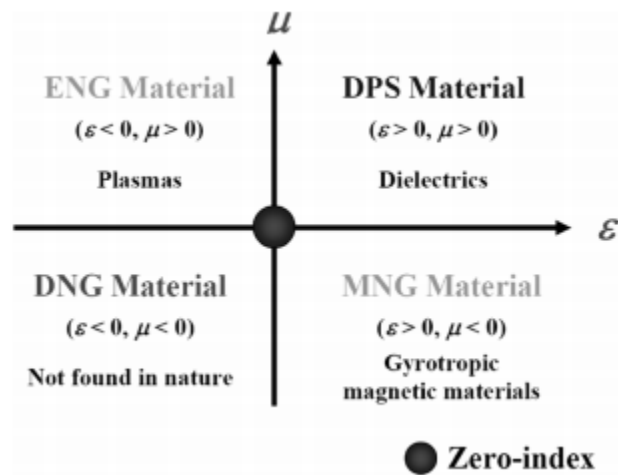


Figure 5-1 Duplicate of Fig. 1 in [113]. Classification of metamaterials by the real parts of their constitutive parameters,  $\epsilon$  and  $\mu$ .

More recent review and summary can be found in [114] which emphasizes more on planar CRLH and substrate integrated waveguide (SIW) based resonant antennas and leaky-wave antennas. A broad range of CRLH concept based antennas were discussed in [114].

Particularly, regarding the metamaterial leaky wave antenna, a closely related paper is written by Jackson *et al.* [81]. Recent leaky-wave antenna techniques including SIW LWA, CRLH LWAs, quarter-wave transformer LWA, and the ferrite LWA, etc., are discussed. The principle of beam

tilting, the range of beam tilting angle, system efficiency and many other design factors are summarized.

From the antenna synthesis theory, the desired antenna radiation pattern, or sometimes referred to as beam shaping, can be designed by controlling the current distribution along the antenna surface [115]. If the current amplitude distribution is controllable, then the antenna can be manipulated to deliver the desired radiation patterns. For example, as theoretically presented in [38], an LWA with uniform current distribution will generate maximum directivity for a given physical length.

In this chapter, a mixed antenna design (comprising of alternating AUC and PUC) will be to demonstrate the improved directivities within the operating band. Since the radiation performances of an LWA is physically determined by the length of the LWA, the measured radiation patterns of the mixed-design LWAs will be presented and compared with the passive LWAs of the same antenna lengths, consisting of the PUCs of exactly the same dimensions.

## **5.1. Leaky-Wave Antenna**

The class of leaky waves represents a very important and fundamental wave type [116]. LWAs have been studied since the 1940s when Hansen introduced the energy leaking cylindrical waveguide [81]. Then Oliner then paved the way to modern LWA applications [117].

LWAs are useful in the microwave bands and above [81] because they can achieve very high directivity and can be designed to give any desired radiation pattern without the need of a complicated and expensive feeding network as usually used in phased array.

Leaky-wave antennas are different from the resonant type antennas like patch antennas, dipole/monopole antennas, and loop antennas. The phase distributions over resonant type antennas are assumed to be constant. The sinusoidal current distribution of long open-ended linear antenna is a standing wave constructed by two waves of equal amplitude and 180 phase difference at the open end traveling in opposite directions along its length [118]. The current and voltage distributions on resonant-type antennas are similar to the standing wave patterns on open-ended transmission lines.

Antennas can also be designed with travelling wave patterns in current and voltage which is similar to the propagating pattern on infinitely long or properly terminated transmission lines. This type of antenna design can be realized by properly terminating the antenna wire so that the reflected wave is minimized [118]. In order to effectively utilize the entire antenna, usually the LWAs are designed such that only about 10% of the input power is terminated [119].

## 5.2. LWA Analysis

A conventional LWA can be considered as a terminated transmission line, and the leaky wave exists only when the guided wave travels faster than the speed of light. More realistically, the requirement is that the leaky wave must have greater phase velocity than the speed of light in free space, into which the leaking wave is radiated. Consequently, the propagating wave along +Z direction can be modeled as a traveling wave with a propagation constant  $\beta$  as follows.

$$A e^{-j\beta z} \tag{5-1}$$

The coefficient A might not necessarily be real. A complex coefficient A contains the excitation phase information as well as the magnitude. A complex valued functional A (a function of location  $z$ ) describes the propagating wave in a physically practical way. Considering that the

propagation wave continuously leaks energy as radiation, the current amplitude must attenuate as the physics law of energy conservation requires. Thus a more practical formulation is given by

$$A_0 e^{-j\beta_d z} e^{-\alpha z}, \quad (5-2)$$

where  $A_0$  is the excited amplitude at the LWA input, and then the direction of the main beam can be estimated through calculations using the integral equation using the travelling wave [115]. Therefore, in tailoring LWAs, it all comes down to achieving the desired phase constant and attenuation constant.

The main beam direction of the LWA is primarily determined by the relation between  $\beta$  and free-space wavenumber  $k_0$  as follows.

$$\theta_0 = \arccos\left(\frac{\beta}{k_0}\right) \quad (5-3)$$

The beam angle  $\theta_0$  is defined as the angle between the broadside direction and the beam direction. This approximate direction was first summarized in [117] and [120], where the complementary angle of  $\theta_0$  denoted by  $\Phi$  is defined in the figure below, i. e.,  $\theta_0 = 90^\circ - \Phi$ .

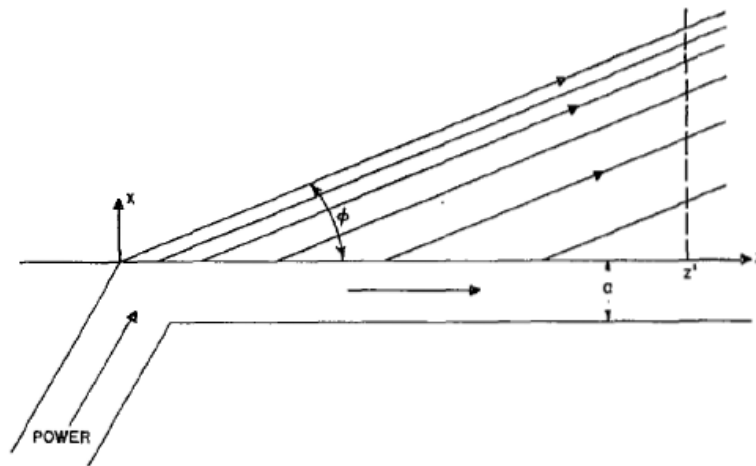


Figure 5-2 The direction of the main beam of a leaky wave antenna [117]. The beam angle  $\Phi$  is defined as the complementary angle of  $\theta_0$  here.

### 5.2.1. Travelling Wave Antenna

Stutzman and Thiele describes a kind of travelling-wave antenna that works similarly to a leaky-wave antenna [115]. A picture that illustrates the travelling wave antenna is given in the following figure.

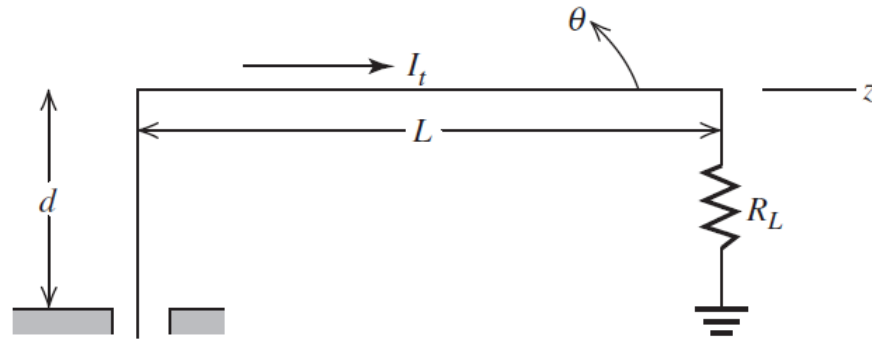


Figure 5-3 Duplicate of Figure 7-2 in Stutzman and Thiele's antenna textbook [115], demonstrating the travelling wave antenna.

The travelling wave antenna is only a long conducting wire fed from one terminal and terminated properly at the other terminal. The reflected wave from the termination side is minimized such that on the conducting wire only the forward wave is present. This distinguishes the travelling wave antenna from the resonant antennas which must have standing wave formed from both forward propagating wave and the reflected backward wave.

The propagating wave along the antenna's longitudinal direction is assumed to be of the same phase constant as free space. The equality relation determines that the radiation pattern must be end-fire pattern. From a line source with arbitrary current pattern, the radiation calculation can be calculated from the integral equation given by [115]

$$f(\theta) = \int_{-L/2}^{L/2} I(z') e^{j\beta z' \cos \theta} dz' \quad (5-4)$$



Assuming the lossless current distribution in the form of (5-1) the radiation pattern equation can be obtained as [115]

$$F(\theta) = K \sin \theta \frac{\sin \left[ (\beta L / 2)(1 - \cos \theta) \right]}{(\beta L / 2)(1 - \cos \theta)}, \quad (5-5)$$

where K is a normalization coefficient dependent on the length of the antenna L. Note that the angle  $\theta$  in (5-4) and (5-5) is not the regular elevation angle in a Cartesian coordinate system but defined in Figure 5-3. From the pattern equation, we can see apparently that the radiation pattern and beam angle are determined by the antenna physical length L.

As previously mentioned, a more practical current distribution function is given in (5-2) with the attenuation due to radiation and material loss accounted for. Consequently, the radiation pattern we used in the integral equation must be changed accordingly. After mathematical manipulation, the pattern function can be found as

$$F_{\alpha}(\theta) = K \sin \theta \frac{\sinh \left[ \alpha L / 2 + (j\beta L / 2)(1 - \cos \theta) \right]}{\alpha L / 2 + (j\beta L / 2)(1 - \cos \theta)} \quad (5-6)$$

The above derived equation can be used to evaluate the effect of the attenuation along the propagating path, although the wire travelling wave antenna is not exactly same as the planar LWAs like CRLH LWA and microstrip LWAs. One may find more similarity between the Beverage antenna and the planar LWAs, however the comparison is not detailed in this work.

### ***5.2.2. Arbitrary Decaying Current Distribution***

Previous calculations assume that the current distributions are either constant in magnitude or decaying exponentially. The resultant radiation patterns are also of the limited styles because amplifying or increasing current distribution is not realizable.

A traveling wave antenna can be designed to give a desired amplitude distribution by realizing current distribution varies with distance away from the excitation (along the propagation path). An example of controlling the side lobe level by tuning  $\alpha$  is given in 1953 by Hines, Rumsey and Walter [121], where the waveguide slot is curved to approximately form a Gaussian amplitude distribution. The artificially shaped slot in a rectangular waveguide is shown in Figure 5-4.

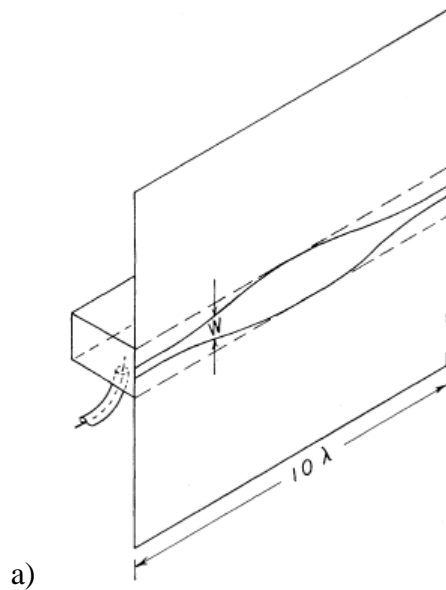


Figure 5-4 Duplicated Fig. 15 in [121]. The slot is engineered to obtain a Gaussian amplitude distribution along the propagation of the slotted waveguide.

Along the guided travelling path, the slot size is first gradually opened wider and then gradually shrinks. It is assumed that the wider slot would cause the leaky wave radiate more power than narrower slots, thus the guided wave amplitude attenuate faster in the middle of the entire slot and attenuate slower when closer to the beginning and end terminals. If this position-dependent attenuation is characterized mathematically, a Gaussian distribution would be assumed to be proper as follows.

$$\frac{1}{\sigma\sqrt{2\pi}} e^{-\left(\frac{z}{\sigma}\right)^2} \quad (5-7)$$

The mean value of the Gaussian distribution function is set to be zero, because physically once the excited wave starts propagating and leaking down the guided leaky path, the magnitude can only decrease. Thus the maximum magnitude can only occur at the origin of the Z axis (or z') where the leaky path is excited. The Gaussian distribution's variation denoted by  $\sigma$  is supposed to be dependent on the position and length of the wide slot and the total length of the leaky wave guide.

The resultant equivalent magnetic current source over the slot when TE mode is excited generates radiated beams of minimum side lobes as shown in Figure 5-5b).

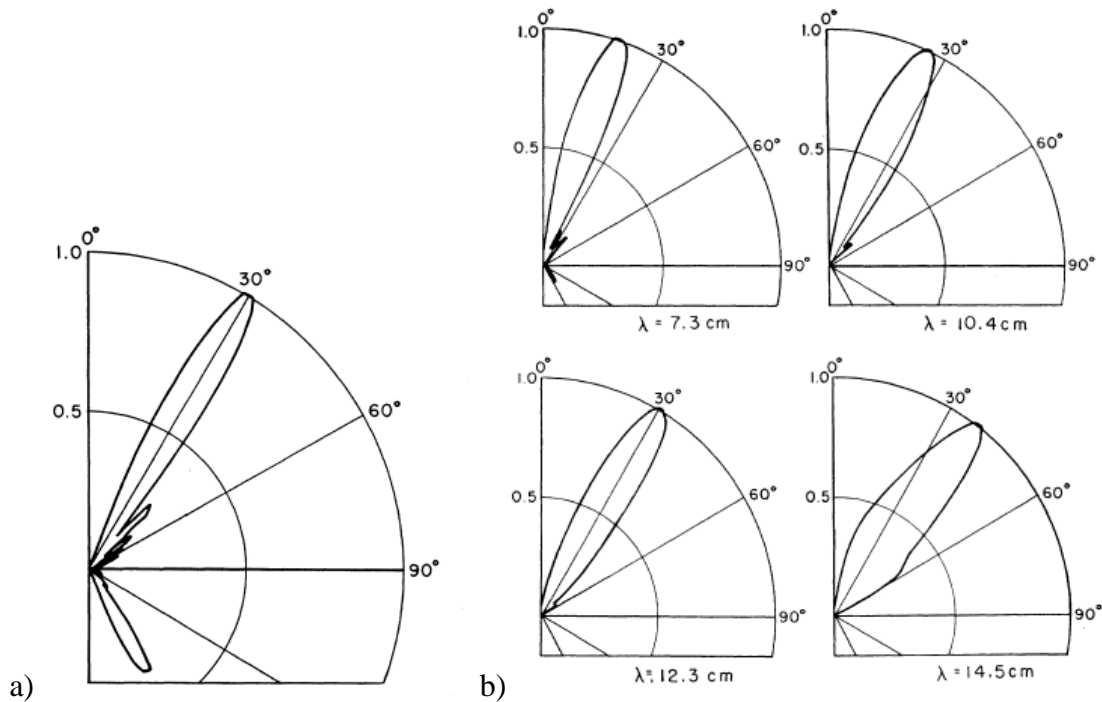


Figure 5-5 Radiation patterns of the LWAs in [121]. a) The radiation pattern of a uniform slot. b) The radiation pattern at different frequencies of an iris slot.

The patterns shown in Figure 5-5 show that the radiation patterns from a Gaussian current amplitude distribution contain zero side-lobe, although the length of the antenna varies. Another example that is pertinent to this work is the long wire travelling wave antenna. Using the integral equations in [115] and [118], the calculated radiation patterns for a long traveling-wave antenna that electrically extends three wavelength long are plotted in Fig. 9 in [38]. It clearly shows that the increased attenuation constant widens the beamwidth thus lowers the directivity.

### 5.3. CRLH LWA

Aside from the RWG slot LWA, the microstrip LWA was developed because of easy fabrication and convenient integration into the rest of the system on printed circuit boards. In 1978, Menzel introduced a microstrip line LWA and showed its application in a 4 element LWA array [122]. The microstrip LWA was shown to tilt the main beam forward (toward the direction of guided wave propagation from the normal direction). The level of interest and the pace of development in this field have recently accelerated significantly partly due to the surge of interest in metamaterials [81] [70]. The similarity between SIW and conventional RWG also intrigued the considerable study on CRLH SIW based LWAs [114].

The CRLH transmission line was first proposed to be used as LWA by Liu *et al.* in [26]. The relation between the propagation constant and the radiating main beam was demonstrated in the figure reproduced below.

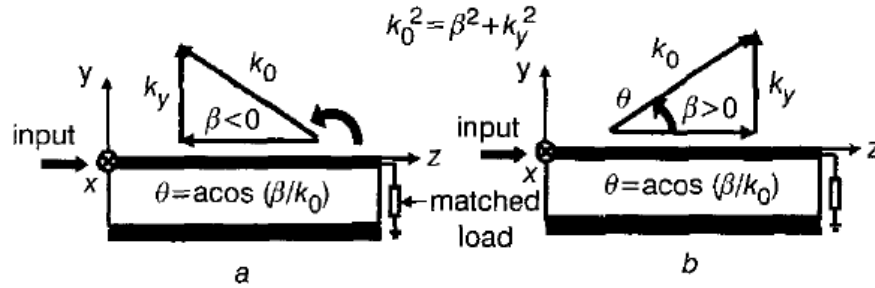


Figure 5-6 Duplicate of Fig. 1 in [26] describing the relation between radiation and propagation constant. In the cross-section view the wave number is decomposed into the direction of guided wave and the direction of the substrate thickness ( $k_y$ ).

A conventional multiple-unit-cell long CRLH LWA is a terminated periodic structure made of identical passive unit cells that behave nearly identically [85], thus the phase propagation across each unit-cell can be assumed to be consistent. Consequently the propagating wave can be modeled as a traveling wave with a propagation constant  $\beta$ . The main beam direction of the LWA is primarily determined by the relation between  $\beta$  and free-space wavenumber  $k_0$  by

$$\theta_0 = \arccos\left(\frac{\beta_d}{k_0}\right) \quad (5-8)$$

Equation (5-8) differs from (5-3) by using a different propagation constant  $\beta_d$ . The subscript d indicate the length of each unit cell of the periodic structure. The same notation is used with the attenuation constant as well.

Presented in Figure 5-7 is an LWA prototype made of CRLH unit cells at Syracuse University Microwave Laboratory. The unit cells have been introduced in the previous chapter. This particular antenna consists 11 symmetric unit cells, including 11 shorted stubs and 12 inter-digital capacitors. The total physical length of the antenna is 129 mm excluding the input/output transmission line for SMA connector junctions.

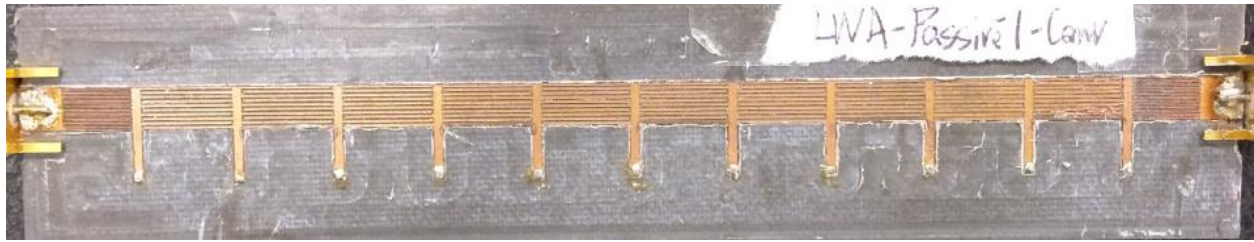


Figure 5-7 Figure of the LWA with conventional dimensions as described in Chapter 4. The LWA presented in this figure is denoted as LWA-1.

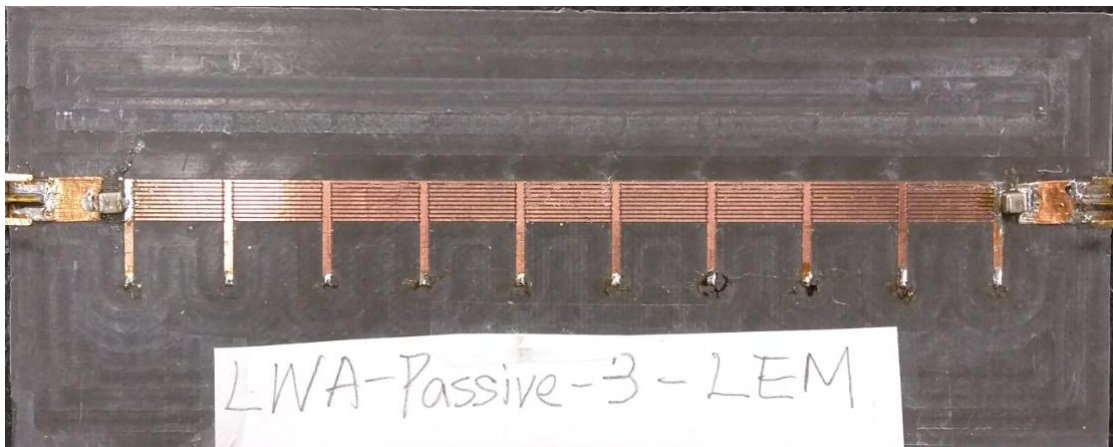


Figure 5-8 Photo of the LWA with optimized dimensions for consistent radiation performance and lumped element matching capacitor.

### 5.3.1. Simulated Radiation Performances

The radiation of a CRLH can be simulated using full-wave electromagnetic simulation software. A simulation model in HFSS is shown in Figure 5-9. The antenna is modeled on the RO/Duroid5880 substrate which is 62 mil thick with 1 Oz copper (0.7mil copper layer thickness).

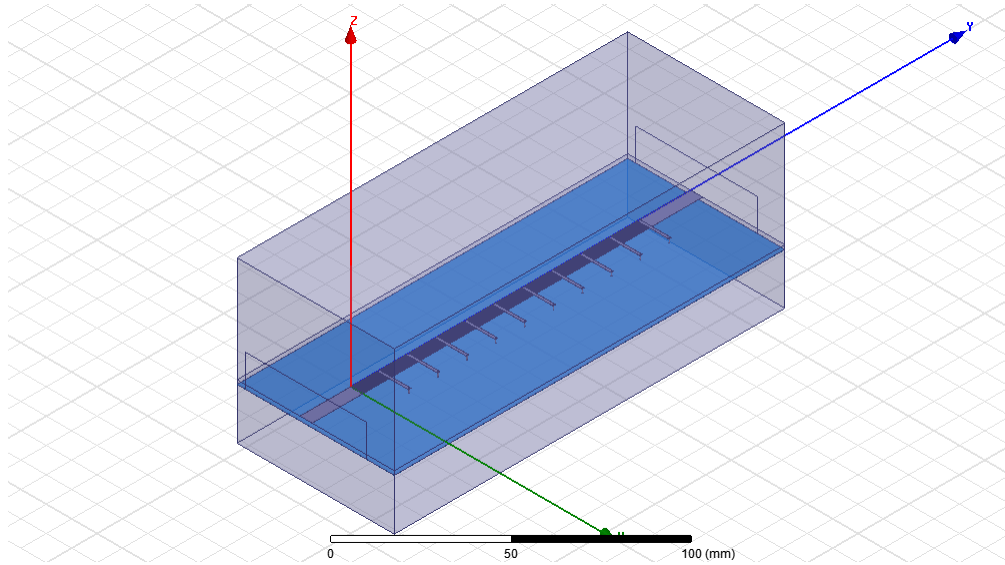


Figure 5-9 HFSS model of a CRLH LWA consists of 11 unit cells. The positive Y direction is toward the right side of the structure. Port-1 is on the left side of the structure ( $y=0$ ).

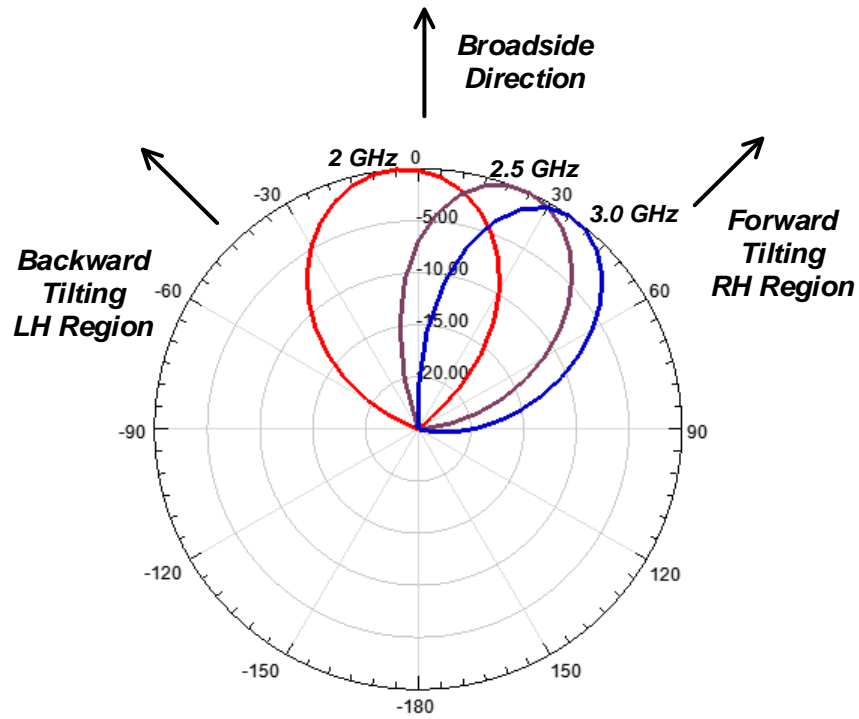


Figure 5-10 Simulation LWA radiation pattern in E- plane co-polarization.

The antenna is excited from port-1 (left terminal) with 1 W input power. The simulated radiation patterns at different frequencies are plotted in the following figures. At each sampled frequency (2 GHz, 2.5 GHz and 3.0 GHz), the E-plane co-pol patterns are plotted in Figure 5-10 in the normalized scale for pattern comparison.

### 5.3.2. Effect of Loss

Instead of simulations, we can calculate the radiation patterns using the previously introduced equations. Modelling the current distribution as (5-2) and using the integral equation, we can estimate the radiation patterns of a continuous current source once the approximate values of propagation constant and attenuation constants are obtained. We have known that the propagation constant is critical in main-beam direction. The effect of attenuation constant has less general effect whereas more specific and different from case to case. Here we present an ideal case where the propagation constant is fixed while the  $\alpha$  is a variable. Four values of  $\alpha$  are used in calculations to demonstrate the effect of loss in Figure 5-11.

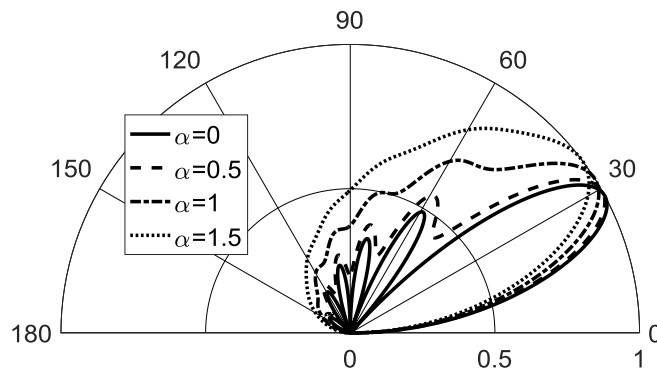


Figure 5-11 Theoretically calculated radiation pattern of multiple current distributions characterized by different attenuation constants.



In the figure above, apparently the beamwidth is obviously widen because of the higher level of loss. Thus the resultant antenna would has smaller gain (and generally less directivity) in the main beam direction and degraded spatial resolution.

### 5.3.3. Array Method

Alternatively, the relation between current distribution and radiation pattern can be predicted using the array factor, particularly for periodic structures [123]. In the array factor method, the periodic structure is treated as an array and each unit-cell is thus a radiating element. Oftentimes actual array elements are physically separated by certain distance and excited at the same magnitude by feeding networks. Conversely, the unit cells of a CRLH LWA are contiguous and excited by the wave propagating along the guided path. The phase difference between adjacent two unit cells are determined by the propagation constant  $\beta d$ , and the magnitude difference between them are determined by the attenuation constant  $\alpha$ . The excitation signals at the  $n$ th unit cell can be obtained from the traveling wave expression as follows [123].

$$I_{\alpha}(n) = I_0 e^{-j\beta_d(n-1)d} e^{-\alpha_d(n-1)d}, \quad n = 1, 2, 3 \dots \quad (5-9)$$

The magnitude term  $I_0$  is the excitation current amplitude at the LWA input. If the antenna is properly terminated at the termination port, the relation between the excitation voltage and current are related by the following relation.

$$I_0 = \frac{V_0}{Z_c} \quad (5-10)$$

The notation  $Z_c$  represents the characteristic impedance of the transmission line that is used as LWA. For periodic structures, the characteristic impedance is taken as the Bloch impedance. If  $Z_c$

is different from the source impedance which is usually the characteristic impedance  $Z_0$  of the feeding transmission line (50 Ohm), tapering from  $Z_c$  to  $Z_0$  is usually practical.

In (5-9), the two natural exponential terms approximately describe the guided and leaky wave propagating along the LWA. The propagation constant  $\beta$  is the same as the  $\beta_d$  used in (5-3), and the term  $e^{-j\beta(n-1)d}$  represents the incident wave at the  $n$ th unit cell. The attenuation constant  $\alpha$ , or interchangeable with  $\alpha_d$ , represents the attenuation before the propagation wave reaches the  $n$ th unit cell, and with  $I_0$  they determine the magnitude of the excitation at the  $n$ th unit cell or array element if the LWA is treated as an array. Note that the periodic structure can be treated as an array of radiating elements because each unit cell behaves the same, hence the total radiated pattern can be calculated from the multiplication of the unit cell radiation pattern and the array factor. The array factor of a CRLH LWA is given by [115]

$$AF(\theta) = \sum_{n=1}^N I_{\alpha}(n) e^{j(n-1)k_0 d \cos(\theta)} \quad (5-11)$$

Assuming the same PUC as in Figure 5-7, the calculated results of a 51-unit-cell long CRLH LWA are shown in the following figure.

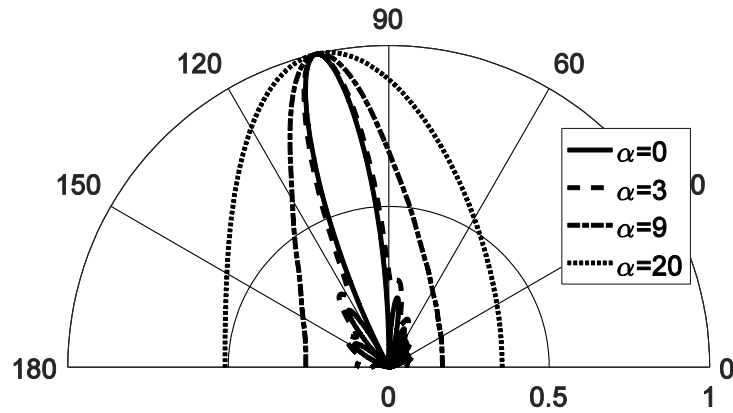


Figure 5-12 Calculated radiation patterns of a periodic structure LWA consisted of fifty one unit cells, yet the electrical length is less than  $\lambda$ . The antenna is assigned with different attenuation constants. The antenna is assumed lying along the bottom horizontal line and the wave is excited to travel toward right side (0 degree). Same as the proposed prototype, at 2.1GHz the main beam tilts backward and the phase constant is approximately -10 Radian/m.

Figure 5-12 illustrates the increased beamwidth due to higher attenuation. It is worth mentioning that the number of unit cells affects the beamwidth. An LWA of more unit cells would show equally great change of beamwidth with less variance of  $\alpha$ .

To this point, the relation between the current distribution and radiation patterns is established. In [38], the authors demonstrated the improved directivity using the unidirectional amplifier to compensate for the power loss. However, radiation patterns at the frequency points other than the broadside radiation frequency are not presented. This is due to the extra phase shift across the inter-section connections and the amplifiers. The applications of long LWAs or TLs using the AUC introduced in tunnel-diode based CRLH [33] have not been presented. This may be due to the differences between the behaviors of an AUC and its counterpart PUC and the greater-than-0dB return loss at the input port that can cause serious stability issue.

## 5.4. Mixed Design

Theoretically, since the Bloch impedance and dispersion relation of an NR-CRLH unit cell show desired behaviors, it is feasible to design an LWA consisting of only the NR-CRLH unit cells. By tuning the active NR circuits, it is possible to design an LWA of arbitrary current distribution. Examples of LWA with all the unit cell having the same forward gain or forward loss is illustrated in Figure 5-13. At the termination of the LWAs, the one having only active unit cells may terminate more powers than excited ( $V_t > V_i$ ) since the current flows toward termination and is amplified across each active unit cell. Whereas, the one that has only passive unit cells must have termination voltage lower than the excitation voltage ( $V_d < V_i$ ). Therefore the power terminated at the termination is greater than the power excited at the input port when AUC is used. The leaky-wave radiation occurs while the wave propagates along the guided transmission line.

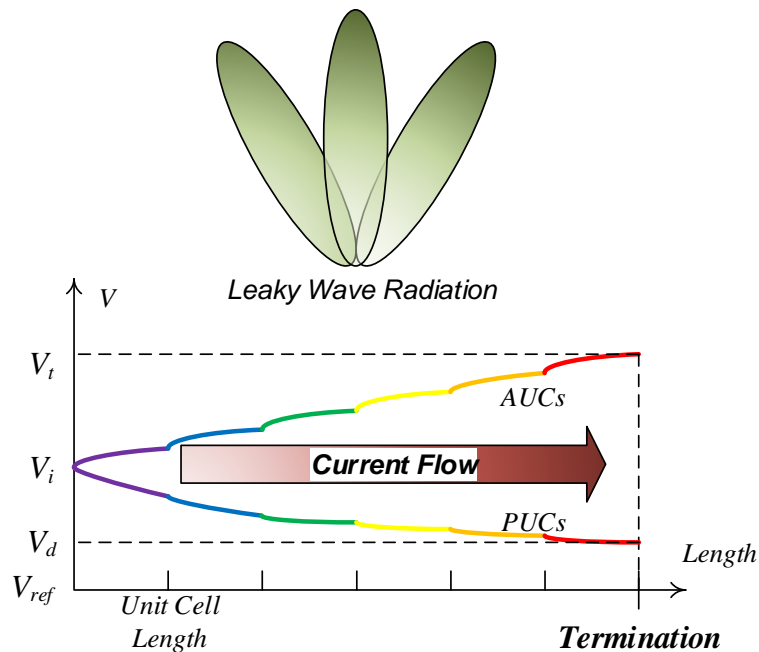


Figure 5-13 An example of LWA with all the unit cells having the same forward gain. The input to termination gain is realized thus the increasing ramp of current distribution.

The similarity between the passive antenna and its active counterpart makes the mixing of the two types of unit cells practical. The overall phase propagation behaviors and thus the radiation patterns of a passive LWA and an LWA with active cells are comparable only if the unit cell behaviors are similar. It is also worth noting that the active unit cell can be designed independently if desired, not having to preserve the same phase propagation constant as the passive counterpart. A figure that illustrates the current amplitude along a mixed LWA is shown in Figure 5-14. In the demonstrated case, the current amplitude fluctuates as the wave travels through active unit cells and passive unit cells, but overall maintains a flat current distribution. It has been shown in the calculations that a flat current distribution along propagation produces the highest directivity and narrowest beamwidth, but increased level of side lobes.

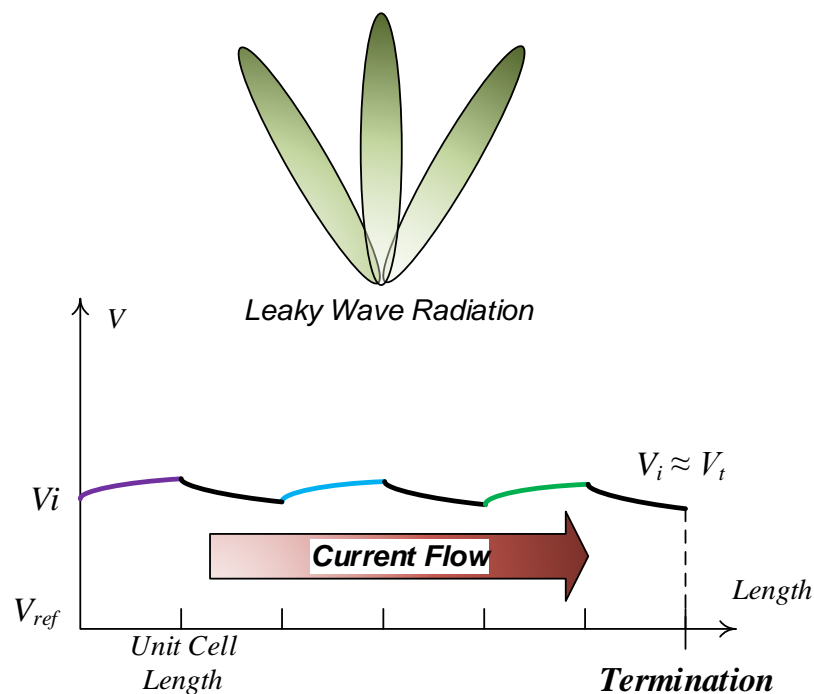


Figure 5-14 An example of LWA with alternative passive unit cell and active unit cell. The unit cells having the same forward gain. The antenna has narrower beamwidth.

The ECM diagram or schematic that demonstrates the mixed antenna design is shown in Figure 5-15. The ABCD matrices describe the passive unit-cell behaviors, while the primed ABCD matrices describe the active unit-cell behaviors. Another perspective that helps understanding the functionality of a mixed antenna is that the combination of a passive unit cell and an active unit cell form a new unit cell, which is about double the phase propagation of a single unit cell (either active or passive one). This new combinational unit cell has unit forward gain, or 0dB, if the negative resistance is adjusted such that the total lost power is just compensated. Such a unit cell possesses the similar propagation constant as a pure passive LWA, thus the radiation directions of the two are almost the same.

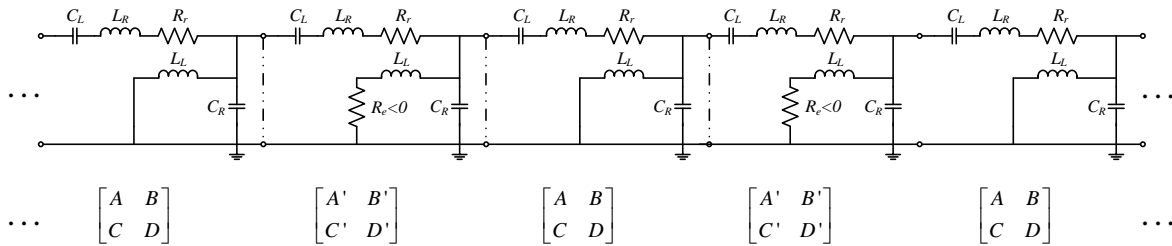


Figure 5-15 A diagram of the LWA containing both active unit cells and passive unit cells in the alternating fashion.

In sum, through the demonstration of the beam-tilting from the LWA consisted of the passive and active unit cells, it can be effectively shown that the active unit cell has the similar phase propagation behavior as the passive one. The observation of beam-tilting is a direct evidence of the unique phase behaviors of this metamaterial transmission line. The return loss at the LWA input port can serve as a proof of matched Bloch impedance.

### 5.4.1. An 11-Unit-Cell Design Example

A photo of the passive and the active LWAs is shown in Figure 5-16. The left side terminal or SMA connector is labeled as Port-1, and the other SMA connector which is terminated by a wideband 50 Ohm RF terminator is labeled as Port-2. The LWA consists of 10 asymmetric unit cells, but with the added matching IDC and the corresponding shorted stub. Equivalently, the antenna is consisted of 11 symmetric unit cells, four out of which are active ones. This design has all the four NR ICC circuits biased at the same voltage level, therefore each active unit cell behaves same as all other three ones.

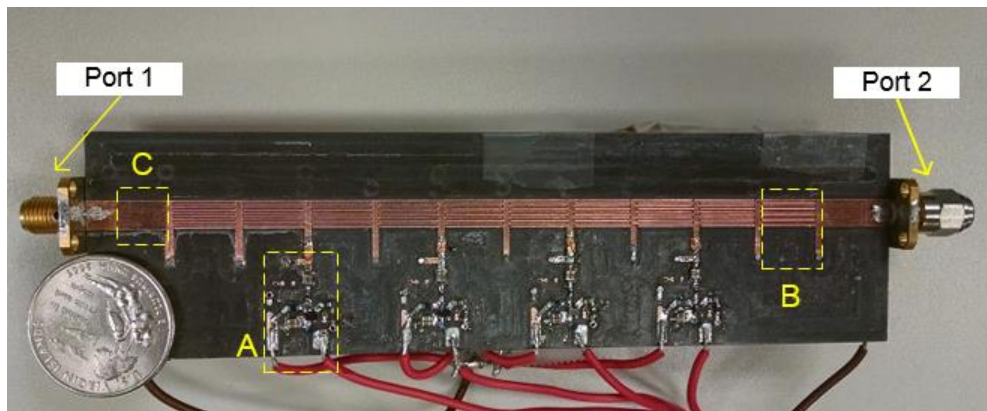


Figure 5-16 Photo of the fabricated mixed-design LWA with active unit cells and passive unit cells. Rectangle-A (dashed line) shows the ICC NR circuit; rectangular-B (dashed line) shows a normal unit cell; rectangle-C (dashed line) encloses a matching IDC which makes the periodic structure a symmetric structure.

The antenna was also measured using a spectrum analyzer connected to the indicated input port (Port 1). This measurement shows no oscillation occurs although multiple NR circuit are connected in a system. Note that the NR values are designed to have relatively small magnitude (compared to the impedance of the stub lines) thus small reflection amplification.

This antenna shown in the Figure 5-16 has the same dimensions as the previously presented passive antennas, except the NR-terminated-stubs. The NR circuit has been analyzed in detail in the previous chapter. The measured S-parameters are shown in Figure 5-17.

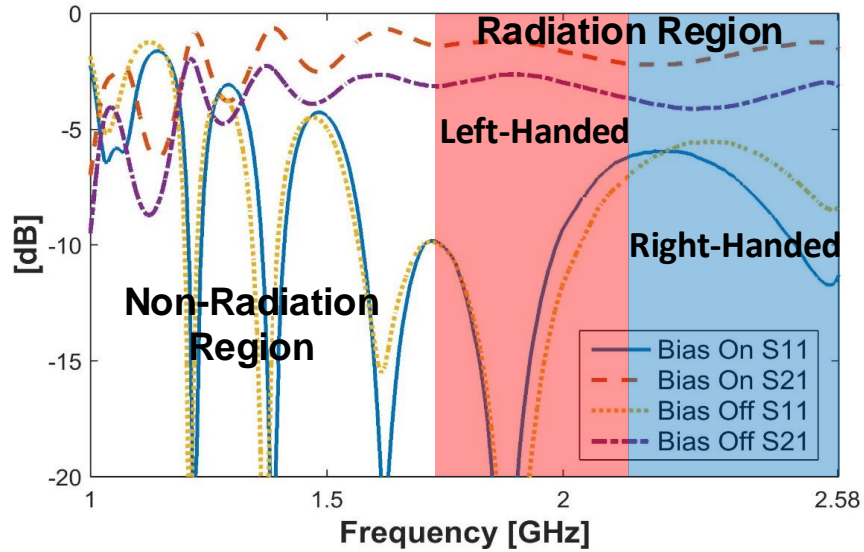


Figure 5-17 Measured return losses and insertion losses of the fabricated NRCRLH LWA prototype with biasing voltage turned on and off. The transition frequency is 2.2GHz.

It is noticed that the insertion loss can be reduced by turning the bias voltages of the NR circuits on and off, while the return loss is minimally affected by the status of the NR circuits. The raised S21 curve is attributed to the compensated power from the active circuits that amplify the guided propagating wave. Due to some minor fabrication error within the matching IDC (marked as B and C in dashed rectangles in Figure 5-16) the impedance matching was not as satisfactory as what was simulated in ADS and S11 curve is not well below  $-10\text{dB}$  in the radiation band. But this can certainly be improved with better fabrication capability and does not affect this demonstration of the NR-CRLH concept.



The antenna is also measured in an anechoic chamber. Figure 5-18 demonstrates the antenna mounted in the chamber and connected to biasing voltage regulators.

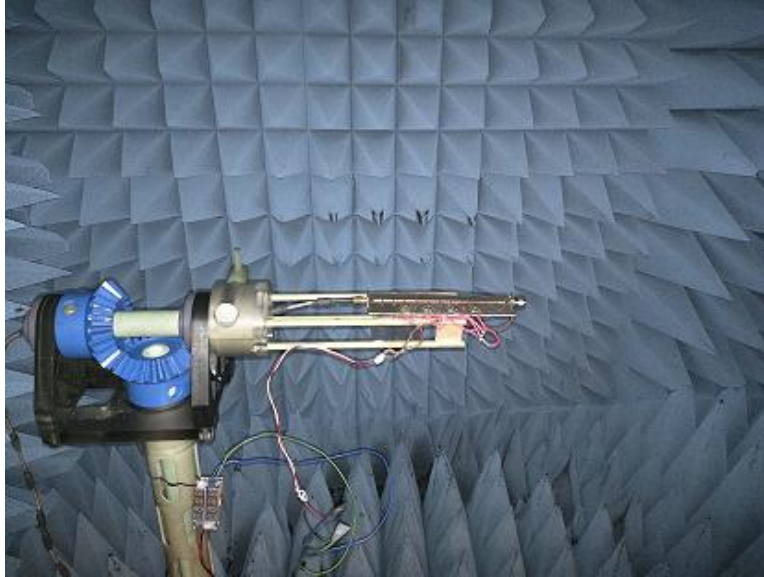


Figure 5-18 Photo of the active LWA mounted in the anechoic chamber. Wires connect DC biasing voltage form the voltage regulator, powered by a lithium-ion battery.

The anechoic chamber could record the radiated power at every angle. From the radiated power measurement we can roughly calculate antenna radiation patterns and various performances. The orientation and coordinate axes definitions can be found in Figure 5-19. The  $\theta = 90^\circ$  direction is the broadside direction with  $\varphi = 90^\circ$  ( $\varphi = 0$  starting at positive  $x$  axis).

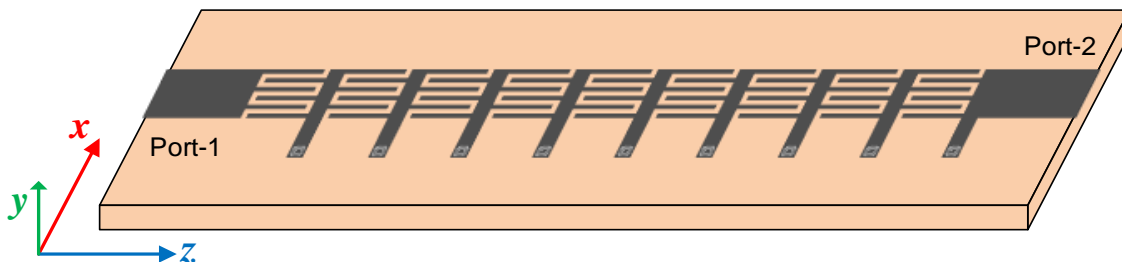


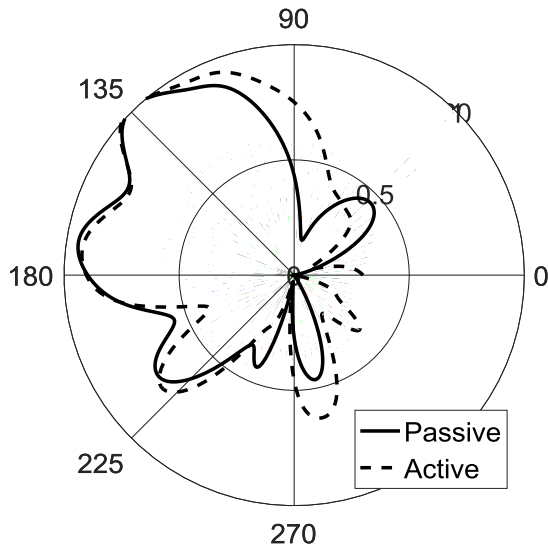
Figure 5-19 Coordinate axes definition diagram.

The measured antenna patterns of the active antenna and the passive counterpart are presented in Figure 5-20. The figure contains 8 polar plots of the measured radiation patterns from 1.9 GHz up to 2.57 GHz. In these plots, the measured radiation power values are in dBm scale. In order to compare the beamwidth, at each single frequency, the data are normalized to the maximum value of the dataset.

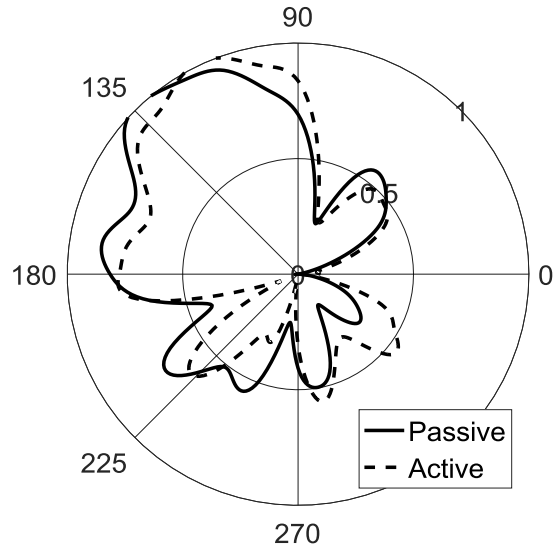
At 1.9 GHz, the active antenna shows wider beamwidth than the passive one. This might be because the NR circuit is not compensating sufficient energy at this frequency and the NR circuit reactive response is not well maintaining the same response as the shorted stub on the passive antenna.

At 2.0 GHz, the two beams begin to show better consistency, both in beamwidth and tilting angle. It is interesting to see that at 2.1 GHz, the active antenna radiates narrower beam than the passive antenna. The similar phenomenon is observed at 2.2 GHz as well. At this frequency, it is also apparent that the side-lobe is higher though the main-beam is narrower. Both observations reflect the assumed flat current distribution along the leaky guide.

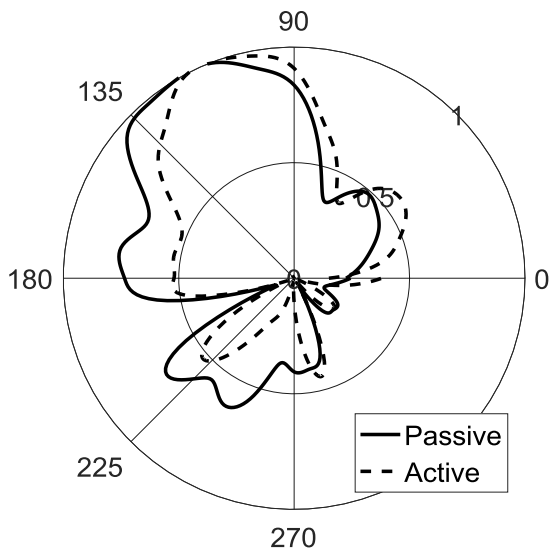
**Compare @ 1900MHz**



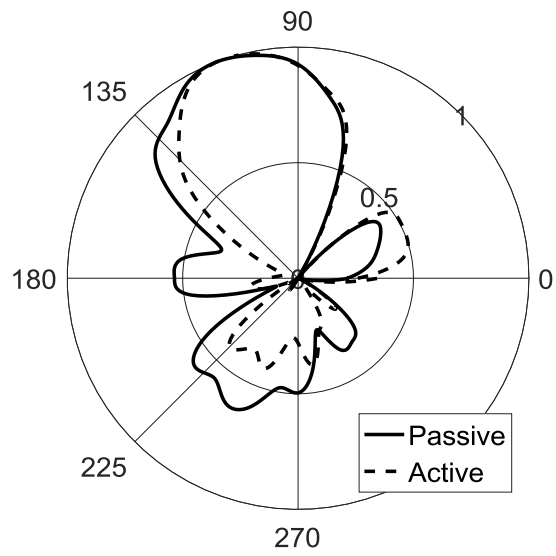
**Compare @ 2000MHz**



**Compare @ 2100MHz**



**Compare @ 2200MHz**



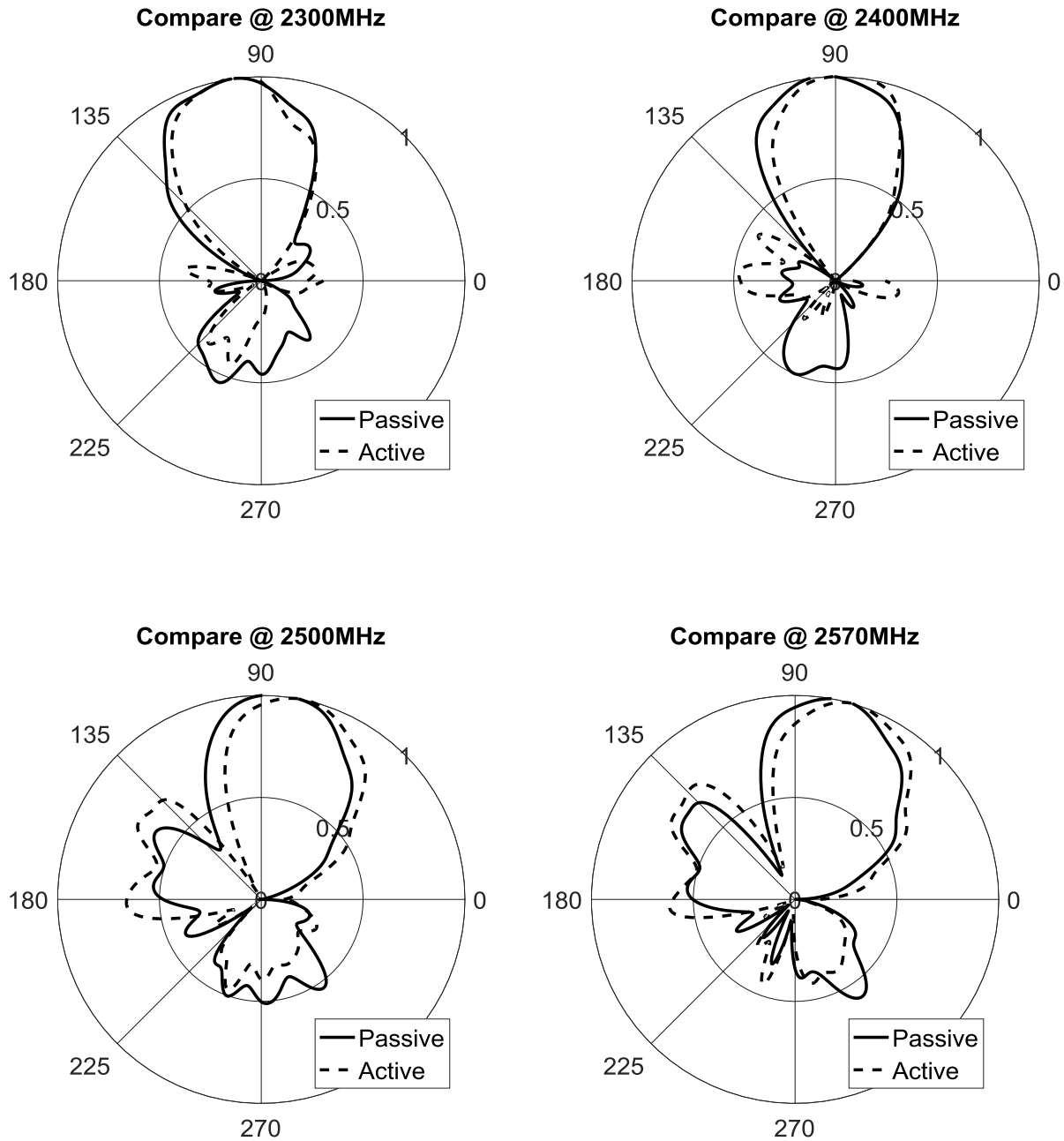


Figure 5-20 Measured E-cut radiation patterns of the passive and the active antennas in an anechoic chamber. The patterns are normalized in each frequency for comparison.

Near the transition frequency at 2.3 GHz, 2.4 GHz and 2.5 GHz, the two antennas radiate toward almost the same directions, while the active antenna has narrower beamwidth as expected. Higher side-lobes can be seen too. At broadside radiation frequency (transition frequency) 2.4 GHz, the active antenna scans to the broad side.

At all the frequencies, the beams plotted in dashed line tilts to a smaller  $\theta$  angle. This implies that the active antenna has a dispersion relation that is consistently lower than the passive one, considering both curves in the dispersion relation.

Although antenna gain and efficiency cannot be obtained from the chamber, the directivity at each frequency can be calculated. A comparison between the mixed-design active antenna and its passive counterpart is shown in Table 5-1.

Table 5-1 The measured directivity at different frequencies of the passive antenna (CRLH) and the active antenna (NR-CRLH).

f [GHz]	1.8	1.9	2.0	2.2	2.3	2.4	2.5
CRLH	10.8	9.4	8.2	7.7	7.8	6.8	6.8
NR-CRLH	10.4	10.7	10.6	10.9	8.3	7.8	7.1

The measured directivity values are obtained in dB scale. At most of the measured frequency points, the obtained directivity of the NR-CRLH LWA is higher than its passive counterpart. The two antennas are exactly the same in physical dimensions except for the stub length and termination. Primarily the increased directivity and narrowed beamwidth are due to that the current distribution on the active LWA is different from that of the passive LWA. This can be verified in the calculations in the following sub-section.

### 5.4.2. Explanations

In Figure 5-20, the two patterns are not significantly different from each other, which brings questions to the credibility of the change of the current distributions. The reason why the two results are similar is because the antenna is relatively short. The array factor calculation method would explain why it is not feasible to demonstrate more significant difference with antennas of 11 unit cells.

The radiation patterns with different attenuation constants from two antennas will be calculated using the array factor method and plotted. The first antenna is a short LWA with only 11 unit cells. The radiation patterns are plotted in Figure 5-21 with backward tilting and forward tilting. It is clearly shown that the curves of minimal loss ( $\alpha=0.5$ ) and moderate loss ( $\alpha=5$ ) are hardly distinguishable. When the attenuation is large ( $\alpha=10$ ), the pattern starts to show small difference, which is similar to the previously demonstrated measurement data. When the attenuation is extremely severe, although it is a very effective radiator since most power can be radiated within a short length, the pattern is still very close to the minimal loss case. The small difference among different patterns is seen in both backward and forward scanning.

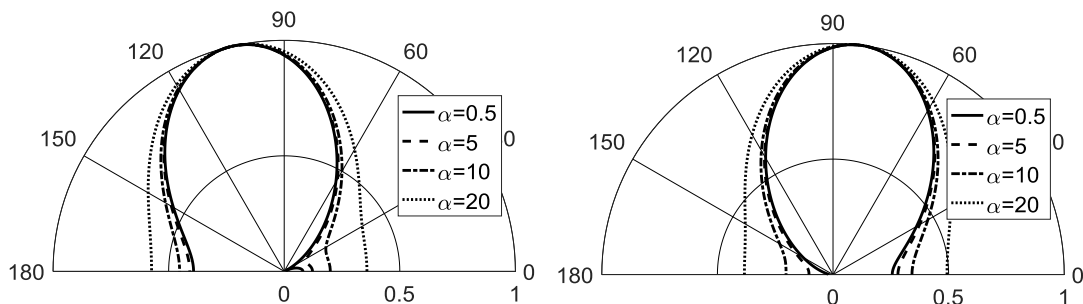


Figure 5-21 Calculated radiation pattern from an 11-unit-cell LWA.

However, when the antenna length is 51, the difference in radiation pattern caused by different attenuation constant become much more drastic. The patterns plotted in Figure 5-22 demonstrate that each pattern is easy to identify from the plots. No two curves are overlapping as in the 11-unit-cell antenna case.

In conclusion, it is the antenna length that limits the demonstration of the beamwidth reducing. If longer antennas can be designed and measured, the reduction in beamwidth would be much more significant. However, the small change in the radiation pattern on a relatively short LWA is a strong proof of the idea because it is difficult to realize such change unless the current distribution is well controlled.

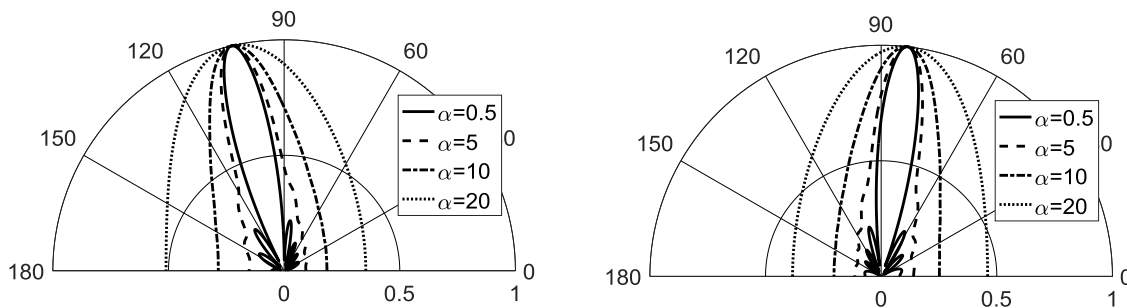


Figure 5-22 Calculated radiation pattern from a 51-unit-cell LWA.

### 5.5. Summary

The possibility of adjusting the radiation pattern by changing the current distribution is calculated and shown. Radiation patterns of the mixed active LWA prototype are presented and compared with those of a conventional passive LWA to prove the increased directivity and narrowed beamwidth. Depending on the manner the AUCs are employed, the current distribution can be controlled at different resolutions, from the highest (adjusting each unit cell) to any arbitrary

level (adjusting every  $n$  unit cells where  $n$  is a positive integer greater than one). A future work could be a design of a mixed (alternative) active LWA or pure active-unit-cell LWA of up to several tens of unit cells long, exhibiting unprecedented directivity and beamforming capability.



## Chapter 6 Conclusions

The wave-guiding problems in two types of unconventional structures are addressed. The characteristics of the guided waves are studied.

The first half of the dissertation described comprehensively the problems and solutions of the RWG filled with a uniaxially anisotropic or uniaxial medium. First we considered the cases when the optic axis is aligned with one of the coordinate axes. We proposed the method of mode decomposition with respect to the direction of the optic axis and demonstrated mathematical derivations and analytic solutions. The cutoff frequencies for  $TE_C$  and  $TM_C$  modes where the subscript C denotes the direction of the optic axis are obtained and found dependent on anisotropic permittivities, so are the dominant modes. Particularly, the  $TM_Z$  mode (similar to the conventional TM modes) can become the dominant mode when the uniaxial anisotropy of the inserted medium is strong enough. Other important wave properties including wave impedance and attenuation constants due to conductor loss are also studied, and closed form equations are obtained. The presence of the medium anisotropy leads to the changes in the wave mode characteristics and field distributions.

Secondly, when the optic axis is tilted but lying in sidewall planes, a computational method is proposed to solve the problems. In these cases  $TE_{0n}$  or  $TE_{m0}$  (to  $z$ ) modes exist depending on whether the optic axis lies on either the  $y$ - $z$  plane or  $x$ - $z$  plane, and the proposed computational method is designed for calculating supported hybrid wave modes in these tiled cases. The methodology is to discretize the wavenumbers in their appropriate domains and examine the boundary condition matrix (BCM) determinant with each set of wavenumbers that satisfy the dispersion relations. As a compromise of speed and accuracy, the calculated data from the

proposed numerical process are then used in curve fitting to search for more accurate numbers. The algorithm was executed using MATLAB scripts and its validity is verified by comparing the results of the limiting cases with the aligned cases whose analytical solutions were obtained previously. Through calculations it was found that although the conventional TE modes exist, they are not necessarily serving as the dominant modes. The lowest hybrid mode can become the dominant mode if certain condition is satisfied. This can be understood considering that in the uniaxial-Z case the  $TM_z$  modes can become the dominant mode, and these tilted cases can be considered as the tilted uniaxial-Z case and the effect of anisotropy could perturb the order of the lowest cutoff frequency modes.

In the future, this method may be applied to verify with the results against gyrotropic RWG problems, and to evaluate other waveguide problems including different types of media. The effect of finite side wall conductivity and dielectric losses are also interesting to investigate. Moreover, we could design an experiment to verify the calculated results. The methodology of this calculation process could also be used in other bounded media problems and to investigate the effect of anisotropy in different types of microwave structures.

In the second half of this dissertation, the novel negative resistance enhanced composite right/left-handed (NR-CRLH) structure is presented with analysis and experiments. It was shown that by adapting a new energy compensating circuit the active unit cell (AUC) incorporating the ICC NR circuit can simultaneously preserve the unique phase behaviors and consistent Bloch impedance in broad bandwidth while realizing zero insertion loss or even forward gain. The AUC was compared with its passive unit cell (PUC) counterpart through calculations and experiments. Unit cell analysis and experiment showed that the involved negative resistance minimally perturbs the phase behaviors of the passive unit cells and does not introduce stability issue, thus the

advantageous phase control and beam scanning capability of the original CRLH are both repeatable in the AUC based design. The novel power compensating mechanism does not prolong the length of each unit cell, therefore it does not break the direct connections between adjacent unit cells thus does not interrupt the periodicity of the original periodic structure. The design of the AUC can follow the mature PUC design guide and needs only to change a section of the stub line and add the NR circuit. By tuning of the NR circuit, the AUC can exhibit different level of forward loss or gain while maintaining the designed phase behaviors.

To demonstrate the application of the NR-CRLH structure as an leaky-wave antenna (LWA), the experiments and analysis of LWA radiation from different current distributions are presented. The possibility of adjusting the radiation pattern by changing the current distribution is calculated and shown in radiation pattern plots. In the experiment, the patterns of the mixed active LWA prototype are measured and compared with those of a conventional passive CRLH LWA to prove the increased directivity and narrower beamwidth. The comparison between the radiation angles also proves that the active unit cells preserved the metamaterial phase behaviors. Depending on the manner the AUCs are incorporated, the current distribution can be controlled at the desired resolutions from the highest (adjusting each unit cell) to any reasonably lower level (adjust after every an arbitrary number of unit cells) for any particular applications.

In antenna applications, the flexibility of including NR-enhanced unit cells in NR-CRLH structure allows the design of active LWAs that can have arbitrary current distributions. Because of the possible forward gain in a NR-CRLH unit cell, these current distributions may accurately follow desired mathematical description as long as the forward gain is high enough to realize the ramp rate. The NR-CRLH structure can also be used for resonant type antennas since the NR-CRLH structure is essentially a new type of transmission line. As well as resonant antenna, many

other microwave circuits/components can be designed using the NR-CRLH structure. Particularly, due to the zero-loss nature of the structure, it is practical to realize resonators of much higher  $Q$  than those realized by conventional microstrip lines and striplines. Furthermore, high- $Q$  resonators can improve the performances of a broader range of microwave components, like oscillators, mixers, and power amplifiers. Therefore, many applications of NR-CRLH structure are to be explored in the future.

## Bibliography

- [1] N. Marcuvitz, *Waveguide Handbook*, MIT Radiation Lab Series, vol. 10, New York, NY: McGraw-Hill, 1951.
- [2] R. E. Collin, *Field Theory of Guided Waves*, 2nd Ed. ed., New York, NY: IEEE PRESS, 1991.
- [3] B. Lax and K. J. Button, *Microwave Ferrites and Ferrimagnetics*, 1st ed., New York, NY: McGraw-Hill, 1962.
- [4] R. E. Collin, *Foundations for Microwave Engineering*, 2nd Ed. ed., New York, NY: Wiley, 2000.
- [5] D. M. Pozar, *Microwave Engineering*, 4th Ed. ed., Hoboken, NJ: Wiley, 2011.
- [6] R. Marques, J. Martel, F. Mesa and F. Medina, "Left-handed-media simulation and transmission of EM waves in subwavelength split-ring-resonator-loaded metallic waveguides," *Phys. Rev. Ltr.*, vol. 19, no. 18, p. 183901, Oct. 2002.
- [7] R. P. Owens, J. E. Aitken and T. C. Edwards, "Quasi-static characteristics of microstrip on an anisotropic sapphire substrate," *IEEE Trans. Microw. Theory Techn.*, vol. 24, no. 8, pp. 499-505, Aug 1976.
- [8] J. B. Davis, "Propagation in rectangular waveguide filled with skew uniaxial dielectric," *IEEE Trans. Microw. Theory Techn.*, vol. 15, no. 6, pp. 372-376, June 1967.
- [9] N. G. Alexopoulos, "Integrated-circuit structures on anisotropic substrates," *IEEE Trans. Microw. Theory Techn.*, vol. 33, no. 10, pp. 847-861, Oct 1985.

- [10] N. G. Alexopoulos and C. Krowne, "Characteristics of single and coupled microstrips on anisotropic substrate," *IEEE Trans. Microw. Theory Techn.*, vol. 26, no. 6, pp. 387-393, June 1978.
- [11] D. M. Pozar, "Radiation and scattering from microstrip patch on a uniaxial substrate," *IEEE Trans. Antennas and Propagat.*, vol. 35, no. 6, pp. 613-621, 1987.
- [12] A.-M. A. El-Sherbiny, "Hybrid mode analysis of microstrip lines on anisotropic substrates," *IEEE Trans. Microw. Theory Techn.*, vol. 29, no. 12, pp. 1261-1266, Dec. 1981.
- [13] W. B. Weir, "Automatic measurement of complex dielectric constant and permeability at microwave frequencies," *Proceedings of the IEEE*, vol. 62, no. 1, pp. 33-36, Jan. 1974.
- [14] N. J. Damaskos, R. B. Mack, A. L. Maffett, W. Parmon and P. L. E. Uslenghi, "The inverse problem for biaxial materials," *IEEE Trans. Microw. Theory Techn.*, vol. 32, no. 4, pp. 400-405, Apr. 1984.
- [15] D. W. Berreman, "Optics in stratified and anisotropic media: 4x4-matrix formulation," *Journal of the Optical Society of America*, vol. 62, no. 4, pp. 502-510, 1972.
- [16] C. M. Krowne, "Fourier transformed matrix method of finding propagation characteristics of complex anisotropic layered media," *IEEE Trans. Microw. Theory Techn.*, vol. 32, no. 12, pp. 1617-1625, Dec. 1984.
- [17] C. M. Krowne, "Green's function in the spectral domain for biaxial and uniaxial anisotropic planar dielectric structures," *IEEE Trans. Antennas Propagat.*, vol. 32, no. 12, pp. 1273-1295, Dec. 1984.

- [18] T. Itoh and R. Mittra, "Spectral-domain approach for calculating the dispersion characteristics of microstrip lines," *IEEE Trans. Microw. Theory Techn.*, vol. 21, no. 7, pp. 496-499, July 1973.
- [19] G. Plaza, F. Mesa and F. Medina, "On the use of SDA for the analysis of boxed planar lines with complex media," *IEEE Trans. Microw. Theory Techn.*, vol. 49, no. 7, pp. 455-458, July 2001.
- [20] D. R. Smith, W. J. Padilla, D. C. Vier, S. C. Nemat-Nasser and S. Schultz, "Composite medium with simultaneously negative permeability and permittivity," *Phys. Rev. Ltr.*, vol. 84, no. 18, pp. 4184-4187, 1 May 2000.
- [21] V. Veselago, "The electrodynamics of substances with simultaneously negative values of permittivity and permeability," *Soviet Physics Uspekhi*, vol. 10, no. 4, pp. 509-514, 1968.
- [22] J. B. Pendry, "Negative refraction makes a perfect lens," *Phys. Rev. Ltr.*, vol. 85, no. 18, pp. 3966-3969, 30 Oct. 2000.
- [23] R. A. Shelby, D. R. Smith, S. C. Nemat-Nasser and S. Schultz, "Microwave transmission through a two-dimensional, isotropic, left-handed metamaterial," *Appl. Phys. Ltr.*, vol. 78, no. 4, pp. 489-491, 22 Jan. 2001.
- [24] R. A. Shelby, D. R. Smith and S. Schultz, "Experimental verification of a negative index of refraction," *Science*, vol. 292, pp. 77-79, 6 April 2001.
- [25] D. R. Smith, D. Schurig, M. Rosenbluth, S. Schultz, S. Anantha Ramakrishna and J. B. Pendry, "Limitations on subdiffraction imaging with a negative refractive index slab," *Appl. Phys. Ltr.*, vol. 82, no. 10, pp. 1506-1508, 10 March 2003.

- [26] L. Liu, C. Caloz and T. Itoh, "Dominant mode leaky-wave antenna with backfire-to-endfire scanning capability," *Electron. Lett.*, vol. 38, no. 23, pp. 1414-1416, Nov. 2002.
- [27] S. Anantha Ramakrishna and J. B. Pendry, "Removal of absorption and increase in resolution in a near-field lens via optical gain," *Phys. Rev. B (Rapid Communication)*, vol. 67, no. 20, pp. 201101(1) -201101(4), 14 May 2003.
- [28] J. Skaar, "Fresnel equations and the refractive index of active media," *Phys. Rev. E*, vol. 73, pp. 026605(1)-026605(7), Feb. 2006.
- [29] M. I. Stockman, "Criterion for negative refraction with low optical losses from a fundamental principle of causality," *Phys. Rev. Lett.*, vol. 98, no. 17, pp. 177404(1)-177404(4), Apr. 2007.
- [30] P. Kinsler and M. W. McCall, "Causality-based criteria for a negative refractive index must be used with care," *Phys. Rev. Lett.*, vol. 101, no. 16, pp. 167401(1)-167401(4), Oct. 2008.
- [31] B. Nistad and J. Skaar, "Causality and electromagnetic properties of active media," *Phys. Rev. E*, vol. 78, no. 3, pp. 036603(1)-036603(10), Sept. 2008.
- [32] D. Bergman and M. I. Stockman, "Surface plasmon amplification by stimulated emission of radiation: quantum generation of coherent surface plasmons in nanosystems," *Phys. Rev. Lett.*, vol. 90, no. 2, pp. 027402(1)-027402(4), Jan. 2003.
- [33] S. Xiao, V. P. Drachev, A. V. Kildishev, X. Ni and U. K. Chettiar, "Loss-free and active optical negative-index metamaterials," *Nature*, vol. 466, p. 738, Aug. 2010.
- [34] M. W. Klein, M. Wegener, N. Feth and S. Linden, "Experiments on second- and third-harmonic generation from magnetic metamaterials," *Optics Express*, vol. 15, no. 8, pp. 5238-5247, Apr. 2007.



- [35] I. V. Shadrivov, A. B. Kozyrev, D. W. van der Weide and Y. S. Kivshar, "Tunable transmission and harmonic generation in nonlinear metamaterials," *Appl. Phys. Lett.*, vol. 93, pp. 161903(1)-161903(3), Oct. 2008.
- [36] A. B. Kozyrev, H. Kim and D. W. van der Weide, "Parametric amplification in left-handed transmission line media," *Appl. Phys. Lett.*, vol. 88, pp. 264101(1)-264101(4), June 2006.
- [37] T. Jiang, K. Chang, L.-M. Si, L. Ran and H. Xin, "Active microwave negative-index metamaterial transmission line with gain," *Phys. Rev. Lett.*, vol. 107, no. 20, pp. 205503(1)-205503(4), 11 Nov. 2011.
- [38] F. P. Casares-Miranda, C. Camacho-Penalosa and C. Caloz, "High-gain active composite right-/left-handed leaky-wave antenna," *IEEE Trans. Antenna Propagat.*, vol. 54, no. 8, pp. 2292-2300, Aug. 2006.
- [39] A. W. Hull, "The dynatron - a vacuum tube possessing negative electric resistance," *Proc. IRE*, vol. 6, pp. 5-35, Sept. 1915.
- [40] E. W. Herold, "Negative resistance and devices for obtaining it," *Proc. IRE*, vol. 23, no. 10, pp. 1201-1223, Oct 1935.
- [41] H. Tohyama and H. Mizuno, "23-GHz band GaAs MESFET reflection-type amplifier," *IEEE Trans. Microw. Theory Techn.*, vol. 27, no. 5, pp. 408-411, May 1979.
- [42] K. K. N. Chang, "(Correspondence) Low-noise tunnel-diode amplifier," *Proc. IRE*, vol. 47, no. 7, pp. 1268-1269, July 1959.
- [43] J. R. Wait, *Electromagnetic Waves in Stratified Media*, Oxford, UK: Pergamon Press, 1970.
- [44] H.-S. Tuan, "Mode theory of waveguide filled with warm uniaxial plasma," *IEEE Trans. Microw. Theory Techn.*, vol. 17, no. 3, pp. 134-137, 1969.

- [45] A. Knoesen, T. K. Gaylord and M. G. Moharam, "Hybrid guided modes in uniaxial dielectric planar waveguides," *Journal of Lightwave Technology*, vol. 6, no. 6, pp. 1083-1144, 1988.
- [46] J. C. Rautio and S. Arvas, "Measurement of planar substrate uniaxial anisotropy," *IEEE Trans. Microw. Theory Techn.*, vol. 57, no. 10, pp. 2456-2463, Oct 2009.
- [47] J. C. Rautio, "Measurement of uniaxial anisotropy in Rogers RO3010 Substrate Material," in *Int. Conf. on Microw. Commun. Antennas and Electronic Systems (COMCAS)*, Tel Aviv, Isreal, 2009.
- [48] S. Hraba, J. Bartolic and Z. Sipus, "Waveguide miniaturization using uniaxial negative permeability metamaterial," *IEEE Trans. Antennas Propagat.*, vol. 53, no. 1, pp. 110-119, Jan. 2005.
- [49] S. Liu, L. W. Li, M. S. Leong and T. S. Yeo, "Rectangular conducting waveguide filled with uniaxial anisotropic media: a modal analysis and dyadic Green's function," *Progress in Electromagnetics Research*, vol. 25, pp. 111-129, 2000.
- [50] R. F. Harrington, *Time-Harmonic Electromagnetic Fields*, New York, NY: McGraw-Hill, 1961.
- [51] J. A. Kong, *Electromagnetic Wave Theory*, Cambridge, Massachusetts: EMW Publishing, 2008.
- [52] K. Wu, D. Deslandes and Y. Cassivi, "The substrate integrated circuits - a new concept for high-frequency electronics and optoelectronics," in *6th Int. Conf. on Telecommunications in Modern Satellite, Cable and Broadcasting Service*, Nis, Yugoslavia, Yugoslavia, 2003.

- [53] A. T. Adams and J. K. Lee, *Electromagnetics*, 1st ed., San Diego, CA: University Readers, 2012.
- [54] J. K. Lee and J. A. Kong, "Dyadic Green's functions for layered anisotropic medium," *Electromagnetics*, vol. 3, no. 2, pp. 111-130, Feb. 1983.
- [55] A. D. Berk, "Variational principles for electromagnetic resonators and waveguides," *IEEE Trans. Antennas Propagat.*, vol. 4, no. 2, pp. 104-111, Apr. 1956.
- [56] G. B. Arfken and H. J. Weber, *Mathematical Methods for Physicists*, 5th ed., Burlington, MA: Academic Press, 2001.
- [57] G. J. Gabriel and M. E. Brodwin, "The solution of guided waves in inhomogeneous anisotropic media by perturbation and variational methods," *IEEE Trans. Microw. Theory Techn.*, vol. 13, no. 5, pp. 641-646, May 1965.
- [58] M. H. Engineer and B. R. Nag, "Propagation of electromagnetic waves in rectangular guides filled with a semiconductor in the presence of a transverse magnetic field," *IEEE Trans. Microw. Theory Techn.*, vol. 13, no. 5, pp. 364-370, May 1965.
- [59] C.-T. Tai, *Dyadic Green Functions in Electromagnetic Theory*, 2nd ed., New York, NY: IEEE PRESS, 1994.
- [60] N. J. Damaskos, A. L. Maffett and P. Uslenghi, "Dispersion relation for general anisotropic media," *IEEE Trans. Antennas Propagat.*, vol. 30, no. 5, pp. 991-993, Sept 1982.
- [61] L. N. Trefethen and D. Bau, *Numerical Linear Algebra*, 1st ed., Philadelphia, PA: SIAM, 1997.
- [62] Hildebrand, *Methods of Applied Mathematics*, 2nd ed., New York, NY: Dover Publications, 1992.

- [63] Y. Huang, "Dyadic green's functions for layered general anisotropic media and their application to radiation of dipole antennas," *PhD Dissertation, Syracuse University*, May 2014.
- [64] G. Barzilai and G. Gerosa, "Modes in rectangular guides filled with magnetized ferrite," *Nuovo Cimento*, vol. 7, no. 5, pp. 685-697, March 1958.
- [65] B. Lax, K. J. Button. and L. M. Roth, "Ferrite phase shifters in rectangular wave guide," *J. Appl. Phys.*, vol. 25, no. 11, pp. 1413-1421, Nov. 1954.
- [66] G. Barzilai and G. Gerosa, "Modes in rectangular guides partially filled with transversely magnetized ferrite," *IRE Trans. Antennas Propagat.*, vol. 7, no. 5, pp. 471-474, Dec. 1959.
- [67] K. Sun, J. K. Lee and J. W. Graham, "Analysis of rectangular waveguide containing uniaxia meidum with aligned optic axis," in *IEEE Int. Symp. on Antennas and Propagation*, Memphis, TN, 2014.
- [68] J. W. Graham and J. K. Lee, "Reflection and transmission at biaxially anisotropic-isotropic interfaces," *Progress in Electromagnetic Research (PIER)*, vol. 136, pp. 681-702, 2013.
- [69] S. Zhang, W. Fan, N. C. Panoiu, K. J. Malloy, R. M. Osgood and S. R. J. Brueck, "Experimental demonstration of near-infrared negative-index metamaterials," *Phys. Rev. Ltr.*, vol. 95, no. 12, pp. 137404(1)-137404(4), Sept. 2005.
- [70] A. K. Iyer and G. V. Eleftheriades, "Negative Refractive Index Metamaterials Supporting 2-D Waves," in *Microwave Symposium Digest, IEEE MTT-S International Symposium*, Seattle, WA, 2002.

- [71] G. V. Eleftheriades, A. K. Iyer and P. C. Kremer, "Planar negative refractive index media using periodically L-C loaded transmission line," *IEEE Trans. Microw. Theory Techn.*, vol. 50, no. 12, pp. 2702-2712, Dec. 2002.
- [72] C. Caloz and T. Itoh, "Application of the transmission line theory of left-handed (LH) materials to the realization of a microstrip "LH Line"," in *IEEE Int. Symp. on Antennas and Propagation*, San Antonio, TX, June 2002.
- [73] C. Caloz and T. Itoh, "Invited - novel microwave devices and structures based on the transmission line approach of meta-materials," in *IEEE MTT-S Int. Symp. Dig.*, Philadelphia, PA, June, 2003.
- [74] C. A. Allen, K. M. Leong and T. Itoh, "Design of microstrip resonators using balanced and unbalanced composite right/left-handed transmission lines," *IEEE Trans. Microw. Theory Techn.*, vol. 54, no. 7, pp. 3104-3112, July 2006.
- [75] C. Caloz and T. Itoh, "Transmission line approach of left-handed (LH) material and microstrip implementation of an artificial LH transmission line," *IEEE Trans. Antennas Propagat.*, vol. 52, no. 5, pp. 1159-1166, May 2004.
- [76] A. Sanada, C. Caloz and T. Itoh, "Characteristics of the composite right/left-handed transmission lines," *IEEE Microwave Wireless Component Letters*, vol. 14, no. 2, pp. 68-70, Feb. 2004.
- [77] C. Caloz, C. Allen and T. Itoh, "Unusual propagation characteristics in CRLH structures," in *IEEE Int. Symp. Antennas and Propagation* , Monterey, CA, June 2004.

- [78] C. Caloz, A. Sanada and T. Itoh, "A novel composite right/left-handed coupled-line directional coupler with arbitrary coupling level and broad bandwidth," *IEEE Trans. Microw. Theory Techn.*, vol. 52, no. 3, March 2004.
- [79] I.-H. Lin, M. DeVincentis, C. Caloz and T. Itoh, "Arbitrary dual-band components using composite right/left-handed transmission lines," *IEEE Trans. Microw. Theory Techn.*, vol. 52, no. 4, pp. 1142-1149, April 2004.
- [80] A. Lai and T. Itoh, "Composite Right/Left-Handed transmission line metamaterials," *IEEE Microwave Magazine*, pp. 34-50, Sep. 2004.
- [81] D. R. Jackson, C. Caloz and T. Itoh, "Leaky-Wave Antennas," *Proceedings of the IEEE*, vol. 1000, no. 7, pp. 2194-2206, July 2012.
- [82] R. F. Harrington, *Field Computation by Moment Method*, New York, NY: Wiley, 1963.
- [83] C. Caloz and T. Itoh, *Electromagnetic Metamaterials: Transmission Line Theory and Microwave Applications*, Hoboken, NJ: Wiley Interscience Publication, 2005.
- [84] F. P. Casares-Miranda, P. Otero, E. Marquez-Segura and C. Camacho-Penalosa, "Wire Bonded Interdigital Capacitor," *IEEE Microw. Wireless Comp. Ltr.*, vol. 15, no. 10, pp. 700-702, Oct. 2005.
- [85] S. Paulotto, P. Baccarelli, F. Frezza and D. R. Jackson, "Full-wave modal dispersion analysis and broadside optimization for a class of microstrip CRLH leaky-wave antennas," *IEEE Trans. Microw. Theory Techn.*, vol. 56, no. 12, pp. 2826-2837, Dec. 2008.
- [86] R. Esfandiari, D. W. Maki and M. Siracusa, "Design of interdigitated capacitors and their application to Gallium Arsenide monolithic filters," *Trans. Microw. Theory Techn.*, vol. 31, no. 1, pp. 57-64, Jan. 1983.

- [87] L.-C. Tsai and C.-W. Hsue, "Dual-band bandpass filters using equal-length coupled-serial-shunted lines and Z-transform technique," *IEEE Trans. Microw. Theory Techn.*, vol. 52, no. 4, pp. 1111-1117, Apr. 2004.
- [88] L. Zhu and W. Menzel, "Compact microstrip bandpass filter with two transmission zeros using a stub-tapped half-wavelength line resonator," *IEEE Microw. Wireless Components Ltr.*, vol. 13, no. 1, pp. 16-18, Jan. 2003.
- [89] M.-L. Chuang and M.-T. Wu, "Microstrip diplexer design using common T-shaped resonator," *IEEE Microw. Wireless Component Ltr.*, vol. 21, no. 11, pp. 583-585, Nov. 2011.
- [90] K. Chang, D. M. English, R. S. Tahim, A. J. Grote, T. Pham, C. Sun, G. M. Hayashibara, P. C. Yen and W. S. Piotrowski, "W-Band (75G-110GHz) Microstrip Components," *IEEE Trans. Microw. Theory Techn.*, vol. 33, no. 12, pp. 1375-1382, Dec. 1985.
- [91] H. Tohyama, "20 GHz band GaAs-FET waveguide-type amplifier," in *IEEE MTT-S Int. Microw. Symp. Digest*, San Diego, CA, 1977.
- [92] M. E. Hines, "Negative-resistance diode power amplification," *IEEE Trans. Electron Devices*, vol. 17, no. 1, pp. 1-8, Jan. 1970.
- [93] P. Gardner and D. K. Paul, "Aspects of the design of low noise, negative resistance, reflection mode transistor amplifiers," *IEEE Trans. Microw. Theory Techn.*, vol. 39, no. 11, pp. 1869-1875, Nov 1991.
- [94] L. Esaki, "New phenomenon in narrow Germanium p-n junctions," *Phys. Rev.*, vol. 109, no. 2, pp. 603-604, 15 Jan. 1958.

- [95] H. G. Dill, "Inductive semiconductor elements and their application in bandpass amplifiers," *IRE Trans. Military Electronics*, vol. 5, no. 3, pp. 239-250, July 1961.
- [96] J. A. Archer, J. F. Gibbons and G. M. Purnaiya, "Use of transistor-simulated inductance as an interstage element in broadband amplifiers," *IEEE J. Solid-State Circuit*, vol. 3, no. 1, pp. 12-21, March 1968.
- [97] A. S. Sedra and K. C. Smith, *Microelectronic Circuits*, 5th ed., New York, NY: Oxford, 2003.
- [98] T. H. Lee, *The Design of CMOS Radio-Frequency Integrated Circuits*, 2nd ed., New York, NY: Cambridge University Press, 2004.
- [99] G. Gonzalez, *Microwave Transistor Amplifiers*, 2nd ed., Upper Saddle River, NJ: Prentice-Hall, 1996.
- [100] R. V. Snyder and D. L. Bozarth, "Analysis and design of a microwave transistor active filter," *IEEE Trans. Microw. Theory and Techn.*, vol. 18, no. 1, pp. 2-9, Jan. 1970.
- [101] J. F. Gibbons, "An analysis of the modes of operation of a simple transistor oscillator," *Proc. IRE*, vol. 49, no. 9, pp. 1383-1390, Sept. 1961.
- [102] D. K. Adams and R. Y. C. Ho, "Active filters for UHF and microwave frequencies," *IEEE Trans. Microw. Theory Techn.*, vol. 17, no. 9, pp. 662-670, Sept. 1969.
- [103] C.-Y. Chang and T. Itoh, "Microwave active filters based on coupled negative resistance method," *IEEE Trans. Microw. Theory Techn.*, vol. 38, no. 12, pp. 11879-1884, Dec. 1990.
- [104] J. Lindmayer and W. North, "The inductive effect in transistors," *Solid-State Electronics*, vol. 8, no. 4, pp. 409-415, Apr. 1965.



- [105] S. C. Dutta Roy, "The inductive transistor (Correspondence)," *IEEE Trans. Circuit Theory*, vol. 10, no. 1, pp. 113-1158, Mar 1963.
- [106] M. R. Moazzam, I. D. Robertson, A. H. Aghvami and M. Guglielmi, "S-band monolithic active filter using actively-coupled resonator technique," in *Proc. 22nd European Microwave Conf.*, 1992.
- [107] S. Hara, T. Tokumitsu, T. Tanaka and M. Aikawa, "Broad-band monolithic microwave active inductor and its application to miniaturized wide-band amplifiers," *IEEE Trans. Microw. Theory Techn.*, vol. 36, no. 12, pp. 1920-1924, Dec. 1988.
- [108] S. C. Dutta Roy, "Theory of exponentially tapered RC transmission lines for phase-shift oscillators," *Proc. IEEE*, vol. 110, no. 10, pp. 1764-1770, Oct. 1963.
- [109] P. R. Gray, P. J. Hurst, S. H. Lweis and R. G. Meyer, *Analysis and Design of Analog Integrated Circuits*, 4th ed., New York, NY: Wiley, 2000.
- [110] T. H. Lee, *Planar Microwave Engineering*, Cambridge: CAMBRIDGE UNIVERSITY PRESS, 2004.
- [111] M. E. Goldfarb and R. A. Pucel, "Modeling via hole grounds in microstrip," *IEEE Microw. Compon. Lett.*, vol. 1, no. 6, pp. 135-137, June 1991.
- [112] E. O. Hammerstad, "Equations for microstrip circuit design," in *1975 5th European Microw. Conf.*, Hamburg, Germany, 1975.
- [113] R. W. Ziolkowski, "Metamaterial-based antennas: research and developments," *IEICE Trans. Electron.*, vol. 89, no. 9, pp. 1267-1275, Sep. 2006.
- [114] Y. Dong and T. Itoh, "Metamaterial-based antennas," *Proceedings. of IEEE*, vol. 100, no. 7, pp. 2271-2285, July 2012.

- [115] W. L. Stutzman and G. A. Thiele, *Antenna Theory and Design*, 2nd ed., New York, NY: Wiley, 1998.
- [116] A. A. Oliner, "Leaky waves: basic properties and applications," in *Asia Pacific Microwave Conference*, Hong Kong, PRC, 1997.
- [117] L. O. Goldstone and A. A. Oliner, "Leaky-wave antennas I: Rectangular Waveguides," *IRE Trans. Antennas Propagat.*, vol. 7, pp. 307-319, May 1959.
- [118] C. A. Balanis, *Antenna Theory - Analysis and Design*, 3rd ed., Hoboken, NJ: John Wiley & Sons, 2005.
- [119] J. L. Volakis, *Antenna Engineering Handbook*, 4th ed., New York, NY: McGraw-Hill, 2007.
- [120] V. H. Rumsey, "Traveling wave slot antennas," *J Appl. Phys.*, vol. 24, no. 11, pp. 1358-1365, Nov. 1953.
- [121] J. N. Hines, V. H. Rumsey and C. H. Walter, "Traveling-wave slot antennas," *Proc. IRE*, vol. 41, no. 11, pp. 1624-1953, Nov. 1953.
- [122] W. Menzel, "A new travelling wave antenna in microstrip," in *8th European Microwave Conference*, Paris, France, 1978.
- [123] C. Caloz and T. Itoh, "Array factor approach of leaky-wave antennas and applications to 1-D/2-D composite right/left-handed (CRLH) structures," *IEEE Microw. Compon. Lett.*, vol. 14, no. 6, pp. 274-276, June 2004.

# Vita

**Name of Author:** Kepei Sun

**Data and Place of Birth:** June 22, 1983, Zhengzhou, Henan Province, China

## Positions

### Academic Appointments

Sept. 2014 – Dec. 2016 Graduate Teaching Assistant, Syracuse University, Department of Electrical Engineering and Computer Science.  
Syracuse, NY, USA

Sept. 2012 – Aug. 2014 Graduate Research Assistant, Syracuse University, Department of Electrical Engineering and Computer Science and CASE.  
Syracuse, NY, USA

### Other Employment

Jan 2017 – Current Microwave/RF Engineer, Anaren Microwave Inc.  
East Syracuse, NY, USA

May 2014 – Aug. 2014 Electrical Engineering Co-op, Arcom Labs, Inc.  
Syracuse, NY, USA

May 2013 – Dec. 2013 Hardware Engineering Co-op, Blue-Highway, Inc.  
Syracuse, NY, USA

Sept. 2011 – Dec. 2011 Embedded Software Engineer Co-op, Anaren Microwave, Inc.  
East Syracuse, NY, USA

July 2006 – July 2010 Beijing Symfun Optic Communication, Ltd.  
Beijing, China

### Degrees

2010 – 2012 M.S., Electrical Engineering, Syracuse University Syracuse  
Syracuse, NY, USA

2002 – 2006 B.E., Electronic and Information Engineering, North China  
University of Technology, Beijing, China

### Publications

## Journal Articals

- J1. K. Sun, J. H. Choi, and J. K. Lee, "Negative resistance enhanced composite right/left-handed transmission line and its application as the leaky-wave antenna," submitted to *IEEE Trans. Antennas and Propagat.*, 2017.
- J1. K. Sun, J. H. Choi, J. K. Lee, and S. Han, "Miniaturized active metamaterial resonant antenna with improved radiation performances based on negative-resistance-enhanced CRLH transmission lines," submitted to *IEEE Antenna and Wave Propagation Ltr.*, 2017.
- J2. K. Sun, J. K. Lee, and J. W. Graham, "Fields and wave modes analysis of rectangular waveguide filled with uniaxial medium," *IEEE Trans. Microw. Theory Techn.*, vol. 64, no. 11, pp. 3429-3440, Nov. 2016.
- J3. M. Yazdani, J. K. Lee, J. Mautz, E. Arvas, and K. Sun, "Ray tracing theory in a radially uniaxial sphere," *IEEE Trans. Antennas Propagat.*, vol. 63, no. 11, pp. 5165-5169, Sep 2015.

## Conference Presentations

- C1. K. Sun and J. K. Lee, "Field distributions of the hybrid modes in rectangular waveguides filled with uniaxial media with tilted optic axis lying in sidewall planes," *32<sup>nd</sup> Int. Union of Radio Science (URSI) General Assembly & Scientific Symp. (GASS)*, Montreal, Canada, August 2017.
- C2. K. Sun and J. K. Lee, "Hybrid mode analysis of rectangular waveguide filled with uniaxial media with tilted optic axis lying in sidewall planes," *2016 IEEE Int. Conf. Antenna Measurements & Applications (CAMA)*, Syracuse, NY, Oct. 23-27, 2016.
- C3. K. Sun, J. H. Choi, and J. K. Lee, "Miniaturized quasi-Yagi antenna based on metaedge reflector," *IEEE Int. Symp. Antennas Propagat.*, Fajardo, Puerto Rico, June 2016.
- C4. K. Sun, J. H. Choi, and J. K. Lee, "High directivity negative-resistance composite right/left-handed leaky-wave antenna," *IEEE MTT-S Int. Mcirow. Symp.*, San Francisco, CA, May 2016.
- C5. M. Yazdani, J. K. Lee, J. Mautz, E. Arvas, and K. Sun, "Shortcut waves in a radially uniaxial sphere," *Proceedings 2015 IEEE Int. Symp. Antennas Propagat.*, pp. 1112-1113, Vancouver, BC, Canada, July 2015.
- C6. K. Sun, J. K. Lee, and J. W. Graham, "Rectangular waveguide containing uniaxial medium with tilted optic axis in sidewall plane," *Proceedings 2015 IEEE Int. Symp. Antennas Propagat.*, pp. 1116-1117, Vancouver, BC, Canada, July 2015.
- C7. K. Sun, J. K. Lee, and J. W. Graham, "Analysis of rectangular waveguide containing uniaxial medium with aligned optic axis," *Proceedings 2014 IEEE Int. Symp. Antennas Propagat.*, pp. 1564-1565, Memphis, TN, June 2014.
- C8. K. Sun, Y. He, H. Chen, L. Murphy, and E. Arvas, "Design of low noise amplifiers with low return loss," *2014 Int. ACES Symp.*, Jacksonville, FL, March 2014.